

## **Heterostructured stainless steel: properties, current trends, and future perspectives**

L. Romero-Resendiz <sup>a</sup>, M. El-Tahawy <sup>b</sup>, T. Zhang <sup>a</sup>, M.C. Rossi <sup>c,d</sup>,

D. M. Marulanda-Cardona <sup>e</sup>, T. Yang <sup>a</sup>, V. Amigó-Borrás <sup>d</sup>, Y. Huang <sup>f,g</sup>,

H. Mirzadeh <sup>h</sup>, I. J. Beyerlein <sup>i,j</sup>, J. C. Huang <sup>k</sup>, T. G. Langdon <sup>g</sup>, Y. T. Zhu <sup>a,l,m\*</sup>

<sup>a</sup> Department of Materials Science and Engineering, City University of Hong Kong,  
Hong Kong

<sup>b</sup> Department of Physics, Faculty of Science, Tanta University, 31527, Tanta, Egypt

<sup>c</sup> Munir Rachid Corrosion Laboratory, Department of Materials Engineering, Federal  
University of São Carlos, Rodovia Washington Luis Km 235, 13565-905 São Carlos, SP,  
Brazil

<sup>d</sup> Universitat Politècnica de València, Institut de Tecnologia de Materials, Camí de Vera  
s/n, 46022 València, Spain

<sup>e</sup> Faculty of Engineering, Universidad Militar Nueva Granada, Bogotá, Colombia

<sup>f</sup> Department of Design and Engineering, Faculty of Science and Technology,  
Bournemouth University, Poole, Dorset BH12 5BB, UK

<sup>g</sup> Materials Research Group, Department of Mechanical Engineering, University of  
Southampton, Southampton, SO17 1BJ, UK

<sup>h</sup> School of Metallurgy and Materials Engineering, College of Engineering, University of  
Tehran, P.O. Box 11155-4563, Tehran, Iran

<sup>i</sup> Materials Department, UC Santa Barbara, Santa Barbara, CA 93106, USA

<sup>j</sup> Department of Mechanical Engineering, UC Santa Barbara, Santa Barbara, CA 93106, USA

<sup>k</sup> Hong Kong Institute for Advanced Study, Department of Materials Science & Engineering, City University of Hong Kong, Kowloon, Hong Kong

<sup>l</sup> Mechanical Behavior Division of Shenyang National Laboratory of Materials Science, City University of Hong Kong, Hong Kong

<sup>m</sup> Heterostructured Materials Center, Nanjing University of Science and Technology, Nanjing, China

\* E-mail: [y.zhu@cityu.edu.hk](mailto:y.zhu@cityu.edu.hk)

---

Nomenclature:  $\gamma$ , Austenite (FCC); 3D, Three-dimensional; ABSP, Air blast shot peening; AGG, Abnormal grain growth; 3S, Surface spinning strengthening; AHSS, Advanced high strengthening steels; ALD, Atomic layer deposition; AM, Additive manufacturing; AM, Additive manufacturing; ARB, Accumulative roll-bonding; BCC, Body-centred cubic; BCT, Body centred tetragonal;  $c$ , Solute atoms concentration at grain boundaries; CFUBMS, Closed field unbalanced magnetron sputtering; CG, Coarse grained/Coarse grain;  $C_m$ , Martensite volume fraction; CPFE, Crystal plasticity finite element; CR, Cold rolling; CRSS, Critical resolved shear stress; CVD, Chemical vapour deposition;  $D$ , Average grain size after applying a specific temperature for a specific time;  $D_0$ , Initial grain size; DED, Directed energy deposition;  $D_f$ , Diffusivity; DFT, Density functional theory; DMT, Laser-aided direct metal tooling; DP, Dual-phase; DPD, Dynamic plastic deformation; DRX, Dynamic recrystallisation;  $dyxz/dy$ , Shear strain gradient;  $d\epsilon_x/dy$ , Normal strain gradient; E. coli, Escherichia coli; EPD, Electrophoretic deposition; EPT, Electropulsing treatment;  $\epsilon_u$ , Unloading strain; FCC, Face-centred cubic; FEM, Finite element method; GND, Geometrically necessary dislocations; GNG, Gradient nano-grained; GNT, Gradient nano-twinned; GS, Gradient structures; HAZ, Heat affected zone; HBAR, Heterozone boundary affected region; HBAR, Heterozone boundary affected region; HCP, Hexagonal close-packed; HDI, Hetero-deformation induced; HIP, Hot isostatic pressing; HLS, Heterogeneous lamella structures; HPDC, High pressure die casting; HPT, High Pressure Torsion; HRS, Hot roll sintering; HS, Heterostructured; HSM, Heterostructured materials; HT, Heat treatment; HZB, Hetero-zone boundaries; IF, Interstitial-free;  $I_p$ , Intrinsic property; IPF, Inversed pole figure; ISSF, International Stainless Steel Forum;  $K_0$ , constant; KS, Kurdjumov-Sachs; LAGB, Low angle grain boundaries; LMD, Laser metal deposition; L-PBF, Laser powder-bed-fusion; LS, Laminate structures; LSP, Laser-shock peening; MC, Monte Carlo method; MD, Molecular dynamics; MHG, Multiphase hierarchical grain;  $M_i$ , Intrinsic saturation magnetization; MIC, Microbiologically influenced corrosion;  $M_s$ , Saturation magnetization;  $n$ , Grain growth exponent; NG, Nanograined; NP, Nanoparticle; NW, Nishiyama-Wasserman; PISG, Pipe inner-surface grinding; PM, Powder metallurgy; PM, Powder metallurgy; PSA, Plasma surface alloying; PVD, Physical vapor deposition;  $Q$ , Apparent activation energy for grain growth; *P. aeruginosa*, Pseudomonas aeruginosa; PF, Phase-field model; Q&P, Quenching and partitioning;  $R$ , Gas constant;  $r$ , Average final particle radius;  $r_0$ , Average initial particle radius; ROM,

## Abstract

The study of heterostructured materials (HSMs) answered one of the most pressing questions in the metallurgical field: “is it possible to greatly increase both the strength and the strain hardening, to avoid the “inevitable” loss of ductility?”. From the synergy between the deformation modes of zones with greatly different flow stress, low stacking fault energy (SFE) alloys can reduce their typical trade-off between strength and ductility. Stainless steel (SS) is a low-SFE material, which is widely applied for structural, biomedical, biosafety, food-processing, and daily applications. The possibility to combine its corrosion resistance and biocompatibility with the outstanding mechanical behaviour of HSMs can convert SS into a promising option for low-cost and high-effective advanced material. This paper reviews all the microstructural aspects of HS SS obtained by different processing methods and their correlation with crystallographic texture and properties such as mechanical, corrosion, biological, and magnetic characteristics. The critical comparison between

---

Rule of mixtures; S2PD, Surface severe plastic deformation technique; SB, Shear band; SCC, Stress corrosion cracking; SEM, Scanning electron microscope; SF, Stacking fault; SFE, Stacking fault energy; SILAR, Successive ionic layer adsorption reaction; SIM, Strain-induced martensite; SLM, Selective laser melting; SMAT, Mechanical attrition treatment; S. aureus, Staphylococcus aureus; SMGT, Surface mechanical grinding treatment; SMRT, Surface mechanical rolling treatment; SPD, Severe plastic deformation; SPS, Spark plasma sintering;  $\sigma_r$ , Effective reloading elastic modulus; SS, Stainless steel; SSD, Statistically stored dislocations;  $\sigma_u$ , Effective unloading elastic modulus;  $\sigma_{u0}$ , Initial flow stress;  $T$ , Temperature;  $t$ , Soaking time;  $th$ , Total thickness/volume of the sample;  $\tau_a$ , Applied shear stress; TRIP, Transformation-induced plasticity; TVA, Thermionic vacuum arc; TWIP, Twinning induced plasticity;  $U$ , Activation energy to move a vacancy; UFG, Ultrafine/Ultrafine; UIP, Ultrasonic impact peening; UIT, Ultrasonic impact treatment; UNSM, Ultrasonic nanocrystalline surface modification; UP, Ultrasonic peening; USET, Ultrasonic strain engineering technology; USR, Ultrasonic surface rolling; USSR, Ultrasonic severe surface rolling; UTS, Ultimate tensile strength; WAAM, Wire-arc additive manufacturing; YS, Yield strength; Z, Zener-Hollomon parameter;  $\alpha$ , Ferrite (BCC);  $\alpha'$ , Martensite (BCT or BCC);  $\epsilon$ , Intermediate martensite (HCP);  $\sigma^*$ , Thermal component of the flow stress;  $\sigma_h$ , HDI stress;  $\sigma_r$ , Reload yielding;  $\sigma_u$ , Unload yielding;  $\sigma_y$ , YS of the whole sample;  $\Delta\sigma$ , Contribution of the synergistic strengthening;  $f_i$ , Fraction of the  $i$  layer/zone;  $\sigma_i$ , YS of the  $i$  layer/zone;  $\sigma(x)$ , YS of each sample layer/zone at the position  $x$  along the thickness/volume;  $\dot{\epsilon}$ , True strain rate.

experimental and modelling findings is also presented in terms of the deformation mechanisms, microstructural and texture features. Thus, the processing-microstructure-properties relationship in HS SS is the focus of this publication. The multi-disciplinary perspectives of HS SS are also discussed. This review paper will serve as a reference for understanding and designing new multi-functional HS SSs.

**Keywords:** Heterostructure; Stainless steel; Mechanical behaviour; Texture; Corrosion

## Contents

<b>1. Introduction .....</b>	<b>7</b>
<b>2. Brief overview of the fundamentals of heterostructured materials (HSMs).....</b>	<b>15</b>
2.1 Principles of HSMs.....	16
2.2 Synergistic strengthening in HSMs .....	19
2.3 Experimental measurement of hetero-deformation induced stress .....	24
2.4 Influence of stacking fault energy in HSMs.....	27
<b>3. Applications of HS stainless steels (SS) .....</b>	<b>34</b>
<b>4. Microstructural features of HSMs.....</b>	<b>37</b>
4.1 Heterogeneous lamella structures (HLS) .....	37
4.2 Gradient structures (GS).....	47
4.3 Layer structures (LS).....	55
4.4 Multiphase structures .....	59
4.5 Harmonic structures.....	64
4.6 Multimodal structures .....	72
4.7 Simulation.....	77
4.7.1 Heterogeneous phase transformation and grain growth.....	77
4.7.2 Deformation and damage behaviour.....	80
<b>5. Crystallographic texture.....</b>	<b>85</b>

<b>6.</b>	<b>Mechanical performance .....</b>	<b>92</b>
6.1.	<i>Tensile properties .....</i>	94
6.1.1.	<i>Tensile behaviour in HLS SS .....</i>	96
6.1.2.	<i>Tensile behaviour of GS SS .....</i>	100
6.1.3.	<i>Tensile behaviour in LS SS .....</i>	102
6.1.4.	<i>Tensile behaviour in harmonic structured SS .....</i>	108
6.1.5.	<i>Tensile behaviour of multiphase SS .....</i>	110
6.1.6.	<i>Tensile behaviour in multimodal SS .....</i>	112
6.2.	<i>Hardness .....</i>	119
6.3.	<i>Fatigue resistance .....</i>	124
6.4.	<i>Wear resistance .....</i>	128
<b>7.</b>	<b>Corrosion susceptibility .....</b>	<b>131</b>
7.1.	<i>Microstructural effect on corrosion resistance of HS SS .....</i>	133
7.2.	<i>Microbial corrosion of HS SS .....</i>	140
<b>8.</b>	<b>Other properties of interest .....</b>	<b>145</b>
8.1.	<i>Biological .....</i>	145
8.2.	<i>Thermal stability .....</i>	152
8.3.	<i>Magnetic properties .....</i>	161
<b>9.</b>	<b>Future directions .....</b>	<b>164</b>

## 1. Introduction

Heterostructured materials (HSMs) constitute a promising and fast emerging field for boosting mechanical properties through cost-effective routes. The highly increasing tendency towards developing heterostructured materials is shown in [Fig. 1](#). Although HSMs are not the only way to improve the mechanical behaviour of metallic materials, they provide a creative answer to a harsh question in nanostructured materials: “is it possible to highly increase both the strength and the strain hardening to avoid the “inevitable” loss of ductility?”. From the development of gradient structures by surface nanocrystallization [1], the scientific community noticed an interesting combination of long-range stress that strengthens the material and maintains good ductility while straining. A systematic study of their physics was motivated to understand those promising results [2]. Currently, multiple advantages, especially a cutting-edge combination of strength and ductility, have been related to HSMs.

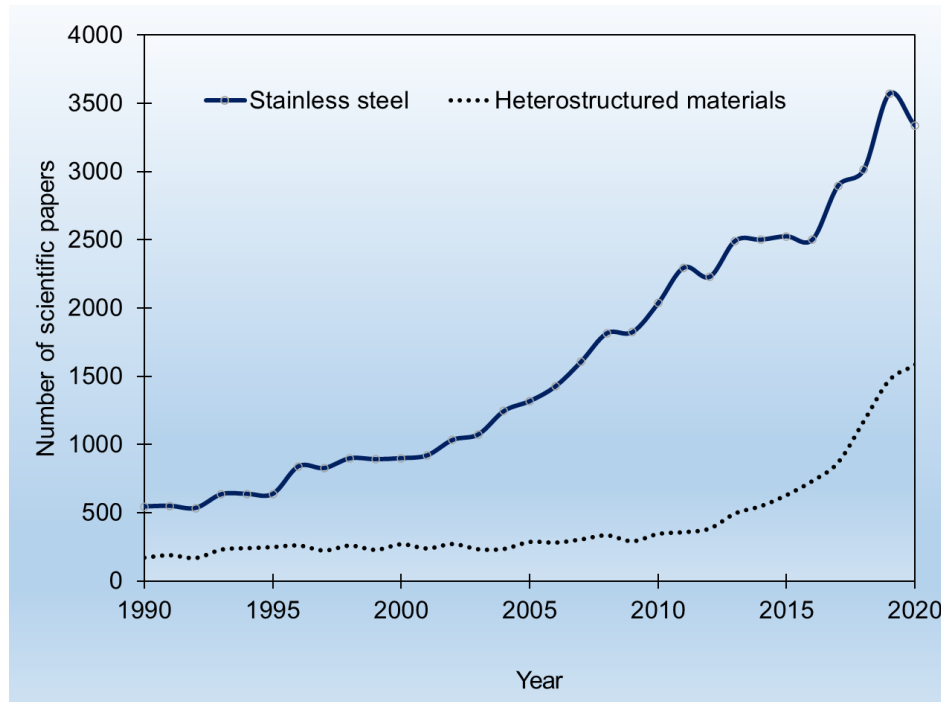


**Fig. 1.** Tendency of scientific papers included in Scopus database with the keywords “stainless steel” and “heterostructure” in their titles.

An important value of HSMs is the possibility to combine different properties to ensure their multifunctional purposes [3]. The reduced strength to ductility trade-off that HS microstructures can overcome can also be combined with properties different from mechanical ones. Some examples are the design of antimicrobial, corrosion-resistant, magnetic, or biocompatible alloys with superior mechanical performance. Besides, the heterogeneous nature of HSMs allows exploring plenty of routes, like heterogeneous grain size, density of defects, crystallographic texture, as well as chemical, magnetic, electrochemical, electric, thermic, and biological, among other disparities.



The outstanding combination of different properties sets the HSMs as promising for replacing multiple conventional materials. Some current and potential applications of HSMs are biosafety, orthopaedic, dentistry, food-processing, automotive, aeronautic, architectural, optoelectronics, biomechanics, tribology, energy-conversion devices, magnetic storage, daily devices, among others, which can combine their main properties with cutting-edge mechanical performance to increase their service life [4–6].

The effectiveness of heterostructures has also been demonstrated by various bio-inspired designs such as gradient microstructures in wood and bamboo stems, horse hoofs, teeth, bones, shells, among others [7–11]. Besides, the use of man-made HSMs is not a new trend. The softcore with a hard edge of the famous Damascus blades (5th century to 19th century) made of Indian steel [12–14] and the ancient Japanese swords (from more than 1000 years) [6,15,16] are examples of heterostructured strong and tough materials. However, the systematic study of the physics underlying the outstanding properties of the HSMs was launched from the explanation of the role of back stress [2,17–19] and forward stress in the hetero-deformation induced (HDI) hardening<sup>2</sup> [20].

Although the design of heterostructures is not the only route to improve the mechanical properties of metallic materials, it is currently the most promising for industrial purposes. From [2], the trade-off between strength and ductility is considerably reduced with the

---

<sup>2</sup> Back stress strengthening and hardening were posteriorly renamed HDI strengthening and hardening due to the contribution of forward stress.

obtaining of heterostructures in comparison with nanometric (NG)/ultrafine (UFG) and coarse grained (CG) materials [21]. **Figure 2** shows the main classification of HSMs, which will be followed in the present review: heterogeneous lamella structures (HLS), gradient structures (GS), layer structures (LS), multiphase structures, harmonic structures, and multimodal structures [4]. Moreover, the characteristic microstructural features and the main obtaining processes of each HSM are also shown in **Fig. 2**. Sections 4 to 8 will describe each classification in more detail.

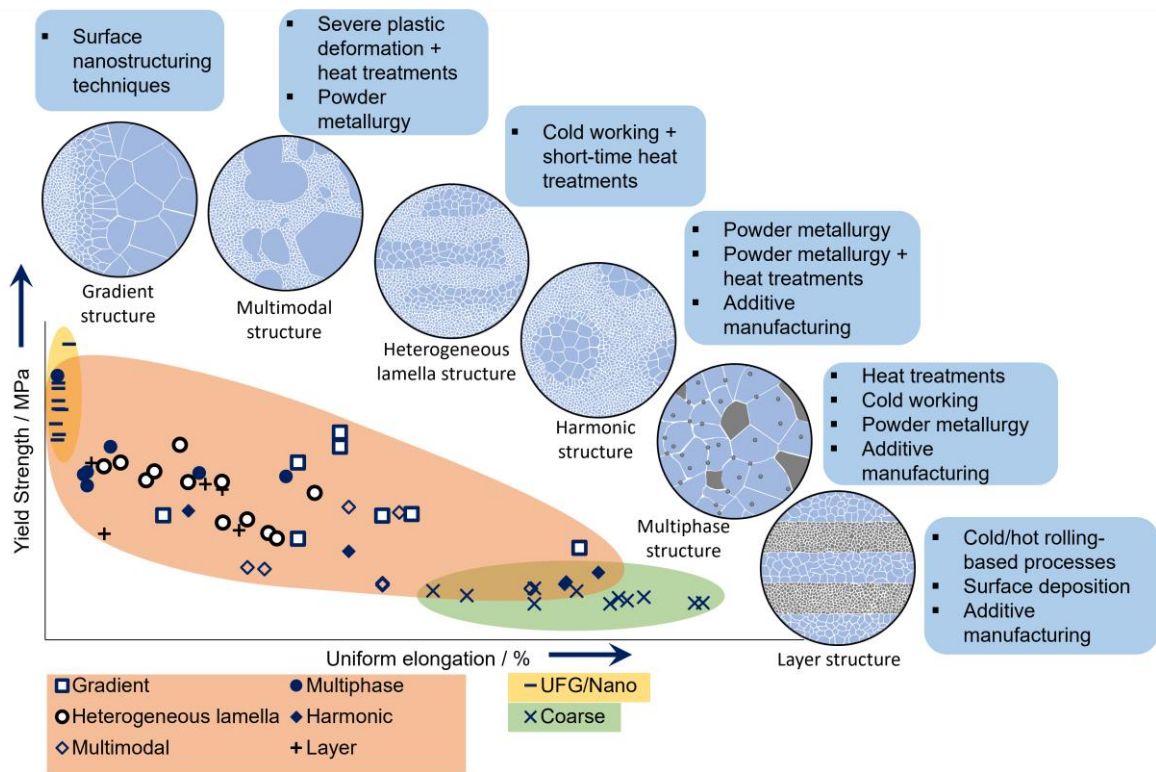


**Fig. 2.** Comparison of yield strength and uniform elongation between nanograined (NG)/ultrafine (UFG) [21–26], coarse (CG) [24,26–28] and heterostructured (HS) stainless steels; gradient structure [29–33], multiphase structure [34,35], heterogeneous lamella

structure [21,36–40], harmonic structure [40–43], multimodal structure [42,44–46], and layer structure [47,48], as well as the main elaboration processes of each kind of HS materials (HSMs).

Moreover, the thermomechanical processes for elaboration of HSMs are frequently low-cost and scalable for industrial production. This feasibility is obtained by the possibility to design new combinations based on conventional thermomechanical bulk or surface processing methods. Examples of these are the use of surface mechanical attrition treatment (SMAT) [49–51], heat treatments (HT) [52], severe cold rolling (CR) and HT [2,21,35,53–55], accumulative roll-bonding (ARB) and HT [56,57], ARB with sprayed surface nanoparticles [58], ARB with rolling and annealing [59], surface mechanical grinding treatment (SMGT) [60], dynamic plastic deformation (DPD) [61], among others. Heterostructured materials can also be produced by severe plastic deformation (SPD) techniques [62–64] or SPD with HT [65–67]. SPD techniques are effective in greatly enhancing mechanical performance [68]. However, some SPD techniques require complex die design [69], which reduces the likelihood of large-scale production through continuous processing routes [70].

The elaboration of heterostructures consisting of zones with high mechanical incompatibility is one of the most effective principles to reduce the trade-off between strength and ductility of several metallic materials [71]. The HSMs create a synergy between the virtues of different microstructural features to reduce conventional trade-offs on

homogeneous alloys as strength-ductility, strength-conductivity, strength-toughness, etc., [4,5,79,25,72–78]. The HSMs require specific microstructural features to secure a dramatic strength change between zones and the synergy of multiple strengthening mechanisms. The heterogeneous zones require adequate size, geometry, and distribution of grains and phases to maximise the occurrence of strain partitioning between them [5]. The size of each zone can vary from micrometres to millimetres and allow dislocations to pile up in both zones, more importantly in the soft one. The HSMs involve heterogeneities in terms of long-range internal stress, defect distributions, and inter-zone interactions. This includes materials with hetero-zone boundaries due to different phases' coexistence, chemical compositions, crystallographic textures, grain sizes, grain morphologies, and defects. A high density of grain boundaries is also desirable to augment their HDI stress [80]. Besides, materials with low stacking fault energy (SFE) promotes dislocation pile ups by reducing cross slip. With its characteristic low SFE, stainless steel is one of the main targets for maximising mechanical properties.

Since its discovery in 1912 [13], stainless steel (SS) has been one of the most accessible and cost-benefit alloys for industrial and daily components. Due to its chemical composition, the SS combines high strength and corrosion resistance, making it suitable for several applications. SS is currently applied in temporal orthopaedic and dental implants, medic tools, orthodontic treatments, food refrigeration devices, cooking utensils, jewellery, fasteners cutlery, pipelines, potable water containers, automobiles, pressure vessels, wastewater treatment, ships, architectural applications, as well as for equipment in

pharmaceutical, chemical, health, sanitation, food-processing, textile, and petrochemical plants, among others [81–83]. Based on data from the International Stainless Steel Forum (ISSF), the world yearly production of SS in 2020 was about 52.2 million metric tons [84] and it has kept an increasing trend since at least 2012. From the above, the SS has gained an important place in social and technological development. Intensive research is being carried out all over the world to improve the current properties of SS and expand its applications (Fig. 1). The objective is to combine the accessibility and low cost of SS with outstanding mechanical and multi-functional properties.

From their microstructure, the wrought SS can be classified as single- and multiphase. The ferritic, austenitic, and martensitic SS belong to the first group, while duplex and precipitation-hardening fit in the second group [85]. From the previous classification, the ferritic SS has a body-centred cubic (BCC) structure with a Cr content from 10.5 to 30 wt.%, is ferromagnetic and possesses good ductility; the austenitic SS has a face-centred cubic (FCC) structure with Cr content from 16 to 26 wt.%, its annealed condition is nonmagnetic, it is a work-hardening alloy that retains good strength at high-temperature; the martensitic SS have a ferromagnetic BCC structure when hardened, they have a Cr content from 10.5 to 18 wt.% and show corrosion resistance in mild environments; the duplex SS possesses a mixture of BCC (ferrite,  $\alpha$ ) and FCC (austenite,  $\gamma$ ) structures, they have high tensile strength and good corrosion resistance in stress-assisted environments; the precipitation-hardening SS may have a martensitic or austenitic structure after being annealed, they use to have a high strength [85]. It should be pointed out that each microstructure is defined by the chemical

composition and thermomechanical process for obtaining SS. One common feature of all the classifications of SS is that they should include at least 12 wt.% of Cr to allow the surface formation of a Cr-rich oxide film [13,86].

Despite their broad applications, medical and structural SS components require advanced material design to reduce their failures. Examples of these deficiencies include the breakage of medic or orthodontic tools as a result of repetitive sterilization and use, due to the wrong handling of devices or unexpected movement of the patient [87]; the hypodermic needles which might suffer breakage during anaesthesia and other clinic procedures [88,89], requiring complex and risky extraction procedures; the hand-holders in public transport, as well as doorknobs, door handles, bed rails and faucets that should resist continuous friction; orthodontic archwires, molar bands and brackets, which should resist compression loads in the oral environment; orthodontic drills that require a high fatigue resistance; among others. From the above, the mechanical and corrosion properties remain at the core of the required characteristics for the good performance of SS components. As a solution for the previous drawback, the design and study of HS SS have shown promising results in the matter of reducing the conventional trade-off between strength and ductility without affecting their corrosion resistance and biological properties [32,90]. Moreover, passivated materials with wide grain size distributions (as the resultant in HSMs) have shown better corrosion resistance due to the formation of a more continuous, compacted and well-adhered surface passivation layer in comparison with that of nanometric or coarse-grained microstructures [91,92].

This review paper aims to present the recent progress in heterostructured stainless steel and its multiple advantages over its conventional counterparts. The unique microstructural features of the HS SS and their effect on the mechanical, crystallographic texture, corrosion, and other important features of SS will be discussed. Recent literature can be found with an in-depth explanation of recent findings in the physics of the strengthening and hardening mechanisms in HSMs [4,5,76,80,93]. However, no clear correlation has been shown with other fundamental properties for the wide applications of SS. The present review paper will be focused on the processing-microstructure-properties relationship on HS SS. Comparison between the results obtained from different heterostructures will also be presented to serve as a basis for further designs of multifunctional HS SS. Overall, this paper will provide a broad understanding of the recent findings in HS SS. Considering that HSMs are an emerging and highly promising field, the future perspectives of HS SS will also be discussed.

## **2. Brief overview of the fundamentals of heterostructured materials (HSMs)**

This section introduces the basics for understanding the features and properties of HSMs. As explained before, the physics of HSMs is not the focus of this review paper. Further information can be found in the literature [4,5,20,76,80,93].

## 2.1 Principles of HSMs

The outstanding mechanical properties of the HSMs are originated from the interactive coupling between soft and hard zones coexisting in the same microstructure. The mechanical incompatibility between adjacent soft and hard zones should be greater than 100% [76]. The differences in flow stress cause a heterogeneous response to the applied strain. The soft (coarse-grained) zones sustain larger deformations, while the hard ones (nano- or ultrafine-grained) act as obstacles to block the gliding of dislocations, increasing the material resistance. The interfaces between those zones, or hetero-zone boundaries (HZB), play a key role in the interactive coupling between different zones. When stress is applied to the HSMs, the soft zones start deforming before the hard ones. To accommodate the strain mismatch in the HZB, geometrically necessary dislocations (GNDs) will be created from Frank-Read sources and they pile up. The dislocations in a pile up have the same Burgers vector, and they originated from the same dislocation source. The pile up of GNDs produces long-range back stress [94]. As shown in [Fig. 3\(a\)](#), with increasing applied stress, the GNDs pile up against the HZB and generate back stress in the soft zones [20]. Simultaneously, the stress exerted by the head of the GND pile up will produce forward stress in the hard zones [5,95,96]. The produced back stress will act against the dislocation source to try to stop the emission of more dislocations [2].

The back stress strengthens the soft zones, while the forward stress makes the hard zone easier to deform [4]. Numerous GND piled ups can be observed within a grain of HS lamella Ti in [Fig. 3\(b\)](#). The distribution of dislocations along the GND piled ups follows a non-linear



function [97]. Consequently, a strain gradient will be created with respect to the Frank-Read dislocation source, which has the highest plastic strain [5]. As a result of the GND pile ups, a distribution of strain gradient with the distance from the HZB can be observed in Fig. 3(c). The strain gradient produces a heterozone boundary affected region (HBAR)<sup>3</sup> [73]. The mentioned strain gradient will be partially accommodated by the creation and interaction of more GNDs near the HBAR. Afterwards, the hard zone remains elastic when the coarse zone starts being plastically deformed. However, the coherency at the interface should be preserved and the soft or coarse zones cannot freely deform plastically, i.e., both zones mutually constrain, which results in a higher strain hardening than the obtained for homogeneous nanostructured materials [98]. The back stress and forward stress do not cancel each other globally, and they collectively produce the HDI strengthening to enhance yield strength (YS) and HDI strain hardening to retain/improve ductility. As a result, the YS of HSMs is greater than predicted by the well-known rule of mixtures (ROM) [99], i.e., greater than the strength contributions of each component weighted by their volume fraction.

---

<sup>3</sup> This zone was previously identified as Interface-Affected-Zone (IAZ).

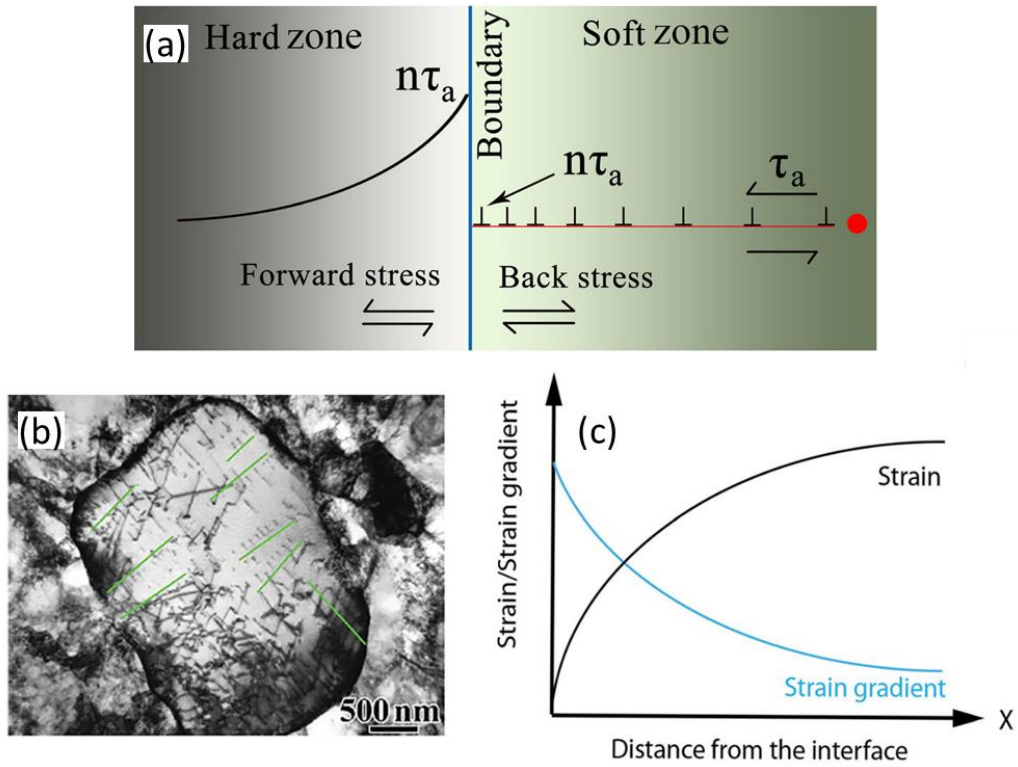


**Fig. 3.** Generation and distribution of long-range back and forward stress by geometrically necessary dislocation (GND) pile ups near the hetero-zone boundary (HZB). (a) Scheme of the generation of GNDs from a Frank-Read source (red circle) that pile up against a zone boundary and produces back stress in the soft zone and forward stress in the hard zone. The curve on the left of the boundary is the distribution of forward stress induced by the back stress in the hard zone. (b) Transmission electron microscopy micrograph of many piled up GNDs (green lines). (c) Distribution of strain gradient with the distance from the HZB. Adapted from [5].

Even the HDI strengthening is dominant in HSMs, their properties come from the synergy of multiple strengthening mechanisms. The microstructural heterogeneities on the HSMs, such as HZBs obtained from multiphase frontiers, multi-order grain sizes, twins, strain bands, among others, encourage the occurrence of heterogeneous deformation and diverse strengthening mechanisms. The contribution of HDI to the total strengthening in HSMs is big enough to no longer be explained by traditional strengthening mechanisms of homogeneous materials (precipitation, grain boundaries, solid solution, or accumulation of dislocation) nor by the conventional ROM.

## 2.2 Synergistic strengthening in HSMs

The HSMs create a synergy between various strengthening mechanisms, from where HDI strengthening is dominant. The HDI strengthening is usually neglected in homogeneous materials and not considered in most classic models, such as the ROM. The occurrence of HDI and the synergistic strengthening effect does not follow a linear function (Fig. 4(a)), and a term for its contribution should be added to the ROM, resulting in a modified ROM shown in Eq. (1) [80,99].

$$\sigma_Y = \Delta\sigma + \sum_{n=i}^n f_i \sigma_i \quad (1)$$

where  $\sigma_Y$  is the YS of the whole sample,  $\Delta\sigma$  is the contribution of the synergistic strengthening,  $f_i$  and  $\sigma_i$  are the fraction and YS of the  $i$  layer/zone, respectively. From Eq. (1), the first term corresponds to the contribution of synergistic strengthening mechanisms,

which are originated from the interaction and mutual constraint between the heterogeneous zones. The second term corresponds to the contribution from the classic ROM. The Eq. (1) can also be expressed in a more general approach by the Eq. (2).

$$\sigma_Y = \Delta\sigma + \frac{1}{th} \int_0^{th} \sigma(x) dx \quad (2)$$

where  $th$  is the total thickness/volume of the sample,  $\sigma(x)$  is the YS of each sample layer/zone at the position  $x$  along the thickness/volume. It should be pointed out that  $\Delta\sigma$  has a nonlinear contribution, revealing that there exists a volume fraction/thickness of fine zone that maximises the mechanical properties. From the inset of Fig. 4(a), the maximum  $\Delta\sigma$  contribution was obtained at a volume fraction of about 0.5 of gradient (fine) layer [99]. This might be related to the fact that an increment of heterogenous fraction leads to a homogeneous microstructure at some point, which implies the decrement of HZBs density. Thus, there is an optimum fraction of coarse and fine grains in which the synergy between GND pile up and dislocation accumulation is maximised. The modelling of the necessary fraction of HZB for maximising the contributions of HDI strengthening in the different HSMs remains in the future opportunities for the scientific community. However, experimental approaches for optimising the volume fraction of fine (hard) zones in harmonic structured 304L SS and Cu to ~40% were reported [41,100]. Dual SS and manganese steel, which are examples of multiphase structured materials, obtained superior mechanical properties at ~30 vol.% of martensite ( $\alpha'$ ) [101,102]. The strength and ductility relationship was maximised in a 316L SS HLS with a 30 vol.% of nano-grained and 10 vol.% of nano-twinned zones [21]. Strength and ductility by prolonged deformation-induced plasticity (TRIP) effect, HDI

strengthening and HDI hardening were optimised in a GS 304 SS alloy [103]. This effect was especially notable at a depth of 60  $\mu\text{m}$  from the surface with initially  $\sim 30$  vol% of  $\alpha'$ . Besides, the HDI strengthening in a GS interstitial-free (IF) steel was optimised at a volume fraction of the fine zone of  $\sim 0.5$  [99].

On the other hand, the origin of such  $\Delta\sigma$  is also partially related to the mismatch of Poisson's ratio between the coarse and fine zones. It is known that no lateral stress is applied in homogeneous materials during tensile strain. However, from qualitative finite element method (FEM) in an IF steel [99], the normal stress ( $\sigma_x$ ) was shown to be positive in the coarse layer and negative in the fine one, i.e., a biaxial stress state is induced in the whole sample (Fig. 4(b)). The biaxial stress increases the interaction and accumulation of dislocations by activating more slip systems [80]. Consequently, the strength of the plastically deformed layer will rise. From Fig. 4(b) a stress gradient can be observed across the thickness, especially at the HZBs.

Moreover, Poisson's ratio evolution incompatibility and mutual constraint generated different strains between coarse and fine layers. A peak of strain gradient at the HZBs was produced (Fig. 4(c)). The strain gradient triggers the generation and accumulation of GNDs, HDI stress production, and work hardening increment following plastic deformation. Additionally, normal ( $d\epsilon_x/dy$ ) and shear ( $d\gamma_{xz}/dy$ ) strain gradients were larger at the edge of the sample (path 4) in comparison with the centre (path 1). The FEM modelling did not consider the contribution of interlayer interaction to constitutive relationships or the gradient structure expected within the fine layer, which remains an opportunity for future efforts. In

summary, the biaxial stress state encourages the accumulation of dislocations while the strain gradients prompt the GND formation. Both strengthening mechanisms, dislocations accumulation and HDI strengthening, together with other possible as grain boundaries density, twinning, second phases, etc., act synergically in a gradient material. However, only the already explained relationship between the first two strengthening mechanisms is proper for HSMs.

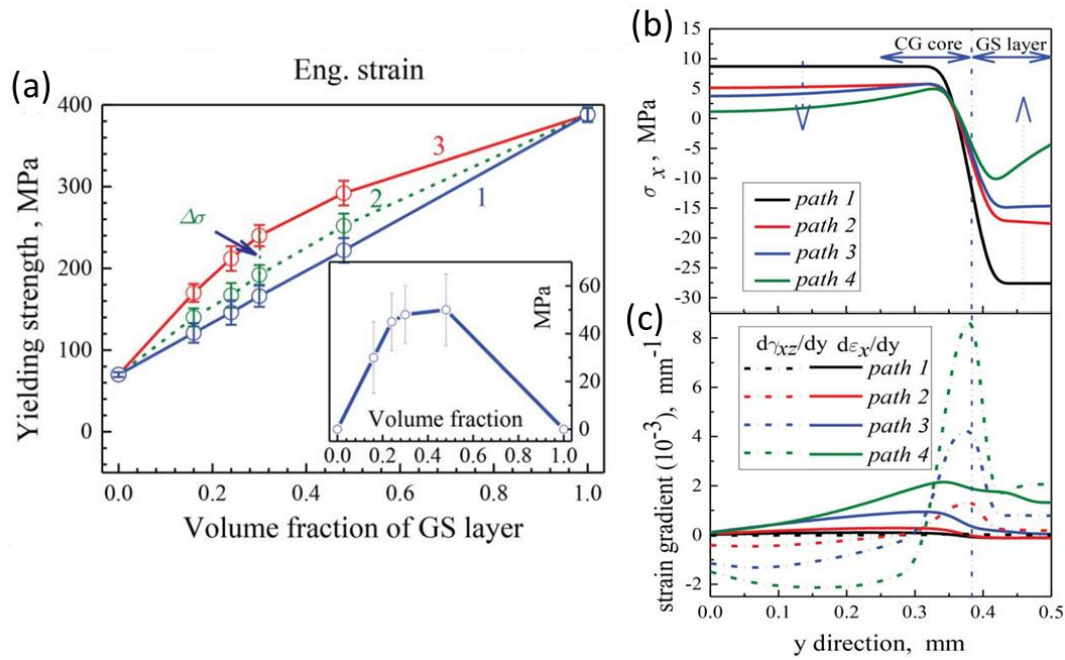


**Fig. 4.** Finite element method (FEM) results for yield strength and distribution of stress and strain gradients in an interstitial-free (IF) steel processed by SMAT [99]. (a) Comparison between experimental (red curve) yield strength and the calculated by the rule of mixtures (ROM) (blue curve) and modified ROM (green curve) in a gradient interstitial-free steel processed by SMAT, (b) normal stress ( $\sigma_x$ ) distribution along the x-axis, and (c) normal

( $d\epsilon_x/dy$ ) and shear ( $d\gamma_{xz}/dy$ ) strain gradients along the x-axis. Path 1 (centre) to 4 (edge) refers to different profiles of the sample selected for FEM modelling.

Posteriorly, a method to consider the strain dependence of hardness in the constitutive relationship of an LS TA1 (Ti alloy)/Al1060 (Al alloy)/430 (SS) was proposed [104]. This method also takes the ROM as a basis for considering the continuous change of hardness of each constituent layer during strain processes, including the contributions of bonding regions. It is well-known that the density of dislocations increases during plastic deformation processes, increasing the work hardening and hardness of the strained material. No considering of previous phenomena during FEM analysis reduces the accuracy of results. Due to the above, the authors of such work considered four main inputs: i) the true stress, ii) the cross-section areas, iii) the strain dependence of hardness of each layer and bonding regions, and iv) the tension force of the whole LS material. This model showed reliability with respect to the experimental data during bending tests, especially for high bending angles. However, at bending angles lower than  $40^\circ$ , the model showed a bigger error in the springback between the reported hierarchical method and the experimental results. No further explanation was included in that publication about such deviation. However, this could be related to the consideration that the ratio of increment of stress to the hardness augmentation is equal for all the layers and bonding zones. However, it has been explained that in HSMs, the soft region reaches the plastic deformation region while the hard one is still elastically deformed. This provides the hard zone with a higher elastic strain to release after retiring the

applied load. This means that the springback occurrence, i.e., return of some atoms to their equilibrium positions in the crystalline lattice (partial recovery), is higher while the hard zone remains elastic. Additionally, at this deformation stage, the soft zone is being hardened mainly by back stress, while the hard zone joins the contributions of mainly dislocations accumulation and forward stress, being why the ratio of increase of stress with hardness cannot be equal for both zones.

### *2.3 Experimental measurement of hetero-deformation induced stress*

The generation of HDI stress is not exclusive to HSMs. Conventional homogeneous alloys also produce it, although it is usually very low. The HDI stress is closely related to the well-known Bauschinger effect because they have the same origin, i.e., the GND pile-ups [105]. The Bauschinger effect refers to the difference between the applied and reversed flow stress, causing lower compressive YS than its tensile YS, and inverse [106]. The directional nature of long-range back stress obstructs dislocation slip in the tensile direction and promotes it in the inverse direction [107]. Recently, it was reported that the strain hardening increased as a function of the compressive residual stress in GS materials [108].

It has been reported that the back stress contribution can count for 88% of the flow stress disparity due to the Bauschinger effect [109]. This means that the higher HDI stress, the higher the Bauschinger effect. This is an effect that influences mainly the HSMs, for example, GS [105,107], HLS [2], alloys with soft/hard interfaces of bulk phases [35] and others with non-shearable precipitates (multiphase structured materials) [110–112], or LS passivated thin



films (with film–oxide/nitride/sulfide interfaces) [113–115]. This is because the strain hardening in homogeneous materials is governed by the forest dislocation hardening (mutual trapping and accumulation of statistically stored dislocations (SSDs)), while strain hardening in HSMs is controlled by HDI hardening, i.e., the pile-ups of GNDs. This means that the contribution of HDI to the total hardening in HSMs is always higher than that of dislocation hardening [17]. This was demonstrated by the higher HDI stress due to GNDs pile up in HS copper [107] compared to pure Cu [116], where the Bauschinger effect was minimal. An experimental approach to estimate the contribution of HDI stress during unloading-reloading loops in tensile tests has been reported [19]. This methodology firstly considered only the contribution of back stress, being renamed HDI stress due to the simultaneous contribution of forward stress, which collectively affects the flow stress [20].

From the unloading-reloading curve, the HDI stress can be estimated using the Eq. (3) and Fig. 5(a) [19]:

$$\sigma_h = \frac{\sigma_r + \sigma_u}{2} \quad (3)$$

where  $\sigma_u$  and  $\sigma_r$  are the unloading and reloading yield stress defined in the unloading-reloading stress-strain curves in Fig. 5(a). The Eq. (3) assumes reversible GND pile up structures during the unloading-reloading process, keeping the HDI stress approximately constant. This methodology was proposed to reduce the measurement errors of previous models, where an arbitrary plastic strain offset was used to determine  $\sigma_u$  and  $\sigma_r$  [94,117,118]. Instead, the  $\sigma_r$  and  $\sigma_u$  from Eq. (3) can be estimated by the slope from the linear elastic segments of the unloading-reloading curves indicated in Fig. 5(a) [19]. This improvement

considers that the slope reduction fraction is directly proportional to the volume fraction undergoing perfect plastic deformation without contributing to the elastic strain. Besides, the slope from the stress-strain curve is a more accurate parameter than the strain for estimating  $\sigma_r$  and  $\sigma_u$ . This is demonstrated in Fig. 5(b) by the slow scattering in HDI stress when considering 5, 10 or 15% slope reductions to estimate the  $\sigma_r$  and  $\sigma_u$ .

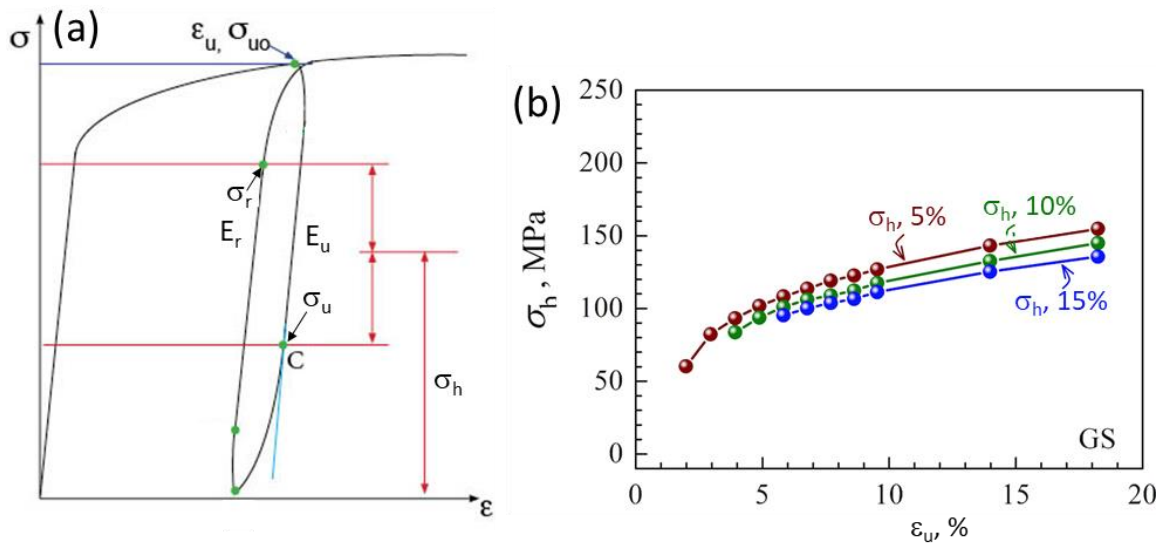


**Fig. 5.** Representation of the unloading-reloading method to estimate the contribution of hetero-deformation induced (HDI) stress. (a) Representation of the unloading-reloading loop for estimating the unload yielding  $\sigma_u$ , reload yielding  $\sigma_r$ , HDI stress  $\sigma_h$ , effective unloading elastic modulus  $E_u$ , and effective reloading elastic modulus  $E_r$  considering that  $\sigma_{u0}$  is the initial flow stress at the unloading strain  $\epsilon_u$  (Adapted from [19]). (b) HDI stress with increasing  $\epsilon_u$  for a GS interstitial-free (IF) steel, where 5, 10, and 15 % represents the use of 5% slope reduction from the effective elastic modulus [19].

Among the limitations of this method are the materials with very short or not clear linear segments, in which case it is suggested to use the slope of the initial elastic loading curve before yielding for the estimation of the  $\sigma_r$  and  $\sigma_u$ . Moreover, the assumption of reversible GND structures during the unloading-reloading cycle might not satisfy materials with high HDI stress, where the  $\sigma_r$  may be lower than the  $\sigma_u$ , which lacks physical sense. To overcome this drawback, it is suggested to stop the unloading process and start the reloading above a certain stress that satisfies the assumption of [Eq. \(3\)](#). The design of an improved method or systematic corrections for estimating HDI stress is an opportunity for future efforts and will also enhance the study of HS SS properties.

#### *2.4 Influence of stacking fault energy in HSMs*

On the other hand, the SFE strongly influences the generation of HDI strengthening. It is known that FCC metals with high SFE promote the cross slip of Shockley partial dislocations (from screw dislocations dissociation) [119], which simultaneously reduces the likelihood of GNDs piling up [4]. This occurs due to the separation between partial dislocations must be shortened to allow their pinching in the original slip plane and extend them to an intersecting cross slip plane under applied shear stress [120,121]. The wide stacking faults, which are bordered by partial dislocations, provide them with primary slip planes for planar slip arrays [120] and the formation of GND pile ups. The highest the SFE, the lowest the splitting of dislocations and the highest the occurrence of cross slip [120].

For HSMs, it is convenient to have a low SFE to obtain the widest stacking faults [35] and highest strain hardening [120]. Taking the 304 SS as a reference, the high amounts of Cr and Ni lower the SFE [122] to an estimated value of  $16.8 \text{ mJ m}^{-2}$  [121], which is quite lower than the reported for other materials as Ni ( $150 \text{ mJ m}^{-2}$ ), Cu ( $80 \text{ mJ m}^{-2}$ ), or Al ( $200 \text{ mJ m}^{-2}$ ) [123]. As shown in Fig. 6, in SS (low SFE), the dislocations dissociate and form stacking faults instead of forming dislocation cells, allowing the formation of GND pile ups. A stress concentration equal to  $n\tau_a$ , where  $n$  is the number of GNDs in the pile up and  $\tau_a$  is the applied shear stress, will be obtained at the head of the pile up [20]. For a homogeneous SS with relatively uniform grain sizes, where the flow stress ( $\sigma_s$ ) between both soft and hard coexisting zones is similar ( $\sigma_{SA} \sim \sigma_{SB}$ , from Fig. 6), the stress concentration might push the leading dislocation to transmit across the grain boundary. In this case, the generation of long-range stress (back and forward) will be weakened, being the reason for the annulled stress represented by the solid black line in Fig. 6.

The HSMs with low SFE present a different behaviour from their homogeneous counterparts. The stress distribution of the long-range stress in HSMs ( $\sigma_{SA} > \sigma_{SB}$ ) can be observed in Fig. 6. The GND pile ups produce high back stresses in the soft zones and forward stresses in the hard zones, collectively producing high HDI stress. In addition, the GND pile ups also increase the storage dislocations capacity, which might be related to the large storage energy from plastic deformation in low-SFE materials [124] and their significant Bauschinger effect. Nonetheless, if the difference of flow stress between both zones is too high ( $\sigma_{SA} \gg \sigma_{SB}$ , from Fig. 6), voids might be formed at the boundaries. This

may lead to premature failure, lowering the ductility. This can be the case of SS with brittle secondary phases [125–128]. For comparison, the dislocation behaviour in a high-SFE material can also be observed in [Fig. 6](#). It is governed by dislocation accumulation, formation of dislocation tangles, spatial re-arrangement for dividing into cell blocks, which due to the tapping of glide dislocations, are sub-divided in dislocation cells (or incidental boundaries) [129]. As discussed above, cross slip will be favoured, and the HDI stress from GND pile ups will be neglected.

The occurrence of cross slip might also be related to the short-range microstructural order and the presence of nano second-phases with an ordered atomic structure, as well as with the increment of friction stress [130,131]. This was recently observed in medium-high SFE FeCoNi alloys with short-range ductile nano-intermetallics, which showed superior strengthening and ductility due to both HDI and forest dislocation strengthening [132].

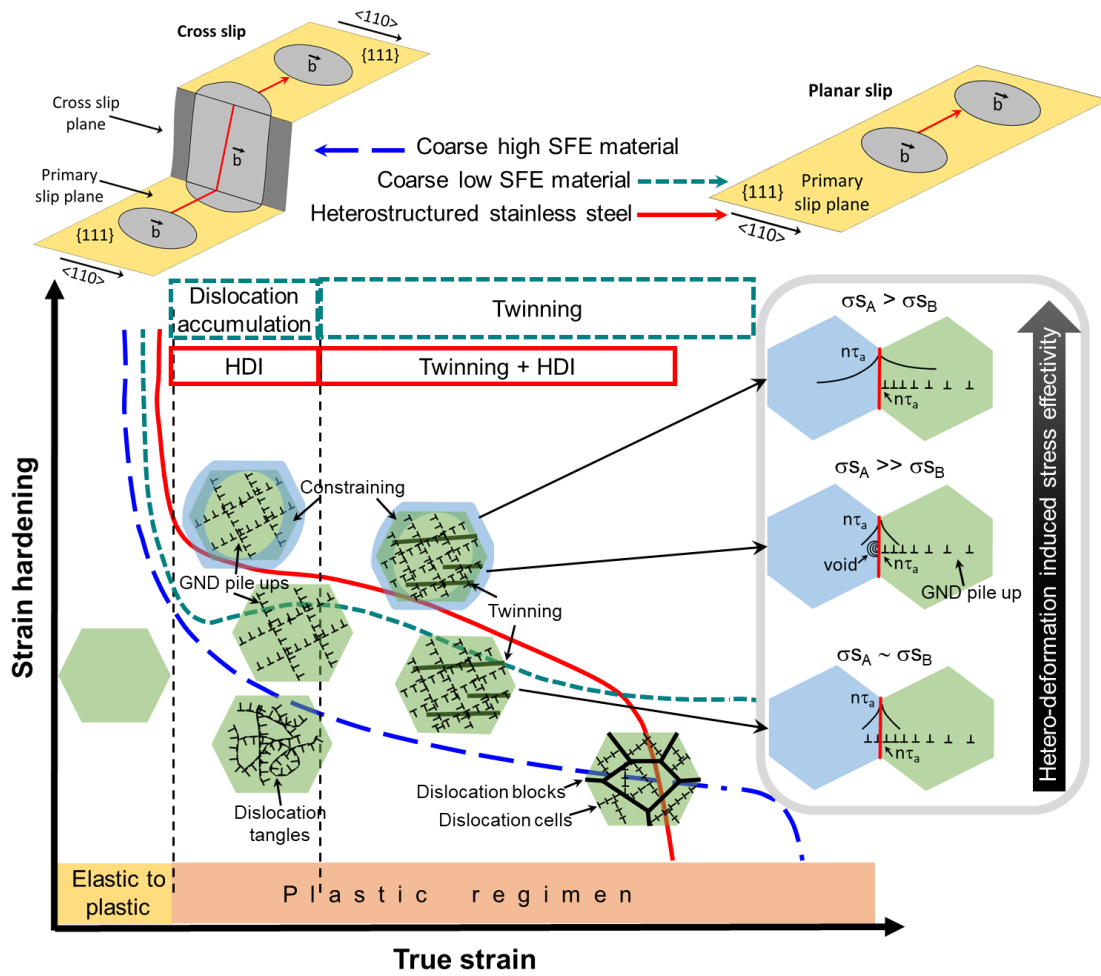


**Fig. 6.** Typical dislocation behaviour and their influence in the effectiveness of hetero-deformation induced (HDI) stress in high (blue dotted line) and low (green dotted line) stacking fault energy (SFE) coarse-grained materials, as well as heterostructured materials (red line) with inherent low SFE.  $\sigma_s$  represents the flow stress of zones A and B coexisting at the microstructure.  $\tau_a$  is the applied shear stress and  $n$  is the number of geometrically necessary dislocations (GND) in the pile up,  $n\tau_a$  is the stress concentration.

Besides, the SFE of SS promotes the martensitic transformation and twinning that occurs at SFE below  $20 \text{ mJ m}^{-2}$  and from 12 to  $45 \text{ mJ m}^{-2}$ , respectively [130,133–135]. The overlapping of stacking faults also triggers the formation of twins or stacking fault bundles [136], generating other simultaneous grain refinement and strengthening mechanisms [121]. This is the reason why the deformation twinning mechanism usually plays a key role in low-SFE materials [137], while the higher dislocation mobility in high SFE materials triggers the multiplication and migration of SSDs (forest dislocation mechanism) [123]. The deformation twinning is more used to occur at high strain rates and low temperatures, which increases the strain hardening of low-SFE materials under such conditions [121,138].

In summary of section 2, the main intrinsic characteristic of HSMs is the HDI strengthening as the major contributor to the global strengthening of the alloy. The microstructural features that encourage the occurrence of HDI strengthening are shown in [Fig. 7\(a\)](#). Those features are an ideally total constraining of the soft zone by the hard one and a difference of flow stress of at least 100% between both zones. Both constraining and mechanical mismatch are necessary to maximise the strain partitioning in the HSM, which will prompt the formation of GNDs. Lastly, the formation of long-range stress, i.e., back and forward stress, will be produced by the GNDs pile ups. As explained before, the formation of GNDs pile ups is a consequence of planar slip in low-SFE materials. The effect of those features of HSMs can be observed during mechanical properties assessments like tensile tests ([Fig. 7\(b\)](#)). Prolonged necking due to continuous increment of strain hardening will be observed in the stress-strain curves. Additionally, the highest the Bauschinger effect

evaluated through the unloading-reloading (section 2.3), the highest the HDI stress. As a result of the above, the mechanical behaviour of HSMs will not be correctly described by the classic ROM. Instead, the modified ROM (section 2.2) should be used to consider the contribution of the synergistic strengthening proper of HSMs.



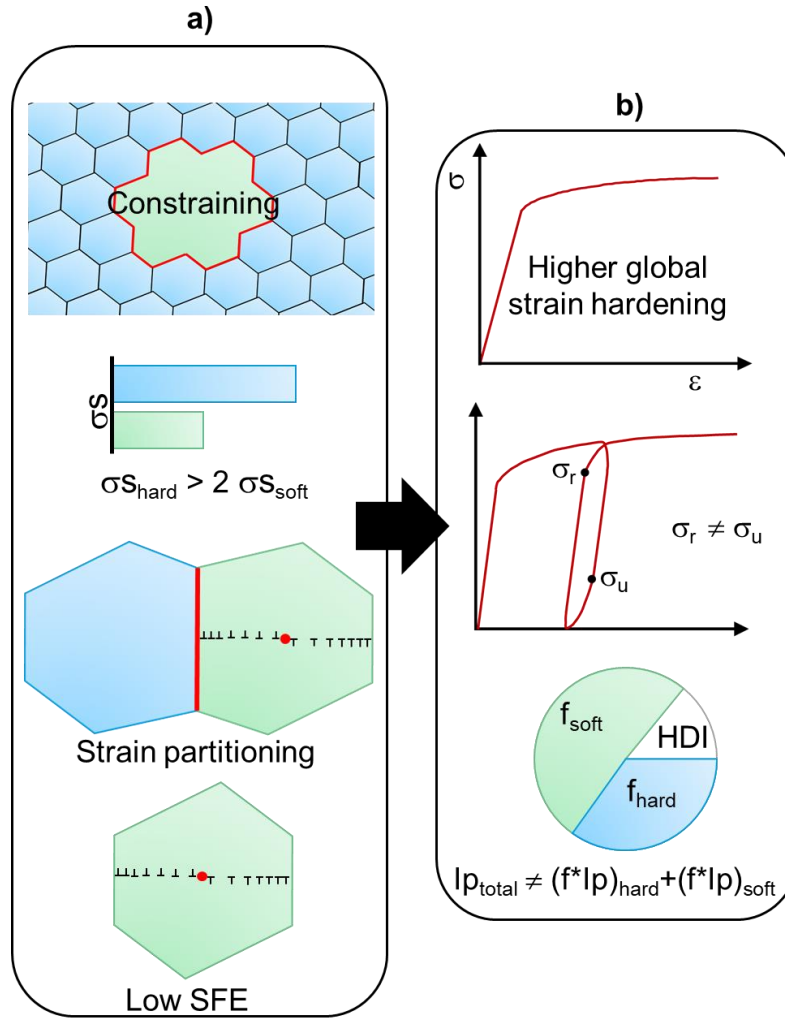


**Fig. 7.** Summary of microstructural features that encourage the occurrence of hetero-deformation induced (HDI) strengthening in heterostructured (HS) stainless steel (SS). (a) Distinctive features and (b) typical mechanical behaviour of HS materials (HSMs).  $\sigma_s$  is the flow stress of hard or soft zones. SFE is stacking fault energy.  $\sigma$ ,  $\varepsilon$ ,  $\sigma_r$ , and  $\sigma_u$  are strength, strain, yield strength during reloading and yield strength during unloading in tensile tests.  $I_p$  and  $f$  are intrinsic properties and volume fractions of soft or hard zones.

### **3. Applications of HS stainless steels (SS)**

Stainless steel is widely used in several industrial, structural, daily, and biosafety applications due to its excellent properties and low cost compared to other materials. This includes magnetic recording, hot spot detection, and stents for magnetic drug targeting, needles, scalpels, forceps, temporal dental and orthopaedic implants, and coronary stents [136,139–141]. SS is also highly applied in the nuclear field, aerospace and manufacturing because of its excellent corrosion and oxidation resistance [142]. However, many of those applications have reported failure mainly due to insufficient strength/ductility ratio during service, corrosion, and fatigue [87,140,143–146]. Therefore, improving its mechanical properties has been of great interest to researchers and industrial communities.

Due to the above, many studies have been published regarding surface modification of steel using processes like nitriding, carburizing or thermo reactive diffusion (TRD) [147], among others. However, tailoring of the microstructure without chemical interventions has gained attention because of the possibility of joining outstanding mechanical properties without affecting other properties of interest for the multiple applications of SS. As seen in section 1, HS microstructures greatly decrease the trade-off between the strength and ductility of stainless steel. Moreover, some of the utilized processes for producing HS SS, such as mechanical attrition, shot peening, and other strike-base surface processes, increase the fatigue and corrosion resistance [32,136,137,148]. This is related to the compressive surface stress state delays crack initiation and propagation, as well as due to the uniform, compacted and well-adhered passive layer in fine-grained SS [108,136,149]. Previous possibilities are

not attainable by conventional homogeneous materials. Besides, one of the biggest advantages of HS SS is that they can be produced using conventional industrial technologies and therefore be commercialized at a low cost [4].

Among their applications, HS SS can be used as superior structural materials in different industries because the high strength obtained reduces the weight of structural components, and the improved ductility helps to maintain the good safety of the structure. From the above, HS SS is a promising next generation of metallic materials for aerospace engineering applications and energy-efficient vehicles, for example, electric cars [4,5,150]. HS SS can also be used for biomedical applications because its improved corrosion resistance produces a better biological behaviour, increasing biocompatibility [151]. In addition, its enhanced pitting corrosion resistance makes it suitable for applications in instruments that are immersed in natural seawater [90,152]. Furthermore, cellular harmonic structured SS made by additive manufacturing (AM) techniques are promising as structural materials for nuclear reactors due to their high density of interfaces (sub-grains and nano-inclusions), serving as sinks for He atoms, as well as improving the hardness and radiation-induced swelling resistance of the SS [153,154]. Besides, AM SS parts have shown high hydrogen embrittlement resistance, which made them suitable for devices and infrastructure for hydrogen production, storage, transport, and utilization [155,156]. Heterostructured SS can also be coated to improve the thermal efficiency of high-temperature service components, e.g., gas turbine, nuclear fusion, diesel, jet and space shuttles engines [157].

Heterostructured SS could also find application as a novel catalyst of high performance in the form of porous stainless steel, in which meso- and nanoporous could enable improved catalytic performance with increased mass/heat transfer efficiency. The large specific surface area and pore volume could improve the contact efficiency between active components and molecules, facilitating the adsorption and reaction [158]. In addition, porous SS could provide an alternative to proton exchange membrane fuel cells because it can act as a catalyst and current collector [159].

There is plenty of room for future applications of HS SS. This review paper exhorts the scientific community for joining multi-disciplinary efforts in the matter of multi-functional HSMs. One example of the above is the immediate challenge of reducing the high risk of infections due to multiple microbes. The covid-19 pandemic made evident the need for more research regarding antibacterial and biosafety materials. Although some antimicrobial SS have been developed [160–168], including one HS [53], the physics underlying their mechanical behaviour has not been developed. This is an essential issue to cover for the scaling of new materials. Multiple SS for magnetic, electric, biological, and biosafety purposes can be combined with HSMs' virtues for broadening their applicability and service life. In summary, there are broad potential applications of HS SS in several industries to improve, or even replace, many current materials for more efficiency, biosafety, and low cost.

#### 4. Microstructural features of HSMs

This section critically discusses the microstructural characteristics of the reported HS SS following the classification indicated in the introduction (section 1) of this review. The microstructural features described in this section will posteriorly be correlated to the crystallographic texture, mechanical properties, corrosion behaviour, and other main properties of HSMs in sections 5 to 8. Aiming for clearance and order of this review, the reports cited in section 4 were classified into one of the six classifications of HSMs (Fig. 2) following the hierarchy of introduction of chemical gradients (due to combination of different materials and not phase transformation during the thermomechanical process), grain colonies morphology and their morphological confinement. However, the microstructural features of some HS SS can meet the characteristics of multiple classifications of HSMs. For example, a high nitrogen duplex SS processed by 80% CR and subsequent short-time annealing reported multiphase, bimodal, and lamellar morphology microstructure [169]. Thus, the previous work can be classified as multiphase structured, multimodal structured, or HLS materials, although, following the explained hierarchy, it was included in section 4.4 of multiphase structured SS.

##### 4.1 *Heterogeneous lamella structures (HLS)*

Heterogeneous lamella structure (HLS) refers to two-dimensional elongated morphologies of zones or defects (such as twin bundles) colonies in the matrix with different microstructures. A representative microstructure was schematized in Fig. 2. Typically, CG

zones are surrounded by NG or UFG zones, which allow effective mutual constraint and strain partitioning in such materials. As explained in section 2 (Fig. 7), those features generate effective HDI strengthening and HDI strain hardening. The HDI strengthening can be synergistic with solid solution, dislocation accumulation, phase-transformation induced strengthening, increment of grain boundaries density, or twinning strengthening to improve mechanical behaviour even more. However, as seen in section 2.2, the HDI is the dominant strengthening mechanism in HSMs. For HLS SS with effective HDI strengthening, the HDI stress at the HZB follows the behaviour explained in Fig. 3 (section 2.1).

Different thermomechanical routes can produce the HLS materials, mainly by combining rolling-based processes with partial recrystallisation heat treatments, i.e., short-time annealing [21,23,173–175,25,37,53,55,150,170–172]. The use of conventional and low-cost processes results on feasible and cost-benefit materials with outstanding properties for multiple applications. Besides, the microstructure of HLS materials can be easily tuned by modifying the time and temperature of annealing [40]. It is noteworthy that achieving UFG or NG microstructures by severe cold rolling, which is a conventional technique, is possible in low-SFE SS due to the grain refinement is accelerated by the deformation twinning mechanism [176]. This is, the mechanical twinning with narrow boundary spacing ( $\sim 20$  nm) contributes to the fragmentation of CG [176–178]. Besides, twinning accumulates strain retention and constrains the adjacent grains. Thus, deformation twinning can be utilized to enhance the strength and improve the ductility of alloys by providing additional slip systems, i.e., twinning induced plasticity (TWIP) [25,27,134,178,179]. Furthermore, the obtaining of

strain-induced martensite (SIM) and the consequent TRIP effect are firstly lead by twinning interfaces as nucleation sites [180]. Thus, the application of the conventional thermomechanical processes for producing low-SFE HS FCC metallic materials might result significantly different from their application in high-SFE FCC metals [181]. Considering that the chemical composition is not altered during the elaboration of the HLS SS, these materials might have potential uses when combined with other important properties. An example of cutting-edge HS designs is the antibacterial HLS 304 SS [53].

The typical microstructural evolution for obtaining HLS SS by CR and short-time annealing is described in Fig. 8. The as-received condition is usually characterized by nearly equiaxed CG and micro-twins from annealing (Fig. 8(a)). As explained in section 2.4, the inherent low-SFE of SS encourages the formation of twins. Since the primary cold-working stage, the CG elongates in the flow direction, and the density of micro-twins, dislocations, and low angle grain boundaries (LAGB), also known as subgrains, increases. As shown in Fig. 8(b), further deformation leads to an increase in the formation of shear bands (SB) [182]. The SBs formed boundaries across the lamellar CG at 45° to the flow direction [177]. Posteriorly, NG zones were obtained by two main mechanisms, shear fracture and subdivision of nano-twin bundles [25]. Resulting in nano-  $\alpha'/\gamma$  grains and nano-twin bundles, respectively [21,25]. The first mechanism consists of shear fracture of micro-twins and austenite within shear bands, resulting in nano-twin/nano-grain lamellas. While the second mechanism was caused by the accumulation of dislocations at twin boundaries, dividing the twin/matrix regions in blocks and changing their misorientation. Nonetheless, the

deformation initiation is encouraged by the grains and crystallographic planes with a lower Schmid factor, which results in smaller resolved shear stress for those slip systems [183]. Considering that twin boundaries have less energy than high-angle grain boundaries (HAGB) and shear bands (due to less local strain and lower stored energy) [184], the stored energy in nano-grains was expected to be higher than that of nano-twin bundles. This was confirmed by annealing treatment, where recrystallisation started in the shear fractured nano-grains (Fig. 8(c)) [21,25].

Besides, nano-twin bundles persisted when mostly NG zones were recrystallised [21,25]. Slight NG coalescence due to grain boundary migration [185] occurred in the unrecrystallised regions. As a result, austenite single-phase HLS microstructures conformed by nano-twin bundles, nano-grains, lamellar CG, and recrystallised grains embedded in an NG matrix were obtained (Fig. 8(d)). It should be clarified that the  $\alpha'$  formed during the deformation processes was reversed to austenite during the annealing treatment. A high density of HZBs was formed from the presence of nano-twins, nano-twin bundles, shear bands, and NG/CG interfaces. As a result, multiple strengthening mechanisms might be combined to obtain tough HLS 316 SS. Also, the HDI strengthening from the effective formation of GNDs piling up, the encouragement of HDI stress, and strong strain partitioning. The final mechanical properties will be deeply explained in further section 6. The representation of the distribution of GND pile ups at the HZB and their experimental observation are shown in Fig. 8(d,e), respectively. For a longer annealing duration, both nano-grains and nano-twin bundles disappeared, obtaining CG microstructures that lost the qualities of HSMs (Fig. 8(f)). The last



recrystallisation stages may occur in narrow SBs in the lamellar CG. From [Fig. 8\(g,h\)](#), annealing up to 20 min at 760°C, or more than 40 min at 750°C, at least 80 vol.% of recrystallised grains was obtained in a 316L SS [25]. The described microstructural evolution was later confirmed by reproducing the same experimental methodology and comparing 70 to 85% CR before annealing the HLS 316L SS [23,150,174].

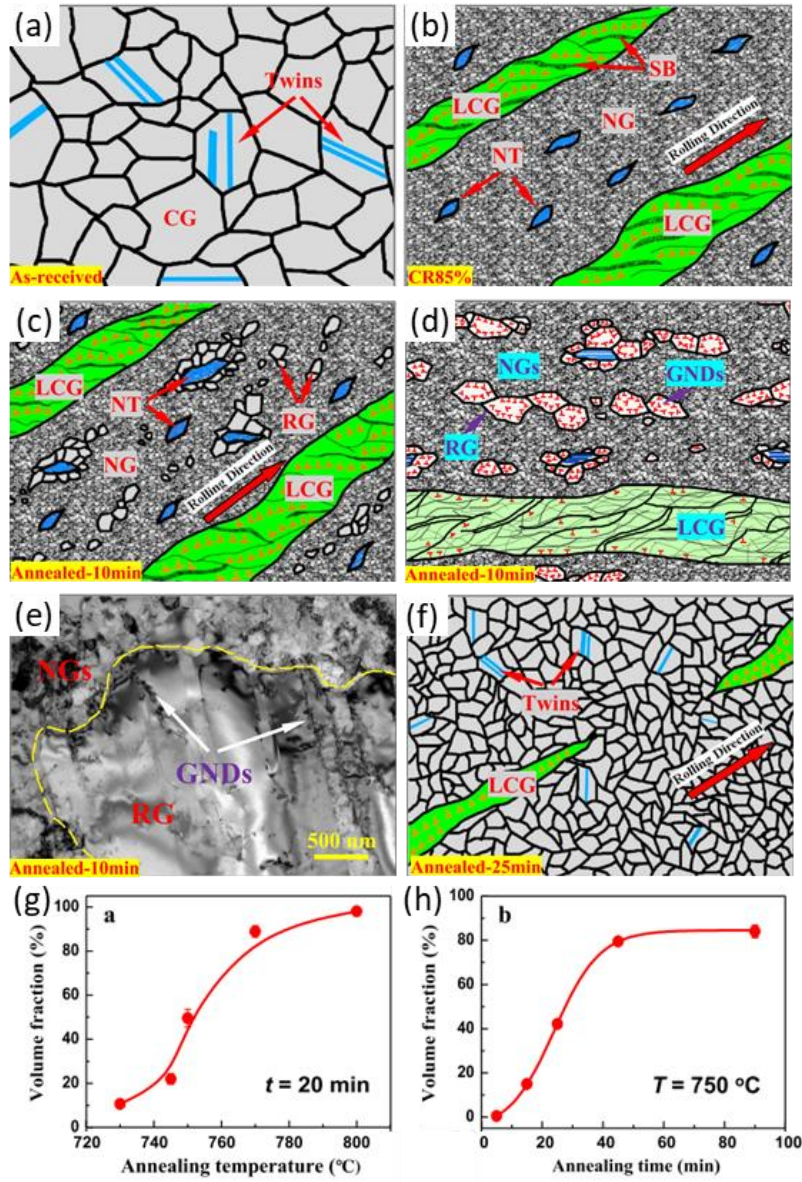


**Fig. 8.** Microstructural evolution representation of a 316L stainless steel (SS) from (a) the as-received coarse condition, (b) after being 85% cold rolled (CR), (c-e) heterostructured by 85% CR + 750 °C annealing for 10 min, and (f) fully recrystallised after 85% CR + 750 °C annealing for 25 min. The (d) representation of the formation of GND pile ups at the

HZB in HS 316L SS and (e) their observation by electron microscopy, as well as the (g-h) grain size evolution at different annealing times and temperatures are also shown [21,25].

Similar processing routes (CR + short-time annealing) from the below explained have been applied to obtain HLS 304L SS and 304 SS [37,53,55,170–173]. However, the microstructural evolution from the CR is different compared to the previously explained for the 316L SS. While the CR in a 316L resulted in 26.4 vol.% of SIM [21], the SIM in CR 314L and 304 SS resulted in ~55 to 80 vol.%, respectively [53,55,170,171]. As explained in previous section 2.4, low SFE values encourage the occurrence of SIM [135]. Due to chemical composition differences, the 304, 304L and 316L SS have SFE values of 17-18 mJ m<sup>-2</sup>, 18 mJ m<sup>-2</sup>, and 52-64 mJ m<sup>-2</sup>, respectively [29,37,184,186]. The lowest SFE value of 314L SS compared to that of 316L SS explains the higher SIM occurrence in the first. It is worth mentioning that a higher SIM occurrence can also be triggered by cryorolling due to the dependence of SFE on the temperature in different steels, including SS [187–189]. One example of this was a 316L SS with 87 to 91% of  $\alpha'$  after 20 and 30% thickness reduction by cryorolling [190]. These  $\alpha'$  percentages are high compared to the 26.4% of  $\alpha'$  obtained in 316L SS with 85% thickness reduction by room temperature rolling [21].

Different techniques other than CR might be used to obtain NG/UFG microstructures to be subjected to partial annealing to induce early stages of recrystallisation. Examples of the above are the use of electropulsing treatment (EPT) at different temperatures or discharge voltages to induce heterogeneous grain growth [191,192], as well as hot rolling [193] or DPD

[25,36]. Despite multiple differences between both processing routes, similar microstructural evolution has been reported in 316L SS processed by CR and DPD [21,25]. With the maximum strain applied (equivalent strain of 1.6 in DPD and 85% reduction in CR), the microstructures were mainly characterized by nanotwins and NG matrix, as well as transverse grain size average of about 40 nm, twin/matrix lamellar thickness of about 20 nm, YS from about 1420 to 1460 MPa, and uniform elongation near to 2% [21,25]. The main features of both processes should be described to understand those similarities. Rolling and DPD subject the material to frictional shear stress and compressive stress, respectively [194,195]. Besides, they induce different equivalent deformation at different strain speeds in the material. DPD was applied up to an equivalent strain of 1.6. The equivalent strain in rolling is a function of reduction, rollers diameter, initial thickness, and friction coefficient [196]. Considering the typical friction coefficient of 0.4 [174,197,198] for the rolling without lubricant, as well as the diameter of rollers of 400 mm [21], the surface equivalent strain can be higher than 8 [196]. Besides, DPD is recognized as an adiabatic process when applied at high strain rates [25]. The similarity might be explained in terms of the Zener-Hollomon parameter,  $Z$ , which can be expressed by Eq. (4) [199].

$$\ln Z = \ln \dot{\varepsilon} + \frac{Q}{RT} \quad (4)$$

where the  $Z$  is useful for describing the collective effect of true strain rate ( $\dot{\varepsilon}$ ) and temperature ( $T$ ) on the flow stress during plastic deformation at or below room temperature of metallic materials.  $Q$  is the operational thermally activated process's activation energy. Considering that grain boundary diffusion dominates over lattice diffusion during cold working [200], the

activation energy for grain boundary diffusion of 316 SS ( $177 \text{ kJ mol}^{-1}$ ) was considered [201]. The deformation temperature,  $T$ , was considered 293 K during CR and from 313 to 329 K for DPD [25]. For last,  $R$  is the gas constant with a value of  $8.31 \text{ J mol}^{-1} \text{ K}^{-1}$ . From the above, values of  $\ln Z$  of  $\sim 69$  and from  $\sim 71$  to  $73$  were obtained for CR and DPD processes, respectively. Those values are nearly similar for both processes, explaining the similarities between the microstructures obtained by both cold work deformation routes.

Regardless of the route to create the starting NG/UFG microstructure, the phase reversion ( $\alpha'$  to  $\gamma$ ) that occurs during annealing is a critical process to understand. The CR 314L SS showed a shear reversion (or diffusionless) process for transforming SIM into austenite during annealing [53,173]. Contrastingly, the CR and DPD 316L showed features of a diffusional reversion mechanism during annealing [21,25,190], while the CR 304 SS showed the presence of diffusional, shear, or combined reverse mechanisms [55,170–172]. This can be related to multiple factors as the chemical composition differences between 304, 314L and 316L SS, as well as the different annealing conditions reported in each work. Diffusional reversion in 304 and 304L sheets was reported for an annealing temperature range from 550–650°C [171,202,203], while the shear reversion process might be activated up to 750°C [171]. It is noteworthy that reversion process used to occur at about 100°C below the recrystallisation temperature of SS [204]. Moreover, the diffusional reversion process was reported for annealing with heating rates less than  $10^\circ\text{C s}^{-1}$ . This is due to the starting and finishing critical reverse temperatures increasing with the heating rate in a 304 SS [55,170]. However, at heating rates over  $40^\circ\text{C s}^{-1}$ , both critical temperatures remained constant, which

indicates the occurrence of shear reversion [55]. A combination of both diffusional and diffusionless reverse mechanisms occurred with heating rates between 10 to 40°C s<sup>-1</sup> [55]. Another related factor for the occurrence of different reverse mechanisms is the Cr/Ni ratio, which has a strong effect on the Gibbs free energy and, consequently, on the SIM reversion temperature [202,205]. Ratios of Cr/Ni of ~1.6 favour the shear reversion mechanism, while ratios of ~2 trigger the diffusional reversion [202]. Furthermore, Mo ( $\alpha$ -stabiliser) increases the minimum temperature for shear reversion to occur [190], being the reason for faster SIM reversion kinetics in the 304L SS compared to that of 316L SS [206,207]. The previous factors explain the occurrence of different SIM reversion mechanisms under different chemical compositions and annealing conditions on different SS.

Confirming the above, an HLS of 304L SS with Cu addition showed the presence of coarse grains surrounded by fine zones [53]. At low annealing temperatures (below 700°C), the coarse grains could be formed by a diffusional reverse mechanism. When increasing the annealing temperature, the shear reversion mechanism was dominant, which explains the presence of dislocation-free coarse grains [53]. The shear reversion mechanism occurs by recovery and recrystallisation of the deformed austenite. The presence of dislocations can be expected after the reverse treatment [202]. The diffusion reverse mechanism occurs by austenite grain nucleation and growth, resulting in nearly equiaxed microstructures [202]. Furthermore, after 1.5 h-annealing in the temperature range of 650–700°C, at least 6 vol.%  $\alpha'$  remained in the microstructure. The authors attributed this behaviour to the occurrence of diffusional reversion followed by shear reversion [53]. This combination of reversion

mechanisms could originate from the high thermal stability of SIM below 700°C in 304L SS [172,208], as well as to the Cu addition that stabilises austenite and favors the shear reversion mechanism [53,168,209].

#### 4.2 *Gradient structures (GS)*

Gradient structured (GS) materials have been of great interest during the last years because they render a unique extra strain hardening that leads to high ductility [99,210–213]. In GS materials, the structure changes gradually from the surface to the interior, showing an NG structure of tens of nanometers on the surface layer to a CG structure of tens of micrometres in the centre of the sample [214]. A typical GS microstructure was shown in [Fig. 9\(a\)](#). The microstructural gradient along the depth can be due to grain size, dislocation density, or crystallographic texture [32]. Chemical composition can also vary as a gradient profile from the surface but never distributed through all the bulk (in which case it would be a multiphase HS SS, which will be described in section 4.4) [215]. However, most GS SS have been focused on grain size gradients increasing from the surface to the centre of the sample, as shown in [Fig. 9\(a\)](#). Therefore, GS materials combine the ultra-high strength of NG and the high ductility of CG. This can be achieved due to the mechanical incompatibility among NG/UFG/CG regions [103]. Significant strain incompatibility will occur among layers during straining, i.e., inter-layer constraining, leading to unique crystallographic and mechanical responses [99,216]. In GS subjected to strain, the CG matrix begins to deform plastically while the NG surface remains elastic. The mechanical incompatibility leads to strain

partitioning, which consequently causes macroscopic strain gradients, as shown by the solid black line in Fig. 9(a) [217]. This leads to an increment of GNDs to accommodate the large strain gradient near the migrating elastic/plastic interfaces and later the migrating stable/unstable interfaces [217]. As a result, extra strain hardening in the overall GS material will be obtained compared to the poor strain hardening capability of the NG zones and extra strengthening compared to the soft CG regions [4,80,217]. As explained in previous section 2, multiple synergistic strengthening mechanisms can be active, such as TWIP, TRIP, SIM, dislocation accumulation, and second phases, but HDI strengthening will be dominant for HSMs [80,210]. The hardness of GS materials will be redistributed under straining from the different mechanical responses between the NG, UFG and CG regions, as shown in Fig. 9(a) by the solid magenta line [218].

Besides the ultra-high-strength, GS SS materials have superior fatigue life due to crack initiation and propagation delay, which is a well-reported effect of compressive stress states in industrial SS and other metallic components [148,219–222]. Besides, the NG surface gains multiple industrial advantages over typical SS as improvement of corrosion resistance due to the formation of a more efficient and adhered surface oxide layer [223], reducing the formation of bacterial surface biofilms due to a minimized electronic surface interaction [224], and increasing atomic diffusion with consequent better cohesion strength and wear resistance of surface films [225]. Improvement of friction and wear resistance have also been reported for GS materials [226]. In addition, GS materials do not need to introduce artificial



defects or additional alloying elements to improve their properties. The superior properties of GS SS will be deeply covered in later section 6 of this review.

The GS materials are obtained by a gradual decrease in the extent of cold SPD from the surface to the centre of processed materials. Resulting in a decreasing gradient of hardness and flow stress with the depth as shown in Fig. 9(a) by the blue dotted line [50]. The surface nanostructuring techniques to produce GS SS are based on the application of high surface compressive stress profiles and work hardening by repetitive local strains, i.e., strains in an immediate small contact area that extends gradually to the whole surface. There are two main mechanisms used for surface nanostructuring: 1) repetitive normal compressive strains at high strain rates, or 2) inducing torsional or shear strain to the surfaces [227]. Examples of the first group of techniques are shot peening processes [29,222,228–234], blasting [224,235–242], SMAT [30,31,244–253,32,254–261,33,49,121,148,220,225,243], surface mechanical rolling treatment (SMRT) [262–264], ultrasonic surface rolling (USR) [62,265,274,266–273], ultrasonic severe surface rolling (USSR) [275], electropulsing-assisted ultrasonic surface rolling process (EP-USRP) [265], ultrasonic nanocrystalline surface modification (UNSM) [137,226,276], ultrasonic impact treatment (UIT) [213], ultrasonic surface mechanical attrition treatment [277], ultrasonic peening (UP) [223,226,229,278], ultrasonic impact peening (UIP) [279], laser-shock peening (LSP) [279], air blast shot peening (ABSP) [226], waterjet peening [280], and the combination of previous techniques with ceramic particles implantation [62,242] or coatings [225]. Among the second

group of techniques are torsional deformation [227], pipe inner-surface grinding (PISG) [281,282], SMGT [283,284], and surface spinning strengthening (3S) [212].

From the mentioned techniques, the most employed have been SMAT and peening. Among the differences between both processes is that the SMAT process involves confined particles' motion with multi-directional colliding angles onto the surface [285,286]. As a result, the strain path varies continuously, and various slip systems are activated. Interaction between active and inactive (created in the previous strain path) dislocations is promoted and assists on the surface grain refinement [260]. Besides, SMAT is an efficient, eco-friendly, and cost-effective surface severe plastic deformation technique (S2PD) [50]. From the GS profile, SMAT results in substantial surface strengthening due to work hardening, increment of grain boundary density, and mechanical twinning strengthening [30,49,220,259,287,288]. Despite the contribution of HDI hardening in SMAT processed SS has been scarcely recognized, the HDI was suggested from the improvement of strain hardening rate (and necking delaying) caused by effective mutual constraining between the NG, UFG and CG zones in a GS 304 SS [49]. Besides, the contribution of back stress in GS materials is well established [217]. Moreover, the strong contribution of HDI to the total strengthening and hardening has been clarified in a double-sided Cu GS [51], which has a GS distribution similar to that of the GS 304 SS [49]. Remarkably, the contribution of HDI synergistic strengthening ( $\Delta\sigma$ , Eq. (1)) is a non-linear function of the volume fraction of the GS layer, being reported higher at about 20% GS layer in GS Cu processed by SMAT [51].

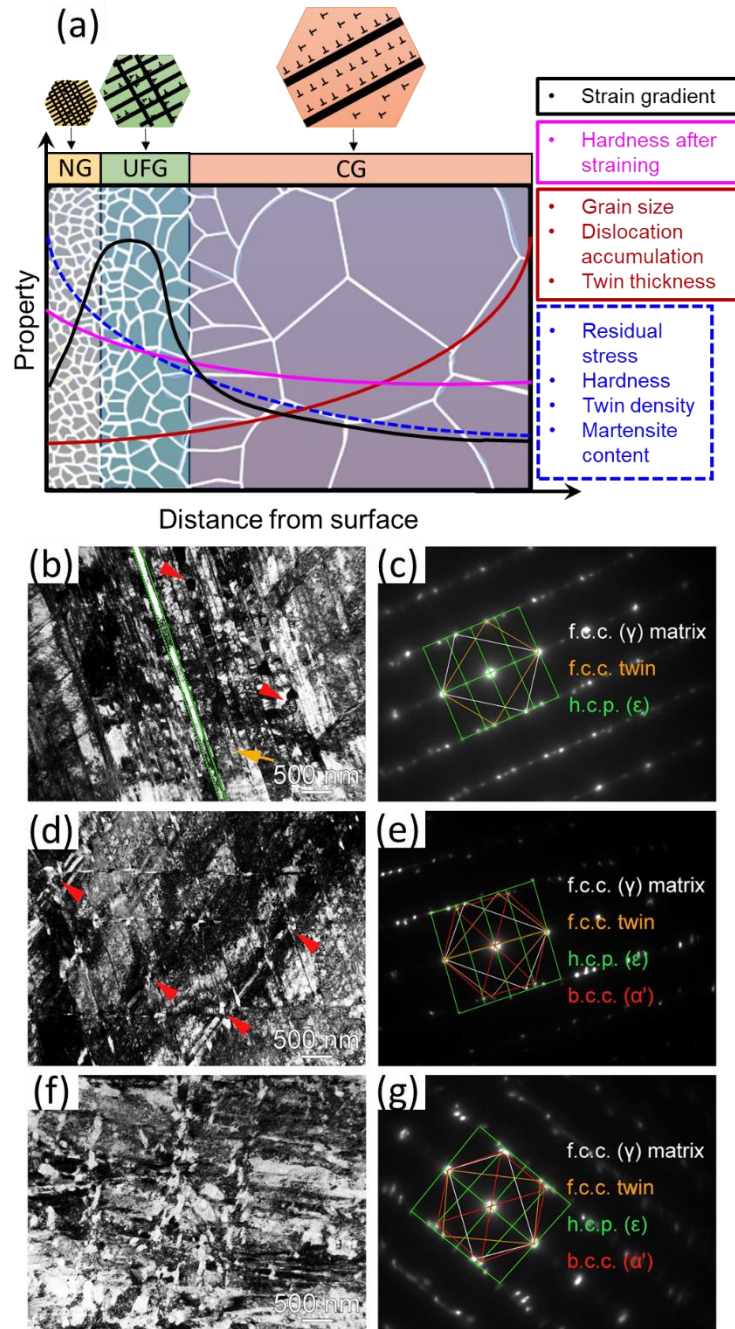


**Fig. 9.** (a) Typical microstructure and features of gradient structured (GS) stainless steels (SS) and (b-g) example of  $\gamma$  to bcc- $\alpha'$  phase transformation by TEM micrographs and

SAED patterns from the surface layer of a 301 SS treated by SMAT for (b,c) 1 min, (d,e) 5 min, and (f,g) 10 min. (b-g) Adapted from [31].

Among different types of SS, austenitic GS SS has been of special attention due to its properties [31,50,288–290]. The grain refinement mechanisms in austenitic GS SS are related to 1) sub-division of coarse grains by twinning and shear bands (SB), and 2) formation of nano-sized  $\alpha'$  due to phase transformation at high plastic deformation [148,226,260]. In the first mechanism, as the austenitic SS surface layer is plastically deformed, SB and twinning form from the surface to the adjacent layers. These defects (twinning, SB, and their interfaces) are the primary deformation microstructures in GS materials, especially in FCC metals with low SFE, such as SS. When twinning increases in density, twins in different  $\{111\}$  planes intersect and fragment the  $\gamma$  grains. This grain refinement mechanism is comparable to the previously explained in section 4.1 for HLS SS materials. In the second mechanism, the grain division progresses via newly formed  $\alpha'$  grains nucleated at preferential sites as stacking faults, twin/twin,  $\varepsilon$  or shear bands boundaries [121,234,291]. Thus, the grain boundaries from the transformation of  $\gamma$  to  $\alpha'$  divide the original CG into NG regions [231]. Furthermore, other secondary grain refinement mechanisms, such as grain rotation or grain boundary sliding, can also be active to accommodate the strain [148,260].

Strain-induced martensite is a common result of surface grain nanostructuring in SS. The  $\gamma$  to  $\alpha'$  transformation has been described as displacive transformation, in which the rearrangement of atoms occurs through short distances movements in unison rather than

diffusing individually over long distances and without producing volumetric changes in the overall material [292,293]. Depending on the chemical composition of the SS and the deformation conditions, the  $\gamma$  phase (FCC) may directly transform to  $\alpha'$  or pass through the intermediate  $\epsilon$ -martensite phase (hexagonal close-packed, HCP) [234,276]. The crystalline structure of final martensite in steels can be either BCC or body centred tetragonal (BCT) depending on the C content, the intersection or not of independent  $\{111\}_{\gamma}$  slip systems, the lattice strain, and the stress state applied to the material [294–296]. However, some reports found challenging results regarding the predictions by the classic Zener's ordering model for the formation of BCT instead of the BCC martensite in high-C steels [297], as well as the formation of martensite from pearlitic steels instead of  $\gamma$  steels [295]. Thus, there is plenty of room for future research about the thermodynamic conditions that govern martensite formation in homogeneous and HS steels.

Several authors have studied the phase transformations described in GS SS [103,231,233,298]. As an example, Figs. 9(b-g) show the transformation  $\gamma$ - $\epsilon$ - $\alpha'$  (BCC) occurred in a 301 SS treated by SMAT at different times [31]. For samples treated for 1 minute, a composite nano-lamellae containing  $\gamma$  matrix and  $\epsilon$ , as well as twins, was obtained (Figs. 9(b,c)). After 5 minutes of treatment, irregular UFG and NG  $\alpha'$  were produced and embedded in the nano-lamellar matrix, which were identified by SAED patterns (Figs. 9(d,e)). After 10 minutes of treatment, there is a large amount of granular  $\alpha'$  that replaces the lamellar structure and is finally composed of  $\gamma$  matrix,  $\epsilon$  and  $\alpha'$  with the presence of twinning (Figs. 9(f,g)). The diffraction spots of the  $\alpha'$  phase are significantly enhanced, indicating a large volume fraction of  $\alpha'$  [103].

It is noteworthy that, additionally to the HZB generated from the mechanical incompatibility between  $\gamma$  and  $\alpha'$  interfaces, other mechanical incompatibilities can be formed by twin/matrix interfaces, SB/matrix, and differences in crystallographic orientations resulting from the  $\gamma$  to  $\alpha'$  phase transformation [276]. Thus, the phase transformation during surface nanocrystallization implies a crystallographic texture gradient with depth. Attrition and peening generated a strong  $\langle 110 \rangle$  and a weaker  $\langle 111 \rangle$  texture on the surface of Cu and Fe with an intensity that decreases with depth [299–301]. Some reports also hypothesised the presence of weak cube  $\langle 100 \rangle$  texture due to attenuated plasticity in dead-metal zones [299]. Similar findings were reported for GS SS by a tendency of  $\gamma$  and  $\alpha'$  towards  $\langle 100 \rangle$  and  $\langle 111 \rangle$  preferred orientations (Kurdjumov-Sachs orientation relationship  $\langle 110 \rangle_{\gamma} // \langle 110 \rangle_{\text{twin}/\varepsilon} // \langle 111 \rangle_{\alpha'}$  [302]) in 316L SS and 304 SS subjected to shot peening and SMAT, respectively [49,303]. Deep analyses of phase transformation in SS have indicated that the Kurdjumov-Sachs orientation is preferred after  $\gamma$ - $\varepsilon$ - $\alpha'$  phases transformation, while the Nishiyama–Wassermann orientation ( $\langle 110 \rangle_{\gamma} // \langle 001 \rangle_{\alpha'}$ ) is preferred for  $\gamma$ - $\alpha'$  and for the starting of the  $\gamma$ - $\varepsilon$ - $\alpha'$  transformation [276,291,304]. A critical discussion of crystallographic texture in different HS SS and its implications will be deeply discussed in the following section 5 of this review.

### 4.3 Layer structures (LS)

Layer structures (LS) refer to 2D composite-like heterostructures with hetero-interfaces [4]. A representative scheme of LS's typical microstructure is shown in Fig. 2. The LS materials are a special kind of composite materials where the thickness of every individual layer varies from a few atomic layers to micrometres [4,305,306]. For an individual layer with thickness down to 100 nm, the LS materials can be classified as nanolaminates, nanolayered, multilayers materials or superlattices [305]. The mechanical properties of nanolaminates are not determined by the ROM unlike the properties of conventional bulk materials [307,308]. Different types of combinations have been used to obtain nanolayer materials, such as ceramic-ceramic [309,310], amorphous-crystalline [311–313], metal-ceramic [314], and metal-metal [315,316], among others.

The LS materials present chemical and stress distribution discontinuities across the HZBs. The occurrence and significance of HDI strengthening in LS materials is closely related to the grain size, grain morphology, crystallographic texture and chemical composition that influence the strain partitioning at the hetero-interface, as well as to the hetero-interface spacing and possible defects as porosity at the interfaces. It is well-known that smaller grain sizes and sharp morphologies lift the mechanical strength of metallic materials, being promising to create high strain partitioning at their interfaces with softer CG zones. Lower porosity at the interface allows a stronger bonding strength between layers and improves the whole LS strength [317].

Different bottom-up (Figs. 10(a-d)) and top-down (Fig. 10(e)) methods have been used to elaborate LS SS. Between the bottom-up techniques, physical and chemical deposition methods as sputtering [318–320], plasma-spray [157], spray pyrolysis [321], sol-gel [321], spin coating [321–324], closed field unbalanced magnetron sputtering (CFUBMS) [325], hydrothermal methods [326,327], click chemistry [328], chemical vapor deposition (CVD) [329–331], successive ionic layer adsorption reaction (SILAR) [332], atomic layer deposition (ALD) [333], electrophoretic deposition (EPD) [334,335], electrodeposition [336,337], thermal evaporation [338], thermionic vacuum arc (TVA) [339], ion-exchange [340], electrosynthesis [341], plasma surface alloying (PSA) [342], or by a combination of different techniques for applying several layers or doping [343–348] or for assembling them [349], as well as AM [48,350–352] have been successful. The substrate of the first deposited layers during bottom-up techniques commonly influences the stress state and epitaxial grain growing (preferred texture) along the heat flow direction [323,324,333,345,350]. The stress state, crystallographic orientation, chemical composition, grain morphology, grain size, and thickness highly impact thin films' surface energy and properties such as magnetic, corrosion, photoelectronic, and elastic, among others [324,353–355]. On the other hand, top-down methods such as explosive welding [356], CR and HT [47] have been reported to produce LS SS. Combinations of previous techniques can also be developed to trigger different strengthening mechanisms through microstructure tailoring. For example, the use of AM techniques with posterior CR and short-time annealing [357] or lamination and nanoparticles printing [358].



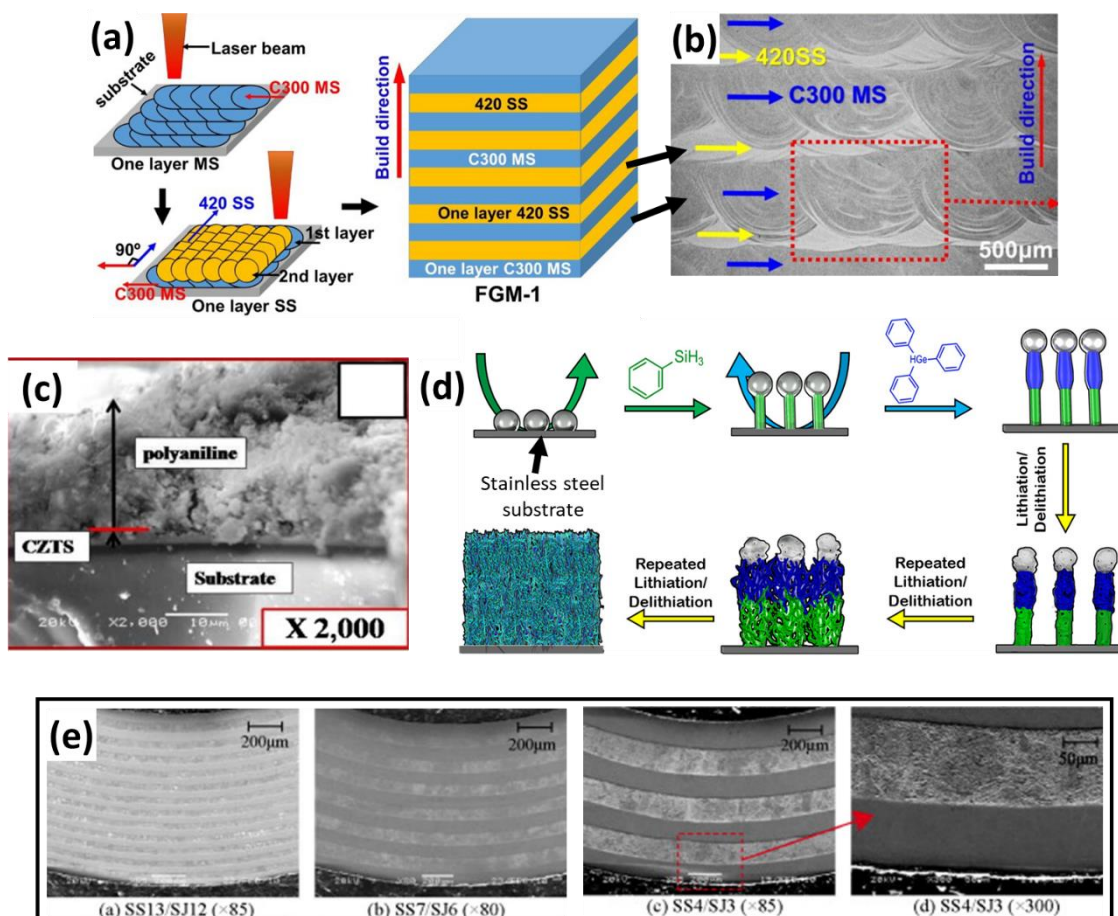


**Fig. 10.** Layer structures (LS) produced by different (a-d) bottom-up and (e) to-down methods as (a,b) additive manufacturing with interleaved layers of stainless steel (SS) and maraging steel [350], (c,d) deposition thin films methods with SS as substrate [332,344], and (e) rolling of interleaved layers of two different SS [47].

Some SS macro-layer materials with micrometric to millimetric thicknesses have been reported [351,352,356]. In these cases, the hardness depended on the morphological and

chemical changes across the microstructure. Other authors reported strong strain partitioning and delayed necking together with significant strengthening in some LS constituted by multiple alternate micrometric layers [47,350]. As an example of the above, the LS 304 SS/420J2 SS resulted in a reduced trade-off between ductility and strength compared to each constituent steel [47]. The authors explained the delay of necking based on the strain partitioning between both steels. This caused different stress state in each layer, increasing the strain hardening rate in the harder zone and the strength in the softer one. The significant contribution of HDI strengthening to improve the mechanical behaviour of LS SS has also been reported [350]. Some others reported decreasing mechanical properties due to macro-segregation and brittle intermetallic phases [351]. A more detailed revision of the mechanical properties of LS and other HSMs can be found in section 6 of this review.

Regarding nanolayer materials, SS substrates have attained much attention because of their low cost and mechanically durability compared with those of other substrates such as fluorine-doped tin oxide (FTO), indium-doped tin oxide (ITO), or glass [346,359]. Other properties of SS substrates as high corrosion resistance [360], the possibility to reduce hydrogen permeability by coating [320], and being a good conductor under alkaline conditions [328] are also advantageous for multiple applications. Besides, SS substrates can also act as a buffer supporting the improvement of adhesion and reducing the interdiffusion of elements from the substrate [348]. Examples of applications of thin films on SS substrates are household, including actuators, flexible sensors, biomedical devices, biosafety devices, thermal sensors, marine environments, water treatment, hydroelectric energy, batteries,

supercapacitor electrodes, among others [323,331,362,363,333,335,341,344,345,348,360,361]. The mechanical and corrosion properties of LS materials will be further developed in section 6 of this review.

#### *4.4 Multiphase structures*

The multiphase structured materials consist of microstructures with at least two coexisting phases distributed in the bulk material with large flow stress variations between them. A representation of the typical microstructures of multiphase structured materials is shown in [Fig. 11](#). To differentiate the different kinds of HSMs, the multimodal structured, HLS, GS, and harmonic structured materials are used to keep similar chemical compositions within the different grain sizes or morphologies. Some local chemical variations, such as segregation or atomic diffusion gradients, may be present, but the chemical composition and crystalline structure remain similar throughout the microstructure. On the other hand, the LS materials pile up regions with different chemical compositions in a very specific array, i.e., as parallel layers. Different from the above, the distinct phases (zones with different chemistry and/or crystalline structure parameters) on the multiphase structured materials can have any of the array (or being random) except as layers. The possible arrays of multiphase structured materials are shown in [Fig. 11](#). The hard phase can be surrounded by a continuous soft matrix (or inverse), similar contents of both phases can be randomly distributed through the microstructure, or they can have an interpenetrating arrange. Interpenetrating arrange refers to interconnected and three-dimensionally continuous phases throughout the microstructure

[364]. However, an important question is still at the core of the correct identification of HSMs. Is the coexistence of different phases enough to obtain a significant HDI strengthening?. The example of an aged duplex SS will be used to clarify this concern.

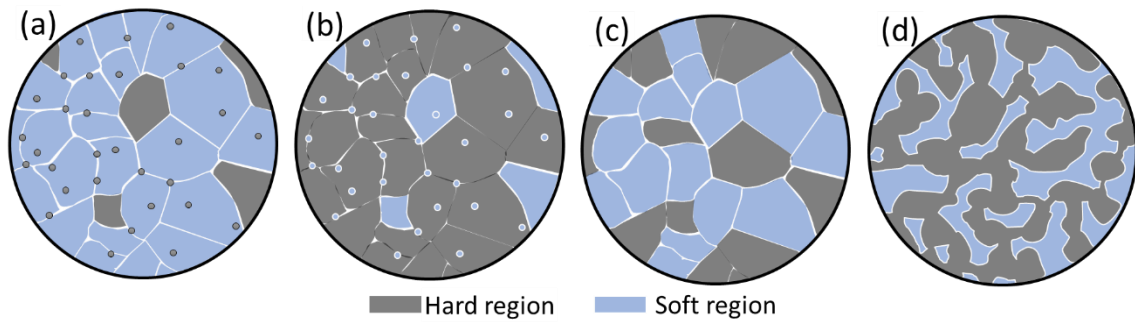


**Fig. 11.** Representation of multiphase structured materials (a) hard core, (b) soft core, (c) similar contents of randomly distributed hard and soft phases, and (d) interpenetrating phases.

A duplex SS (ferrite + austenite) was obtained by artificial ageing at 400°C [52]. After prolonged thermal ageing, spinodal decomposition of ferrite generated  $\alpha_{\text{Fe}}$  (Fe-rich) and  $\alpha_{\text{Cr}}$  (Cr-rich) phases, G-phase (silicide) was also obtained at the inner ferrite. The hardness of the as-cast duplex SS showed a 2.7-fold increment after ageing for 10,000 h, which was related to the formation of the  $\alpha_{\text{Cr}}$  phase and G-phase [52,365–367]. Nevertheless, the precipitation of intermetallic G-phase at the interfaces (preferred sites for cracking) leads to a toughness reduction of 4.7 times of the total impact energy after 20,000 hours of ageing compared to

the as-cast condition. The likely reason for the negligible effect of HDI strain hardening in providing additional ductility in the duplex SS could be the reduced strain partition between the phases and, consequently, the reduced amount of HZBs in the microstructure. The HZB between soft and hard zones in the HSM require at least 100% strength differences between them [76]. The hardness difference between ferrite and austenite in duplex SS has been reported to be below 20% [368,369], being why these phases do not accomplish the requirements for efficient strain partitioning. Moreover, the G-phase intermetallic, which has been pointed out as a strong contributor to hardening in duplex Mo-bearing steels [365,367], has a low percentage in the microstructure, providing insignificant HZB density. The HZB density is an important factor since it promotes mutual constraining between the soft and hard regions. As explained in Fig. 7, this is the requirement for obtaining HDI stress [78]. Furthermore, ideally, the soft zone in HSMs is surrounded by the hard one, maximising the occurrence of strain partitioning. However, in the example of the aged duplex SS, the hard zone was heterogeneous and widely distributed in the microstructure. Moreover, after 10,000 h ageing, the expected coarse grain sizes of both  $\gamma$  and  $\alpha$  phases do not encourage the strain partitioning.

The above reasons explain why several multiphase alloys, including some alloys with coarse phases, solute macro-segregations, or soft/low-content precipitates, do not meet the requirements for a significant contribution of HDI strengthening and hardening. On the other hand, as seen in section 2.4, when the mechanical mismatch between hard and soft zones is too large (case of  $\sigma_{SA} \gg \sigma_{SB}$  in Fig. 6), failure might occur due to high local stress

concentration that might exceed the interface bonding strength and trigger cracking [125–128]. Besides, if the second phase particles are so small, coherent, or there is a low mechanical mismatch (case of  $\sigma_{SA} \sim \sigma_{SB}$  in Fig. 6), stress shielding occurs, and the matrix leads to the mechanical performance of the overall material [370], promoting properties as the fracture toughness but decreasing others as the contribution of HDI stress. This is the reason why second phase nanoparticles with volume fractions homogeneously distributed throughout the matrix are not used to be enough for decreasing the trade-off between strength and ductility on SS [162,163,167,371]. So, as described in Fig. 7 (section 2.4), effective constraining, at least 100% difference in flow stress, enough density of HZB, and low-SFE are required to reduce the strength to ductility trade-off in multiphase structured or any other HSM. For multiphase structured materials with effective HDI strengthening, the HDI stress at the HZB follows the behaviour explained in Fig. 3 (section 2.1). Besides, the coherency at the hetero-interfaces should be considered. While dislocations can be dissociated at coherent interfaces, they might have a low diffusion through incoherent interfaces [372].

Different processing routes can be used to produce multiphase structured SS. The possibility of mixing low solubility components makes powder metallurgy (PM) and additive manufacturing (AM) some of the most efficient techniques for making hard core, soft core, or nearly equiphase multiphase structured SS (Fig. 11(a-c)) [34,125,373–379]. However, traditional casting and ageing to precipitate second phases can also be useful to produce hard core or soft core multiphase SS [160,167,380–383]. Different HT can also be applied to as-cast or cold worked SS to obtain multiphase structured SS. Examples of the above are the

three generations of advanced high strengthening steels (AHSS) that control the microstructures by using cold work and/or single-stage or multi-stage HT [384–388]. Based on the already discussed low-SFE of SS, these materials boost the occurrence of SIM and twinning induced-plasticity to assist in the improvement of mechanical properties in AHSS. The first AHSS generation includes some SS as dual-phase (DP) or duplex, martensitic, and TRIP steels [35,169,397–402,389–396]. Other SS are also included in the second generation of AHSS, like metastable austenitic and TWIP SS [403–405], while the third generation includes medium-Mn TRIP SS and quenching and partitioning (Q&P) SS [406–408]. To elaborate interpenetrating multiphase structured materials (Fig. 11(d)) with SS as matrix [409–411], reinforcement [412,413,422–425,414–421] or coating [426], preform porous structures can be done by PM methods [409,411,419], AM [412,416–418,420,423], pressing and sintering [410,413–415,422,424], squeeze casting [422], welding of mesh [421], freeze-casting, or replication process, etc. Those preforms will be lately infiltrated with molten alloy by high pressure die casting (HPDC), spring-driven centrifugal casting, capillarity-driven infiltration, vacuum-assisted melt infiltration, etc. Different modelling efforts have been done to study the elastoplastic behaviour and its relationship with different properties and damage evolution of interpenetrating arrangements with SS as matrix or reinforcement [427,428].

As explained in section 1 of this review, HSMs are an emerging field and the contribution of HDI stress and HDI strengthening need to be further studied in diverse HS SS. Some multiphase structured SS have been studied together with its HDI strengthening contribution. An austenitic A13Cr multiphase structured alloy consisting of a 13Cr–5Ni–2Mo

supermartensitic SS with 8 wt.% Mn was reported [35]. The Mn content supported the reduction of SFE of  $\gamma$ , and with that, the formation of shear bands, which served as nucleation sites for SIM and allowed a synergistic contribution of the TRIP effect. By CR and HT, a HS constituted by UFG laths of  $\gamma$  and  $\alpha'$ , as well as equiaxed  $\gamma$  embedded in micrometric  $\gamma$  was obtained. The multiphase structured A13Cr showed a reduced trade-off between strength (923 MPa) and uniform elongation (UE, 28.6%) compared to the as-received (YS=912 MPa, UE=9.2%) and quenched (YS=278 MPa, UE=51.2%) conditions. Considering a high density of HZB due to the coexistence of different order size zones, the encouragement of GND pile ups, the TRIP effect, high grain boundaries density, and the solid solution contribution, a strong synergy of various strengthening mechanisms could improve the mechanical behaviour of the HS A13Cr alloy. The authors confirmed the contribution of HDI stress by the unloading-reloading method (section 2.3). They reported values of HDI stress ranged from 454 to 485 MPa at 3% strain, which was a strong contribution considering that the flow stress is 955 MPa. Besides, the estimated HDI strength was estimated from 343 to 348 MPa from the modified ROM.

#### 4.5 Harmonic structures

Harmonic structured materials, also called core-shell materials, refer to microstructures with CG cores surrounded by NG or UFG shells [42,429–432]. A typical harmonic microstructure representation was included previously in Fig. 2, and a harmonic structured 304L SS is shown in Fig. 12(a). The harmonic structure is essentially a bimodal structure



with a specific three-dimensional (3D) periodic arrangement of CG and NG zones. As shown in Fig. 12(a), the hard UFG/NG regions (shell) form a continuously connected network surrounding the soft CG (core) regions in three dimensions [429]. Unlike the interpenetrating multiphasic SS discussed above (Fig. 11 (d)), chemical composition variations between shell and core zones are not essential for harmonically structured SS [41].

Previous description of harmonic structured materials might be met by microstructures whether at local or volumetric ranges, i.e., by soft cellular structures surrounded by harder high-dislocation density networks, all embedded in grains (Fig. 12(b)) or by colonies of soft grains surrounded by the harder volumetric matrix that involves several grains (Fig. 12(a)). The first type of HSM refers to dislocation networks in bulk materials that can be mostly obtained by AM techniques [433–435], including laser powder-bed-fusion (L-PBF) [154,436,445–454,437,455–462,438–444], selective laser melting (SLM) [153,156,469–478,434,479–488,435,489–491,463–468], 3D printing [492], directed energy deposition (DED) [485,493–495], wire-arc additive manufacturing (WAAM) [480], laser metal deposition (LMD) [470], laser-aided direct metal tooling (DMT) [155], among others. The dislocation density networks and/or their alignment can be mainly controlled by the scan speed and the temperature gradient direction during solidification, respectively [435]. Compared to other homogeneous materials, stainless steel with cellular structures obtained by AM has reduced strength to ductility trade-off [434,435,456,460,462,469]. There are two main paths to improve the strength-ductility relationship: 1) promoting dislocation accumulation for improving intra-granular dislocation plasticity (e.g., grain refinement or

nano-twinned grains), and 2) HDI hardening already explained in section 2 [496]. A significant strengthening due to forest dislocation has been reported in cellular harmonic structured SS [497]. Other authors pointed out a significant contribution of long-range stress (back and forward or HDI stress) to the total strengthening of a cellular AM SS [462,486,495], as well as the dominant effect of GNDs on the strengthening of these materials [450]. However, cellular boundaries can act as weaker barriers for dislocation motion compared with traditional HAGBs [433], allowing the penetration of GNDs through the cellular boundary and their annihilation with the opposite dislocations [486]. The scenario with a weak cellular boundary might be similar to the case of  $\sigma_{SA} \sim \sigma_{SB}$  explained in Fig. 6. The study of stress diffusion through the cellular boundary and its comparison with stress diffusion along other HZB conformed by soft/hard grains interfaces remains to be studied and simulated. Cellular networks might have higher energy and more structural disorder than HAGBs. Thus, they might have faster stress diffusion along the boundaries but slower diffusion through the inside cells [498]. The thick dislocation network boundaries, which can be of some tens of nanometers (insert of Fig. 12(b)), should also be considered. Furthermore, the arrangement and interactions of the high density of dislocations inside the cellular walls should be thoughtfully investigated [461].

Furthermore, other authors correlated a pronounced Bauschinger effect with both back stress and intragranular stress [459]. Moreover, as explained in section 2.2, HS SS is used to combine different strengthening mechanisms. The contribution of different strengthening mechanism on cellular harmonic structures, as well as different HZB as coexistence of grains

with different dislocation density networks, heterogeneous grain size distributions, second phase particles (precipitates and segregates), solute heterogeneity, twinning, SIM, ceramic particle-reinforcement, among others [433,435,461,462,469,473,476,483,485,486,492,494,440,495,497,447,448,451,453,454,457,458] is still not completely clear. Plenty of research can be done to clarify the strengthening mechanisms in cellular hierarchical HSM AM materials [433], including the interaction and possible interference between GND pile ups formation, twinning, dislocation slip, and cells boundaries [433,483,486,490]. As high densities of dislocation network boundaries are used to limit the formation of twinning, the reduced occurrence of SIM due to lack of nucleation sites for  $\alpha'$  is a common phenomenon in cellular AM SS during straining [155,156,468]. This phenomenon might be beneficial for corrosion because martensite is used to be a preferential active site [156]. A more detailed review of corrosion in HS SS will be developed in section 7.

Furthermore, the hierarchical dislocation networks or cellular structures from [Fig. 12\(b\)](#) are different from the dislocation cells structures typical of wavy slip on many homogeneous high-SFE materials ([Fig. 6](#)). The origin of dislocation networks in low-SFE harmonic structured SS is the high temperature and grain growth gradients with low atomic diffusion during the high solidification rate and consequent thermal disorder of AM techniques [433–435,479,485]. On the other hand, dislocation cells in medium- to high-SFE and other homogeneous materials used to be related to dislocation accumulation during strain processes with wavy or cross slip occurrence [129]. Despite their different origins, both dislocation

networks strengthen the alloy as a function of the cell size [433,460,479,499]. It was recently reported that considering the grain size or the sub-grain size instead of the cell size for estimations of mechanical properties from the Hall-Petch equation in AM 316L SS reduces the calculation error [452,484]. However, the accumulation of SSDs in homogeneous materials used to imply a significant sacrifice of ductility [500]. Nonetheless, dislocation networks in AM SS contribute to obtaining extra strain hardening, i.e., extra ductility [434,435,456,460,462,500]. This means that the dislocation and misorientation distributions play a critical factor in the mechanical behaviour of HS metallic materials [500], including AM SS [452]. Besides, it was recently reported that stacking faults (SF) can form from dislocation dissociation inside the dislocation cells and contribute to strengthening the SS [461].

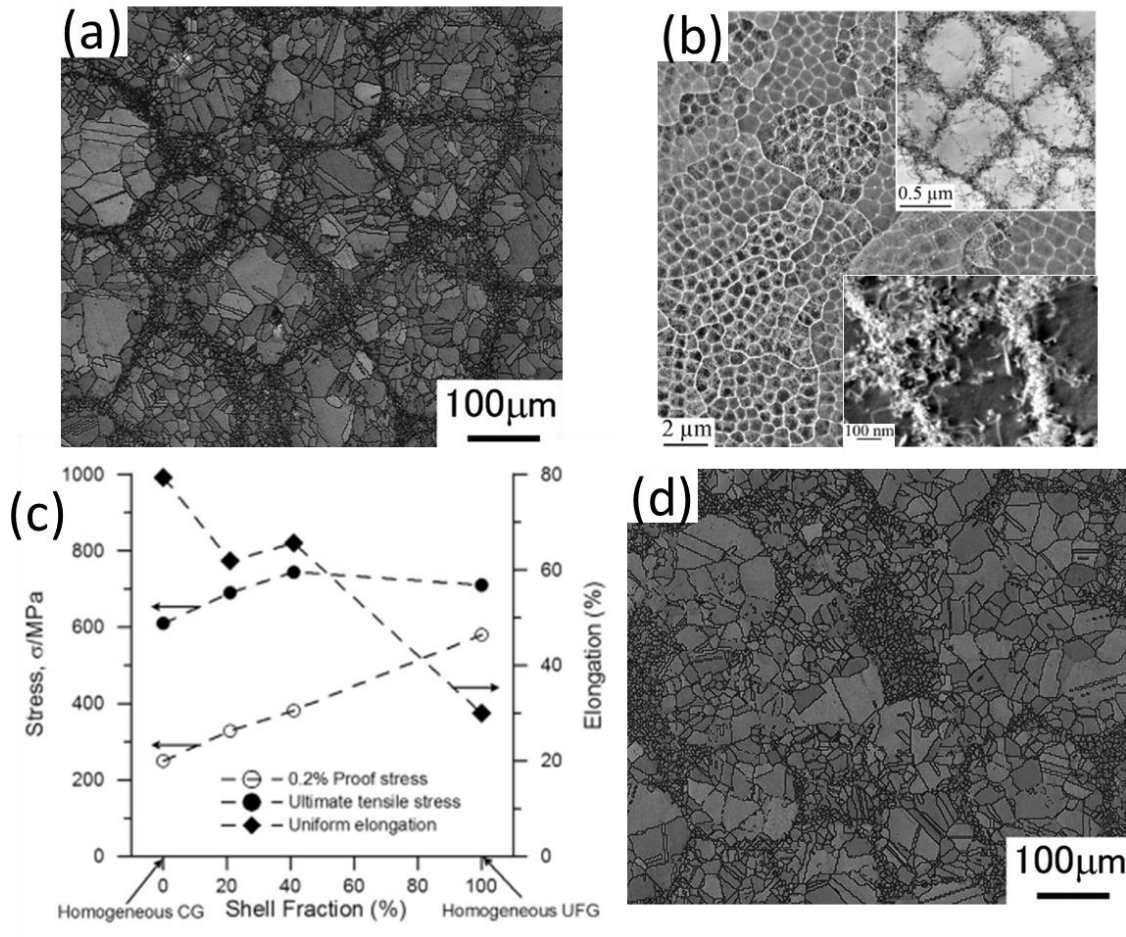


**Fig. 12.** Typical harmonic structured microstructure in stainless steel constituted by (a) a volume of several grains and [42] (b) local dislocation networks hard zones surrounding the soft zones [461]. (c) Comparison with bimodal structure with same chemical composition both different sintered conditions of those in (a) [42]. (d) Dependence of ultimate tensile strength (0.2% proof stress) and uniform elongation on shell fraction in harmonic structured 304L stainless steel (SS) [41].

Related to the materials which met the description of harmonic structured materials at larger volumetric ranges, powder metallurgy (PM) is the main technique for producing harmonic structured SS [429,430,501]. This technique involves mechanical milling, mixing initial powders of different order sizes, and compacting them under controlled conditions to preserve the HS microstructure. Some harmonic structured SS of 304L, 329J1, and 316L have been created by powder consolidation methods [41,43,502]. The microstructure and the properties of harmonic structured SS strongly depend on the volume/area fraction of shell/core regions, the average grains size of coarse grains, and the size of the network shell [502]. These factors can be experimentally controlled by changing the mechanical milling and consolidation conditions [432,501,502]. The dependence of mechanical properties on the volume fraction of shell in harmonic structured SS has been investigated [41]. [Figure 12\(c\)](#) shows how the strength and uniform elongation change with the volume fraction of the shell in harmonic structured 304L [41]. The graph shows that the 0.2% proof stress increases monotonically when the shell fraction increases. However, at a shell fraction of 41%, the ultimate tensile strength (UTS) reached a strength peak (744 MPa). A slight decrease in the UTS was obtained with a further increase of shell fraction to 100%. Normally, the uniform elongation decreases with increasing the UFG-structured. However, this dependence was non-linearly in the harmonic structured 304L SS on contrary to the homogenous microstructure. Namely, the increase of shell fraction from 21% to 41% led to a noticeable enhancement in uniform elongation besides increasing strength. As a result, the harmonic structured 304L SS containing 41% of the UFG shell regions was pointed as a favourable structure for joining high strength and good ductility. Detailed information about the

mechanical properties of harmonic structured and other HSMs can be found in section 6 of this review.

Furthermore, in harmonic structured SS, the shell and core zones may have different phases distribution due to heterogeneous heat distribution [502], but no chemical bulk changes are common in this classification; those are reserved for multiphase structured SS. An example of the above is a 316L SS with shell zones composed of NG  $\gamma$  and  $\sigma$  phases, while its core zones are composed of CG  $\gamma$ . It was observed that the UFG/NG  $\gamma$  in the shell region transformed to  $\alpha$  phase during the mechanical milling SPD process and during the solidification process, while the  $\alpha$  in shell zones became UFG or NG  $\gamma$  by reverse phase transformation. Besides, some of the  $\alpha$  acted as active nucleation sites to form the  $\sigma$  phase [502].

To clarify the difference between bimodal and harmonic structured materials, Fig. 12(a,d) show two morphologies of 304L SS samples fabricated by spark plasma sintering (SPS) under different processing conditions [42]. The microstructure of Fig. 12(a) was obtained from compaction of UFG powders milled for 180 ks, while the microstructure from Fig. 12(d) was obtained by compacting a mix of micrometric and UFG powders (milled for 360 ks). As a result, both samples had a bimodal microstructure with different spatial distributions of soft and hard zones. The microstructure from Fig. 12(a) shows CG zones surrounded by a continuous network of the UFG region. Morphologically, this structure fully concurs with the aforementioned definition of harmonic structured materials. On the other hand, Fig. 12(d)

shows an irregular heterogeneous distribution of CG and UFG regions that corresponds to the definition of bimodal structure (multimodal structured material).

#### *4.6 Multimodal structures*

The work hardening and consequent ductility of NG SS improved by incorporating small or large volume fraction of CG into a UFG and/or NG metallic matrix [21,41,42,44,45,502]. The multimodal structured materials typically consist of a mixture and grain size distribution of NG, UFG, and CG, as exemplified in [Fig. 13](#). However, multimodal microstructures can also be composed of grain morphologies with different aspect ratios [457]. These microstructures significantly reduced the ductility penalization of NG materials when increasing strength ([Fig. 2](#)). The multimodal structured materials deform by the same mechanism described in section 2 for all HSMs, and the HDI stress is distributed at the HZB in the same way previously described in [Fig. 3](#). This is, the soft (CG) zones sustain much higher plastic strain than the harder zones, leading to a significant strain partitioning when increasing the applied stress. This results in the generation of long-range stress (back and forward stress) and increasing strain hardening, i.e., providing more ductility [503]. Those characteristics make the multimodal structured SS attractive for various commercial applications.

The conventional and, in most cases, low-cost obtaining processes of multimodal structured SS increase their potential for scalability. Bulk multimodal structured SS are commonly synthesized through combined processing routes that can be described in two



main approaches [41,45,46,429,500]. The top-down approach is based on thermomechanical processing, including plastic deformation by conventional and/or SPD techniques followed [504,505] or not [506] by HT. For example, after high-pressure torsion (HPT) processing and post-HT, a bimodal austenitic 316L SS was obtained [505]. Usually, a phase transformation from  $\gamma$  to  $\alpha'$  occurs during the plastic deformation of austenitic SS [507]. However, the  $\alpha'$  reverses to  $\gamma$  after HT [508]. Therefore, multimodal structured SS might have different phase compositions between the UFG and CG zones [509]. The second approach for producing multimodal structured materials is the so-called bottom-up route, which is mainly based on PM and AM methods consisting of mechanical milling of powders and consecutive bulk or layer-by-layer consolidation, respectively [41,46,429,457,486]. The final multimodal structured microstructure can be controlled by altering the degree of milling, the fraction of milled and nonmilled powders in the mixture, as well as the consolidation (temperature, time, pressure, laser power, layer thickness, laser scan rate, or hatching distance) conditions [429,510,511]. In typical PM methods, mechanical milling is performed either by ball milling (BM) or jet milling (JM) to achieve desired grain refinement and plastic deformation in powders. Then, a mixture of NG and/or UFG milled powders, and as-received CG powders consolidate together at appropriate temperatures to produce bulk multimodal structured SS [41,46]. The sintering process can be performed using various techniques such as hot isostatic pressing (HIP), hot roll sintering (HRS) [502], or SPS [42,46]. On the other hand, AM processes are near net-shape processes that reduce or avoid further processing steps [510,511].

Recently, extensive research focused on the grain size distributions in multimodal structured SS [42,45,512]. It was reported that processing of 304L SS by cold rolling with subsequent thermal cycles at various temperatures resulted in a bimodal grain size distribution in ranges from 300 to 1000 nm and from 1 to 2  $\mu\text{m}$  in UFG and CG zones, respectively [45,512]. Ball milled combined with SPS is also a successful processing method for producing a bimodal structure in 316L SS [46].

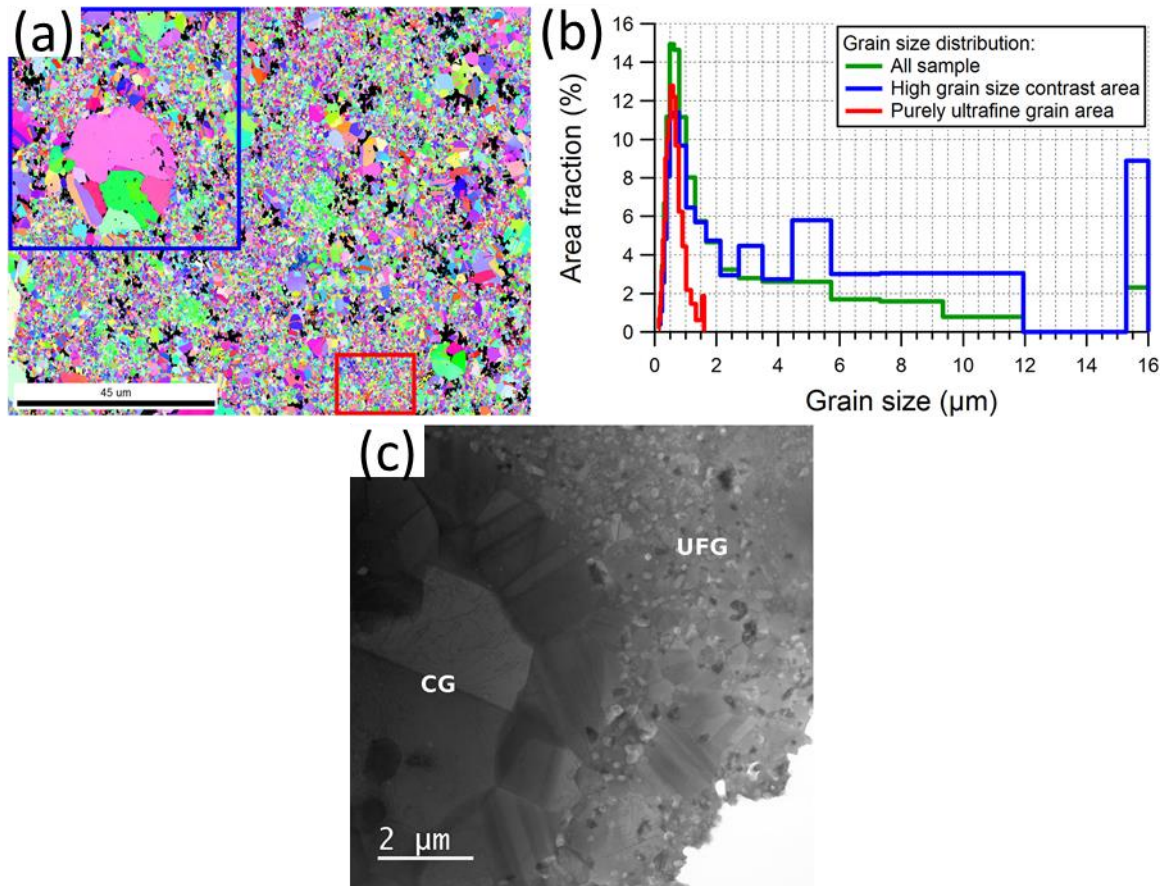


**Fig. 13.** Typical features of multimodal structured stainless steel (SS). (a) EBSD orientation maps and its (b) associated grain size distribution for the different regions indicated by blue and red solid lines, as well as (c) STEM micrograph of an interface between CG and UFG regions on a multimodal structured 316L SS constituted by 75% UFG and 25% CG [46].

The thermomechanical history of material strongly influences the phases distribution and morphology of multimodal structured SS [507,508]. The  $\gamma$  grains are gradually transformed into the  $\alpha'$  structure during plastic deformation. On the contrary, the annealing leads to a

reverse transformation of the  $\alpha'$  phase to  $\gamma$  structure [508]. The reversion of  $\alpha'$  to  $\gamma$  may occur by two competing diffusional controlled and non-diffusional shear processes, which were previously discussed in section 4.1. The prior SIM may significantly affect the formation of austenitic multimodal structures in the austenitic SS [44]. It was reported that the morphology of the reverted  $\gamma$  is quite dependent on both the prior morphology of the  $\alpha'$  structure and the mechanism of reversion [44]. For example, the reversed  $\gamma$  in the CR and annealed 304L SS occurred by the shear mechanism, and the resulting structure had different grain sizes dependent on the parent  $\alpha'$  structure [44]. The 304L SS was rolled up to 80%, then annealed at 700°C for 300 min, forming a bimodal austenite structure. The observed bimodal austenite grains were related to different types of martensite structures: lath and dislocation-cell types in the steel before the annealing process [44]. Increasing the rolling reduction to 93% prior to heat treatment at 700°C for 300 min led to changing the microstructure to a monomodal grain structure. This occurred due to the rolling up to 93% produced UFG  $\alpha'$ , which during annealing acted as random nucleation sites for new  $\gamma$  grains resulting in equiaxed  $\gamma$  grains. The bimodal structure in 304L SS enhanced the ductility of the 80% rolled and annealed sample while maintaining a high tensile strength compared to the 93% rolled and annealed sample [44].

Recently, a novel route based on submerged friction stir processing (FSP) was used to create bimodal grain size in austenitic 316L SS [506,509]. In this process, a rotating cylindrical tool was plunged into the CG 316L SS sample with an average grain size of 22  $\mu\text{m}$ , and the tool moved along the length of the specimen, creating a UFG structure with an

average grain size of 0.9  $\mu\text{m}$  [509]. Alternatively, rotating the cylindrical tool at a specific area on the as-received specimen produced a bimodal grain structure that contained fine grains within a coarse-grained matrix. In this bimodal structure, highly fine grains with an average of 500 nm were embedded among CG structures of approximately 10  $\mu\text{m}$  size. The fine grains were  $\alpha'$ , while the coarse grains were  $\gamma$ . The volume fraction of  $\alpha'$  was nearly 30% and 8% in bimodal and UFG specimens, respectively. The microstructural effect of CG, bimodal, and UFG 316L SS on the mechanical properties will be deeply discussed in section 6 of this review.

#### *4.7 Simulation*

Although systematic experiments on different length scales have been carried out to study the microstructure evolution as well as the deformation behaviour of the HSMs, the modelling and simulation works are also important to reveal the underlying mechanisms of HSMs during formation and deformation, such as the phase transformation, recrystallisation, and mechanical responses. The state of the art of simulation methods has been developed to analyze the HSMs at different length scales and deformation stages.

##### *4.7.1 Heterogeneous phase transformation and grain growth*

Multiphase structured materials with distinct mechanical contrast among different phases can promote HDI strengthening [513]. As demonstrated above, to generate a sufficient strain

partitioning within the HZB, the production of the second phase with large hardness contrast or high-volume fraction is critically important. The interpenetration of soft austenite and hard martensite is one of the typical HS SS, resulting in a high fraction of HZB regions. The multiphase-field model has proven that the volume fraction and spatial distribution of retained austenite are determined by the partitioning of  $\gamma$ -stabilisers (e.g., C/Mn in steel) [385,514]. Such partitioning is affected by the solute diffusivities, heat treatment temperatures and times, and other thermomechanical histories [385,514,515]. FEM simulation of SIM transformation, grain refinement, and grain growth in deformed and annealed austenitic SS has been investigated [516] and can be extended to HS SS. Via phase-field (PF) modelling of the effect of austenite grain size on martensitic transformation in SS; it was reported that refining the grains led to the decreased martensitic transformation starting temperature, indicating strengthening of austenite [517]. However, simulated fine grains gave rise to higher martensite content during transformation than coarse grains. These models can be applied to the complicated case of HS SS microstructure formation.

The microstructures with dispersed hard precipitates, including carbides, nitrides, Laves phases or intermetallic compounds, among others, are the other category of multiphase HS materials. The size and location of these precipitates depend on the driving force and nucleation barrier during phase transformation. For instance, the polycrystalline simulations in a duplex SS illustrate that the austenite-ferrite and the ferrite-ferrite phase/grain boundaries are the preferred nucleation sites of the  $\chi$ -phase and sigma phase [518], which has also been proved experimentally [519]. The cooling rate also influences the accumulation of elements

like Mo and Cr in the sigma phase, which leads to different volume fractions of the hard second phase [518]. In addition, when the supersaturation is high or the nucleation energy barrier is low enough (e.g., low lattice misfit across the phase boundaries), intragranular nucleation could also be activated, leading to high density of nanoscale particles to promote hetero-deformation [520–524]. Among various precipitates, micro-/nano-intermetallic particles are most effective to enhance strength-ductility combination by obstructing the dislocation movement and producing high back stress with large HZB regions [513–515,518,520,521]. On the other hand, the pinning effect of the grain boundary precipitates is important for grain growth, which has been simulated using a 3D Monte Carlo method [525], showing good agreement with the experimental observations. Moreover, the combination of FEM and PF methods for simulation of austenite grain growth has been discussed by Shi et al. [526]. These models can be applied to the complicated case of HS SS annealing. Therefore, modifying the alloy composition or heat treatments can optimise the heterostructure for mechanical properties enhancement and grain growth inhibition.

Alloys with non-uniform grain sizes ranging from nanometres to micrometres also render a synergistic strengthening effect and strain partitioning capacity. Various models have been proposed to simulate the recrystallisation process in metals. Using the Monte Carlo (MC) method, Srolovitz et al. showed that bimodal grain size distribution is a result of the pockets of unrecrystallised grains surrounded by the growth of individual recrystallised grains [527,528]. The stored energy, density of potential nuclei/embryos, and the fraction of external particles [529] play important roles in the recrystallisation process. Raabe et al.

further hybridized the cellular automation with MC to depict the detailed recrystallisation processes, which agree with the experimental results [530,531].

#### *4.7.2 Deformation and damage behaviour*

Except for the formation process, another main issue of the heterostructured materials is their complex deformation mechanism. By establishing a heterogeneous nano-zoned heterostructure with random NG dispersed in a CG matrix, the crystal plasticity finite element (CPFE) model showed a clear hetero-deformation phenomenon. On the one hand, the small-sized or high fraction NGs effectively promote the accumulation of dislocations in the CGs, which increases the critical resolved shear stress (CRSS) of different slip systems and strengthens the alloy. On the other hand, since the NG zones are harder than the CG ones, the surrounding areas of NGs can store a much higher density of dislocation with smaller plastic strain. Further analysis showed that such heterostructure also reduces the anisotropy of strength in the material [183]. Similar results of the FEM simulation also proved that the length scale effect and the unique spatial arrangement of NG-CG are the origins of the strengthening effect of the harmonic structure, which represents the obstruction of the dislocation motions by the boundaries [532]. The fine grains bear a high fraction of the external load. In addition, the FEM simulation showed that the subgrain structure (e.g. precipitates, etc.) also plays an important part in strengthening, which is highly dependent on the alloy system [532].



The stress and strain partitioning are also evident in gradient materials. A CPFE model revealed that, in the cross-section of nano-grained GS metals, the axial tension leads to both the gradient stress and gradient plastic strain across different grains, resulting from the progressive yielding among different grains with gradient sizes under an overall uniform deformation [533]. The high strain hardening capacity of the nano-grained GS steel stems from the abundant GNDs in the NG layers [214]. Based on another multiscale physical model incorporated with a dislocation-based stress/strain-gradient theory, it was shown that the gradient microstructure exhibits a better combination of strength and ductility compared to the same steel with homogeneous microstructures [77]. The banded nano-microstructure can achieve even higher ductility by delaying strain localization [77]. The atomic-scale evidence provided by molecular dynamics (MD) simulations confirms that the existence of gradient grain size distribution effectively suppresses the shear localization. Compared to fine-grained metals, where the plastic deformation is predominantly governed by grain boundary movement, including grain rotation, grain boundary sliding, grain coalescence, etc.; or the coarse-grained metal, where the plastic deformation is dominated by slip bands with large localized atomic shear strain and high dislocation densities emitted from triple junctions and free surfaces; the localized shear is effectively suppressed by GS structures at a high strain level of 20% [534].

As shown in Fig. 14, not only does the gradient distribution of grain size (Fig. 14(b)) influence the yield strength and ductility of SS. Gradient distributions of twin spacing in nano-twinned GS 304 SS (Fig. 14(c)) revealed a strong influence on the mechanical

behaviour studied by a constitutive model [535]. This physics-based constitutive model was further employed to predict the dynamic plastic deformation behaviour in the nano-twinned GS 304 SS with different gradient distributions [536,537]. The mechanical properties of HS nanostructured 316 SS have also been evaluated by the CPFE model [538]. They showed that the deformation process of the HS 316 SS depends strongly on the tensile direction, and the strength of the alloy increases with the volume fraction of the twin zones. The nano-twin and lamellar inter-spacing also contribute to the strengthening effect [538].

In addition, MD simulations on the 316 SS suggest a correlation between grain size and the forming probability of deformation twinning [275]. The larger grains are easier to activate twinning during deformation [275]. MD is also useful in studying the rate-dependent deformation behaviour of the HS alloys from the atomic viewpoint, which proved that the GB strengthening and lattice-friction stress improve the yield strength of the HS alloys while the back stress and dislocation contribute to the strain hardening [539,540]. By combining gradient grain size and twin thickness, superior work-hardening and strength can be achieved. Combined with experimental observations, the large-scale 3D MD simulations showed that the bundles of concentrated dislocations form in the interior of the nano-twinned GS structure during tensile deformation. In addition, the suppression of the Shockley partial dislocations' movement contributes to the extra strengthening effect [98]. Consequently, the heterogeneous structures at different length scales allow for a simultaneous high strength and high ductility with extra work hardening capacity.

The mechanisms of damage nucleation and crack propagation are increasingly important in HSMs. A CPFE model revealed that the damage does not necessarily nucleate at the locations with the highest local strain (energy) values. Indicating also that the imperfect slip transfer results in the extra residual dislocation in the boundary planes, and such slip interactions arise damage nucleation [541]. PF modelling method has also been widely used in simulating the cracking behaviour of HSMs. A PF model based on direct imaging and digitalizing of microstructural features has been proposed. This model is meshed independent and reproduces the crack path efficiently [542]. In more recent work, the model was developed to track the fracture mode in the layered HSMs. It showed that the materials' mismatch ratio strongly influences the crack penetration and branching mechanisms. The transition zone determines the crack paths and damage mechanisms when the cracks cut across the interface [543]. By minimizing the output parameters and assumptions, the spatial distribution, density, and propagation paths can be accurately predicted without introducing the predefined crack location [544]. In a 3D model, it was shown that the nucleation and propagation of cracks in the heterogeneous materials are highly affected by the spatial distribution of the heterogeneity features [545]. Therefore, the numerical model can provide useful insights into damage behaviour during the complex deformation process.

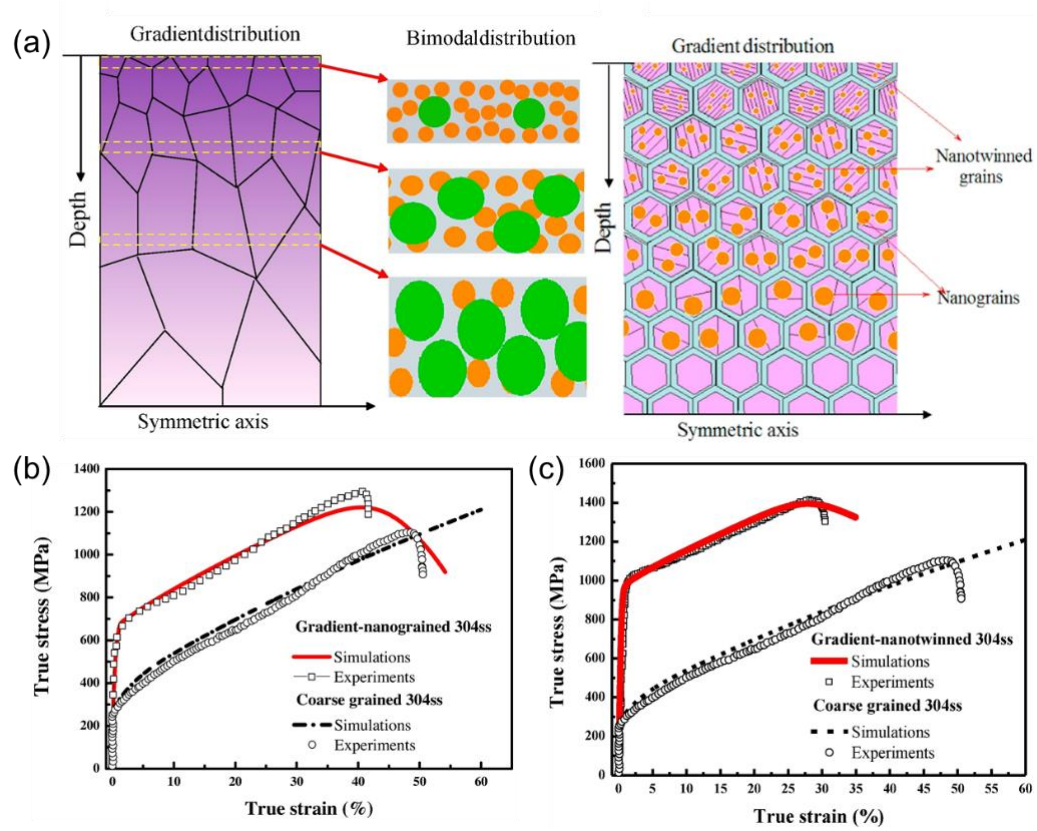


**Fig. 14.** Comparison between depth-dependent grain size and twin spacing structured 304 stainless steel (SS). (a) Representations of gradient structured (GS) 304 SS with depth-dependent grain size and twin density, as well as the comparison between the experimental and simulated stress-strain curves of (b) nano-grained GS and (c) nano-twinning GS 304 SS [535].

## 5. Crystallographic texture

Texture is a microstructural description of a polycrystalline material [546,547]. It is defined as the distribution of crystallographic orientations. In multiphase HSMs, comprised of hard and soft phases separated by biphasic interfaces, the texture of the HSM is composed of the texture of each crystalline phase. When the underlying mechanisms controlling the mechanical properties of the HSM are crystallographic slip and/or twinning in the grains, then the material texture, the crystallographic orientation of those grains relative to the applied load direction, becomes an influential microstructure characteristic.

Material textures can be strong, meaning all grains are highly oriented in nearly one direction or a few directions, or weak or non-existent, meaning all grains are nearly uniformly distributed over the entire orientation space. The orientations that emerge and their intensity are primarily the result of the processing method. In HSMs, the texture can further be altered by the presence of biphasic interfaces. These causes for texture are examined below through examples focused on FCC/FCC, BCC/BCC, FCC/BCC, and in a few cases, HCP/BCC multiphase or LS HSMs systems. While none of these cases considers SS, they are analogous in many ways to the crystal structure combinations and low SFE FCC phases encountered in duplex SS and precipitate-containing austenitic SS [548–551].

As mentioned, texture development depends on the fabrication process for the HSMs. [Figure 15](#) shows using  $\{111\}$  pole figures some unusually strong phase textures of FCC/BCC or HCP/BCC LS materials, made either by deposition or metal forming [552]. In [Fig. 15\(a-b\)](#), the physical vapour deposition (PVD) texture corresponds to a Cu/Nb LS film deposited

on a silicon substrate. The Cu phase is characterized by a strong  $\{111\}$  texture, meaning the  $\{111\}$  poles are aligned through the thickness of the film. The Nb phase in Fig. 15(d) bears a strong  $\{110\}$  texture. Figure 15(c) presents the phase textures of an Mg/Nb LS, also formed by PVD. The Mg with an HCP crystal structure forms a strong basal  $\{0002\}$  texture, and as in the deposited Cu/Nb system, the Nb phase bears a strong  $\{110\}$  texture [553]. These types of textures are common for FCC/BCC and HCP/BCC LS systems made by deposition.

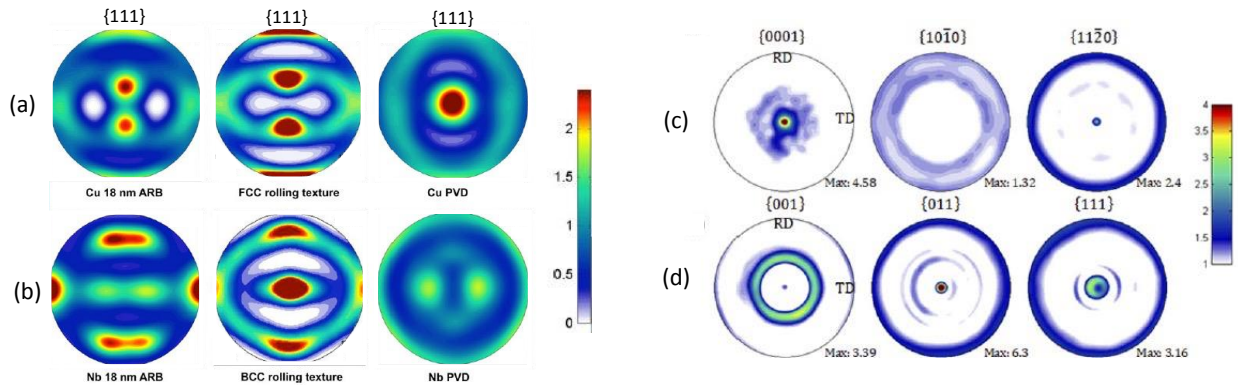


**Figure 15.** Pole figures of Cu/Nb (FCC/BCC) and Mg/Nb (HCP/BCC) layer structured (LS) materials. (a-b) Pole figures of the textures measured by neutron diffraction of the (a) Cu phase and (b) Nb phase in the accumulative roll bonded LS (left), alone in a typical rolled texture (middle) and in the deposited nanolayered composite (right) [552]. (c-d) Pole figures of textures measured by XRD of (c) the Mg phase and (d) Nb phase in a Mg/Nb LS material with layer thickness 50 nm [553]. In the Mg/Nb LS with 5 nm layer thickness, the Mg and Nb phase textures are the same as those shown in (c-d).

The textures of the other Cu/Nb LS material shown in Fig. 15(a-b) were manufactured by an SPD technique, i.e., ARB, which involves repeated rolling, cutting, and stacking at room temperature [554]. The Cu and Nb phase textures in this SPD sheet are also strong, with the  $\{112\}$  poles aligned through the thickness of the sheet [555]. Figure 15 compares their  $\{111\}$  pole figures to show that despite being composed of the same two materials, Cu and Nb, the textures are different from those of the PVD film by virtue of their distinct manufacturing processes. The texture of the HSM from rolling is not, however, as the rolled textures of either phase when rolled alone. As shown in Fig. 15, classic rolled textures of FCC materials (Fig. 15(a)) and BCC materials (Fig. 15(b)) are unlike those that developed in the HSM sheet from SPD. Highly oriented sharp textures in the LS materials in Fig. 15 result from the prevalence of both the a) crystallographic character of the biphasic interfaces and b) unidirectional morphology of the layers (referred to as the morphological texture) across the entire sample. These two aspects are discussed in turn below.

Like the PVD method that made the Cu/Nb and Mg/Nb HSMs in Fig. 15, many near-equilibrium processing techniques produce biphasic materials with preferred internal interfaces. These interfaces are favoured because they tend to have the lowest energy among all possible interface characters, a descriptor that includes the crystallographic orientation relationships and interface plane. Only a few such low energy interface characters exist, and it is, therefore, common for one or at most two interface types to prevail ubiquitously across the nanolaminates. The Cu/Nb PVD material contained the two most commonly occurring interface orientation relationships for an FCC/BCC system: the Kurdjumov-Sachs (KS) and

Nishiyama-Wasserman (NW), and interface planes, the densely packed FCC {111} and BCC {110} planes. These interfaces are often seen in duplex SS with ferrite grains, the austenitic SS with martensite precipitates, and austenitic SS with ferrite precipitates [548–551].

The PVD method was also used to make a very fine 5 nm/5 nm Mg/Nb LS material. The texture of both the Mg and Nb phase corresponded to the outstandingly strong textures shown in Fig. 15(d). This material represents an extreme example of how the energy of the interface can change the texture of the laminate. In this case, the drive to create a low-energy coherent interface caused a pseudomorphic phase transformation in the Mg phase. This phenomenon causes one phase to adopt the crystal structure and lattice parameter of an adjoining phase [556]. It results when the reduction in the interface energy outweighs the increase in the strain energy when going from the incoherent HCP/BCC interface to the coherent BCC/BCC interface. The critical layer thickness to transform HCP Mg to BCC Mg in an Mg/Nb nanolaminate is estimated by density functional theory (DFT) calculations to be approximately 5 nm [557]. The resulting Mg/Nb nanolaminate gains a low energy interface and exhibits higher deformability since the BCC pseudomorphic phase of Mg is more ductile than the stable HCP phase [558]. However, strong textures can lead to plastic anisotropy, wherein mechanical response depends on the orientation of the applied deformation. Compression or tension tests finds that the strengths of these LS materials are anisotropic, being stronger when deformed normal to the interface than parallel to them [556,558].

Strong but different textures develop in LS HSM fabricated by thermomechanical ARB processes. The Cu/Nb interface ubiquitous in the ARB processed sheet in Fig. 15(a,b) has the



same KS orientation relationship as those in the Cu/Nb PVD foil, but has a different interface plane, namely the {112} planes of Cu and Nb [559]. According to atomistic calculations, this interface has higher energy than the classic KS or NW interface (ranging from 650 to 850 mJ/m<sup>2</sup> compared to 576 to 586 mJ/m<sup>2</sup> for Cu/Nb) but corresponds to a local minimum in the interface energy landscape and has a regular, periodic atomic structure [560]. Thus, its selection is not arbitrary, and interface energy played a chief role, although not the only. This interface character dominated the ARB Cu/Nb sheet because it satisfied two constraints, 1) the interface was energetically stable, corresponding to a local minimum, and 2) both adjoining crystal orientations are geometrically stable with respect to the rolling deformation [555].

The few interface characters selected because of HSM processing would not have led to strong textures without the strong morphological texture. Due to the prevailing stacked two-layer morphology, all interface planes are aligned with the through thickness direction of the sample (e.g., foil, sheet). Only one or at most two crystals span the layer thickness when layers are merely nanometers thick. Therefore, for all the crystals in the material, the normal of the crystalline plane corresponds to the interface plane. Consequently, the texture of a material with one or two interface characters, such as the deposited or rolled material, will be comprised of only one or two predominant orientations, and hence will be strong.

As alluded to earlier, an important consequence of strong textures, consisting of relatively few orientations or components is plastic or strength anisotropy. Tension testing finds that the strengths of the ARB Cu/Nb nanolaminates are anisotropic, being stronger when

deformed along the TD than along the RD [561]. This texture-influenced anisotropy is also responsible for enabling kink banding on subsequently compression tests, a mechanism that is not common to metallic materials but common to fibrous or highly anisotropic ones [562].

The two processes discussed thus far, PVD and ARB, produce nanolaminates with a pervasive layered architecture, i.e., LS materials. Another method for manufacturing nanostructured metallic HSMs in bulk is thermomechanical treatments, which at the microscale produces a 3D hierarchical structure. Figure 16 displays the nanostructures of two examples, one a Ag/Cu composite of eutectic 60/40 at.% composition and another, a two-phase Zr-2.5Nb wt.% alloy. The Ag/Cu material shown in Fig. 16(a,b) was made via deep undercooling of ultrahigh-purity Ag and Cu process starting with melting and followed by water quenching [563]. The material is comprised of randomly oriented colonies containing alternating lamellae of Cu and Ag, as seen in Fig. 16(a). Figure 16(b) is a scanning electron microscope (SEM) micrograph of a single central Ag-Cu colony to highlight the nanolamellae. Two types of  $\{111\}\text{Cu} // \{111\}\text{Ag}$  interfaces, cube-on-cube orientation relationship or twin orientation relationship and  $\{111\}\text{Ag} // \{111\}\text{Cu}$  interface planes, coexist in this material since they have similarly low interfacial energies [564]. The Zr-2.5Nb alloy was synthesized using a thermomechanical phase transformation method [565]. The material consists of nearly equiaxed CG filled with microscale colonies, which are marked by dashed lines in Fig. 16(c). Like in the Ag/Cu material, these colonies are also randomly oriented. Any individual colony is a nanolaminate, consisting of UFG ( $\sim 220$  nm) layers of  $\alpha$ -hcp Zr separated by a 20-nm-thick layers of  $\beta$ -bcc Zr-Nb (Fig. 16(d)). The biphasic  $\alpha/\beta$  interface has

a preferred Burgers orientation relationship of  $(0001) \parallel (011)/[1120] \parallel [11]$  (Fig. 16(d)). Because the colonies are randomly oriented, the bulk textures of these materials are uniformly random, meaning they lack texture. However, crystallographic orientation of the crystals within a given nanolaminate colony are aligned with the predominant interface and hence strongly textured.

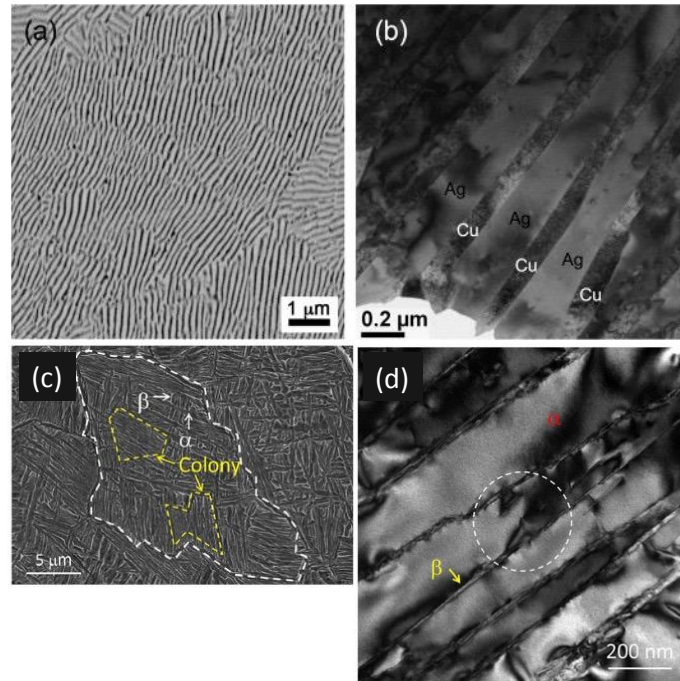


**Figure 16.** (a) Nanostructure of Ag/Cu material of eutectic 60/40 at.% composition [563], (b) scanning electron microscope micrograph of a single central colony with Ag/Cu nanolamellae [563], (c) Nanostructure of Zr-2.5wt%Nb hierarchical material [565], (d) Transmission electron micrograph of the  $\sim 220$  nm layer of  $\alpha$ -hcp Zr separated by a 20-nm-thick  $\beta$ -bcc Zr-Nb layers [565].

The findings from the studies discussed connect HSMs fabrication methods to crystallographic texture and to biphasic interface character for a common class of crystal structures—FCC, BCC, and HCP. The understanding and proof of principle reviewed in this section are built on characterization and calculations of model HSMs, those comprised of soft, single-phase metals. The concepts are fundamental, and as such, should provide a starting point for applying to harder, stronger SS and other alloys.

## **6. Mechanical performance**

From the current classification of heterostructures: i) heterogeneous lamella structures (HLS), ii) gradient structures (GS), iii) layer structures (LS), iv) multiphase structures, v) harmonic structures, and vi) multimodal structures, different mechanical behaviour can be expected. Heterogeneous lamella structured materials, which consist in bulk soft zones embedded in hard zones (microstructural features explained in section 4.1), are considered the most promising to reduce the trade-off between strength and ductility. This is due to the strong constraint that the hard zones can exert on the soft zones. It is expected that the most effective the constraint, the highest strain partitioning and the highest the strain hardening, i.e., ductility improvement. However, Frank-Read sources have been observed to be continuously created and deactivated in materials under straining [566]. The strain partitioning and the generated HDI strengthening cannot be directly correlated to GND pile up density near the HZB [567]. Besides, the GND might be absorbed by the boundary [566]. Thus, further research and revising of the strain gradient plasticity theory are needed.

Comparatively, the GS materials used to concentrate the finest grained region in a small superficial layer and the bulk used to be in the micrometric or ultrafine region. Consequently, the grain boundary length is significantly reduced compared to the HLS materials. The GS effectively accumulates dislocations in the coarse bulk, but the limited density of grain boundaries also limits their HDI work hardening capability. In the LS materials, constituted by soft and hard layers of different chemical compositions, the strain partitioning is reduced due to the layers are subjected to the same strain. In the multiphase structured materials, formed by chemical disparities along the bulk microstructure, the hard zone used to be embedded in the soft matrix. The continuous hard zones surrounded by the soft matrix create a lower strain constraining when compared to HLS, where the soft zone is embedded in the hard one. This leads to a lower yield strength with high ductility. The harmonic structured or core-shell materials are constituted by soft zones embedded in a hard matrix. The balance between both volume fractions should be optimised (apparently at about 40% of the hard zone [41]) to allow adequate strain partitioning. For the last, the multimodal structured materials, characterized by a coexistence of colonies of different order sizes, the HZB density is usually not maximised, reducing the HDI strengthening occurrence.

### 6.1. Tensile properties

In a general way, the deformation process of HSMs can be divided in the three stages shown in Fig. 17. Stage I is described by the elastic deformation of soft and hard zones. Stage II is characterized by dislocation slip of soft zones until reaching the plastic deformation range. Meanwhile, the hard zone remains elastic. This mechanical mismatch will generate a plastic strain gradient near the HZB. As explained in previous section 2, the strain gradient will be accommodated by GNDs, which will pile up against the HZB in the soft region and create HDI stress. Simultaneously, the hard zone constrains the soft zones (making it looks stronger), while the soft zone accommodates more strain than the hard one. Thus, strain partitioning starts occurring. As a result, the YS will increase beyond the ROM predictions. The hardening created by long-range stress can be estimated through kinematic hardening theory [568]. For last, stage III is characterized for the visible effect of the strain partitioning when both zones are plastically deforming. This is due to the soft zones sustain higher plastic strain than the hard ones. Nonetheless, there should be a continuity in the plastic strain at the boundary, so a strain gradient near the HZB is required for accommodating the strain partitioning. GNDs accommodate that strain gradient.

From Fig. 17, the applied shear stress,  $\tau_a$ , will drive the generation and pile up of GNDs. This representation assumes the emission of GNDs with the same Burgers vector towards the HZB on a slip plane. As a result, long-range stress,  $\tau_b$ , will be produced against the dislocation source. The effective stress,  $\tau_e$ , can be estimated by Eq. (5).

$$\tau_e = \tau_a - \tau_b \tag{5}$$

where for the dislocation source to emit more dislocations, the  $\tau_e$  should be higher than the critical stress to operate the source,  $\tau_c$ . This means that before reaching saturation, the density of GNDs to be piled up increases as a function of the applied stress. For reference, high densities of GNDs in the order of  $\sim 10^{13}$ - $10^{14}$  are commonly found in as-built and pre-strained AM and wrought SS [448,450,486,492,495,569,570]. Parallely, the HDI stress will also increase with more GNDs piling up pushing against the HZB. Due to the generation of GNDs, the soft region is still accommodating more strain than the hard zone. The strain partitioning leads to strain gradients near the HZB in both, soft and hard zones. Consequently, HDI work hardening will increase with strain partitioning, providing superior ductility to the material. From the Considère criterion, necking starts when the work hardening rate is lower than the true flow stress, i.e., necking is mainly caused by insufficient strain-hardening [71]. From the above, the HDI hardening is the reason for high ductility during tensile tests in HSMs [18,49,75,78].

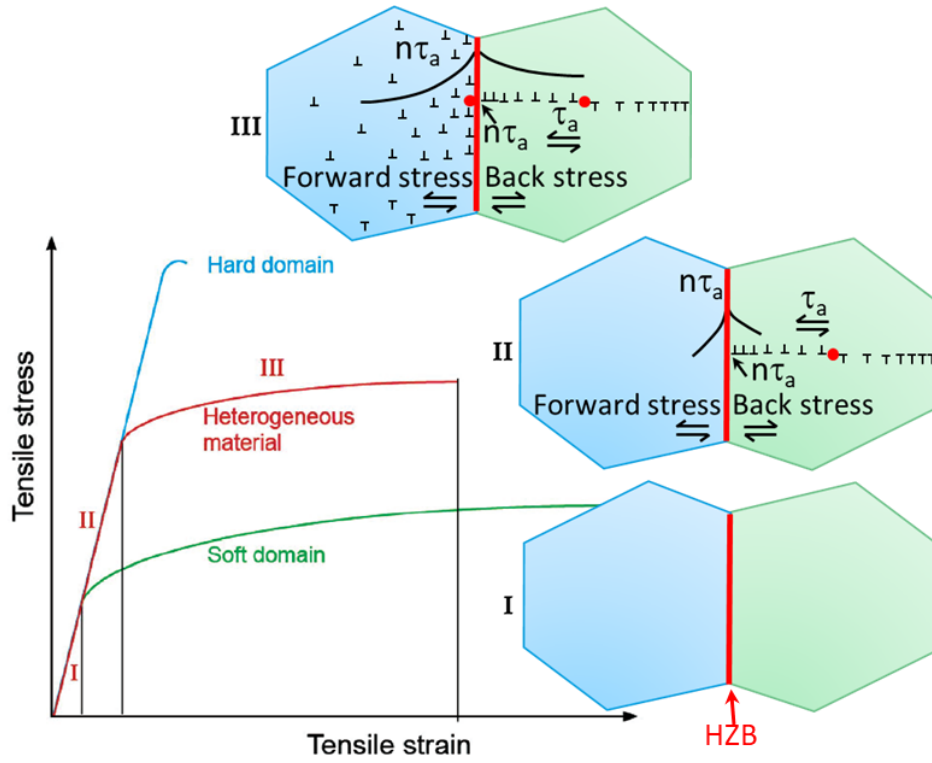


**Fig. 17.** Representation of the three deformation stages (I, II, and III) and their effect on dislocation behaviour and stress distribution near a hetero-zone boundary (HZB).  $\tau_a$  is the applied shear stress. Red circles represent the dislocation sources. Adapted from [80].

#### 6.1.1. Tensile behaviour in HLS SS

As explained in section 6.1, the HDI hardening is attributed to GND pile ups at the hetero-interfaces. So far, the HLS has been the most effective heterostructure for producing both high strength and HDI hardening, i.e., ductility [2,93]. One example is an HLS 316L SS



obtained by DPD and partial recrystallisation annealing [25]. The HLS microstructure produced a decrement of the strength – ductility classic trade-off, which the authors explained in terms of nano-twins acting as ductile grain boundaries. Such explanation was based on the possible “network” between recrystallised grains (~22 vol.%) and twins to provide superior ductility to the alloy. However, this hypothesis did not agree with a previous report of DPD and annealed high-purity Cu, which required at least 80 vol.% of recrystallised grains to produce such a superior UE [571]. It should be added that the DPD and annealed Cu also presented nano-twins bundles and recrystallised grains embedded in a nano-grained matrix. However, Cu has an SFE ( $80 \text{ mJ m}^{-2}$ ) around 4 times higher than the expected for 316L SS (6.6 to  $22 \text{ mJ m}^{-2}$ ) [27,123]. This is related to a smaller separation of Shockley partials and a higher occurrence of cross slip in Cu in comparison with the 316L. As explained in section 2, the HDI strengthening is strongly dependent on the GND pile up formation, while the GND piling up is maximised when cross slip is diminished. From the above, it is thought that the reduced trade-off between strength and ductility for the HLS 316L SS resulted from the contribution of HDI strengthening and HDI hardening. Moreover, twinning used to occur in a preferred range of SFE from 12 to  $45 \text{ mJ m}^{-2}$ , which is clearly not the case with Cu. Due to factors such as the low-SFE of SS, the high strain rate of the DPD process, and the room processing temperature, the dominant deformation mechanism was twinning. Twinning can act as a source of dislocations but can also block them, contributing to the material's strength while improving its strain hardening rate [137]. The abovementioned reasons explain the classical behaviour like-banana of the strength-ductility relationship for the HLS Cu compared to the reduced trade-off in the HLS 316L SS.

Subsequently, an HLS 316L SS processed by CR and short-time annealing firstly pointed out the contribution of HDI hardening and strengthening (back then known as back stress strengthening) to the superior mechanical properties of HLS SS [21]. In this work, a high density of HZB was formed from the presence of nano-twins, nano-twin bundles, shear bands, as well as the martensite/austenite and nanograins/coarse grains interfaces. As a result, the GNDs pile ups (Fig. 8(e)) encouraged the long-range HDI stress, and a strong strain partitioning provided an extra strain hardening rate. From the ROM, a YS of 945 MPa was estimated for the sample annealed for 10 min. However, it was lower than the measured value of 1000 MPa. This was an indication of the contribution of  $\Delta\sigma$  in the modified ROM (Eq. (1), section 2). It should also be remarked that an overestimation of YS of the lamellar coarse grain was used due to it was considered constant after the annealing treatment. This could reduce the estimated contribution of  $\Delta\sigma$  to the classic ROM. As expected, the increment of annealing time prompted the grain coarsening, improving the work hardening rate, as shown in Fig. 8(c). This improvement was generated from the highest dislocation accumulation capability in recrystallised grains compared to the strained counterparts, but also from the production of hetero-zones with HZB that encouraged the GNDs pile ups and long-range stress formation. The best combination of mechanical properties, YS (1059 MPa) and final elongation (FE) (19.4%), was obtained for the 10 min-annealed sample. Compared to the YS (1451 MPa) and FE (5.9%) of the cold-rolled condition, previous results represented a decrement of 27% and a 3.3-fold increment, respectively. HDI strengthening and work hardening played a considerable role in reducing the strength-ductility trade-off of the HLS SS316L. This was the first work on HS SS to clarify the contribution of HDI strengthening

to superior mechanical properties. The results from previous work were confirmed by other reports that reproduced the same experimental methodology, adding a comparison of 70 to 85% CR before annealing the HLS SS316L [23,150,174].

Other HLS materials have also been obtained of 304 SS by processes different from CR, like cryogenic and warm DPD with consecutive annealing for 60 min [36]. This work compared the tensile strength and ductility behaviours of two different microstructures: 1) duplex (17 vol.%  $\alpha'$ -phase + rest of  $\gamma$ -phase) and 2) single-phase (recrystallised and nano-twinned  $\gamma$ -phase). As a result, both materials obtained a yield strength of ~900 MPa but different UE of ~21% and 12% for single- and bi-phasic materials. The work-hardening rate of both materials showed a linear dropping until a strain of about 5%. However, for later strain, the bi-phasic microstructure decreased continuously until a strain of about 10%, while the single-phase structure remained nearly constant until ~21%. The authors attributed the best combination of strength and ductility in the nano-twinned sample to a synergy between the following phenomena: 1) higher capability to accommodate strain due to the presence of recrystallised grains and reduced dislocation density, 2) higher work-hardening due to the presence of nano-twins, stacking faults, and SIM transformation. A successive work based on the same DPD and annealed samples, varying only the annealing time to 45 and 15 min [37]. The authors reported similar work hardening decreasing tendency until a strain of about 6% for both materials. However, the UE of both materials was quite different. For this stage, the 15-min annealed sample sustained a smaller increase in hardening rate from the strain range of 5% to 8%. The authors considered this could be related to the higher flow stress of

this sample compared to that of the 45 min-annealed, which due to the Considère criterion, could generate an early necking [572]. On the other hand, the 45 min-annealed sample showed activation of synergistic strengthening mechanisms encouraged by the increasing presence of stacking faults and strain-induced martensite transformation as a function of the applied strain. This resulted in an increment of the hardening rate in the range from 6% to 14% of applied strain. Considering that stacking faults strongly contribute to the GNDs pile up occurrence, the 45 min-annealed sample could have a greater contribution of HDI strengthening than the 15 min-annealed. Besides, the lower dislocation density in the 45-min sample compared to the 15 min-annealed allowed a better accommodation of partial dislocations that contributed to work hardening and ductility. Other similar HLS 304L SS was prepared by ~88% CR and annealed at 700°C for 15 min, obtaining similar microstructure and mechanical properties [38].

#### *6.1.2. Tensile behaviour of GS SS*

As explained in previous section 2.2, in HS SS, including GS SS, several mechanisms can act synergistically to improve the mechanical behaviour of HS SS. However, one of the most influencing factors is the grain size gradient, typical of the trans-scale grain hierarchy, where grain sizes can span 3 or 4 orders of magnitude from NG to CG. Thus, it has been proposed that strain hardening in GS SS is the result of the contribution of different mechanisms [93]; i) additive effect of individual layers by forest hardening in the GS, ii) compressive residual stress that is commonly generated during surface plastic deformation methods (more details

about techniques in section 4.2), iii) HDI strain hardening, and iv) nano-twin boundary mediated strain hardening [93]. However, in GS SS, not all the mechanisms are necessarily active. Their contributions depend on the processing technique, final microstructure, and inherent properties like SFE and slip systems. For example, in GS 316L SS prepared by SLM and USSR, nano-twins played an important role in enhancing strain hardening [275]. Another GS 316L SS processed by ultrasonic strain engineering technology (USET) indicated the extremely fined NG surface as the main contribution to strain hardening [573]. One more example is a GS 304 SS processed by 3S, where the grain size gradient and twinning fragmentation were pointed out as the major modes for the strengthening [212]. However, the occurrence of HDI is expected in all HS SS that meet the requirements indicated in Fig. 7. Considering that HSMs are still an emerging field, the estimation of HDI stress by the unloading-reloading method (section 2.3) or other future improved methods should be encouraged to deeply understand the deformation and strengthening mechanisms of GS SS.

For GS SS, a novel design was proposed by tailoring the twinning density instead of the density of conventional grain boundaries, showing that nano-scale twin boundaries play a key role in the strain hardening [252]. A superaustenitic S31254 SS with low yield strength (280 MPa) was used to assess the role of a twin-density gradient structure on the mechanical properties of the SS. Compared to the CG S31254 SS, the twin density gradient S31254 SS doubled its yield strength, showing the crucial role of deformation twins in the synergistic enhancement of strength and ductility. The twin boundaries showed a higher contribution to the strain hardening than the conventional grain boundaries. In addition, the study of HDI

stress was realized by the unloading-reloading method and from the GNDs formation suggested from the increment of kernel misorientation values. The HDI stress and HDI strain hardening strongly contributed to the reduced strength to ductility trade-off in the GS S31254 SS [252].

#### 6.1.3. *Tensile behaviour in LS SS*

From section 4.3, LS materials are produced by bottom-up and top-down techniques that result in layers with nanometric to micrometric thicknesses. The strengthening of LS materials follows the typical Hall-Petch relationship within each homogeneous layer unless the grain size or layer thickness becomes nanometric ( $t < 100$  nm). Deviations from the Hall-Petch behaviour may occur due to a decrement of the intragranular dislocation accumulation capability in nanometric grain size [4,574–576]. It should be mentioned that despite the evidence of dislocation-based plasticity deformation mechanism in CG and UFG zones, to grain boundary sliding in nanometric grains, as well as multiple proposed models [577–579], there is still no consensus about the origin of the so-called inverse Hall-Petch relationship [580]. However, LS materials have shown superior mechanical performance, i.e., high strengthening and strain hardening, that exceeds the typical behaviours predicted by Hall-Petch and the ROM. The key factor for the superior mechanical performance of LS materials is the density of hetero-interfaces. As explained in section 2, a mechanical incompatibility  $>100\%$  between two interacting zones boosts high strain partitioning, and it is considered a hetero-interface delimited by HZBs.

Figure 18(a) shows micrographs of Cu-bronze hetero-interfaces with a mechanical incompatibility higher than 100% ( $\overline{HV}_{\text{Cu}} \cong 700 \text{ MPa}$  and  $\overline{HV}_{\text{bronze}} \cong 1500 \text{ MPa}$ ) caused by different strengths, stacking fault energy, chemical composition, and crystallographic texture between both layers [56]. That experiment was designed to evaluate the mechanical behaviour of LS Cu-bronze with variable hetero-interface spacing (density of hetero-interfaces) but comparable chemical, grain size, hardness, and crystallographic texture heterogeneities across the hetero-interfaces. From section 2, the generation of GNDs to accommodate the strain gradient near the HZBs will produce long-range HDI stress, which produces effective HDI strengthening and HDI strain hardening in the overall LS. However, the distribution of GNDs is non-homogeneous across the layers. From Fig. 18(b), the GNDs density is dependent on the distance from the hetero-interface, forming a GND density gradient [56]. The HBAR extends to a few micrometres regardless of the interface spacing [56]. The highest density of GNDs at the hetero-interfaces compared to the intragrain space has also been observed in LS SS produced by AM [350]. Thus, the density of hetero-interfaces is a key factor in increasing the GND pile up density and, consequently, the UTS (by HDI strengthening) and the YS and ductility (by HDI strain hardening). Figure 18(c) shows the increment of UTS and uniform elongation when the density of hetero-interfaces increases. Therefore, a high density of layers (thin layers) produces better mechanical performance than thick layers.

From the above, it was hypothesised that the space between interfaces should not be smaller than the HBAR extension to allow enough space for GNDs to pile up. The Cu-bronze

LS material later confirmed this hypothesis with a broad comparison of hetero-interface spacings (from 3.7 to 125  $\mu\text{m}$ ) [73]. The results are shown in Fig. 18(d), where the optimised hetero-interface spacing ( $\sim 15 \mu\text{m}$ ) allowed the simultaneous enhancement of YS and ductility resulting from the HDI strain hardening. It was shown that the optimum hetero-interface spacing, with the best combination of YS and ductility, was comparable to the necessary distance to avoid overlapping between the HBARs of each ledge of the hetero-interface Cu/bronze ( $\sim$ twice the HBAR from Fig. 18(b)). After overlapping both HBARs, the HDI stress generation seems limited. On the other hand, insufficient HDI stress is produced to boost mechanical performance if the hetero-interface spacing is too large. However, when the hetero-interface spacing is smaller than  $\sim$ twice the HBAR, there is not enough space for GNDs to pile up, limiting the HDI stress generation. Therefore, the optimum hetero-interface spacing maximises the HDI strain hardening and HDI strengthening to produce the best combination of mechanical properties. The hetero-interface spacing is crucial for designing LS materials with superior mechanical behaviour.

The above principle can be extrapolated to other low or medium SFE materials, such as SS. Effective delayed necking, i.e., strain hardening rate increment, has been shown in an LS constituted by 304 SS/420J2 SS layers, where 304 SS and 420J2 have a high mechanical mismatch ( $\text{UTS}_{304} \sim 500 \text{ MPa}$  and  $\text{UTS}_{420J2} \sim 1700 \text{ MPa}$ ) [47]. It was shown that ranges of hetero-interface spacing to  $\sim 40$  to  $77 \mu\text{m}$  considerably increased the ductility, YS, and UTS of the 304 SS/420J2 SS LS with respect to their monolithic counterparts. From the above, it can be expected that the LS SS with only one hetero-interface, e.g., the surface films on SS



mentioned in section 4.3, might not maximise their mechanical behaviour, but they can be useful for other multifunctional applications.

Other factors such as crystallographic orientation incompatibility between layers also influence the tensile properties of LS materials. An LS 316 SS processed via SLM was fabricated with different crystallographic orientations ( $\langle 011 \rangle$  and  $\langle 001 \rangle$ ) in layers alternately stacked along the y-axis [581]. The crystallographic layered microstructure largely improved the tensile properties and corrosion resistance of the austenitic LS 316L SS [581].

Further research should be done to model and experimentally probe the parameters between both coexisting zones (coherency, crystalline structure, crystallographic texture, stacking fault energy, among others) that affect the extension of the HBAR in different materials, e. g., SS. This will allow the prediction of the optimum hetero-interface spacing for designing new HSMs. Furthermore, the elaboration route of LS materials with multiple thin layers might be low-scalable, being a drawback for commercial purposes. The design of thermomechanical and thermochemical top-down and bottom-up routes to produce large-scalable LS materials is also an important fact to study. Some bulk multilayer LS SS have been produced by rolling combined with short-time heat treatments (304 SS/420J2 SS) [47], AM (C300 maraging steel/420 SS) [350], and AM combined with CR and partial annealing (304L SS/CoCrFeMnNi) [357]. Those LS SS reported considerable improvement in mechanical performance due to the design of hetero-interfaces with variable spacing and high mechanical mismatch to boost the strain partitioning and generation of GNDs. However, other bulk LS SS based on layers with millimetric hetero-interface spacing or gradual

chemical composition variations might present a less advantageous mechanical behaviour if tested under tensile test [351,352,356]. Lastly, additional research on the multifunctional properties of different LS SS should also be carried out to broaden their understanding and industrial applications.

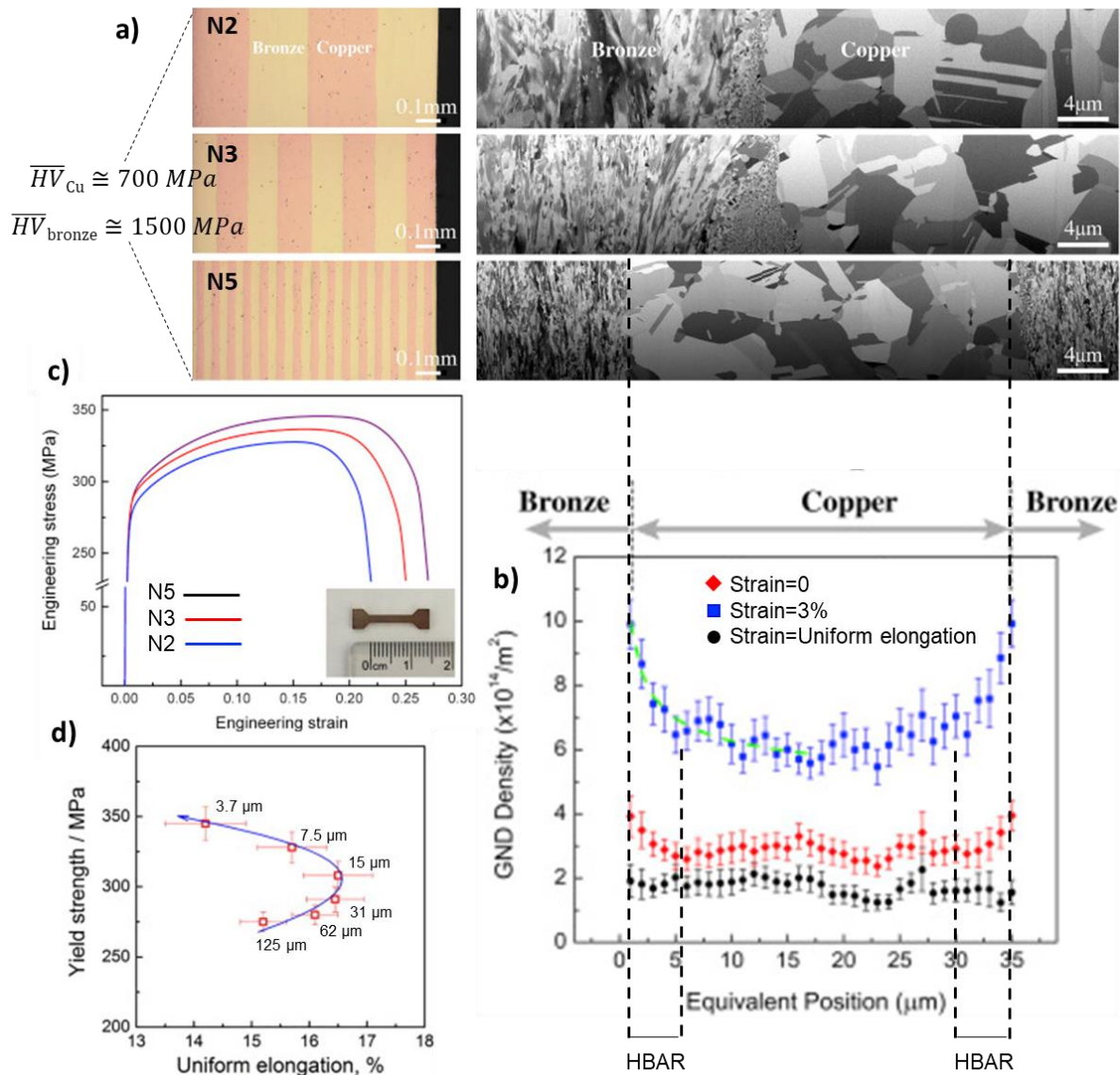


**Fig. 18.** Importance of hetero-interfaces on the mechanical properties of layer structured (LS) materials. (a) Micrographs of a three Cu-bronze LS materials with different densities of interfaces but comparable chemical composition, grain size, micro-hardness, and crystallographic texture, (b) comparison of engineering stress-strain graphs for the three Cu-bronze LS materials, (c) distribution of geometrically necessary dislocations (GNDs) through

the softer (Cu) layer [56], and (d) tendency of yield strength respect to ductility as a function of the interface spacing (density of interfaces) [73].

#### *6.1.4. Tensile behaviour in harmonic structured SS*

From section 4.5, harmonic structures are essentially core-shell structures with a specific 3D periodic arrangement of CG and NG zones, which are homogeneous on macro-scales but heterogeneous on the micro-scale [582]. Harmonic structured materials have an exceptional combination of high strength and ductility, resulting from optimised hierarchical features in the microstructure [501]. A harmonic 304L SS prepared via controlled mechanical milling of pre-alloyed powders followed by SPS [41], demonstrated an outstanding combination of high strength (382 MPa for 0.2% YS and 744 MPa for UTS), high uniform elongation (65%), and large total elongation (80%). The authors proposed that the fraction of the shell area is an important parameter controlling the balance of the mechanical properties [41]. Another example of the good mechanical properties of harmonic SS is a bi-phasic 329J1 SS processed using SPD and SPS [43]. The YS obtained for the harmonic structure was ~40% higher than the bulk, while tensile strength was improved by >25% with uniform elongation of ~17% [43]. The improvement of mechanical properties in the harmonic 329J1 SS was attributed to its heterogeneous microstructure, i.e., UFG mid-shell and an outer shell composed of a duplex structure with UFG precipitates. Other work showed that the high density of dislocations and twinning was responsible for simultaneous superior strength and ductility in a 316L SS prepared by SLM [489]. Besides, for a plasma sintered unimodal 316L SS, another

mechanism based on defects such as pores or second phase precipitates was reported [46]. The authors propose that a decrease in grain size below a critical value produces intergranular back stresses large enough to induce grain decohesion. This, in turn, controls the mechanical behaviour and therefore, it does not depend on grain size anymore [46].

The effect of high temperature on the tensile properties of harmonic HS SS has also been studied. A harmonic structured 304 SS processed via ball milling and SPS showed a superior combination of strength and ductility at room temperature. However, for high temperature, despite that tensile strength was still higher than the obtained for the CG structure, reduced strength was observed [583]. In another work, for an austenitic 316LN SS produced by HPT with a subsequent annealing process, it was found that UTS and YS of the initial harmonic structured 304 SS was highly improved, but the uniform elongation was low. However, when annealing at temperatures higher than 750°C, although tensile strength decreased, the elongation increased significantly. The increased grain size after annealing was the cause of the decrease in strength and the improvement of elongation [584].

Regarding cellular structured SS produced by AM, the excellent combination of strength and ductility decreased when increasing the annealing temperature for a 316L SS synthesized by SLM [467]. This effect was explained based on variations from the starting AM microstructure composed of a very fine cellular microstructure with small subgrains and dense dislocation networks within individual grains, dislocation pile ups near the walls, and misorientations in subgrains that repels dislocation movements [467]. The degradation of

tensile properties with increasing annealing temperature led to grains and cells growth, decreasing the dislocation network.

Density is another factor influencing the tensile properties of harmonic HSMs produced by AM or PM. Some authors pointed out that eliminating pores can be considered a strategy to improve the yield strength of AM alloys [442]. However, other factors such as the geometry of the samples and built-in flaws can also play crucial roles in the tensile properties [442].

#### *6.1.5. Tensile behaviour of multiphase SS*

As seen in Fig. 2, the dual-phase and multiphase SS, including precipitation type and microstructures with intermetallic phases, are representative of HS SS [496]. Their mechanical properties can be modified by adding a second phase [585]. A multiphase HS SS consisting of ferrite embedded in nano-grains was obtained by a combination of cryogenic and room temperature rolling with posterior tempering and short-time annealing [175]. Due to a final broad grain size distribution, including NG, UFG and CG regions, as well as a combination of  $\gamma$  and BCC- $\alpha'$ , The final microstructure was called multiphase hierarchical grain (MHG). A yield strength of 1.2 GPa was reached in the MHG SS (Fig. 19), which is more than two times higher than the CG counterpart, with little loss of ductility [175]. The engineering stress-strain curve of the MHG SS is shown and compared with its CG and single-phase hierarchical grain (HG) in Fig. 19(a) [175]. The persistent work hardening in the MHG (Fig. 19(b)) was a suggestion that HDI strain hardening originated from plastic

strain incompatibility at the hetero-interfaces formed by the different grain sizes and the coexistence of ferrite, martensite, and nano-precipitates [175]. However, the TRIP and TWIP effects also played an important role in the reduced strength to ductility trade-off of the MHG SS.

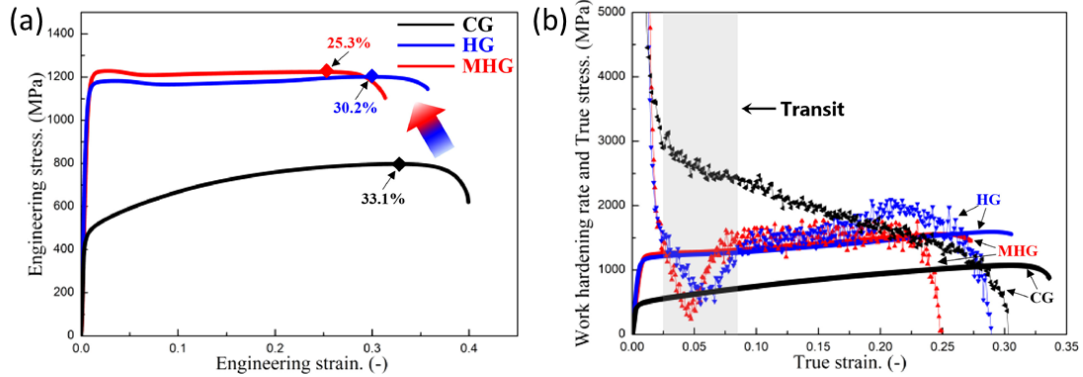


**Figure 19.** (a) Engineering tensile stress-strain curves and (b) corresponding work hardening rate of coarse grain (CG), single-phase hierarchical grain (HG), and multiphase hierarchical grain (MHG) stainless steel [175].

In another work, a medium manganese SS composed of 74% reversed austenite, 16% deformed austenite and 10% tempered martensite was reported [586]. The  $\text{Cr}_{23}\text{C}_6$  precipitates were also found in the microstructure. This multiphase and HLS SS also reported high YS (1324 MPa), UTS (1401 MPa), high strain hardening, and uniform elongation of 34.7%. The outstanding properties of the multiphase and HLS SS resulted from the combination of several strengthening mechanisms like TWIP, TRIP, dislocation accumulation, grain refinement, second-phase, solid solution, and HDI stress due to the heterogeneous distribution of nano/ultrafine grains and phases [586]. It should mention that the TRIP effect

in steels refers to the transformation of the metastable retained austenite (soft phase) to martensite (hard phase) during plastic deformation. For the medium manganese SS, the deformation mechanism works according to the phases, where a strain gradient between phase boundaries appears and is accommodated by GNDs. Additionally, the high SSDs density improves the strength [587].

#### *6.1.6. Tensile behaviour in multimodal SS*

Recently, extensive researches were devoted to studying the relationships between the grain size distribution and the mechanical properties of multimodal SS [42,45,512]. For example, a bimodal 304L showed a good ductility and total elongation of 44%, which is slightly lower than the total elongation of the CG 304L (58%). Meanwhile, the bimodal structure exhibited threefold increments in the yield strength, reaching 703 MPa (i.e., the yield strength in the coarse-grained specimen, 210 MPa). The high strength of the bimodal structure was attributed to the fine grains in the shell areas, while the high ductility was related to the coarse grains in the core regions. The presence of CGs in the matrix of UFGs improves the ductility by modifying both the strain hardening and the localizing strain regions [46].

Recently, a novel route of submerged friction stir processing (FSP) has been used to create bimodal grain size in austenitic 316L SS [509]. By rotating the cylindrical tool at a specific area on the as-received specimen, the FSP produces multimodal materials. The mechanical properties of CG, bimodal, and UFG 316L SS were studied by tensile testing at room



temperature [509]. Fig. 20(a) shows the engineering stress-strain curves of all these samples. The bimodal structure sample demonstrated a higher YS of 620 MPa than the UFG specimen of ~450 MPa. Additionally, the uniform tensile ductility of the bimodal sample was 35% compared to 30% in the UFG sample. The limited ductility in UFG materials is mainly due to the instability of fine grains, which is related to the limited capacity to store dislocations within fine grains [588,589]. The above results are in line with the observation reported by Flipona et al. for a bimodal 316L SS [46]. However, it is in contrast with the study introduced by Renk et al., as they observed a reduction in both ductility and strength of bimodal 316L SS [505]. The unusual decrease of ductility of the bimodal structure in the Renk et al. study is unclear. Therefore, further studies may be necessary to clarify it. Moreover, the bimodal SS showed a higher work-hardening rate than the UFG sample as shown in Fig. 20(b) [509]. The work hardening rate is quite dependent on the volume fraction and dispersion, shape, and particle size of the second phase [590,591]. Considering hard second phase particles with constant diameter, increments in their volume fraction produce increments of tensile strength with a synchronous decrease in elongation. In contrast, the work hardening rate increases when the size of the second phase is smaller. Therefore, the strength can be enhanced by increasing the volume fraction of the second phase, while the strain hardening and ductility can be improved by decreasing the size of the second-phase particle [590]. For the bimodal 316L SS, the average size of martensite grains was similar to or smaller than the grain size of the UFG sample, whereas the  $\alpha'$  volume fractions were 30% and 8% for the bimodal and UFG conditions, respectively [509]. Therefore, the higher yield strength and work-hardening rate for the bimodal 316L SS compared to the UFG sample was related to the higher volume

fraction of fine martensite grains. The good ductility for the bimodal 316L SS may be attributed to a high dislocation density around the hard-small  $\alpha'$  grains and the high dislocation storage capacity of coarse  $\gamma$  grains. Moreover, the large work hardening reduces tensile instability in the material and therefore delays the onset of crack propagation [592,593]. In conclusion, the bimodal 316L SS exhibited higher YS, higher work hardening rate, and larger elongation than the UFG sample.

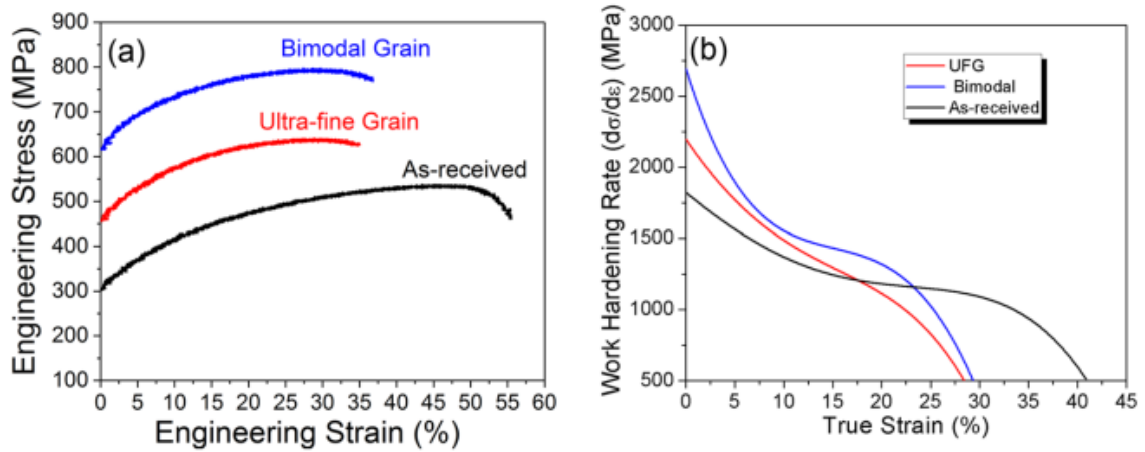


**Fig. 20.** Comparison of mechanical behaviour between as-received, ultrafine (UFG), and bimodal structured 316L stainless steel (SS). (a) Engineering stress-strain curves and (b) work-hardening rate versus strain [509].

From section 6.1, the key factor in optimising the strength to ductility relationship of HSM is to maximise the HDI strengthening and HDI strain hardening. Microstructural features such as the flow stress mismatch at the soft/hard interfaces or HZBs trigger different strain

partitioning, GNDs densities, and interaction between multiple strengthening mechanisms. As a result, different mechanical performances can be obtained for the same material with different HS arrangements. [Table 1](#) compares the mechanical properties of different HS 316L or 316 SS obtained by various processing routes. As explained in section 1, HDI was renamed in 2019 [20] from back stress strengthening and hardening due to the contribution of forward stress.

**Table 1.** Comparison of mechanical properties of different HS 316L or 316 SS that have reported the contribution of HDI strengthening.

<b>Processing route</b>	<b>HSM classification</b>	<b>Microstructure</b>	<b>YS / MPa</b>	<b>UTS / MPa</b>	<b>UE / %</b>	<b>TE / %</b>	<b>Ref</b>
85% CR + short time annealing at 750°C for 5-25 min	HLS*	Lamellar CG zones between surrounded by NG zones and nano-twins	1108.0 – 572.0	1242.0 – 849.0	2.1 – 27.5	10.0 – 36.1	[21]
SLM + stress-relief HT at	Harmonic-like and multimodal	Cellular structure with bimodal grains	~290.0	~530.0	~65.0	~85.0	[486]

300°C for 1 h		distribution form by small grains along molten pool boundaries and bigger grains					
SLM + USSR	GS and harmonic- like	NG surface layer with deep- dependant grain size, phases, dislocation, twins, and cellular structure.	740.9 - 665.2	856.0 - 763.4	~7.5 — 17.0	13.1 - 21.6	[275]
70–85% CR + short time annealing at 750°C for 5-25 min	HLS*	Lamella recrystallised grain clusters and CG between nano-sized twin bundles and UFG grains	~560.0 — 1250.0	-	~3.0 -27.0	-	[23]

L-PBF with variable parameters	Harmonic-like and multiphase*	Cellular and dendritic structures with N, O, and H impurities, Cr and Mo segregation, and precipitation of transition-metal-rich silicates.	450.0 — 680.0	-	25.0 — 59.0	-	[462]
80% CR + short time annealing at 720°C for 20 min + annealing from 200 to 700°C for 12 h	HLS**	Lamellar CG zones between UFG grains and nano-twin bundles	~410.0 - 1080.0	~850.0 - 1180.0	~4.0- 33.0	~16.0 — 36.0	[594]

L-PBF + annealing from 700 to 1200°C for 10 and 40 min	Harmonic and multiphase**	Cellular structured with segregates of Cr and Mo on cell walls, as well as Si-rich precipitates	384.4 — 556.3	-	-	-	[450]
20 and 30% cryorolling + annealing at 650 °C for 10 min and 1 h	HLS**	Refined $\gamma$ grains surrounded by martensitic ( $\alpha'$ ) islands.	305.0 - 886.0	785.0- 1147.0	8.4- 39.7	~20.0 — 50.0	[190]
SLM	Harmonic- like and multiphase**	Cellular structure with segregation of Mo, Cr, Mn and Ni, depletion of Fe, and precipitates rich	500.0	570.0	34.0	42.0	[471]

		in O, Si, and Mn.					
DED + 1 h annealing at 400, 800, 1000, and 1060°C	Harmonic-like and multiphase**	Cellular structures with segregation of Mo and Cr	184.0 — 459.0	411.0 — 648.0	40.0 — 72.0	~58.0 — 82.0	[495]
*Reported as back-stress strengthening.							
** Reported as effect of GNDs or dislocation pile ups accumulation at different HZBs.							

## 6.2. Hardness

Heterostructured materials are characterized by coexisting fine grains/hard phase and coarse grains/soft phase zones. The hetero-zones deform inhomogeneously during plastic deformation, and the material has large deformation gradients [350,595]. From previous section 2.1, The soft zones deform more plastically first and form back stress, while the harder zones remain elastic and develop forward stress [20,350]. Such an incompatibility of deformation responses between the soft and hard zones leads to strain partitioning and inhomogeneous distribution of the hardness in the HSMs [41,44]. GNDs will be formed to accommodate the strain hardening at the HZB. However, the production of HDI stress, i.e., back stress and forward stress, produced an additional hardening effect that benefits to the global mechanical performance [20]. An example of the above is shown in [Fig. 21\(a-e\)](#),

which corresponds to a layer structured material formed by 420 SS and 300 maraging steel [350]. [Figure 21\(b\)](#) shows the difference in hardness between the different layers obtained by AM process, while the preferred GNDs formation at the HZB is observed in [Fig. 21\(e\)](#).

It should be remarked that hardness is a very localized study that is widely used for quick evaluation of mechanical properties and measuring the plastic response of materials [596,597]. However, the wide range scattering of hardness values in heterostructured materials makes such evaluation of mechanical properties intractable. The very local hardness test can now be performed with a high degree of precision using high-speed nanoindentation testing, which provides an opportunity to measure large networks of indents [597]. Therefore, the indentation mapping technique is used to measure the local mechanical properties of multiphase alloys and small areas of HSMs [598].

The hardness of SS depends on various factors such as the grain size ([Fig. 21\(f,h\)](#)), chemical composition ([Fig. 21\(g\)](#)), phase composition, and crystalline structure [44,507,599–601]. The HS SS neighbourhood areas may be different from one another, at least in one of these factors, which results in soft and hard zones. Namely, the areas of HS SS exhibited dramatic variations in hardness values. Such a large scattering of hardness depending on the grain size is observed in [Fig. 21\(f\)](#), where the hardness profiles as a function of the depth in GS 304 SS produced by different surface nanocrystallization techniques are compared to the hardness of the CG 304 SS. Regarding chemical composition gradients, [Fig. 21\(g\)](#) shows the hardness profile for an AM layer structured SS composed of multiple layers with different



Cr/Ni ratios [352]. One more example of hardness disparities in HS SS is the bimodal grain structure of 304L SS [44] (Fig. 21(h)).

The grain size is the major factor that controls the hardness of the SS [507,599]. This grain size dependence can be clearly observed in Fig. 21(f), where under similar chemical composition (304 SS), the hardness decreased as a function of the grain size increment. The small grain size implies a lower capacity for storing the dislocation as well as more barriers for sliding the dislocation, which enhances the material hardness [218]. In contrast, the CG regions are generally displaying low hardness. Fig. 21(h) shows the hardness of sintered 304L SS compacts versus the ratio of average grain size in the core regions ( $D_{core}$ ) to average grain size in the shell regions ( $D_{shell}$ ) [41]. The  $D_{core}/D_{shell}$  ratio was used to describe the grain size heterogeneity in the material. The hardness measurements were carried out separately in the shell and the core regions of the harmonic structured 304L SS [41]. The disparity of hardness between the core and shell areas increases monotonically with increasing the  $D_{core}/D_{shell}$  ratio. At high deformation, the hardness in the shell areas of 40% higher than that in the core regions [41]. Similar higher hardness was measured in the harmonic structured 316L SS shell regions, which can be attributed to their high density of grain boundaries [602]. As explained

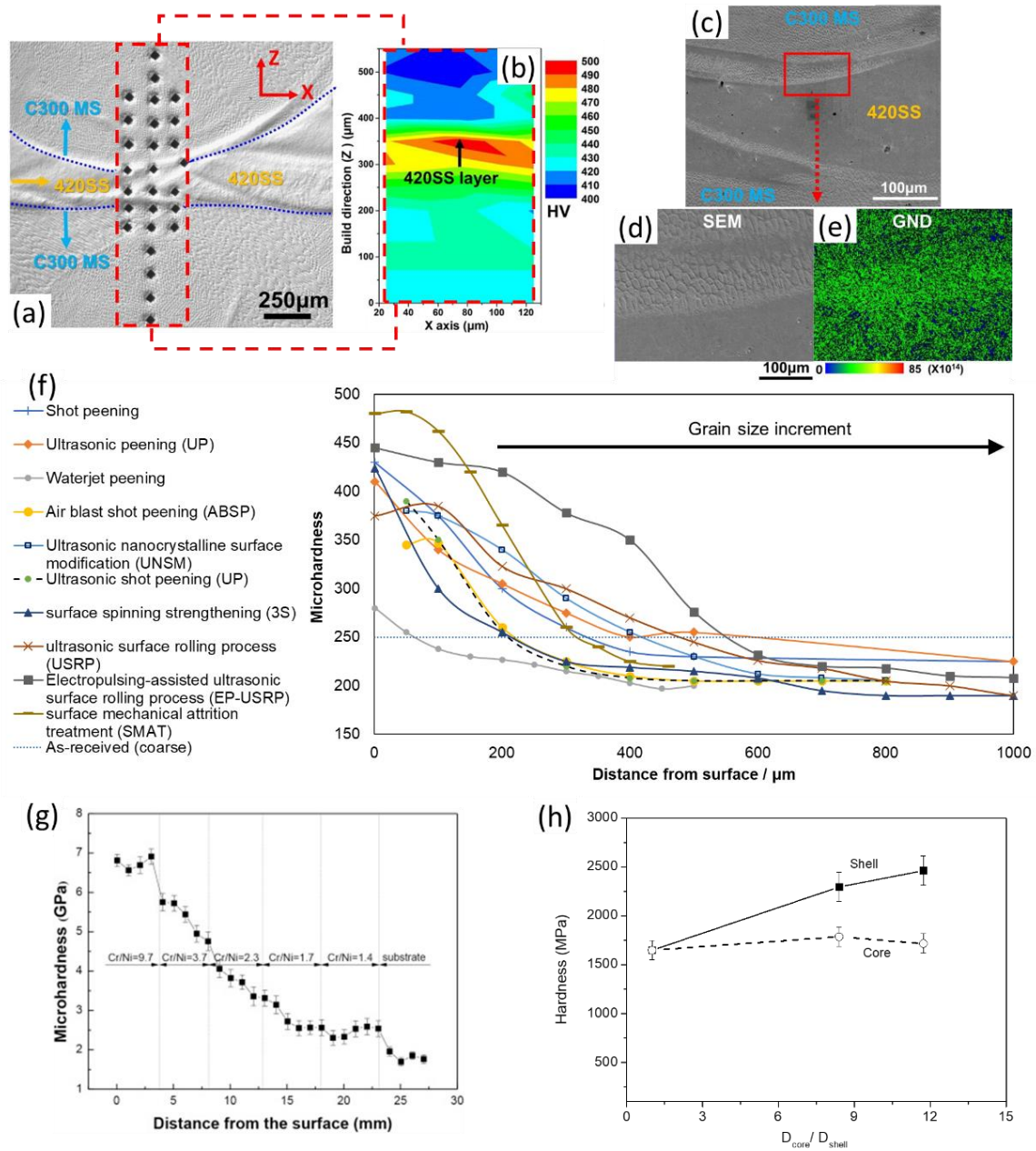


**Fig. 21.** Hardness profiles in different heterostructured (HS) stainless steel (SS). (a) micrograph with microhardness indentations of a layer structured material composed by 420 SS and 300 maraging steel (C300 MS) and its (b) hardness distribution map, as well as (c,d) magnifications and (e) density of geometrically necessary dislocations (GND) at the

420SS/C300 MS hetero-interface (adapted from [350]). (f) Comparison of microhardness profiles as function of the distance from the surface between gradient structured (GS) 304 SS processed by different surface nanocrystallization techniques (data collected from [212,226,229,272,280,603]) and its coarse grained counterpart [225]. (g) Microhardness profile of a layer structured stainless steel fabricated by additive manufacturing with gradient Cr/Ni ratios [352]. (h) Dependence of the core and shell microhardness of a sintered bimodal 304L SS compacts on the ratio of the average grain size core regions ( $D_{core}$ ) to average grain size in the shell regions ( $D_{shell}$ ) (adapted from [41]).

The scattering of hardness values can also be related to multiple phases in HS SS [601]. It is well known that the BCT and BCC martensite exhibits a limited plastic deformation and is harder than the FCC austenitic structure. Consequently, the hardness increases significantly with increasing the fraction  $\alpha'$ -martensite phase [589,600,604,605]. However, it was reported that the hardness of 316L SS is more controlled by grain size than by phase composition [507].

Furthermore, as the study of HDI strengthening and hardening is still emerging, their contribution to the final mechanical properties has not been clarified for many HSMs. For example, a porous 420 SS matrix with variable content of reinforced TiN particles was elaborated by SLM [378]. Due to the TiN powder decreasing the laser absorptivity of the final alloy, it generated more zones with insufficient fusion. This means that the relative

density decayed as a function of the TiN content. As a result, the global hardness of the alloy decreased for the smallest relative densities. However, for constant TiN contents, the increment of the laser power increased the relative density of the bulk, also increasing the hardness. The authors reported that the increment of hardness was because of solid solution and TiN phase strengthening. However, the maximum hardness reported of 56.7 HRC (~6.6 GPa) is above the maximum estimated by the ROM. For such estimation, the hardness values and the weight ratios of the components can be considered, i.e., FeCr (~10 GPa) [606] formed considering an overestimation of the 50% of the Cr content, this is in a 6 wt.%, to join with a 6 wt.% of Fe for a 1:1 stoichiometric component, as well as 1% TiN (~31 GPa) [607] and rest of SLM 420 SS (~5 GPa) [378]. By using the ROM in the hypothetical 12FeCr-1TiN-420SS, the maximum hardness obtained could be ~6 GPa, which is ~13.6% lower than the experimental. This rough estimation suggests that an extra strengthening mechanism acted in the aged 420 SS. The difference between hypothetical and experimental hardness can be due to HDI strengthening. As described in section 2, to probe the above, an experimental estimation of HDI stress by unloading-reloading tensile test loops might be useful [19].

### *6.3. Fatigue resistance*

Superior fatigue behaviour has been reported in HS SS, including high fatigue limit under stress control, high-cycle fatigue [608,609] and low-cycle fatigue [610], as opposed to the traditional trade-off reported in conventional homogeneous CG and NG materials. The

mechanisms responsible for this behaviour in SS have been mainly studied for GS SS [262,270,273,284,611,612]. For example, austenitic GS 316L SS showed higher fatigue strength and fatigue life compared to its CG counterpart [262,610,611]. The mechanisms for this strengthening have been explained in terms of different contributions: 1) as most fatigue cracks initiation occurs on the surface because of manufacturing processes defects [613], the suppression of surface roughening and cracking in NG surfaces produce a higher fatigue resistance by retarding surface fatigue crack initiation [262]; 2) the resistance to fatigue crack propagation or crack growth is enhanced by altering the stress/strain distribution around crack tips [611]. Cracking and propagation delay because of surface compressive stress states is a common result in GS SS [108,148,219–222].

The grain size also strongly contributes to the fatigue resistance of HS SS. The fatigue properties of harmonic structures of 316L and 304L SS were investigated by axial fatigue tests and fatigue crack propagation tests [614–616]. Fig. 22(a,b) show the SEM micrograph and the corresponding inversed pole figure (IPF) map around a crack in the harmonic structured 304L SS after axial fatigue test [614]. It was observed that fatigue cracks initiated at the coarse-grained regions in the harmonic structure 304L SS. The fine grains smaller than 4  $\mu\text{m}$  are shown by the colour map in Fig. 22(c). The crack path is shown as a white line in Fig. 22(b,c). Fatigue cracks propagate in both CG and fine-grained structures without any additional effect of the UFG structure. Accordingly, a harmonic structure does not affect fatigue crack propagation or crack profiles. As a result, the harmonic structure SS demonstrated a higher endurance limit due to the presence of fine grains [614].

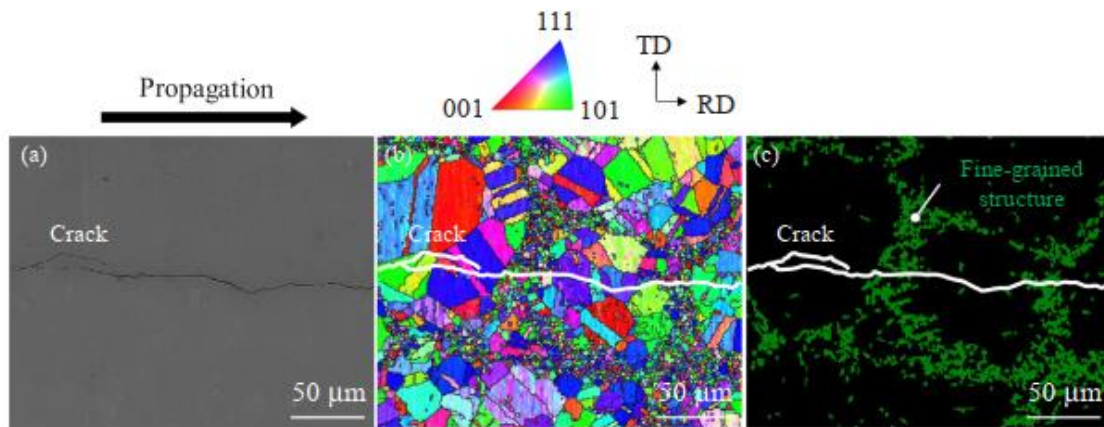


**Fig. 22.** (a) SEM image, (b) IPF map, and (c) grain size color map of a region near a crack profile (white lines) for the harmonic structure 304L SS sample after axial fatigue test at a stress ratio 0.1 [614].

Improved fatigue properties were reported for a nanotwinned 316L SS fabricated by DPD and annealing. Crack initiation and propagation were retarded because of the elastic homogeneity and cyclic deformation compatibility between nanotwinned and recrystallised grains [617]. In the same line, for a nanotwinned austenitic 304 SS, dislocation activity, detwinning and martensitic transformation have been proposed as mechanisms for the enhanced fatigue resistance. This is because of the release in strain localisation and suppression of the surface roughening and cracking [618]. Similarly, in a metastable austenitic 304 SS with nanotwin bundles, detwinning followed by martensitic transformation enhanced the crack growth resistance [619].

The corrosion fatigue crack initiation was studied in a GS martensitic 420 SS [612]. The authors showed a significant improvement in corrosion fatigue resistance in acidic, neutral, and alkaline NaCl solutions because of the compressive residual stress induced by the surface NG structure, which was perpendicular to the crack propagation direction. Compressive surface stress states delay crack initiation and propagation, and a high density of grain boundaries promotes a uniform, compacted and well-adhered passive layer in fine-grained SS [108,136,149]. More details about the corrosion performance of HS SS will be given in section 7. In addition, martensitic lath refinement and nano-sized dispersed carbide fragments also contributed to improving corrosion fatigue life [612].

Despite the simultaneous enhancement in fatigue properties that different studies have shown in HS SS, another work showed that in 2205 duplex SS the hard brittle martensite phase decreased the ductility of the gradient NG layer, accelerating crack propagation and decreasing the low-cycle fatigue life [270]. This means that there is not a consensus about the effect of HS microstructures on the fatigue resistance of SS. More systematic studies are needed regarding the effect of different HS microstructures on the fatigue resistance of SS and their modelling to predict crack initiation and propagation.

#### 6.4. *Wear resistance*

Wear resistance is a key factor in determining the working life of the material in service, and it is required in a wide range of technology and engineering applications [620,621]. Therefore, researchers are striving to improve the wear resistance of materials. Although the wear resistance of homogenous CG and NG SS has been extensively studied [622–625], the wear behaviour of HS SS is still unclear [174,626]. Wear in SS is primarily caused by oxidative, adhesive, and abrasive mechanisms [174,624,625,627]. However, the wear mechanism of SS may be dependent on many parameters such as the chemical composition, crystalline structure, grain size and morphology, phases distribution, among others. Essentially, the wear resistance will be affected by all the factors that influence plastic behaviour in metallic materials [628].

The role of the chemical composition, the grain size, phase compositions, and microstructure in controlling the wear resistance of SS was recently reported by many authors [174,622–624,629,630]. More surface martensite in SS leads to less wear resistance [627]. By comparing ferritic and martensitic SS, the metastable austenitic SS offers the best overall wear resistance [631].

Decreasing the grain size to UFG or NG regimes improves the wear resistance of SS by improving its hardness [623,630,632]. Usually, the wear loss of SS increases with increasing the normal loads [630,633]. However, for a relatively high applied load and a further increase in hardness, the wear resistance of nanostructured SS decreases. It was reported that the wear resistance of austenitic 316L SS containing nano-scale twin increased with increasing the



normal loads up to 20 N and then decreased at an applied load of 30 N [632]. It can be concluded that the wear resistance of fine-grained SS was better than the CG steel due to the higher hardness in small grains areas [623].

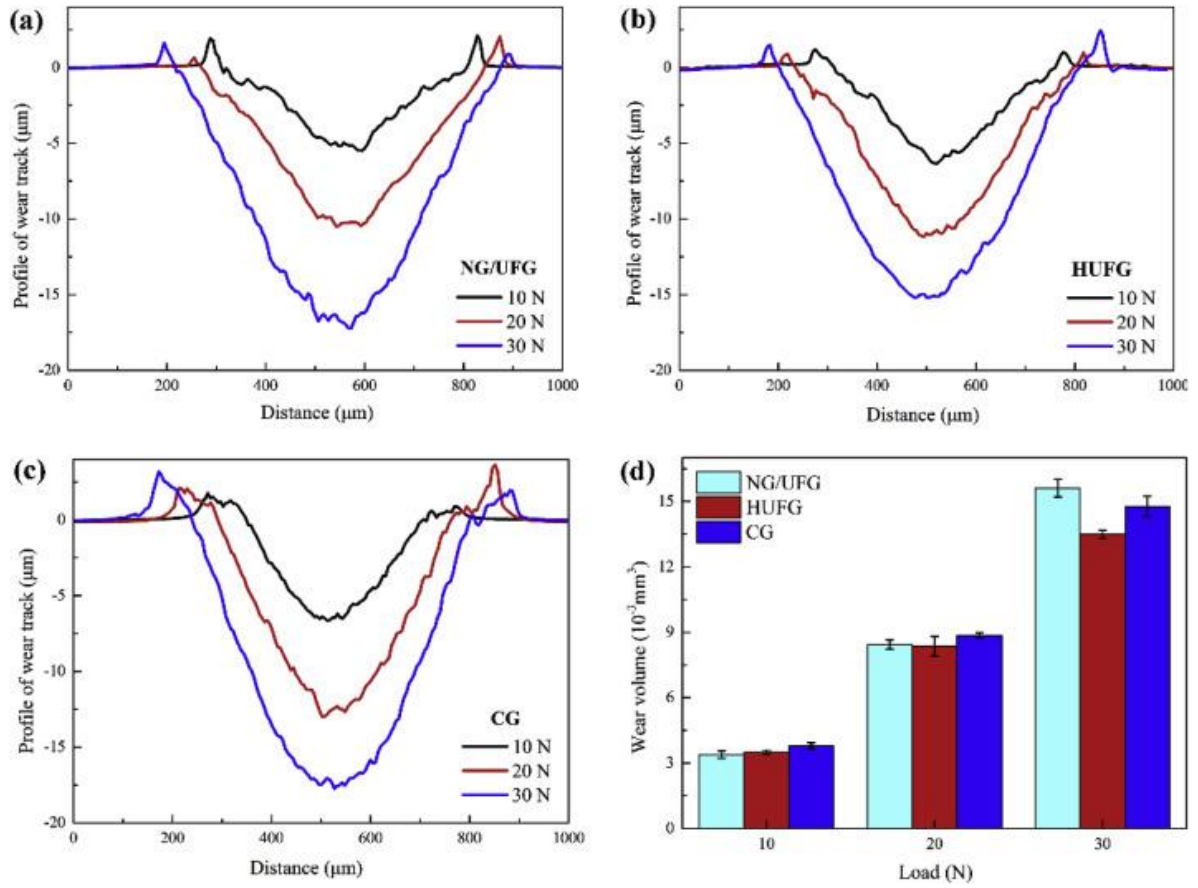
The HLS 316L SS is more susceptible to severe tribo- and abrasive wear processes, leading to an increase in wear rates and wear loss. Furthermore, increasing normal loads accelerates oxidation, reduces more oxide particles, and reduces the wear resistance of HLS 316L SS compared to the CG SS [174].

Figure 23(a-c) shows the typical cross-sectional profiles of the wear scratches formed on the NG/UFG, heterogeneous ultrafine-grained and CG austenitic 18Cr–8Ni SS under different loads [630]. It can be seen that the wear track of the different specimens has a similar feature. However, wear volume varies in the different samples depending on the applied load. Fig. 23(d) shows the change in the wear volumes for the different samples under three applied loads. Under the smallest applied normal load of 10 N, the NG/UFG sample demonstrated a better wear resistance than its CG counterpart. This improving of the wear performance for NG/UFG SS was related to the higher hardness and grain refinement in the sample. However, at a high normal load of 30 N, the NG/UFG specimen with the highest hardness has the poorest wear resistance, while the UFG (indicated as HUFG in Fig. 23) specimen exhibits the best wear resistance.

The wear performance of HSMs are also dependent on the amount of plastic deformation, where the increase of grain boundaries, dislocation, and twins lead to access more oxygen species inside the materials and, thus, it can accelerate the oxidative wear process [629,634].

Furthermore, the presence of nanograins and nanotwins in HSMs enhanced the strength and hardness, improving wear resistance according to Achard's law [635,636]. The harmonic structured austenitic 304L SS showed a lower wear resistance at relatively higher normal loads of 10 N compared to a sintered non-harmonic structured 304L SS and a low carbon conventional 304 SS [626]. It was concluded that the shell areas of harmonic structured SS are less wear-prone than core areas. Similar wear behaviour was observed for harmonic structured 316L SS, extending to better wear resistance at a lower normal load [602]. According to Achard's law, the better wear resistance in the shell regions of HS SS may be due to the higher hardness in these areas.

Recently, the tribological behaviour of HLS 316L SS produced by 85% cold rolling and subsequent heat treatment in air at 750°C for 10 min was studied [174]. It was reported that the wear resistance of HLS 316L SS was slightly smaller compared to that of the CG specimen under a normal load of 5 N. With increasing the load to 15 N, a remarkable decrease in wear resistance was observed for the HLS, which nearly 50% lower than that of CG material. The lower wear resistance of HLS compared to that of the CG SS is due to the HLS 316L SS being more susceptible to severe tribo- and abrasive wear processes, leading to an increase in wear rates and wear loss. Furthermore, increasing normal loads accelerates oxidation, therefore increasing oxide particles, which reduces the wear resistance of HLS 316L SS [174].



**Fig. 23.** Cross-sectional profiles of (a) nanogained/ultrafine grained (NG/UFG), (b) Heterogeneous UFG (HUFG) and (c) CG 18Cr–8Ni austenitic stainless steels (SS) under different loads, and (d) the wear volumes versus normal loads in three SS [630].

## 7. Corrosion susceptibility

Corrosion is a degradation process consisting of a series of electrochemical reactions occurring between anodic and cathodic sites on a metal surface when in contact with an

aqueous solution/electrolyte [637]. From section 3, SS (homogeneous and HS) is an excellent material to be applied in different sectors due to its good corrosion resistance and mechanical behaviour [638]. In general, the corrosion resistance of SS depends on the alloying elements and environment. The corrosion resistance of SS is mainly determined by their Cr and Mo contents and their microstructure. A chromium enriched nanometric thin film layer grows when it encounters the atmosphere, enhancing the corrosion resistance properties. Conversely, the presence of different ions in the environment, especially chloride, is a destructive factor for the corrosion resistance of SS [361,639]. Chloride ions develop the rust on SS, leading to pitting and/or crevice corrosion [360,640]. This pitting is particularly destructive because it undercuts the protective nascent Cr-rich oxide surface of SS [641]. Chloride ions may promote a fast failure of SS.

Much attention has been paid to the corrosion mechanisms of SS based on their different microstructures to understand the corrosion initiation and improve its resistance. One of the main corrosion mechanisms is pitting or local corrosion, which creates pores of local degradation of the microstructure, leading to failure. Microstructural defects such as grain boundaries, inclusions, intermetallic particles, among others, are typical regions for pitting starting in SS [642–645]. The reason for that preferred attack is the higher available energy at those defects compared to that in the free-of-defect inner grain.

In general, good corrosion resistance has been related to CG alloys due to their lower grain boundary density compared to NG or UFG materials, being a synonym of lesser active sites for the preferential attack [646]. However, CG surfaces allow a poor adherence of the passive

surface layer compared to those nanostructured on passive systems [91,92,647,648]. The UFG and NG materials have demonstrated easier passive layer formation than the CG materials [91], resulting in better pitting corrosion resistance. One example is an NG 316 SS with a high grain boundary density, which made the growth of the oxide passive layer more feasible than in the CG 316 SS [151]. The potentiodynamic curves showed a significant decrease (seven times) in corrosion rate in the NG SS compared to the CG SS when tested in Ringer's solution [151]. Thus, HS SS allow exploring the interaction and effect of coexisting heterogeneous zones with different electrochemical potential and active sites density on the corrosion and passivation performance.

#### *7.1. Microstructural effect on corrosion resistance of HS SS*

Regarding multiphase structured HS, the partitioning of  $\gamma$ -stabilisers (Ni, N) and  $\alpha$ -stabilisers (Cr, Mo) results in different chemical compositions, electrochemical potential, and corrosion performance between those phases [649–651]. The galvanic activity  $\gamma$  and  $\alpha$  triggers stress corrosion cracking (SCC) in duplex SS, where the  $\alpha$  phase acts as cathodic protection for  $\gamma$  in acidic (chloride-containing) environments [652]. However, the interaction of  $\alpha$  and  $\gamma$  phases in duplex SS does not increase local corrosion because it improves the surface passive film formation. The passive current density to sustain the passive film on the individual phases is higher than for a duplex microstructure where both phases are coupled [653,654]. Higher content of  $\text{Cr}_2\text{O}_3$  was found in the oxide film of the duplex microstructure, while more  $\text{Cr}(\text{OH})_3$  was observed in the film of the individually passivated phases. The

presence of  $\text{Cr}(\text{OH})_3$  was related to the decrement of the passive film effectiveness, being the reason for the better corrosion performance of  $\alpha$  and  $\gamma$  coupled in the microstructure [653,654]. In soft core multiphase structured SS (Fig. 11(b)), where the  $\gamma$  islands have higher corrosion potential than the  $\alpha$  matrix, pitting and environment-assisted corrosion are started at the  $\alpha$  phase, resulting in cracking to be propagated along grain boundaries [654]. Due to the difference in potential between  $\gamma$  and  $\alpha$ , the anodic activity at the cracking tip (started at  $\alpha$ ) is reduced, and the cracking is delayed when getting in contact with the  $\gamma$  phase [655]. This is an effective mechanism to delayed cracking in multiphase HS SS if no embrittlement mechanisms of  $\gamma$  are activated (like mechanical overload). It should be mentioned that galvanic activity is not exclusive to bulk multiphase SS. It can also be encouraged by contamination, impurities or segregation in SS. SCC was also observed in austenitic SS fabricated by AM, where Si-rich oxides along the grain boundaries were preferentially dissolved, accelerating the oxidation and cracking [125,437]. From the above, studying electrochemical and passivation mechanisms of the phases in SS is a key factor in understanding and predicting the global electrochemical behaviour of the alloy [649]. Deep research in clarifying the changes in electrochemical properties of multiphase HS SS under environment-assisted corrosion is needed.

As explained before, the density of grain boundaries plays a key role in the electrochemical behaviour of SS. Thus, heterogeneous grain size distributions strongly influence the electrochemical behaviour of HS SS. The narrow distribution of fine grain boundaries and triple junctions (intersection of at least three adjacent crystals [656]) in NG

SS allows more uniform and compact Cr-rich oxide surface layers compared to those in CG SS [91,92]. However, the high fraction of defects in NG materials increases the stored energy and reactivity in non-passivating environments [91]. Thus, the grain size distribution is expected to have a dual effect on corrosion performance depending on the material/environment system [92,657]. NG SS may show high corrosion resistance when tested in passivating media, while reporting decrement of corrosion resistance in non-passivating electrolytes [92,657]. Besides, a high density of grain boundaries improves the atomic diffusion over the surface [658,659], which can be translated into better Cr diffusion towards the surface of NG SS.

Compared to CG Fe, the improvement of Cr diffusion in GS Fe obtained by SMAT has been reported [659]. Thus, improved passivation behaviour due to better Cr diffusion may be expected for GS SS. This was observed in a GS 304 SS with improved Cr diffusivity in the NG surface compared to that in CG microstructures [660]. As a result, the improved adherence and continuity of the passivation layer and the higher content of Cr in the surface oxides positively influenced the corrosion behaviour of the GS 304 SS [660]. The behaviour of the passive layer on most metallic materials can be compared to a highly doped semiconductor, where the electrochemical behaviour of the surface layer and base material are mutually affected [661]. More research about the passivation and corrosion performance of GS SS in different passivating and non-passivating environments is needed to understand their corrosion mechanisms [149].

Regarding the effect of defects on the electrochemical behaviour of metals, only the pitting initiated at recrystallised grains can form stable pits and then be propagated to form micro pits [149,151,152,662]. Thus, an HLS 316L SS consisting of recrystallised, NG, and UFG regions exhibited better pitting resistance than the CG 316L SS [152]. Compared to the CG condition, the better pitting resistance of the HLS SS was observed by the increment of pitting potential from 320 to 425 mV when tested in 3.5 wt.% NaCl [152]. As observed in Fig. 24(a), the best pitting resistance of the HLS 316L SS was confirmed by delayed pitting propagation of stable corrosion pits at the HZB between recrystallised, NG and UFG regions. Fast kinetics of metastable pitting formation and re-passivation of uniform, continuous, and thick Cr-rich oxide layer might be related to the enhanced pitting resistance of NG surfaces [149,457,663]. Contrastingly, pitting propagated across the grains to form macro and micro pits when polarization potential increases in the CG SS.

Regardless of the grain size distribution, interfaces such as conventional grain boundaries or HZB are the preferred nucleation sites for pitting [645,664]. Therefore, pitting initiates preferentially at high-energy boundaries instead of low-energy boundaries. Although, high-energy boundaries also encourage the Cr diffusion to the surface [149,665] to form a thicker and more efficient passive layer [82]. Thus, the boundary energy also has a significant impact on the corrosion behaviour of HS SS. Considering that twin boundaries have less energy than HAGBs [184], the high density of twin boundaries in NG SS may encourage a higher corrosion resistance than NG SS with a high HAGBs density [666]. Thus, the presence of low-energy boundaries, as twins, has a strong effect on the electrochemical behaviour of HS



SS but also on their microstructural evolution, where nano-twin regions are more stable than conventional NG regions when temperature increases (Fig. 8, section 4.1). Systematic experimental and modelling research for optimising electrochemical behaviour of HS SS through tailoring grain size and grain boundaries distributions is required.

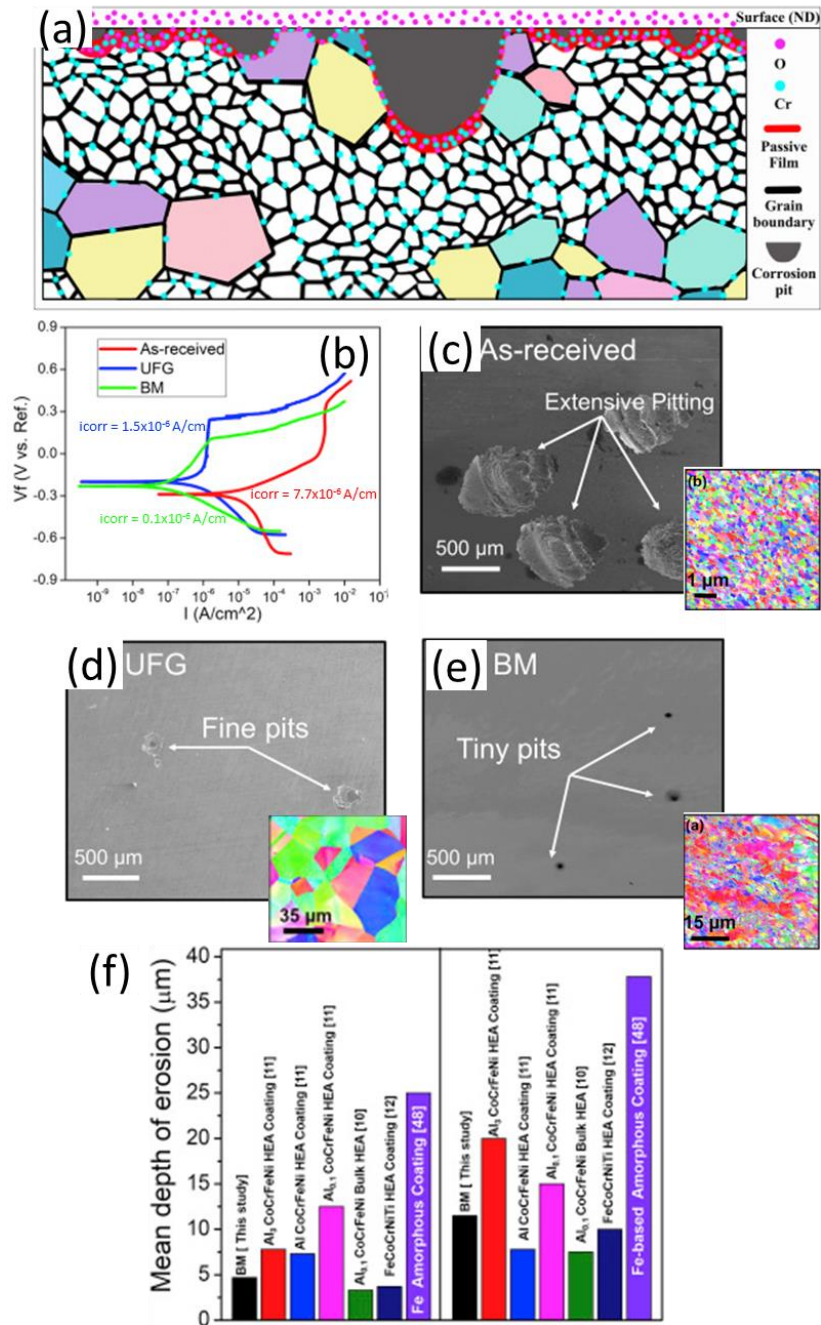


**Fig. 24.** Electrochemical behavior of heterostructured (HS) stainless steel, (a) propagation of local corrosion (pits) on the surface of a heterogeneous lamella structured (HLS) 316L stainless steel (SS) [152], (b) polarization curves and (c-e) pitting morphology of bimodal

(BM), nanograined (NG), and as-received coarse grained (CG) 316L SS [506]. The BM, NG, and CG microstructures can be appreciated at the insert of (c-e). (f) Comparison of mean depth of erosion during cavitation and corrosion processes among the BM 316L SS and different high entropy alloys (HEA), amorphous coatings, and bulk metallic materials.

Modelling and experimental studies in pure Mg and Al-alloys suggested that grain size distribution rather than average grain size plays a dominant role in determining their corrosion response [91,667–669]. The passivation kinetics is faster for the UFG material than that in CG condition [91]. However, the uniformity of the passive surface layer is dependent on grain size distribution. The corrosion performance of the bimodal structured 316L SS was compared to its UFG and as-received CG counterparts (Fig. 24(b-e)) [506]. The bimodal SS showed the best corrosion resistance compared to UFG and CG SS, which was attributed to higher stability and favourable electronic properties of the passive layer. Bimodal SS showed an order of magnitude lowest current density ( $i_{\text{corr}}$ ) compared to the as-received CG alloy (Fig. 24(b)). As a result, the corrosion rates were 0.001, 0.017, and 0.088 mm/year for the bimodal, UFG and CG SS, respectively. Thus, the bimodal 316L SS demonstrated an exceptional low corrosion rate. Furthermore, the average pit depth for bimodal SS was nearly 2.5 times smaller than the CG SS, supporting the best electrochemical performance of the bimodal SS (Fig. 24(c-e)). Moreover, the kinetic results from potentiodynamic polarisation measurements suggested exceptional corrosion resistance of bimodal grain structure in 3.5% NaCl solution (Fig. 24(b)). The lowest corrosion rate for the bimodal condition is likely

attributed to a higher fraction of  $\text{Cr}_2\text{O}_3$ , which suggests higher atomic diffusivity. As explained before, the high Cr diffusivity is related to the high density of grain boundaries, as well as to the atomic packing fraction of martensite in the bimodal 316L SS. The lower atomic packing fraction of BCT-martensite compared to that of the FCC-austenite supported the increment of atomic diffusion of Cr, O, and Fe at the martensite phase [506]. Furthermore, the bimodal 316L SS showed outstanding erosion resistance during cavitation erosion and erosion-corrosion tests compared to some high entropy alloys (HEA), amorphous coatings, and bulk metallic materials from the literature (Fig. 24(d), [506]). Plenty of research should be carried out to optimise grain size distributions based on their passivation, diffusion, and energetic behaviour. This might allow the prediction of corrosion performance during multiple industrial uses of HS SS.

## *7.2. Microbial corrosion of HS SS*

It is well known that biofilm formed by bacterial cells can influence corrosion processes, potentially leading to either acceleration or reduction of material degradation [670,671]. Biofilms formed on metallic surfaces can act as an oxygen/ion concentration cell, with different oxygen/ion levels inside and outside the biofilm. Bacteria presence may also trigger the production of corrosive metabolites, such as iron sulphide and organic (ormic, succinic, citric, isocitric, aconitic, oxoglutaric) and inorganic (acetic, formic, lactic, succinic) acids [672–675]. One or more of these factors are often responsible for microbiologically influenced corrosion (MIC), which is the electrochemical corrosion initiated and/or

accelerated by the activities of microorganisms [672]. MIC is a bio-electrochemical process that occurs under the combination of an energy source, carbon source, electron donor, electron acceptor, and water. MIC has a strong economic impact as it can occur in various environments such as soil, freshwater, seawater, power generation, marine engineering, and oil field [672]. As a result, many industrial fields may be affected by MIC, e.g., cooling water circulation systems of power plants, ship systems, oil exploitation, storage and transportation systems, sewage and drinking water pipelines, locomotive fuel storage tanks, among others. IC is strongly characterized by local corrosion (pitting) formation, and its kinetics and extension are still unpredictable. MIC is responsible for 20% of all the corrosion damages [676], 75% of corrosion of oil well pipes, and 50% of failures of buried pipelines in the USA [677,678]. The direct cost of MIC is estimated to exceed RMB 50 billion per year in China [677,678]. However, that data is out of date and might not reflect the actual losses today.

Nevertheless, the high losses caused by MIC are difficult to mitigate. Microstructure, chemical composition, surface roughness, bacterial species, test medium, immersion temperature and availability of nutrients play an important role in initial bacterial attachment and subsequent biofilm formation [672,679–682]. Thus, the microstructural design of HS SS should try to decrease its likelihood. Therefore, improving our understanding of MIC on different microstructural systems is essential to take mitigation measurements in metallic systems, especially those promising for multi-disciplinary fields, such as the HS SS.

Regardless of the high corrosion and pitting resistance of austenitic and duplex SS (provided by the high contents of Cr, Mo, and Ni), the pitting corrosion caused by MIC is still inevitable [675,683–689]. Some studies reported that the *Pseudomonas aeruginosa* (*P.*

*aeruginosa*) biofilm could accelerate the corrosion of austenitic 304L SS and duplex 2205 SS [690,691]. Besides, *Chlorella vulgaris* (*C. vulgaris*) could promote local corrosion on 316L SS [692]. After 21 days of *C. vulgaris* incubation, local corrosion was observed with a pit depth of 20  $\mu\text{m}$  from the surface [692]. In another report, the largest pit on dual-phase 2205 SS caused by *P. aeruginosa* reached 14  $\mu\text{m}$  [595]. From the above, a strong MIC effect can be expected for HS SS systems, whether involving or not chemical disparities. There is plenty of room for research on the effect of HS microstructures on MIC occurrence, being of especial attention for HS SS to be applied in biomedical devices and liquid transportation or storage transportation systems. Furthermore, MIC should be deeply studied in SS as based material but also in SS welds.

As a structural material, welding of SS is essential for many applications and requires singular attention. The heat-affected zone (HAZ), i.e., not melted region exposed to the effect of welding temperature, produces different grain sizes and grain morphologies distributions as a function of its distance from the welding point (due to temperature gradient). Thus, GS SS profiles are used to form between the HAZ and the unaffected base metal [649,693,702–704,694–701]. Besides, a welding process can join parts or use a filler metal with different chemical compositions from the base metal. In that case, multiphase welding combined with gradient grain size and morphology profiles might be obtained [695,705,714–720,706–713]. However, as explained in section 2, their classification as HSMs due to a significant formation of HDI stress will strongly depend on the difference in flow stress ( $>100\%$  for HS SS) between the soft and hard zones.

It was reported that in 304L SS welds, bacteria might colonize preferentially near welds with an area of attachment inversely proportional to the average grain size [721]. As the bacteria started colonizing, attachment mainly occurred on the grain boundaries of the base metal and the  $\gamma$ - $\alpha$  interfaces. The higher density of grain boundaries in the welded regions resulted in more bacterial attachment than the base metal. Another example was the *Pseudomonas sp* attachment significantly higher on weld and HAZ regions than on 304L SS base metal [721]. Thus, base metal microstructure influences bacterial attachment and MIC [721]. Consistently, it was reported that whether single or multiphase SS, the welded regions are the highest influenced by MIC [722]. Another factor to consider in welded SS is chemical disparities due to sensitization during welding. It was reported that sensitized 304 SS had the highest bacterial density, followed by solution-annealed and oxidized conditions of the same 304 SS [723]. Those results were significant considering that preferential attack on welded devices might occur in microbiologically-influenced environments [723].

Despite the above, pitting corrosion triggered by MIC might occur on both base metal and weld seam. The pits can be formed by the bacterial colonies or their metabolism products instead of the culture media [724–726]. It should be remarked that local corrosion is the main reason for the fast and unexpected failure of SS. Pitting was observed in the base metal and welded regions of two austenitic and one duplex SS in contact with sulfate-reducing bacteria [722]. The pitting depth found in their work were 4.9, 5.6, and 7.4  $\mu\text{m}$  for the two austenitic SS and duplex SS base metals, respectively. The deepest pits on the weld seam areas were 6.2, 10.4, and 12.3  $\mu\text{m}$ , respectively [722]. The deepest pit on the weld seam was deeper than that on the base metal. As explained before, welded regions alter the surface and local

microstructure characteristics. The weld seam area of duplex SS seemed to have larger grains, but a large number of fine sub-grains could be observed within the grains, which suggested that the weld seam area contributed to a longer grain boundary per unit area than the base metal. As grain boundaries are preferential sites for bacterial attachment, the local microstructural condition at the weld seam increased bacterial attachment and resulted in more severe MIC occurrence [721]. It was concluded that there was no large fraction of biofilm and/or bacteria observed on the weld seam areas, but the weld seam microstructure accelerated the MIC process. The main features related to these findings are the microstructure and surface roughness [723,727]. Bacterial attachment occurs preferentially at grain boundaries in SS [721]. Typically, the smaller the grain size, the worse the MIC resistance.

The use of alloying elements to assist in grain size control can also be explored for tailoring the corrosion performance of HS SS. For example, an austenitic SS with lower Cu content had smaller grains than another with higher Cu content [721]. The pitting corrosion and MIC resistance of the sample with small grains might decrease compared to the microstructure with larger grains [722]. Then, the austenitic SS with higher Cu content could act as antimicrobial material, which means that Cu is a desirable element to provide antimicrobial capabilities to various materials [728,729].

It is worth mentioning that bacterial biofilms can either increase or inhibit corrosion rates, depending mainly on the type of microorganisms involved and the test medium used [730]. Exploiting the possible advantages of bacterial biofilms, austenitic and duplex SS with different Cu contents were exposed to bacteria cells, revealing improvement of MIC



resistance as a function of the Cu content [722]. The microbial corrosion of Cu bearing 316L SS in contact with an acid-producing bacterium *Acidithiobacillus caldus* (*A. caldus*) *SM-1* was reported [380]. The Cu bearing 316L SS samples showed effective antimicrobial activities in the biotic medium through a lower biocorrosion rate in the presence of *A. caldus* *SM-1*. The authors showed that the direct contact of copper oxides in the surface film and indirect ionic  $\text{Cu}^{2+}$  released from the substrate might be synergistically responsible for the enhanced anti-biofilm and anti-MIC properties of the 316L-Cu SS [380].

## **8. Other properties of interest**

### *8.1. Biological*

Metallic SS implants (mostly temporal) meet many essential criteria for biomedical applications, including high wear and corrosion resistance, biocompatibility, appropriate strength to ductility relationship, cost-effectiveness, and are commonly obtained by simple production processes [140,731]. For example, 316L SS is suitable for orthopaedic wires and screws, cardiovascular applications, artificial joints, and spinal fixation devices [151,322,732]. Many dental and surgical implants are made of SS because of their low risk of thrombosis and notable *in vitro* and *in vivo* biocompatibility [733].

It is well reported that nanostructuring methods provoke significant changes in the physical and mechanical properties of metallic materials [734]. In addition to making the metal implant itself more bioactive, changing the grain size has also been shown to alter

biological properties [735–739]. Increments in surface area by nanostructuring result in higher surface reactivity and promote cells interactions [740]. Thus, the high surface energy of fine-grained materials triggers the protein adsorption and subsequent cell attachment, cell proliferation, and cell differentiation [741]. Thus, nano-and/or sub-micrometre biomaterials are known to be more advantageous for tissue growth than the CG ones. Besides, the high biocompatibility of NG microstructures implies high corrosion resistance [741]. The difference in biological behaviour between the NG and CG SS is a consequence of reducing ion release due to the higher corrosion resistance and higher presence of chrome oxide at the passive surface layer of NG SS.

Regarding ion release, decreasing the presence of some metallic ions common in SS, such as nickel, significantly decreases cell deaths [151]. The presence of nickel in the body environment may intensify the excitement of the surrounding organic tissue, resulting in necrosis and poisoning [151]. Thus, the biocompatibility of metallic implants fundamentally depends on their reaction to the surrounding environment [742,743]. Reducing the corrosion rate and release of poisonous ions drastically increases the implant biocompatibility [743]. Due to the high nickel content, SS is mainly used for non-permanent biomedical implants.

Concerning surface layer composition, the high presence of chrome oxide on the surface of the SS significantly improves the implant biocompatibility, i.e., its biological behaviour. As explained in previous section 7.1, a high density of grain boundaries improves the Cr diffusion towards the surface of NG SS. Chrome oxide can be considered a favourable factor in bioactivity and corrosion behaviour [744]. From the above, it is considered that the NG surfaces of GS SS might strongly contribute to improving the biological behaviour of HS SS.

For example, a 316L SS reduced gram-positive bacteria adhesion after surface nanostructuring by severe shot peening [745].

Intensive efforts are being made to improve the antimicrobial properties of SS. One route is applying chemical surface treatments, i.e., by elaborating layer structured SS. A nitride surface layer on a 303 SS reduced the viability of gram-negative *Escherichia coli* (*E. coli*) within 24 h [746]. The strong microbicidal effect of the nitride layer is shown in Fig. 25. From Fig. 25(a), the *E. coli* bacteria on the conventional 304 SS remains intact, while it has an irregular shape on the antimicrobial nitride surface of 303 SS (Fig. 25(b)). Thus, the nitrided layer significantly inhibited the growth of gram-negative *E. coli* on the layer structured 303 SS [746]. Another example is a duplex SS coated with Ti-Cu that improved the wear resistance, corrosion resistance and surface bacterial inhibition [325]. Another work demonstrated that Cu coating in 317L SS possessed a satisfactory antimicrobial ability against *Staphylococcus aureus* (*S. aureus*), decreasing its proliferation by 98.3 % after 24 h in contact with the samples [381]. A similar result was obtained in 430 ferritic SS coated with Cu with a rapid inactivation ability against *E. coli* [383]. However, the antimicrobial properties of layered SS are not exclusive to Cu additions. The aged 2205 duplex coated with polygonal Ag-NPs showed high antimicrobial properties against *E. coli* and *S. aureus* [160]. Another SS was covered with Ag and Cu nanofilms, finding that Cu nanofilms were the most efficient against *S. aureus*, *Enterococcus faecium*, *Enterococcus faecalis*, *P. aeruginosa*, and *Bacillus anthracis* [339].

A different route to provide antimicrobial properties to SS is by elaborating multiphase SS by adding bulk second phases or metallic nanoparticles (NPs). However, the size and concentration of the second phase have inverse and direct relationships, respectively, with the antimicrobial efficacy [747–749]. Reducing NPs agglomeration also benefits the antimicrobial efficacy due to the increment of surface area for interaction with bacterial membranes [750]. NPs are highly promising against microbes' multidrug resistance that resulted from the broad use of antibiotics [750]. The NPs are useful for multiple applications as medicine, food production and packaging, catalysis, chemical reactions, optoelectronics, among others [751].

From the reported metallic and antimicrobial NPs, Ag and Cu NPs are most effective against multiple microorganisms, including bacteria, viruses, fungi and algae [751]. Ag and Cu NPs have shown efficiency against microorganisms such as influenza A (H1N1), *candida albicans*, *E. Coli*, *S. aureus*, *salmonella enterica*, SARS-CoV-2, among others [747,751,752]. However, Cu is much more accessible and costs less than Ag. It is worth mentioning that antimicrobial copper alloys are currently included in the list of supplemental residual antimicrobial products against COVID-19 of the U.S. Environmental Protection Agency (EPA) [753]. Diverse antimicrobial mechanisms of Cu have been reported [754], including fragmentation and cell death [755], membrane damage [756] or interruption of biochemical processes of microbes [754], pointing to Cu as a highly efficient antimicrobial material. Despite its toxic effect on microbes, Cu is non-toxic to humans and is an essential trace element for physiological and metabolic processes [757].

The strong microbicidal effect of NPs can be combined with the already mentioned advantages of SS. Moreover, SARS-CoV-2 is more stable on the surface of SS in comparison with that of Cu [758,759]. [Figure 25\(c\)](#) shows the inhibition of *Porphyromonas gingivalis* on the surface of the aged 304 SS with 3.9 wt.% Cu after being cultured for 4, 6 and 8 h compared to a conventional 304 SS [164]. The sterilization rate of the multiphase 304 SS-Cu was 36.8, 71.6, 96.3, and 100 % after 4, 6, 8, and 10 culture hours [164]. Besides, Cu additions in austenitic 316L SS improved corrosion resistance in an  $H_2SO_4$  medium [760]. Other antimicrobial multiphase SS have used Ag NPs, obtaining a high effectivity against multiple microbes [160–162]. Deep and systematic studies on corrosion, toxicity, biocompatibility, and microbicidal mechanisms in antimicrobial HS SS remain for further explanation.

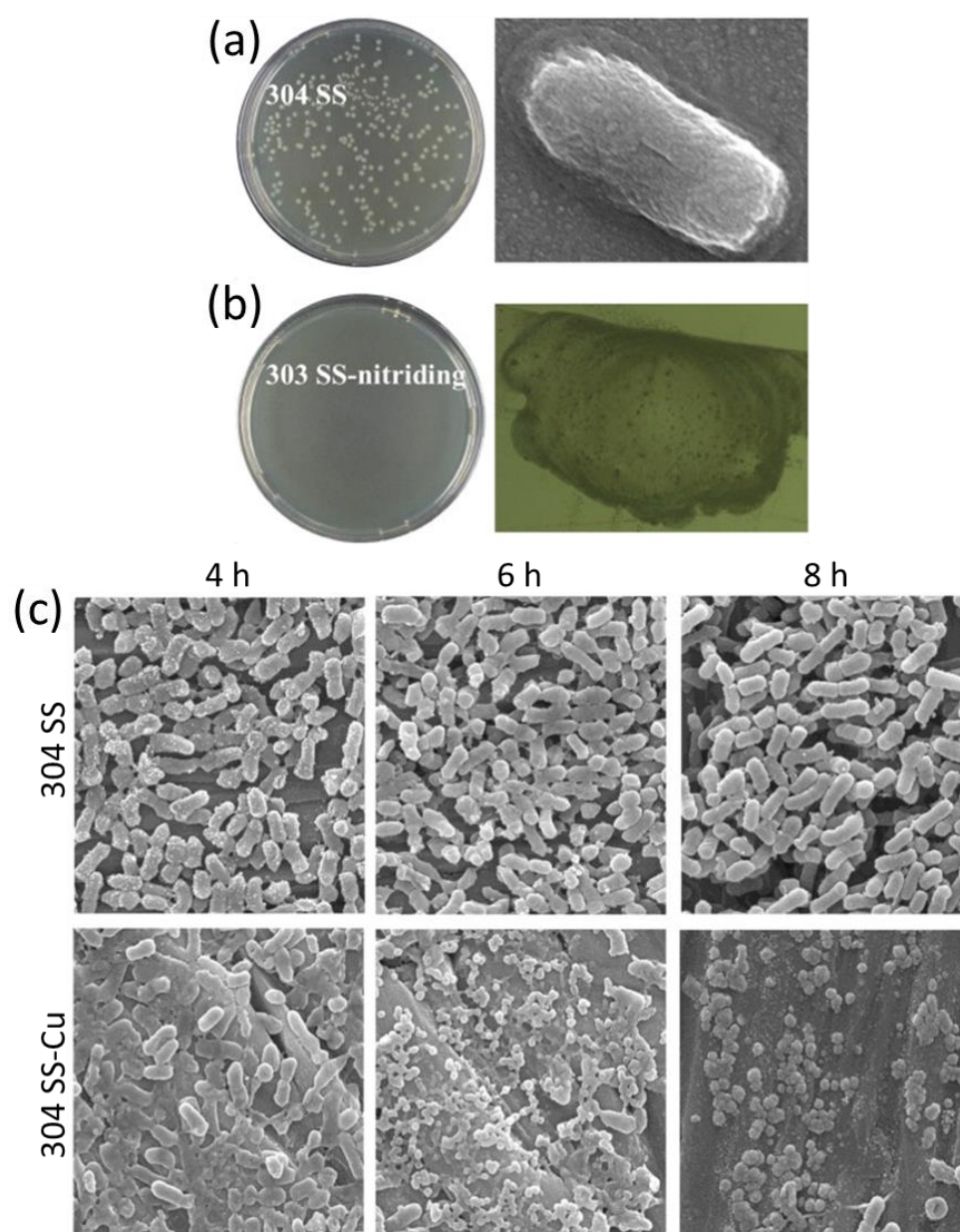


**Fig. 25.** Antimicrobial activity and SEM images of the *Escherichia coli* morphologies on (a) 304 stainless steel (SS) and (b) 303 SS with surface nitride layer [746], as well as (c) morphologies of *Porphyromonas gingivalis* on conventional 304 SS and antimicrobial 304 SS with 3.9 wt.% Cu after cultured for 4, 6 and 8 h [164].

Thus, NPs or bulk antimicrobial second phases additions are up-and-coming options to develop HS SS with a practical combination of outstanding mechanical and antimicrobial properties. However, the coherent and soft nature of low contents of Cu NPs could be related to negligible mechanical performance tailoring of HS SS. The introduction of HZB (with a large difference in flow stress) into those multiphasic microstructures might be necessary to drive the mechanical behaviour simultaneously with the antimicrobial. There is still scarce research on antimicrobial SS with superior mechanical properties, but some reports can be taken as starting points. HLS SS with Cu additions have been developed without seeking the formation of Cu NPs [54,168,761]. Another HLS SS with Cu NPs was reported without deep information about the NPs distribution and the antimicrobial mechanisms [53]. Other antimicrobial multiphase SSs with Cu NPs have been reported without improvement of the mechanical performance of the alloy [164–167]. Efforts on designing and understanding the fundamental mechanical and biological mechanisms of new antimicrobial HS SS should be carried out. Those efforts should also aim for low-cost and large scalable fabrication routes.

Another important ability of metallic biomaterials is protein adsorption, indicating their biocompatibility and being a key factor for their feasibility as biomedical implants. A GS 316L SS with an average surface grain size of 10 nm prepared via an ultrasonic shot peening revealed a significant enhancement in human osteoblasts compared to the CG 316L SS surface when tested *in-vitro* [762]. This enhancement may be related to the ultra-high boundary density on the NG surface, which promoted protein adsorption by providing continuous protein adsorption sites with a partially exposed surface when encountering

biological environments. A significant increment of protein adsorption and surface area was also reported for GS 304 SS compared to conventional CG 304 SS [763].

## 8.2. Thermal stability

Heterogeneous grain size, like those in GS, HLS, multimodal, and harmonic SS, and chemical disparities, like those in layer and multiphase structured SS, are the most studied heterogeneities in SS up to now. Regarding the stability of different phases. An HS 304 SS reported a microstructural evolution described by deformed  $\gamma$  recrystallisation, vanishing of dislocations and twins, increasing fraction of NG  $\gamma$ , and non-evident  $\gamma$  grain growth after annealing at 700 °C for 1 h [764]. Moreover, from section 4.1, cold deformation leads to SIM in metastable austenitic SS [765], which affects the response of the material to the subsequent annealing. The formation of  $\alpha'$ -martensite during deformation by HPT in 304 and 316 SS was observed, while the  $\epsilon$ -martensite formed only in the former [766]. Low-temperature annealing ( $\sim 350^\circ\text{C}$ ) led to the decrement of  $\alpha'$ -martensite content in the 316 SS, but its increment in the 304 SS [766].

Regarding grain size, the nanostructures with a high density of HAGBs possess higher surface area, surface energy and, consequently, less thermal stability than coarse grains [218]. This is because surface energy is the driving force for grain growth [767]. Similarly, a decrement in thermal stability in materials with broad grain size distributions (nanometric to micrometric) can be expected compared to CG materials. For instance, an HLS 314L SS



showed a faster grain growth kinetics in the microstructure with a smaller grain size (after CR) than that processed by warm rolling [173].

Another example of the strong effect of grain size on the thermostability of HS SS is an HLS 316L SS consisting mainly of nano-twins, nano-grains, and lamellar coarse grains. This HS SS showed a preferential initiation of recrystallisation in the NG regions, followed by the nano-twin regions, and lastly, the CG regions [21]. Recrystallisation nucleation usually starts in high stored energy regions. The higher thermal stability of the coarse lamellar grains can be observed in the microstructural evolution of [Fig. 26\(a\)](#) [21]. Thus, the grain size has an inverse relationship with its thermal stability. The thermal stability of HLS 316L SS (with nano-twin, UFG, recrystallised and lamellar coarse grain regions) after 12 h annealing up to 650°C was reported to be good (in terms of remaining as an HS microstructure). In contrast, rapid grain growth of recrystallised grains at 700°C revealed the industrial service limit temperature for HLS 316L SS [594].

The thermal stability of NG regions was studied in a SMAT-processed GS 316L SS [256]. The NG surface was stable up to 600°C for 10 min. However, further increment in temperature led to a fast increment in grain size ([Fig. 26\(b\)](#)), the change in strength and ductility ([Fig. 26\(c\)](#)), as well as abnormal grain growth (AGG), leading to the formation of larger grains with poorly defined grain boundaries (e.g. after annealing at 700 °C for 2 h) [256]. It is noteworthy that the occurrence of AGG has been reported at temperatures ~850 °C in UFG [171] and CG [768,769] austenitic SS. Therefore, the presence of nanograins seems to take part in the observed behaviours. Similarly, Jiang et al. [770] reported that the obtained hierarchical nanostructure (with UFG grains, UFG precipitates, nano-twins and high

densities of dislocations) by HPT remained stable up to ~600 °C. Annealing at higher temperatures led to uninhibited grain growth and decreased hardness [770]. In another study [771], heterogeneous NG 316LN SS with different Mn contents (obtained by 90% CR) retained its hardness up to 600 °C.

Discontinuous dynamic recrystallisation (DRX) during hot rolling might lead to HS microstructures [772,773], resulting in different storage energy in deformation bands and DRX grains. DRX led to broad grain size distributions upon heating a 316H SS to elevated temperatures [193]. With longer holding times at 1000 °C, grains gradually grew up, and the larger grains continued to swallow adjacent smaller grains, even presenting abnormal annexation or growth. However, stepped heating from low to high temperatures might solve the problem. Accordingly, a grain size uniform distribution can be achieved, which is a novel idea for regulating grain size in deformed and annealed SS [193]. Another study showed that an isothermal annealing is an effective way for acquiring an UFG microstructure in severe CR-processed austenitic SS [774]. Heating rate and critical recrystallisation finish temperature were important factors in that regard..

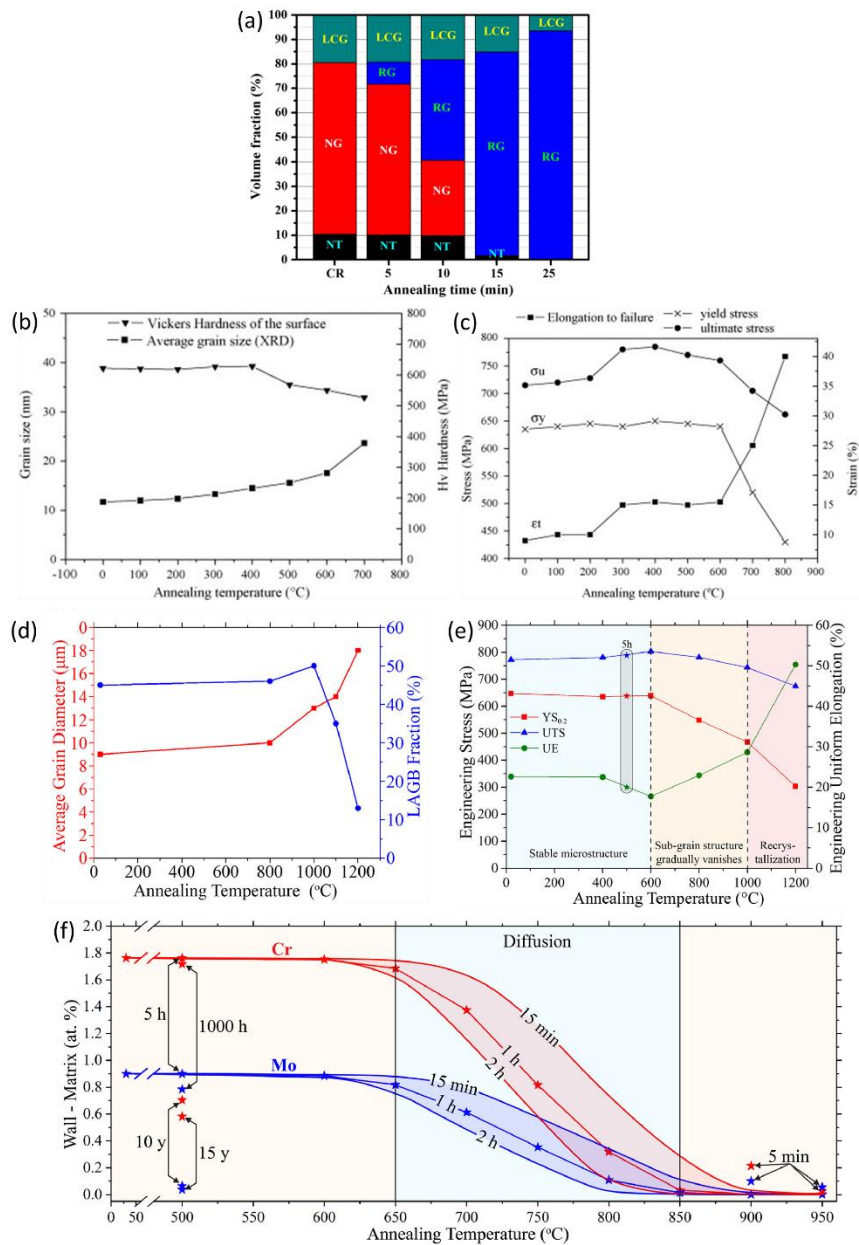


**Fig. 26.** Effect of annealing temperature on the microstructural and mechanical properties evolution of different heterostructured (HS) stainless steel (SS). (a) Microstructural evolution during annealing at 750°C for different times of a heterostructure lamella structured (HLS) 316L SS, where NT refers to nano-twin, NG to nano-grained, LCG to

lamellar coarse grained, and RG to recrystallised grained regions [21]. (b) Variations of the surface average grain size, near-surface hardness, and (c) mechanical properties with different annealing temperature for 10 min on a gradient structured (GS) 316L SS [256]. (d) Changes in grain size, LAGB fraction, (e) and mechanical properties on an harmonic cellular structured 316L SS as a function of annealing temperature for 1 h, as well as (f) calculated differences on Cr and Mo contents between cell walls and cell interior as a function of annealing temperature and time [461].

The dynamic recovery and grain boundary mobility are less efficient in low-SFE materials (like SS) than in high-SFE materials [775]. However, some microstructural defects might influence the dynamic recovery of SS. The effect of hetero-interfaces formed by soft/hard zones, as well as the typical high density of defects (explained in detail for each kind of HS SS in section 4) as grain boundaries, twins, shear bands, stacking faults, dislocations, among other, should be considered due to the different thermal tolerances between them. From the above, the energy of different defects' boundaries is also an important factor to consider when increasing temperature. It is well reported that recovery and recrystallisation processes are preferentially initiated at high energy interfaces/boundaries. Thus, the presence of low-energy twins, LAGB or coherent second-phases [218] might contribute to the strengthening and thermal stabilisation of materials.

Considering that nano-twins have lower stored energy (commonly an order of magnitude smaller than HAGB), i.e., higher thermal stability than nano-grains determined by HAGB in

SS [25,218], the recrystallisation in HS SS occurs preferentially at the NG/UFG regions instead of at twin regions [21,770]. As a result, the nano-twin regions remained in the microstructure when the temperature increased, even when the NG zones mostly vanished [21]. Such microstructural evolution after annealing was deeply explained from Fig. 8 of previous section 4.1.

Besides, it is well reported that LAGB has lower energy than HAGB [218], which was also observed in an HS 316L with harmonic cellular structures elaborated by AM [461]. From Fig. 26(d), the LAGB showed thermal stability up to 1000 °C, while the grain delimited by HAGB remained stable up to 800 °C [461]. Furthermore, the microstructure remained stable with reduced strength to ductility trade-off even after annealing up to 600 °C, as can be seen in Fig. 26(e) [461]. However, annealing beyond 600 °C led to the gradual disappearance of cellular dislocation walls, also provoking the decrement of mechanical properties through the strength to ductility inverse relationship typical of homogeneous metallic materials [461]. Thus, the stability of the dislocation cells strongly affects the strength retention in the material [441]. The previous result was similar to the other cellular structure 316L SS produced by AM, which were stable after annealing up to 800-900 °C for 6 to 15 min [441,464,477]. In fact, the recrystallisation and grain growth took place just after the disappearance of the dislocation cellular structures, which implies its stabilisation effect.

The non-equilibrium high-angle grain boundaries might show higher mobility than nanotwinned and low-angle boundaries [776]. On the other hand, the coherent interphase boundaries (5–200 mJ m<sup>-2</sup>) are less energetic than the semi-coherent (200–800 mJ m<sup>-2</sup>) and

the incoherent (800–2,500 mJ m<sup>-2</sup>) ones [218]. This interface energy provides the thermal dynamic driving force for particle growth.

Coherent second phases in multiphase SS are more effective to restrict dislocation slip than their incoherent counterparts because they create higher lattice strains at the interphase. However, that increment of energy can reduce the thermostability of the alloy. For example, the dynamic dislocations recovery of an austenitic HS SS elaborated by HPT and 1 h annealing at temperatures from 400 to 900°C was encouraged by the high density of dislocations and the presence of Cu-rich UFG-precipitates [770]. The UFG size of the Cu particles suggested a low coherency with the matrix. However, Cu nanoparticles used to be coherent with the SS matrix [777,778]. As explained before, the coherent interfaces have low interface energy, which triggers high strain energy to act as resistance for precipitate growth. Thus, low interface energy and high strain energy can be expected when coherent Cu particles exist in the SS matrix, which leads to slow precipitate coarsening kinetics [777]. The resistance to particle coarsening when temperature increases is an important factor for particle pinning effect [767]. The kinetics of coarsening of pinning particles can be expressed by Eq. (6) [779].

$$r^3 - r_0^3 \propto D_f t \quad (6)$$

where  $r_0$  and  $r$  are the average initial and final radii, respectively, and  $t$  is the soaking time based on the diffusivity  $D_f$ . Moreover, grain growth kinetics can be decreased by drag solutes or pinning particles dispersed in the matrix [767,780]. A common example of the above is the delayed atomic diffusion in 316L SS due to its Mo content compared to 304 SS. Molybdenum is an  $\alpha$ -stabiliser that increases the minimum temperature for shear reversion

to occur [190]. This is the reason for the faster SIM reversion kinetics in 304L SS compared to that of 316L SS [206,207]. However, the increment of temperature allows a point where the impurities of SS can no longer restrict the diffusion and grain mobility. Thus, the concentration of solute atoms at the boundaries ( $c$ ) decreases as a function of the temperature, as indicated in Eq. (7) [767].

$$c \propto e^{\frac{U}{RT}} \quad (7)$$

where  $R$  is the gas constant,  $T$  is temperature, and  $U$  is the activation energy to move a vacancy. Thus, by increasing temperature, the completion of reversion (SIM to  $\gamma$ ) followed by the recrystallisation of the retained  $\gamma$  and grain growth can be accelerated in both 316L and 304L after  $\sim 1000$  °C [206,207,781]. Regarding the atomic diffusion of solute, the diffusion of Cr and Mo was simulated by CALPHAD for a harmonic cellular structure 316L SS at different temperatures and times [461]. The results are shown in Fig. 26(f), where the diffusion of Cr and Mo starts and finishes from about 650 °C to 850 °C. After annealing at 800 °C for 1 h, the chemical content differences between the cell wall and the cell interior are less than 0.4 at.% of Cr and 0.1 at.% of Mo. Both elements, Cr and Mo, are homogenised in the matrix below 900 °C. However, much longer annealing times are necessary for diffusion to occur at temperatures below 500 °C. As indicated in Fig. 26(f), 1000 h at 500 °C annealing could be necessary to detect a difference in the chemical composition between the cell wall and the cell interior due to diffusion of Cr and Mo [461].

The grain growth kinetics can be studied by the parabolic grain growth kinetics formula of Eq. (8) combined with the Arrhenius equation expressed by Eq. (9) [173,781–783]:

$$D - D_0 = K t^{\frac{1}{n}} \quad (8)$$

$$K = K_0 e^{\left(-\frac{Q}{RT}\right)} \quad (9)$$

where  $D$  is the average grain size after applying the temperature  $T$  for the time  $t$ ,  $D_0$  is the initial grain size,  $K_0$  is a constant,  $n$  is the grain growth exponent, and  $Q$  is the apparent activation energy for grain growth. The values of  $n$  and  $Q$  are the basis of kinetics grain growth analysis and can be experimentally determined by plotting the parabolic grain growth functions. From Eq. (8), it can be seen that  $n$  is expected to be high for small grain growth, i.e., for slow kinetics. During annealing, the temperature of the previous deformation step significantly affects the grain growth kinetics. For instance, Tikhonova et al. [784] reported  $n$  of  $\sim 2$  for 304 SS subjected to multidirectional forging at 600 °C and then annealed at 800 °C; whereas a larger  $n$  of  $\sim 4.6$  was obtained for the samples multidirectional forged at 800 °C. Moreover, the other influencing factors regarding the deviation of the kinetics parameters ( $n$  and  $Q$ ) from the expected values have been recently summarized [767]. However, the kinetics of grain growth has remained to be studied for HS SS.

More studies on the thermostability of HS SS are needed considering their multiple common factors as heterogeneous distributions of grain size, defects, hetero-interfaces of low and high energy, crystallographic texture, alloying elements, second phases, stress, segregation of solutes at boundaries, pinning particles, grain boundary mobility, diffusivity disparities, thermal coefficient disparities, and thermal conductivity disparities. Furthermore, the kinetics of abnormal grain growth requires experimental and modelling efforts to identify its origins and construct suitable models that contemplate all the previously mentioned



variables [767]. Regarding the origins, pinning particles, crystallographic texture, or distributions of grain boundaries with different mobilities have been pointed out as possible initiation points for abnormal grain growth [785–788]. However, these hypotheses should be systematically investigated. Machine learning might serve as a powerful tool for considering the multiple variables in the grain growth mechanisms.

### *8.3. Magnetic properties*

Stainless steels have not been used as magnetic materials since their magnetic capacity is always below that of conventional magnetic materials [789,790]. However, there are circumstances and applications where the accuracy of calculation of the magnetic properties is required, such as using SS in superconducting accelerator magnets for high energy physics [791]. It is well known that the fully austenitic SS grades are paramagnetic, while hard or permanent magnetic behaviours can be attributed to the presence of ferromagnetic structures (ferrite and/or martensite) [790,792–795]. Both the  $\gamma$  and the  $\varepsilon$ -martensite phases are paramagnetic (nonmagnetic), while  $\alpha'$ -martensite and delta ferrite phases are ferromagnetic (magnetic) phases [792,796]. During plastic deformation, most austenitic SS undergo a martensitic transformation from FCC-austenite phase to BCC-  $\alpha'$ -martensite through HCP- $\varepsilon$ -martensite as an intermediate structure [507]. Therefore, the magnetic properties of SS are strongly dependent on the plastic deformation-induced martensite transformation [789,797,798].

The magnetic properties of multiphase SS strongly depend on the fraction of magnetic (ferromagnetic) phases [795,798–800]. Saturation magnetization changes monotonically with the amount of magnetic phase in SS [795,796]. Consequently, magnetic characterization has been used to estimate the volume fraction of the  $\alpha'$ -martensite phase in SS [794,797,798,801]. The amount of ferromagnetic phase can be determined as a function of the saturation magnetization ( $M_s$ ). The formula of S. Tavares et al. [794,799,800] can be used for this purpose (Eq. (10)).

$$C_m = \frac{M_s}{M_i} \quad (10)$$

where  $C_m$  is the martensite volume fraction and  $M_i$  is the intrinsic saturation magnetization of the magnetic phase in a unit of  $\text{Am}^2/\text{kg}$  (or  $\text{emu/g}$ ). It was reported that the second phase precipitation in a hot-forged duplex 2304 SS by ageing treatment reduced the volume fraction of the martensite from 92% to about 68%, decreasing the magnetic properties [802].

In addition to the phase composition, the magnetic properties of SS are influenced by the microstructure and texture [795,803]. Generally, the magnetic properties of SS are mainly affected by grain size, shape, and distribution of  $\alpha'$ -martensite phase in the SS [796,801,803]. A large amount of martensite influences the magnetic saturation value, whereas the coercive force is an essential magnetic property that is influenced by particle size, shape and distribution of  $\alpha'$ -martensite [797,801]. Moreover, the minor-loop coefficient gives information about the size of  $\alpha'$ -martensite clusters and their interaction with the  $\gamma$ -austenitic matrix [796].

Recently, the magnetic properties of austenitic HLS 317L SS produced by CR and annealing were studied [793]. The CR 317L SS had about 2.3%  $\alpha'$ -martensite and 4% delta ferrite, while  $\gamma$  was the predominant phase. After CR, the SS had an HLS microstructure with eye-shaped nanostructures and elongated delta ferrite islands. The saturation magnetization changed significantly with annealing temperatures reaching higher magnetization at 400°C. After this temperature, both austenite reversion and delta ferrite transformation into a sigma (paramagnetic) phase occurred, and therefore,  $M_s$  decreased with increasing the annealing temperature. At the same time, the coercive force changed similarly to the saturation magnetization, except at 700°C, where a significant increase of coercive force was observed. Such magnetic anisotropy behaviour of the HLS 317L SS can be related to the fragmentation of the elongated delta ferrite islands [793,795].

In summary, the magnetic properties of HS SS are not clearly in the literature. More studies are needed to clarify the relationship between the magnetic properties of HS SS and its microstructural features. Therefore, extensive studies are required to investigate the influence of texture, residual stress, grain size, grain shape, twinning, dislocations, and hetero-interfaces regions on the magnetic behaviour of HS SS. Advanced simulation and modelling studies may be useful to predict and optimise the magnetic properties of HS SS.

## 9. Future directions

Each previous section of this review included particular opportunities for future studies. However, Fig. 27 illustrates the main general paths to boost the development of HS SS for multiple multidisciplinary applications. Those paths included the unknowns in fundamental physics of deformation and strengthening mechanisms, final properties, simulation efforts to design improved HSMs, and communication to motivate more international scientific groups to study and develop HSMs.

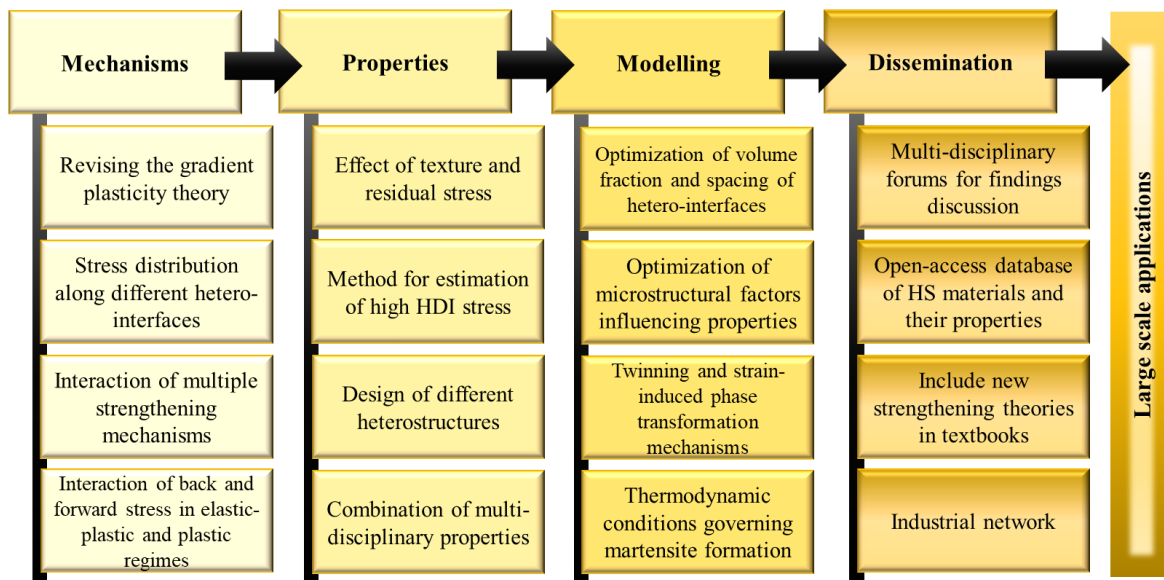


**Fig. 27.** Future directions for heterostructured (HS) stainless steel (SS) field.

The research on the fundamental physics of mechanisms to understand and design HS SS includes revising the strain gradient plasticity theory and supporting the improvements with experimental and modelling results. The following main point to be studied is the stress

distribution along different hetero-interfaces. Considering that different hetero-interfaces can be formed among boundaries with different energies, such as HAGBs, LAGBs, hard/soft zones, twinning, second phases, shear bands, stacking faults, etc., the HBAR defined by the stress distribution might be different for each particular kind of HS SS. Besides, cellular dislocation networks in the AM SS [433–435] are formed by high dislocation density arrangements within zones of similar chemical composition, crystalline structure, and grain sizes (explained in section 4.5). Different from the “typical” hard/soft hetero-interfaces of HS SS, in which the back stress is formed in the soft region and consequent forward stress is formed in the hard zone (explained in section 2), the cellular structures are constituted by soft/hard (dislocation network)/soft regions. Thus, the magnitude and the distribution of stress through the cellular borders are unclear.

On the other hand, the interaction among the multiple strengthening mechanisms in HS SS (solid solution, dislocation accumulation, second phases dispersion, HDI, twinning, and strain-induced phase transformation) should be further studied to determine their mutual influence on the microstructural evolution and final properties of HS SS.

For last, from section 2, the formation and interaction of back and forward stress during the elastic-plastic and plastic regimes are crucial for tailoring and optimising the processing-microstructure-properties relationship of HS SS. It has been reported that there is not a continuous linear increment of HDI with the strain applied to HS SS [99,567]. The fast increment of back stress in the elastic-plastic regimen and slower in the plastic one should be

revised and explained [20,46,486]. Besides, it is not clear how back and forward stress interact to produce the HDI stress.

Understanding these issues will allow describing the fundamental physics and processing-microstructure-properties relationship of HSMs. Furthermore, like SS, most HSMs studied until now have been on the FCC system. Efforts to study the deformation and strengthening mechanisms on HSMs with crystalline structures different from FCC are also needed. This may improve the designing and final properties of multiphase or LS SS materials with phases of different crystalline systems.

In terms of properties of HS SS, systematic studies of texture and residual stress effects on different properties such as mechanical, corrosion, magnetic, thermic, biological, etc., are needed. Additionally, improved routes for estimating HDI stress can also be designed. The unloading-reloading method for estimating the HDI stress (Fig. 5, section 2.3) considers that the GND structures are reversible during the unloading-reloading cycle [19], which may not satisfy materials with high HDI stress. The design of an improved route for estimating HDI stress will also enhance the study of HS SS properties.

The design of new HSMs through innovative combinations of conventional thermomechanical processes or by designing new processing methods also remains for future developments. As illustrated in Fig. 28(a) and explained in section 3, the outstanding mechanical properties of HS SS can be exploited for several multidisciplinary purposes as biomedical, biosafety, automotive, aeronautic, architectural, optoelectronics, energy-conversion, tribology, nuclear, structural, magnetic, food-processing, daily uses, sensors,

among others [4–6]. Some examples are the design of antimicrobial, corrosion-resistant, magnetic, or biocompatible alloys combined with the superior mechanical performance of HS SS. Those studies should be based on the different low-cost and large-scalable thermomechanical routes to ensure the cost-effectivity of the HS SS.

Besides, the heterogeneous nature of HSMs allows exploring plenty of microstructural disparities, like heterogeneous grain size, density of defects, crystallographic texture, as well as chemical, magnetic, electrochemical, electric, thermic, biological, among other disparities (Fig. 28(b)). As a result, the HSMs, including HS SS, are promising to reduce multiple typical trade-offs of the materials science field. As seen in section 6, the trade-off that has gained the most attention from the HSM community is the typical increase in strength with a decrease in ductility, or inverse. However, there are other several trade-offs to overcome (Fig. 28(b)) by adding different disparities to materials. The authors of this review encourage the scientific community to join multidisciplinary research efforts and develop improved HS devices to improve or replace the conventional ones.

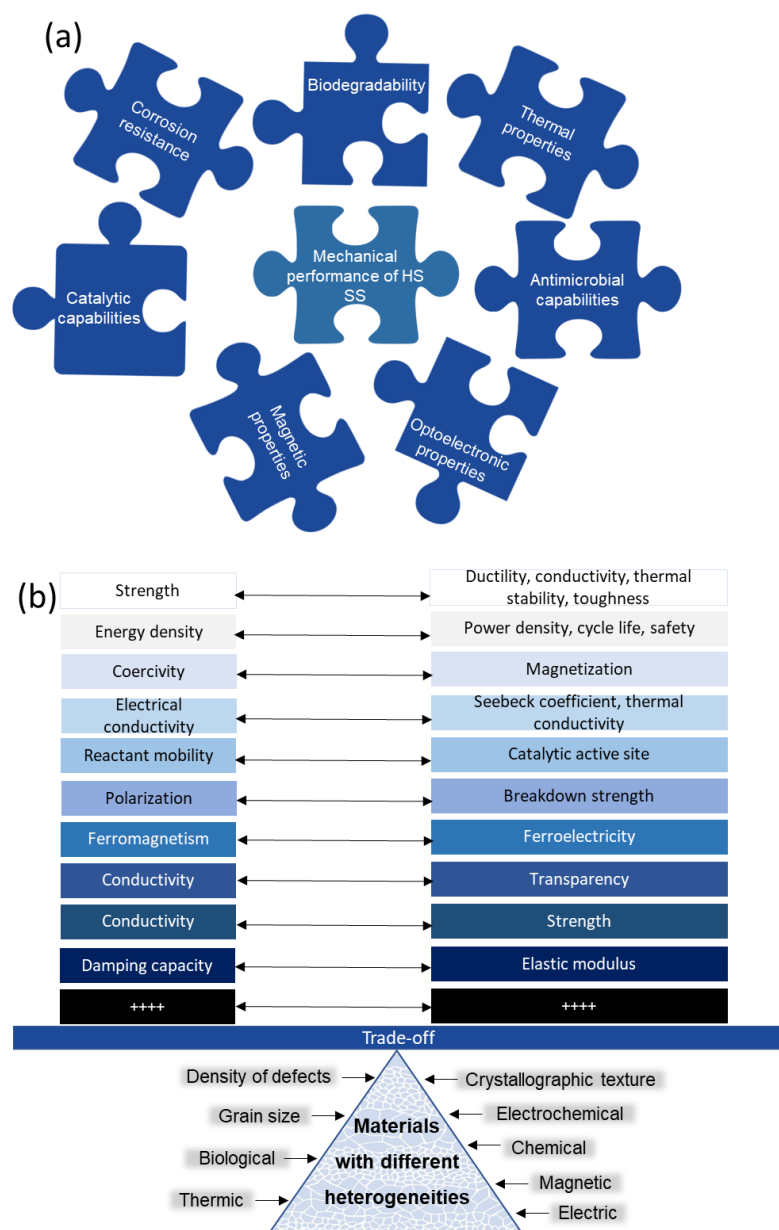


**Fig. 28.** Future perspectives for designing multifunctional heterostructured (HS) materials by (a) combining the outstanding mechanical properties of HS stainless steel (SS) with different multidisciplinary properties and (b) by combining different kind of disparities to reduce typical trade-offs (adapted from [3,804]).



Considering that modelling is a powerful tool to predict and optimise materials' behaviour, there is plenty of work in emerging fields such as HSMs. The advanced modelling methods can study the deformation and strengthening mechanisms of HSMs to predict and design improved materials. Further development of the models is also necessary to reproduce the microstructure evolution and mechanical responses in the more realistic time and length scales. For instance, although the current FE model can reproduce the effect of grain size and distribution on strengthening mechanisms that are controlled by intragranular dislocation plasticity in polycrystals, it is still challenging to simultaneously track the movement of grain boundaries. Since shear rotation, migration of grain boundaries, and deformation-induced grain growth can occur in polycrystalline materials, it is essential to develop advanced continuum modelling techniques further.

Optimising the volume fraction, density and space between hetero-interfaces to maximise the mechanical properties of HSMs also remains for further simulation efforts. Other microstructural factors such as texture, residual stress, grain size, grain morphology, twinning and SIM can also be modelled to predict their effect on different properties of HSMs. The PF model has been widely used to study the microstructure evolution as well as the deformation behaviour (e.g., crack propagation, etc.). However, the large-scale simulation requires high computing resources and is time-consuming. Similarly, MD simulation is powerful to depict the detailed deformation processes in multiscale, including dislocations, twinning, and grain boundary activities. Nevertheless, due to the limitation of computing capacity, most MD simulations are conducted with grain size of  $\sim 10$  nm, which is far smaller than multiple HS

SS systems with nanometric to micrometric grains. Therefore, combined with advanced computing techniques, it will be promising to increase the scale and accuracy of such models. In addition, integrating the novel machine learning approach with the physical or atomic model is another promising way to study and optimise the microstructure and properties of advanced materials [805].

For a complete HSMs development scheme, the dissemination of findings, exchanging ideas, and establishing multidisciplinary collaborations are necessary actions to promote HSMs applications. Some forums to discuss heterogeneous materials have been created, such as the symposia “Tailoring Mechanical Incompatibility for Superior Properties”, “Heterogeneous and Gradient Materials”, and “Heterogeneous Materials” during the Annual Meeting of The Minerals, Metals & Materials Society (TMS) 2016 and 2019, and the Gordon Research Conference, 2019. However, the fast-growing HSMs field requires a specialized forum dedicated to this topic. In response to this need, the First International Conference on Heterostructured Materials (HSM I) will be held in July 2022. Simultaneously, the creation of free-access updated textbooks and databases with the last findings of HSMs may trigger the understanding of this emerging field and motivate new generations of young researchers toward its study. Considering that the last aim of new materials development is their applications to solve real industrial problems, creating industrial forums to exploit and disseminate the cost-benefit of HSMs applications is also necessary.

## **Funding**

This review article was made possible with funding support from various sources. This work was supported by the Ministry of Science and Technology of China (2021YFA1200202), the National Natural Science Foundation of China (11988103), the Hong Kong Research Grants Council (GRF 11214121), the Hong Kong Institute for Advanced Study (HKIAS), and City University of Hong Kong (CityU). M.C.R. was supported by the Fundação de Amparo a Pesquisa do Estado de São Paulo (grant 2021/03865-9). T.Y. was supported by the Hong Kong Research Grant Council (RGC) with CityU grant 21205621. I.J.B acknowledges support by the U.S. Dept. of Energy, Office of Basic Energy Sciences Program DE-SC0018901. J.C.H. acknowledges support by the HKIAS under the project number 9360157. T.G.L. was supported by the European Research Council under ERC Grant Agreement No. 267464-SPDMETALS.

## **Acknowledgements**

Fruitful discussions with Prof Gonzalo Gonzalez Reyes from IIM-UNAM and Dr Manmohan Jain from CINVESTAV-IPN are gratefully acknowledged. Hamed Mirzadeh would like to greatly thank the members of the Advanced Steels and Thermomechanically Processed Engineering Materials Laboratory of University of Tehran for their help and support.

## **Conflict of interest**

The authors declare that they have no known competing financial interests or personal relationships that could have appeared to influence the work reported in this paper.

## **References**

- [1] K. Lu, J. Lu, *J. Mater. Sci. Technol.* 15 (1999) 193–197.
- [2] X. Wu, M. Yang, F. Yuan, G. Wu, Y. Wei, X. Huang, Y. Zhu, *Proc. Natl. Acad. Sci. U. S. A.* 112 (2015) 14501–14505.
- [3] X. Zhang, *Mater. Res. Lett.* 8 (2020) 49–59.
- [4] Y. Zhu, K. Ameyama, P.M. Anderson, I.J. Beyerlein, H. Gao, H.S. Kim, E. Lavernia, S. Mathaudhu, H. Mughrabi, R.O. Ritchie, N. Tsuji, X. Zhang, X. Wu, *Mater. Res. Lett.* 9 (2021) 1–31.
- [5] Y. Zhu, *Metall. Mater. Trans. A* 52A (2021) 4715–4726.
- [6] S. Suresh, *Science* (80-. ). 292 (2001) 2447–2451.
- [7] D. Jiao, Z.Q. Liu, R.T. Qu, Z.F. Zhang, *Mater. Sci. Eng. C* 59 (2016) 828–837.
- [8] A.R. Studart, *Adv. Funct. Mater.* 23 (2013) 4423–4436.
- [9] S.E. Naleway, M.M. Porter, J. McKittrick, M.A. Meyers, *Adv. Mater.* 27 (2015) 5455–5476.

- [10] P. Fratzl, R. Weinkamer, *Prog. Mater. Sci.* 52 (2007) 1263–1334.
- [11] Z. Liu, M.A. Meyers, Z. Zhang, R.O. Ritchie, *Prog. Mater. Sci.* 88 (2017) 467–498.
- [12] J.D. Verhoeven, A.H. Pendray, W.E. Dauksch, *JOM* 50 (1998) 58–64.
- [13] J.D. Verhoeven, *Metallurgy of Steel for Bladesmiths & Others Who Heat Treat and Forge Steel*, 2005.
- [14] J. Wadsworth, O.D. Sherby, *Prog. Mater. Sci.* 25 (1980) 35–68.
- [15] M.R. Notis, *Mater. Charact.* 45 (2000) 253–258.
- [16] M. Yaso, T. Takaiwa, Y. Minagi, T. Kanaizumi, K. Kubota, T. Hayashi, S. Morito, T. Ohba, *J. Alloys Compd.* 577 (2013) S690–S694.
- [17] X. Wu, Y. Zhu, *Mater. Res. Lett.* 5 (2017) 527–532.
- [18] R. Xu, G. Fan, Z. Tan, G. Ji, C. Chen, B. Beausir, D.B. Xiong, Q. Guo, C. Guo, Z. Li, D. Zhang, *Mater. Res. Lett.* 6 (2018) 113–120.
- [19] M. Yang, Y. Pan, F. Yuan, Y. Zhu, X. Wu, *Mater. Res. Lett.* 4 (2016) 145–151.
- [20] Y. Zhu, X. Wu, *Mater. Res. Lett.* 7 (2019) 393–398.
- [21] J. Li, Y. Cao, B. Gao, Y. Li, Y. Zhu, *J. Mater. Sci.* 53 (2018) 10442–10456.
- [22] A.T. Krawczynska, P. Suchecki, B. Adamczyk-Cieslak, B. Romelczyk-Baishya, M. Lewandowska, *Mater. Sci. Eng. A* 767 (2019) 138381.
- [23] J. Li, B. Gao, Z. Huang, H. Zhou, Q. Mao, Y. Li, *Vacuum* 157 (2018) 128–135.

- [24] I. Üçok, T. Ando, N.J. Grant, *Mater. Sci. Eng. A* 133 (1991) 284–287.
- [25] F.K. Yan, G.Z. Liu, N.R. Tao, K. Lu, *ACTA Mater.* 60 (2012) 1059–1071.
- [26] Z.J. Zheng, J.W. Liu, Y. Gao, *Mater. Sci. Eng. A* 680 (2017) 426–432.
- [27] D. Molnár, X. Sun, S. Lu, W. Li, G. Engberg, L. Vitos, *Mater. Sci. Eng. A* 759 (2019) 490–497.
- [28] E. Ulvan, A. Koursaris, *Metall. Trans. A, Phys. Metall. Mater. Sci.* 19 A (1988) 2287–2298.
- [29] J.S. Li, W.D. Gao, Y. Cao, Z.W. Huang, B. Gao, Q.Z. Mao, Y.S. Li, *Adv. Eng. Mater.* 20 (2018) 1–9.
- [30] L. Chen, X.L. Wu, *Mater. Sci. Forum* 682 (2011) 123–130.
- [31] Q. He, Y.F. Wang, M.S. Wang, F.J. Guo, Y. Wen, C.X. Huang, *Mater. Sci. Eng. A* 780 (2020) 139146 Contents.
- [32] Q. He, W. Wei, M. Wang, F. Guo, Y. Zhai, Y. Wang, C. Huang, *Nanomaterials* 11 (2021) 2356–2367.
- [33] X.H. Yang, W.Z. Dui, G. Liu, *Key Eng. Mater.* 353–358 (2007) 1810–1813.
- [34] C. Tan, Y. Chew, F. Weng, S. Sui, F.L. Ng, T. Liu, G. Bi, *Int. J. Mach. Tools Manuf.* 172 (2022) 103817.
- [35] J. He, L. Chen, Z. Guo, H. Zhi, S. Antonov, Y. Su, *Mater. Sci. Eng. A* 793 (2020) 139835.

- [36] H.Y. Yi, F.K. Yan, N.R. Tao, K. Lu, *Mater. Sci. Eng. A* 647 (2015) 152–156.
- [37] H.Y. Yi, F.K. Yan, N.R. Tao, K. Lu, *Scr. Mater.* 114 (2016) 133–136.
- [38] J. Li, C. Fang, Y. Liu, Z. Huang, S. Wang, Q. Mao, Y. Li, *Mater. Sci. Eng. A* 742 (2019) 409–413.
- [39] G.Z. Liu, N.R. Tao, K. Lu, *J. Mater. Sci. Technol.* 26 (2010) 289–292.
- [40] R. Zheng, M. Liu, Z. Zhang, K. Ameyama, C. Ma, *Scr. Mater.* 169 (2019) 76–81.
- [41] Z. Zhang, S.K. Vajpai, D. Orlov, K. Ameyama, *Mater. Sci. Eng. A* 598 (2014) 106–113.
- [42] Z. Zhang, D. Orlov, S.K. Vajpai, B. Tong, K. Ameyama, *Adv. Eng. Mater.* 17 (2015) 791–795.
- [43] O.P. Ciuca, M. Ota, S. Deng, K. Ameyama, *Mater. Trans.* 54 (2013) 1629–1633.
- [44] S. Sabooni, F. Karimzadeh, M.H. Enayati, A.H.W. Ngan, *Mater. Sci. Eng. A* 636 (2015) 221–230.
- [45] B. Ravi Kumar, D. Raabe, *Scr. Mater.* 66 (2012) 634–637.
- [46] B. Flipon, C. Keller, L.G. de la Cruz, E. Hug, F. Barbe, *Mater. Sci. Eng. A* 729 (2018) 249–256.
- [47] J. Yanagimoto, T. Oya, S. Kawanishi, N. Tiesler, T. Koseki, *CIRP Ann. - Manuf. Technol.* 59 (2010) 287–290.

- [48] Y. Liu, J. Yang, H. Yang, K. Li, Y. Qiu, W. Zhang, S. Zhou, *Surf. Coatings Technol.* 428 (2021) 127868.
- [49] A. Chen, J. Liu, H. Wang, J. Lu, Y.M. Wang, *Mater. Sci. Eng. A* 667 (2016) 179–188.
- [50] S. Ghosh, N. Bibhanshu, S. Suwas, K. Chatterjee, *Mater. Sci. Eng. A* 820 (2021) 141540.
- [51] J. Yang, L. Xu, H. Gao, X. Li, H. Pan, B. Shu, T. Itoh, Y. Zhu, X. Zhu, *Mater. Sci. Eng. A* 826 (2021) 141963.
- [52] B. Zhang, F. Xue, S.L. Li, X.T. Wang, N.N. Liang, Y.H. Zhao, G. Sha, *ACTA Mater.* 140 (2017) 388–397.
- [53] M.C. Somani, M. Jaskari, S. Sadeghpour, C. Hu, R.D.K. Misra, T.T. Nyo, C. Yang, L.P. Karjalainen, *Mater. Sci. Eng. A* 793 (2020) 139885.
- [54] A. Kisko, A.S. Hamada, J. Talonen, D. Porter, L.P. Karjalainen, *Mater. Sci. Eng. A* 657 (2016) 359–370.
- [55] G.S. Sun, J. Hu, B. Zhang, L.X. Du, *Mater. Sci. Eng. A* 732 (2018) 350–358.
- [56] X. Ma, C. Huang, J. Moering, M. Ruppert, H.W. Höppel, M. Göken, J. Narayan, Y. Zhu, *ACTA Mater.* 116 (2016) 43–52.
- [57] J.S. Carpenter, S.C. Vogel, J.E. Ledonne, D.L. Hammon, I.J. Beyerlein, N.A. Mara, *ACTA Mater.* 60 (2012) 1576–1586.



- [58] C.W. Schmidt, M. Ruppert, H.W. Höppel, F. Nachtrab, A. Dietrich, R. Hanke, M. Göken, *Adv. Eng. Mater.* 14 (2012) 1009–1017.
- [59] J.S. Carpenter, S.J. Zheng, R.F. Zhang, S.C. Vogel, I.J. Beyerlein, N.A. Mara, *Philos. Mag.* 93 (2013) 718–735.
- [60] N. Copper, T.H. Fang, W.L. Li, N.R. Tao, K. Lu, *Science* (80-. ). 331 (2011) 1587–1590.
- [61] Y.S. Li, N.R. Tao, K. Lu, *ACTA Mater.* 56 (2008) 230–241.
- [62] X.H. Zhao, D.W. Nie, D.S. Xu, Y. Liu, C.H. Hu, *Tribol. Trans.* 62 (2019) 189–197.
- [63] S. Zharebtsov, E. Kudryavtsev, S. Kostjuchenko, S. Malysheva, G. Salishchev, *Mater. Sci. Eng. A* 536 (2012) 190–196.
- [64] D. Orlov, Y. Todaka, M. Umemoto, N. Tsuji, *Scr. Mater.* 64 (2011) 498–501.
- [65] W. Yinmin, C. Mingwei, Z. Fenghua, M. En, *Nature* 419 (2002) 912.
- [66] H. Jin, D.J. Lloyd, *Scr. Mater.* 50 (2004) 1319–1323.
- [67] M.C. Zhao, F. Yin, T. Hanamura, K. Nagai, A. Atrens, *Scr. Mater.* 57 (2007) 857–860.
- [68] Y. Cao, S. Ni, X. Liao, M. Song, Y. Zhu, *Mater. Sci. Eng. R Reports* 133 (2018) 1–59.
- [69] R.Z. Valiev, Y. Estrin, Z. Horita, T.G. Langdon, M.J. Zehetbauer, Y. Zhu, *JOM* 68 (2016) 1216–1226.

- [70] T.C. Lowe, Y.T. Zhu, *Adv. Eng. Mater.* 5 (2003) 373–378.
- [71] I.A. Ovid'ko, R.Z. Valiev, Y.T. Zhu, *Prog. Mater. Sci.* 94 (2018) 462–540.
- [72] R.O. Ritchie, *Nat. Mater.* 10 (2011) 817–822.
- [73] C.X. Huang, Y.F. Wang, X.L. Ma, S. Yin, H.W. Höppel, M. Göken, X.L. Wu, H.J. Gao, Y.T. Zhu, *Mater. Today* 21 (2018) 713–719.
- [74] L. Ke, *Science* (80-. ). 345 (2014) 1455–1456.
- [75] X. Li, L. Lu, J. Li, X. Zhang, H. Gao, *Nat. Rev. Mater.* 5 (2020) 706–723.
- [76] X. Wu, Y. Zhu, *MRS Bull.* 46 (2021) 244–249.
- [77] H. Lyu, M. Hamid, A. Ruimi, H.M. Zbib, *Int. J. Plast.* 97 (2017) 46–63.
- [78] Z.K. Li, X.T. Fang, Y.F. Wang, P. Jiang, J.J. Wang, C.M. Liu, X.L. Wu, Y.T. Zhu, C.C. Koch, *Mater. Sci. Eng. A* 777 (2020) 139074 Contents.
- [79] S.Z. Han, E.A. Choi, S.H. Lim, S. Kim, J. Lee, *Prog. Mater. Sci.* 117 (2021) 100720.
- [80] X. Wu, Y. Zhu, *Heterostructured Materials: Novel Materials with Unprecedented Mechanical Properties*, 1st ed., Jenny Stanford, 2021.
- [81] L. Gardner, *Thin-Walled Struct.* 141 (2019) 208–216.
- [82] A. Hemmasian Ettefagh, S. Guo, J. Raush, *Addit. Manuf.* 37 (2021) 101689.
- [83] R.T. Loto, *J. Bio- Tribo-Corrosion* 3 (2017) 1–8.
- [84] *Stainless Steel in Figures 2020*, 2020.

- [85] A.I.H. Committee, Properties and Selection: Irons, Steels, and High Performance Alloys, 10 th, ASM International, 1990.
- [86] M. Okayasu, D. Ishida, Metall. Mater. Trans. A Phys. Metall. Mater. Sci. 50 (2019) 1380–1388.
- [87] J. You, S. Kim, J. Oh, H. Choi, M. Jih, J. Dent. Anesth. Pain Med. 17 (2017) 225–229.
- [88] S. Seon, B. Lee, B. Choi, J. Ohe, J. Lee, J. Jung, B. Hwang, M. Kim, Y. Kwon, Maxillofac. Plast. Reconstr. Surg. 43 (2021) 1–6.
- [89] S. Acham, A. Truschnegg, P. Rugani, B. Kirnbauer, K.E. Reinbacher, W. Zemmann, L. Kqiku, N. Jakse, Clin. Oral Investig. 23 (2019) 1109–1119.
- [90] Y.B. Lei, Z.B. Wang, B. Zhang, Z.P. Luo, J. Lu, K. Lu, ACTA Mater. 208 (2021) 116773.
- [91] S. Gollapudi, Corros. Sci. 62 (2012) 90–94.
- [92] K.D. Ralston, N. Birbilis, Corrosion 66 (2010) 0750051–07500513.
- [93] X. Wu, Y. Zhu, K. Lu, Scr. Mater. 186 (2020) 321–325.
- [94] X. Feaugas, ACTA Mater. 47 (1999) 3617–3632.
- [95] F. Mompiau, D. Caillard, M. Legros, H. Mughrabi, ACTA Mater. 60 (2012) 3402–3414.
- [96] H. Mughrabi, Philos. Mag. 86 (2006) 4037–4054.

- [97] J.D. Eshelby, F.C. Frank, F.R.N. Nabarro, London, Edinburgh, Dublin Philos. Mag. J. Sci. 42 (1951) 351–364.
- [98] Z. Cheng, H. Zhou, Q. Lu, H. Gao, L. Lu, Science (80-. ). 362 (2018) eaau1925.
- [99] X.L. Wu, P. Jiang, L. Chen, J.F. Zhang, F.P. Yuan, Y.T. Zhu, Mater. Res. Lett. 2 (2014) 185–191.
- [100] C. Sawangrat, S. Kato, D. Orlov, K. Ameyama, J. Mater. Sci. 49 (2014) 6579–6585.
- [101] K. Park, M. Nishiyama, N. Nakada, T. Tsuchiyama, S. Takaki, Mater. Sci. Eng. A 604 (2014) 135–141.
- [102] M. Calcagnotto, Y. Adachi, D. Ponge, D. Raabe, ACTA Mater. 59 (2011) 658–670.
- [103] X.L. Wu, M.X. Yang, F.P. Yuan, L. Chen, Y.T. Zhu, ACTA Mater. 112 (2016) 337–346.
- [104] T. Huang, M. Zhan, Y. Pei, N. Xiang, F. Yang, Y. Li, J. Guo, X. Chen, F. Chen, JOM 71 (2019) 3962–3970.
- [105] X. Hu, S. Jin, H. Zhou, Z. Yin, J. Yang, Y. Gong, Y. Zhu, G. Sha, X. Zhu, Metall. Mater. Trans. A Phys. Metall. Mater. Sci. 48 (2017) 3943–3950.
- [106] J. Bauschinger, Zivilingenieur 27 (1881) 289–348.
- [107] X. Liu, F. Yuan, Y. Zhu, X. Wu, Scr. Mater. 150 (2018) 57–60.
- [108] M.X. Yang, R.G. Li, P. Jiang, F.P. Yuan, Y.D. Wang, Y.T. Zhu, X.L. Wu, Mater. Res. Lett. 7 (2019) 433–438.

- [109] H. Kato, R. Moat, T. Mori, K. Sasaki, P. Withers, *ISIJ Int.* 54 (2014) 1715–1718.
- [110] R.E. Stoltz, R.M. Pelloux, *Metall. Trans. A* 7 (1976) 1295–1306.
- [111] A.P. Reynolds, J.S. Lyons, *Metall. Mater. Trans. A Phys. Metall. Mater. Sci.* 28 (1997) 1205–1211.
- [112] M.X. Yang, F.P. Yuan, Q.G. Xie, Y.D. Wang, E. Ma, X.L. Wu, *ACTA Mater.* 109 (2016) 213–222.
- [113] C. Zhou, R. Lesar, *Comput. Mater. Sci.* 54 (2012) 350–355.
- [114] Y. Xiang, J.J. Vlassak, *Scr. Mater.* 53 (2005) 177–182.
- [115] Y. Xiang, J.J. Vlassak, *ACTA Mater.* 54 (2006) 5449–5460.
- [116] O.B. Pedersen, L.M. Brown, W.M. Stobbs, *Acta Metall.* 29 (1981) 1843–1850.
- [117] J.I. Dickson, J. Boutin, L. Handfield, *Mater. Sci. Eng.* 64 (1984) 7–11.
- [118] B. Fournier, M. Sauzay, C. Caës, M. Noblecourt, M. Mottot, *Mater. Sci. Eng. A* 437 (2006) 183–196.
- [119] T.H. Simm, *Crystals* 8 (2018) 212.
- [120] A. Das, *Metall. Mater. Trans. A Phys. Metall. Mater. Sci.* 47 (2016) 748–768.
- [121] H.W. Zhang, Z.K. Hei, G. Liu, J. Lu, K. Lu, *ACTA Mater.* 51 (2003) 1871–1881.
- [122] C.G. Rhodes, A.W. Thompson, *Metall. Trans. A* 8 (1977) 1901–1906.
- [123] G. Faraji, H.S. Kim, H.T. Kashi, *Sev. Plast. Deform.* (2018) 19–36.

- [124] A. Abel, H. Muir, *Philos. Mag.* 27 (1973) 585–594.
- [125] X. Lou, P.L. Andresen, R.B. Rebak, *J. Nucl. Mater.* 499 (2018) 182–190.
- [126] A. Shamsolhodaei, J.P. Oliveira, N. Schell, E. Maawad, B. Panton, Y.N. Zhou, *Intermetallics* 116 (2020) 106656.
- [127] T. Pasang, S.S. Pramana, M. Kracum, W.Z. Misiolek, M. Aziziderouei, M. Mizutani, O. Kamiya, *Metals (Basel)*. 8 (2018) 863;
- [128] A.C. Stauffer, D.A. Koss, J.B. Mckirgan, *Metall. Mater. Trans. A* 35A (2003) 1317–1324.
- [129] J.Y. Huang, Y.T. Zhu, H. Jiang, T.C. Lowe, *ACTA Mater.* 49 (2001) 1497–1505.
- [130] I. Gutierrez-Urrutia, D. Raabe, *ACTA Mater.* 59 (2011) 6449–6462.
- [131] V. Gerold, H.P. Karnthaler, *Acta Metall.* 37 (1989) 2177–2183.
- [132] T. Yang, Y.L. Zhao, Y. Tong, Z.B. Jiao, J. Wei, J.X. Cai, X.D. Han, D. Chen, A. Hu, J.J. Kai, K. Lu, Y. Liu, C.T. Liu, *Science (80-. )*. 362 (2018) 933–937.
- [133] J. Lu, L. Hultman, E. Holmström, K.H. Antonsson, M. Grehk, W. Li, L. Vitos, A. Golpayegani, *ACTA Mater.* 111 (2016) 39–46.
- [134] B.C. De Cooman, Y. Estrin, S.K. Kim, *ACTA Mater.* 142 (2018) 283–362.
- [135] S. Allain, J.P. Chateau, O. Bouaziz, S. Migot, N. Guelton, *Mater. Sci. Eng. A* 387–389 (2004) 158–162.

- [136] K.H. Lo, C.H. Shek, J.K.L. Lai, *Mater. Sci. Eng. R Reports* 65 (2009) 39–104.
- [137] C. Ye, A. Telang, A.S. Gill, S. Suslov, Y. Idell, K. Zweiacker, J.M.K. Wiezorek, Z. Zhou, D. Qian, S.R. Mannava, V.K. Vasudevan, *Mater. Sci. Eng. A* 613 (2014) 274–288.
- [138] X. Zhou, X.Y. Li, K. Lu, *Scr. Mater.* 153 (2018) 6–9.
- [139] M. Niinomi, M. Nakai, J. Hieda, *Acta Biomater.* 8 (2012) 3888–3903.
- [140] G. Manivasagam, D. Dhinasekaran, A. Rajamanickam, *Recent Patents Corros. Sci.* 2 (2010) 40–54.
- [141] Y. Ren, H. Zhao, W. Liu, K. Yang, *Mater. Sci. Eng. C* 60 (2016) 293–297.
- [142] S.F. Yang, C.W. Li, A.Y. Chen, B. Gan, J.F. Gu, *J. Manuf. Process.* 65 (2021) 418–427.
- [143] V.M. Linton, N.J. Laycock, S.J. Thomsen, A. Klumpers, 11 (2004) 243–256.
- [144] M.S. Kumar, M. Sujata, M.A. Venkataswamy, S.K. Bhaumik, 15 (2008) 497–504.
- [145] K. Ravindranath, R. Alazemi, *Eng. Fail. Anal.* 102 (2019) 79–86.
- [146] R.W. Fuller, J.Q.E. Jr, W.F. Heard, S.D. Robert, R.D. Stinson, K. Solanki, M.F. Horstemeyer, 15 (2008) 835–846.
- [147] D.M. Marulanda, D. Toro, F.E. Castillejo, J.J. Olaya, 26 (2018) 440–447.
- [148] T. Roland, D. Retraint, K. Lu, J. Lu, 54 (2006) 1949–1954.

- [149] R.K. Gupta, N. Birbilis, *Corros. Sci.* 92 (2015) 1–15.
- [150] J. Li, Q. Mao, J. Nie, Z. Huang, S. Wang, Y. Li, *Mater. Sci. Eng. A* 754 (2019) 457–460.
- [151] K. Hajizadeh, H. Maleki-Ghaleh, A. Arabi, Y. Behnamian, E. Aghaie, A. Farrokhi, M.G. Hosseini, M.H. Fathi, *Surf. Interface Anal.* 47 (2015) 978–985.
- [152] J. Li, Q. Mao, M. Chen, W. Qin, X. Lu, T. Liu, D. She, J. Kang, G. Wang, X. Zhu, Y. Li, *J. Mater. Res. Technol.* 10 (2021) 132–137.
- [153] X. Sun, F. Chen, H. Huang, J. Lin, X. Tang, *Appl. Surf. Sci.* 467–468 (2019) 1134–1139.
- [154] G. Meric de Bellefon, K.M. Bertsch, M.R. Chancey, Y.Q. Wang, D.J. Thoma, J. *Nucl. Mater.* 523 (2019) 291–298.
- [155] S.W. Baek, E.J. Song, J.H. Kim, M. Jung, U.B. Baek, S.H. Nahm, *Scr. Mater.* 130 (2017) 87–90.
- [156] D. Kong, C. Dong, X. Ni, L. Zhang, H. Luo, R. Li, L. Wang, C. Man, X. Li, *Corros. Sci.* 166 (2020) 108425.
- [157] H. Cetinel, B. Uyulgan, C. Tekmen, I. Ozdemir, E. Celik, *Surf. Coatings Technol.* 174–175 (2003) 1089–1094.
- [158] L. Chen, D. Zhang, Y. Chen, F. Liu, J. Zhang, M. Fu, J. Wu, D. Ye, *Chemosphere In Press* (2021) 132778.



- [159] J. Xuan, L. Xu, S. Bai, T. Zhao, Y. Xin, G. Zhang, L. Xue, L. Li, *Int. J. Hydrogen Energy* 46 (2021) 22920–22931.
- [160] J.K. Du, C.Y. Chao, L.L. Wei, C.H. Wang, J.H. Chen, K.K. Chen, R. Bin Huang, *Metals (Basel)*. 11 (2021) 1–14.
- [161] L.T. Liu, Y.Z. Li, K.P. Yu, M.Y. Zhu, H. Jiang, P. Yu, M.X. Huang, *Mater. Res. Lett.* 9 (2021) 270–277.
- [162] C.F. Huang, H.J. Chiang, W.C. Lan, H.H. Chou, K.L. Ou, C.H. Yu, *Biofouling* 27 (2011) 449–457.
- [163] L. Ren, L. Nan, K. Yang, *Mater. Des.* 32 (2011) 2374–2379.
- [164] D. Zhang, L. Ren, Y. Zhang, N. Xue, K. Yang, M. Zhong, *Colloids Surfaces B Biointerfaces* 105 (2013) 51–57.
- [165] K. Yang, M. Lu, *J. Mater. Sci. Technol.* 23 (2007) 333–336.
- [166] K.K. Chen, C.Y. Chao, J.H. Chen, J.H. Wu, Y.H. Chang, J.K. Du, *Metals (Basel)*. 11 (2021) 1–8.
- [167] F. Luo, Z. Tang, S. Xiao, Y. Xiang, *Mater. Technol.* 34 (2019) 525–533.
- [168] H. Dong, Z.C. Li, M.C. Somani, R.D.K. Misra, *J. Mech. Behav. Biomed. Mater.* 119 (2021) 104489 Contents.
- [169] Y. Zhang, C. Wang, K.M. Reddy, W. Li, X. Wang, *ACTA Mater.* 226 (2022) 117670.

- [170] G. Sun, L. Du, J. Hu, B. Zhang, R.D.K. Misra, *Mater. Sci. Eng. A* 746 (2019) 341–355.
- [171] M. Shirdel, H. Mirzadeh, M.H. Parsa, *Mater. Charact.* 103 (2015) 150–161.
- [172] I. Shakhova, V. Dudko, A. Belyakov, K. Tsuzaki, R. Kaibyshev, *Mater. Sci. Eng. A* 545 (2012) 176–186.
- [173] M. Odnobokova, A. Belyakov, N. Enikeev, D.A. Molodov, R. Kaibyshev, *Mater. Sci. Eng. A* 689 (2017) 370–383.
- [174] W. Qin, J. Kang, J. Li, W. Yue, Y. Liu, D. She, Q. Mao, Y. Li, *Materials (Basel)*. 11 (2018) 1–12.
- [175] Y. Li, W. Li, S. Li, N. Min, L. Jiang, Q. Zhou, X. Jin, *Scr. Mater.* 193 (2021) 81–85.
- [176] V. Randle, *ACTA Mater.* 47 (1999) 4187–4196.
- [177] H. Miura, M. Kobayashi, Y. Todaka, C. Watanabe, Y. Aoyagi, N. Sugiura, N. Yoshinaga, *Scr. Mater.* 133 (2017) 33–36.
- [178] Y.T. Zhu, X.Z. Liao, X.L. Wu, *Prog. Mater. Sci.* 57 (2012) 1–62.
- [179] Y.F. Shen, X.X. Li, X. Sun, Y.D. Wang, L. Zuo, *Mater. Sci. Eng. A* 552 (2012) 514–522.
- [180] N. Nakada, H. Ito, Y. Matsuoka, T. Tsuchiyama, S. Takaki, *ACTA Mater.* 58 (2010) 895–903.
- [181] Y.H. Zhao, Z. Horita, T.G. Langdon, Y.T. Zhu, *Mater. Sci. Eng. A* 474 (2008) 342–

347.

- [182] S.G. Chowdhury, S. Das, P.K. De, *ACTA Mater.* 53 (2005) 3951–3959.
- [183] T. Chen, C. Zhou, *J. Mater. Res.* 34 (2019) 1555–1563.
- [184] C. Donadille, R. Valle, P. Dervin, R. Penelle, *Acta Metall.* 37 (1989) 1547–1571.
- [185] J. Hu, Y.N. Shi, X. Sauvage, G. Sha, K. Lu, *Science* (80-. ). 355 (2017) 1292–1296.
- [186] B. Ravi Kumar, B. Mahato, N.R. Bandyopadhyay, D.K. Bhattacharya, *Mater. Sci. Eng. A* 394 (2005) 296–301.
- [187] R.M. Latanision, A.W. Ruff, *Metall. Trans.* 2 (1971) 505–509.
- [188] L. Remy, A. Pineau, *Mater. Sci. Eng.* 36 (1978) 47–63.
- [189] S. Curtze, V.T. Kuokkala, *ACTA Mater.* 58 (2010) 5129–5141.
- [190] S. Chattopadhyay, G. Anand, S.G. Chowdhury, I. Manna, *Mater. Sci. Eng. A* 734 (2018) 139–148.
- [191] Y.R. Ma, H.J. Yang, Y.Z. Tian, J.C. Pang, Z.F. Zhang, *Mater. Sci. Eng. A* 713 (2018) 146–150.
- [192] Y. Dong, D. Ben, H. Yang, X. Shao, X. Wang, Z. Zhang, *Adv. Eng. Mater.* (2022) 2101623.
- [193] Z. Wang, F. Gao, S. Tang, C. Li, Z. Liu, *Mater. Lett.* 308 (2022) 131134.
- [194] M.A. Tolcha, H. Altenbach, *Metals (Basel)*. 9 (2019) 1–24.

- [195] W.S. Zhao, N.R. Tao, J.Y. Guo, Q.H. Lu, K. Lu, *Scr. Mater.* 53 (2005) 745–749.
- [196] T. Inoue, H. Qiu, R. Ueji, *Metals (Basel)*. 10 (2020) 6–8.
- [197] W. Jin, D. Piereder, J.G. Lenard, *Lubr. Eng.* 58 (2002) 29–37.
- [198] N. Hattori, R. Matsumoto, H. Utsunomiya, *Key Eng. Mater.* 622–623 (2014) 1000–1007.
- [199] C. Zener, J.H. Hollomon, *J. Appl. Phys.* 15 (1944) 22–32.
- [200] B.P. Kashyap, K. Tangri, *Mater. Sci. Eng. A* 149 (1992) 13–16.
- [201] R. V. Patil, B.D. Sharma, *Met. Sci.* 16 (1982) 389–392.
- [202] K. Tomimura, S. Takaki, Y. Tokunaga, *ISIJ Int.* 31 (1991) 1431–1437.
- [203] G.S. Sun, L.X. Du, J. Hu, H. Xie, H.Y. Wu, R.D.K. Misra, *Mater. Charact.* 110 (2015) 228–235.
- [204] A.F. Padilha, R.L. Plaut, P.R. Rios, *ISIJ Int.* 43 (2003) 135–143.
- [205] S. Takaki, K. Tomimura, S. Tanimoto, Y. Tokunaga, *Tetsu-To-Hagane/Journal Iron Steel Inst. Japan* 74 (1988) 1052–1057.
- [206] M.J. Sohrabi, H. Mirzadeh, C. Dehghanian, *J. Mater. Eng. Perform.* 29 (2020) 3233–3242.
- [207] M. Naghizadeh, H. Mirzadeh, *Metall. Mater. Trans. A Phys. Metall. Mater. Sci.* 49 (2018) 2248–2256.

- [208] M.J. Sohrabi, H. Mirzadeh, C. Dehghanian, *Vacuum* 174 (2020) 109220.
- [209] M.C. Niu, K. Yang, J.H. Luan, W. Wang, Z.B. Jiao, *J. Mater. Sci. Technol.* 104 (2022) 52–58.
- [210] T.O. Olugbade, J. Lu, *Nano Mater. Sci.* 2 (2020) 3–31.
- [211] D.O. Panov, R.S. Chernichenko, S. V. Naumov, A.S. Pertcev, N.D. Stepanov, S. V. Zherebtsov, G.A. Salishchev, *Mater. Lett.* 303 (2021) 130585.
- [212] C.X. Ren, Q. Wang, Z.J. Zhang, H.J. Yang, Z.F. Zhang, *Mater. Sci. Eng. A* 754 (2019) 593–601.
- [213] X. Yang, X. Wang, X. Ling, D. Wang, *Results Phys.* 7 (2017) 1412–1421.
- [214] J. Li, G.J. Weng, S. Chen, X. Wu, *Int. J. Plast.* 88 (2017) 89–107.
- [215] K.S. Osipovich, E.G. Astafurova, A. V. Chumaevskii, K.N. Kalashnikov, S. V. Astafurov, G.G. Maier, E. V. Melnikov, V.A. Moskvina, M.Y. Panchenko, S.Y. Tarasov, V.E. Rubtsov, E.A. Kolubaev, *J. Mater. Sci.* 55 (2020) 9258–9272.
- [216] X. Wu, P. Jiang, L. Chen, F. Yuan, Y.T. Zhu, *Proc. Natl. Acad. Sci. U. S. A.* 111 (2014) 7197–7201.
- [217] L.G. Sun, G. Wu, Q. Wang, J. Lu, *Mater. Today* 38 (2020) 114–135.
- [218] K. Lu, *Nat. Rev. Mater.* 1 (2016) 1–13.
- [219] W. Cui, *J. Mar. Sci. Technol.* 7 (2002) 43–56.

- [220] Y. Sun, Tribol. Int. 57 (2013) 67–75.
- [221] K. Dai, L. Shaw, Int. J. Fatigue 30 (2008) 1398–1408.
- [222] M.A. S Torres, H.J. C Voorwald, Int. J. Fatigue 24 (2002) 877–886.
- [223] B.N. Mordyuk, G.I. Prokopenko, M.A. Vasylyev, M.O. Iefimov, Mater. Sci. Eng. A 458 (2007) 253–261.
- [224] B. Yu, E.M. Davis, R.S. Hodges, R.T. Irvin, D.Y. Li, Nanotechnology 19 (2008) 335101.
- [225] T. Fu, Z.F. Zhou, Y.M. Zhou, X.D. Zhu, Q.F. Zeng, C.P. Wang, K.Y. Li, J. Lu, Surf. Coatings Technol. 207 (2012) 555–564.
- [226] Y. He, K. Li, I.S. Cho, C.S. Lee, I.G. Park, K. Shin, Microsc. Microanal. 20 (2014) 844–845.
- [227] J. long Tian, G. Hu, W. Wang, Y. yin Shan, Z. hua Jiang, J. Iron Steel Res. Int. 28 (2021) 722–728.
- [228] E.R. de los Rios, A. Walley, M.T. Milan, G. Hammersley, Int. J. Fatigue 17 (1995) 493–499.
- [229] H. sang Lee, D. soo Kim, J. sung Jung, Y. shik Pyoun, K. Shin, Corros. Sci. 51 (2009) 2826–2830.
- [230] T. Wang, J. Yu, B. Dong, Surf. Coatings Technol. 200 (2006) 4777–4781.
- [231] Y. He, K.B. Yoo, H. Ma, K. Shin, Mater. Lett. 215 (2018) 187–190.

- [232] Y.F. Al-Obaid, Eng. Fract. Mech. 51 (1995) 19–25.
- [233] S. Pour-Ali, A.R. Kiani-Rashid, A. Babakhani, Vacuum 144 (2017) 152–159.
- [234] M. Jayalakshmi, P. Huilgol, B.R. Bhat, K. Udaya Bhat, Surf. Coatings Technol. 344 (2018) 295–302.
- [235] D. Kanesan, M.E. Mohyaldinn, N.I. Ismail, D. Chandran, C.J. Liang, J. Nat. Gas Sci. Eng. 65 (2019) 267–274.
- [236] M. Faller, S. Buzzi, O. V. Trzebiatowski, Mater. Corros. 56 (2005) 373–378.
- [237] Z. Makama, I. Doble, D. Nicolson, M.E. Webb, I.B. Beech, S.A. Campbell, J.R. Smith, Trans. Inst. Met. Finish. 89 (2011) 237–243.
- [238] W. Morton, S. Green, A.E.W. Rennie, T.N. Abram, Innov. Dev. Virtual Phys. Prototyp. - Proc. 5th Int. Conf. Adv. Res. Rapid Prototyp. (2012) 503–509.
- [239] H. Begg, M. Riley, H. de Villiers Lovelock, J. Therm. Spray Technol. 25 (2016) 12–20.
- [240] N.L. Tshimanga, G.A. Combrink, M.W. Kalenga, Mater. Today Proc. 38 (2021) 544–548.
- [241] X.Y. Wang, D.Y. Li, Electrochim. Acta 47 (2002) 3939–3947.
- [242] M. Multigner, S. Ferreira-Barragáns, E. Frutos, M. Jaafar, J. Ibáñez, P. Marín, M.T. Pérez-Prado, G. González-Doncel, A. Asenjo, J.L. González-Carrasco, Surf. Coatings Technol. 205 (2010) 1830–1837.

- [243] A.M. Gatey, S.S. Hosmani, R.K.P. Singh, S. Suwas, *Adv. Mater. Res.* 794 (2013) 238–247.
- [244] S. Bajda, W. Ratuszek, M. Krzyzanowski, D. Retraint, *Surf. Coatings Technol.* 329 (2017) 202–211.
- [245] M. Novelli, J.J. Fundenberger, P. Bocher, T. Grosdidier, *Appl. Surf. Sci.* 389 (2016) 1169–1174.
- [246] Z. Sun, D. Retraint, T. Baudin, A.L. Helbert, F. Brisset, M. Chemkhi, J. Zhou, P. Kanouté, *Mater. Charact.* 124 (2017) 117–121.
- [247] T. Balusamy, S. Kumar, T.S.N. Sankara Narayanan, *Trans. Indian Inst. Met.* 64 (2011) 507–511.
- [248] J. Zhou, Z. Sun, P. Kanouté, D. Retraint, *Int. J. Fatigue* 103 (2017) 309–317.
- [249] S. Bahl, P. Shreyas, M.A. Trishul, S. Suwas, K. Chatterjee, *Nanoscale* 7 (2015) 7704–7716.
- [250] B. Thangaraj, S.N.T.S. Nellaiappan, R. Kulandaivelu, M.H. Lee, T. Nishimura, *ACS Appl. Mater. Interfaces* 7 (2015) 17731–17747.
- [251] Y. wei HAO, B. DENG, C. ZHONG, Y. ming JIANG, J. LI, J. *Iron Steel Res. Int.* 16 (2009) 68–72.
- [252] T.-T. Chen, J. Wang, Y. Zhang, P. Jiang, F.-P. Yuan, P.-D. Han, X.-L. Wu, *Mater. Sci. Eng. A* 837 (2022) 142727.



- [253] S. Qin, M. Yang, F. Yuan, X. Wu, *Nanomaterials* 11 (2021) 1–12.
- [254] T. Balusamy, S. Kumar, T.S.N. Sankara Narayanan, *Corros. Sci.* 52 (2010) 3826–3834.
- [255] X.H. Chen, J. Lu, L. Lu, K. Lu, *Scr. Mater.* 52 (2005) 1039–1044.
- [256] T. Roland, D. Retraint, K. Lu, J. Lu, *Mater. Sci. Eng. A* 445–446 (2007) 281–288.
- [257] T. Bai, P. Chen, K. Guan, *Mater. Sci. Eng. A* 561 (2013) 498–506.
- [258] T. Balusamy, T.S.N. Sankara Narayanan, K. Ravichandran, I.S. Park, M.H. Lee, *Corros. Sci.* 74 (2013) 332–344.
- [259] D. Bernoulli, S.C. Cao, J. Lu, M. Dao, *Surf. Coatings Technol.* 339 (2018) 14–19.
- [260] K. Lu, J. Lu, *Mater. Sci. Eng. A* 375–377 (2004) 38–45.
- [261] Y. Wu, B. Guelorget, Z. Sun, R. D  turche, D. Retraint, *Mater. Charact.* 155 (2019) 109788 Contents.
- [262] H.W. Huang, Z.B. Wang, J. Lu, K. Lu, *ACTA Mater.* 87 (2015) 150–160.
- [263] M.X. Shen, K.J. Rong, D.J. Liu, G.Y. Xiong, D.H. Ji, X.G. Wang, *Surf. Topogr. Metrol. Prop.* 8 (2020) 035009.
- [264] L. Carneiro, X. Wang, Y. Jiang, *Int. J. Fatigue* 134 (2020) 105469.
- [265] H.B. Wang, X.H. Yang, H. Li, G.L. Song, G.Y. Tang, *J. Mater. Res.* 33 (2018) 3827–3840.

- [266] J. Liu, C. Wang, W. Zhang, T. Xia, X. Zhang, T. Liang, T. Ahmad, B. Yang, *Mater. Sci. Technol. (United Kingdom)* 35 (2019) 907–915.
- [267] D. Liu, D. Liu, X. Zhang, C. Liu, N. Ao, *Mater. Sci. Eng. A* 726 (2018) 69–81.
- [268] C. Li, R. Zhu, X. Zhang, P. Huang, X. Wang, X. Wang, *Surf. Coatings Technol.* 383 (2020) 125280.
- [269] C. Wang, J. Han, J. Zhao, Y. Song, J. Man, H. Zhu, J. Sun, L. Fang, *Coatings* 9 (2019) 276.
- [270] Y.X. Liu, H. Chen, R.Z. Wang, Y.F. Jia, X.C. Zhang, Y. Cui, S.T. Tu, *Int. J. Fatigue* 147 (2021) 106170.
- [271] X. Han, C. Li, C. Chen, X. Zhang, H. Zhang, *Nanomaterials* 11 (2021) 1769.
- [272] H. Wang, G. Song, G. Tang, *Mater. Sci. Eng. A* 662 (2016) 456–467.
- [273] D. Liu, D. Liu, X. Zhang, C. Liu, A. Ma, X. Xu, W. Zhang, *Int. J. Fatigue* 131 (2020) 105340.
- [274] Q. Zhang, Z. Hu, W. Su, H. Zhou, C. Liu, Y. Yang, X. Qi, *Surf. Coatings Technol.* 321 (2017) 64–73.
- [275] Y. Liu, J. Sun, Y. Fu, B. Xu, B. Li, S. Xu, P. Huang, J. Cheng, Y. Han, J. Han, G. Wu, *Addit. Manuf.* 48 (2021) 102373.
- [276] Y. He, K. Wang, K. Shin, *J. Mater. Sci.* 56 (2021) 4858–4870.
- [277] M. Novelli, P. Bocher, T. Grosdidier, *Mater. Charact.* 139 (2018) 197–207.

- [278] G. Liu, J. Lu, K. Lu, *Mater. Sci. Eng. A* 286 (2000) 91–95.
- [279] B.N. Mordyuk, Y. V. Milman, M.O. Iefimov, G.I. Prokopenko, V. V. Silberschmidt, M.I. Danylenko, A. V. Kotko, *Surf. Coatings Technol.* 202 (2008) 4875–4883.
- [280] Y. Zou, Z. Sang, Q. Wang, T. Li, D. Li, Y. Li, *Mater. Sci.* 26 (2020) 161–167.
- [281] H. Zhang, Y. Zhao, Y. Wang, C. Zhang, Y. Peng, *J. Mater. Sci. Technol.* 44 (2020) 148–159.
- [282] H. Zhang, Y. Zhao, Y. Wang, H. Yu, C. Zhang, *J. Mater. Sci. Technol.* 34 (2018) 2125–2130.
- [283] Y.Z. Zhang, J.J. Wang, N.R. Tao, *J. Mater. Sci. Technol.* 36 (2020) 65–69.
- [284] H.W. Huang, Z.B. Wang, X.P. Yong, K. Lu, *Mater. Sci. Technol. (United Kingdom)* 29 (2013) 1200–1205.
- [285] Y. Samih, B. Beausir, B. Bolle, T. Grosdidier, *Mater. Charact.* 83 (2013) 129–138.
- [286] J. Vishnu, G. Manivasagam, *J. Bio- Tribo-Corrosion* 7 (2021) 1–19.
- [287] A. Chen, C. Wang, J. Jiang, H. Ruan, J. Lu, *Nanomaterials* 11 (2021) 1624.
- [288] J. Fan, T. Fu, *Mater. Sci. Eng. A* 552 (2012) 359–363.
- [289] Q.Y. Long, J.X. Lu, T.H. Fang, *Mater. Sci. Eng. A* 751 (2019) 42–50.
- [290] A. Farid, S. Guo, *ACTA Mater.* 55 (2007) 1467–1477.
- [291] P. Mangonon, Thomas G, *Metall. Trans.* 1 (1970) 1577–1586.

- [292] A. Eres-Castellanos, C. Garcia-Mateo, F.G. Caballero, *Metals* (Basel). 11 (2021) 1–19.
- [293] X.S. Yang, S. Sun, X.L. Wu, E. Ma, T.Y. Zhang, *Sci. Rep.* 4 (2014) 1–7.
- [294] Y. Gao, Y. Wang, *Phys. Rev. Mater.* 2 (2018) 1–11.
- [295] S. Djaziri, Y. Li, G.A. Nematollahi, B. Grabowski, S. Goto, C. Kirchlechner, A. Kostka, S. Doyle, J. Neugebauer, D. Raabe, G. Dehm, *Adv. Mater.* 28 (2016) 7753–7757.
- [296] H. Fu, S. Yuan, W. Sun, J. Wan, K.C. Chan, J. Zhu, X.S. Yang, *Scr. Mater.* 204 (2021) 114153.
- [297] Y. Chen, W. Xiao, K. Jiao, D. Ping, H. Xu, X. Zhao, Y. Wang, *Phys. Rev. Mater.* 2 (2018) 1–5.
- [298] U. Krupp, I. Roth, H.J. Christ, M. Kübbeler, C.P. Fritzen, 13th Int. Conf. Fract. 2013, ICF 2013 5 (2013) 4119–4127.
- [299] Z. Wang, M. Rifat, C. Saldana, S. Basu, *Materialia* 2 (2018) 231–249.
- [300] R. Blonde, H.L. Chan, N. Allain-Bonasso, B. Bolle, T. Grosdidier, J. Lu, *J. Alloys Compd.* 504 (2010) S410–S413.
- [301] W. Chen, W. Tong, C. He, X. Zhao, L. Zuo, *Mater. Sci. Forum* 706–709 (2012) 2663–2667.
- [302] G. Kurdjumow, G. Sachs, *Z. Phys* 64 (1930) 325–343.

- [303] S. Bagherifard, S. Slawik, I. Fernández-Pariente, C. Pauly, F. Mücklich, M. Guagliano, *Mater. Des.* 102 (2016) 68–77.
- [304] Schumann V. H., Von Fircks H-J, *Arch. Fuer Das Eisenhuettenwes.* 40 (1969) 561–568.
- [305] A. Misra, in: *Nanostructure Control Mater.*, 2006, pp. 146–176.
- [306] M. Nasim, Y. Li, M. Wen, C. Wen, *J. Mater. Sci. Technol.* 50 (2020) 215–244.
- [307] R.M. Costescu, D.G. Cahill, F.H. Fabreguette, Z.A. Sechrist, S.M. George, *Science* (80-. ). 303 (2004) 989–990.
- [308] P. Dayal, N. Savvides, M. Hoffman, *Thin Solid Films* 517 (2009) 3698–3703.
- [309] S.J. Lloyd, J.M. Molina-Aldareguía, W.J. Clegg, *J. Microsc.* 217 (2005) 241–259.
- [310] H.C. Barshilia, M.S. Prakash, A. Jain, K.S. Rajam, *Vacuum* 77 (2005) 169–179.
- [311] W. Guo, E.A. Jägle, P.P. Choi, J. Yao, A. Kostka, J.M. Schneider, D. Raabe, *Phys. Rev. Lett.* 113 (2014) 1–5.
- [312] B. Cheng, J.R. Trelewicz, *ACTA Mater.* 153 (2018) 314–326.
- [313] M.C. Liu, X.H. Du, I.C. Lin, H.J. Pei, J.C. Huang, *Intermetallics* 30 (2012) 30–34.
- [314] I. Knorr, N.M. Cordero, E.T. Lilleodden, C.A. Volkert, *ACTA Mater.* 61 (2013) 4984–4995.
- [315] N. Mara, A. Sergueeva, A. Misra, A.K. Mukherjee, *Scr. Mater.* 50 (2004) 803–806.

- [316] M.A. Monclús, S.J. Zheng, J.R. Mayeur, I.J. Beyerlein, N.A. Mara, T. Polcar, J. Llorca, J.M. Molina-Aldareguía, *APL Mater.* 1 (2013) 1–8.
- [317] H.R. Jafarian, M.M. Mahdavian, S.A.A. Shams, A.R. Eivani, *Mater. Sci. Eng. A* 805 (2021) 140556.
- [318] D. Wei, F. Cao, Z. Wu, Y. Liu, J. Wang, Q. Wang, X. Liu, Q. Zhang, *J. Mater.* 7 (2021) 648–655.
- [319] T.H. Wu, J.Z. Chen, C.C. Hsu, I.C. Cheng, *J. Phys. D. Appl. Phys.* 47 (2014) 255102.
- [320] T.W. Kang, T.W. Kim, *Appl. Surf. Sci.* 150 (1999) 190–194.
- [321] C.B. Anucha, I. Altin, E. Bacaksiz, I. Degirmencioglu, T. Kucukomeroglu, S. Yilmaz, V.N. Stathopoulos, *Separations* 8 (2021) 1–21.
- [322] S. Sutha, G. Karunakaran, V. Rajendran, *Ceram. Int.* 39 (2013) 5205–5212.
- [323] M. Es-Souni, M. Kuhnke, S. Iakovlev, C.H. Solterbeck, A. Piorra, *Appl. Phys. Lett.* 86 (2005) 10–13.
- [324] V. Chernikova, O. Shekhah, M. Eddaoudi, *ACS Appl. Mater. Interfaces* 8 (2016) 20459–20464.
- [325] X. Jin, L. Gao, E. Liu, F. Yu, X. Shu, H. Wang, *J. Mech. Behav. Biomed. Mater.* 50 (2015) 23–32.
- [326] G. Suo, D. Li, L. Feng, X. Hou, X. Ye, L. Zhang, Q. Yu, Y. Yang, W. (Alex) Wang,

- J. Mater. Sci. Technol. 55 (2020) 167–172.
- [327] S. Jung, K. Yong, Chem. Commun. 47 (2011) 2643–2645.
- [328] D.K. Behara, G.P. Sharma, A.P. Upadhyay, M. Gyanprakash, R.G.S. Pala, S. Sivakumar, Chem. Eng. Sci. 154 (2016) 150–169.
- [329] X. Li, Y. Zhong, M. Cai, M.P. Balogh, D. Wang, Y. Zhang, R. Li, X. Sun, Electrochim. Acta 89 (2013) 387–393.
- [330] Y. Zhong, Y. Zhang, M. Cai, M.P. Balogh, R. Li, X. Sun, Appl. Surf. Sci. 270 (2013) 722–727.
- [331] R. Lei, J. Gao, L. Qi, L. Ye, C. Wang, Y. Le, Y. Huang, X. Shi, H. Ni, Int. J. Hydrogen Energy 45 (2020) 28930–28939.
- [332] N.M. Shinde, P.R. Deshmukh, S. V. Patil, C.D. Lokhande, Sensors Actuators, A Phys. 193 (2013) 79–86.
- [333] M.B. Sreedhara, S. Gope, B. Vishal, R. Datta, A.J. Bhattacharyya, C.N.R. Rao, J. Mater. Chem. A 6 (2018) 2302–2310.
- [334] S. V. Mahajan, S.A. Hasan, J. Cho, M.S.P. Shaffer, A.R. Boccaccini, J.H. Dickerson, Nanotechnology 19 (2008) 0–8.
- [335] A. Sarkar, A. Sarkar, B. Paul, G.G. Khan, ChemistrySelect 4 (2019) 9367–9375.
- [336] A. Lamouchi, I. Ben Assaker, R. Chtourou, Appl. Surf. Sci. 478 (2019) 937–945.
- [337] S. Kilian, K. McCarthy, K. Stokes, T.E. Adegoke, M. Conroy, I.S. Amiin, H.

- Geaney, T. Kennedy, K.M. Ryan, *Small* 17 (2021) 1–8.
- [338] R.D. Prabha, R. Kandasamy, U.S. Sivaraman, M.A. Nandkumar, P.D. Nair, *Indian J. Med. Res.* 144 (2016) 580–586.
- [339] I. Codiță, D.M. Caplan, E.C. Drăgulescu, B.E. Lixandru, I.L. Coldea, C.C. Dragomirescu, C. Surdu-Bob, M. Bădulescu, *Roum. Arch. Microbiol. Immunol.* 69 (2010) 204–212.
- [340] Y. Wang, Y. Long, Z. Yang, D. Zhang, *J. Hazard. Mater.* 351 (2018) 11–19.
- [341] S. Cometa, R. Iatta, M.A. Ricci, C. Ferretti, E. De Giglio, *J. Bioact. Compat. Polym.* 28 (2013) 508–522.
- [342] X. Zhang, X. Huang, Y. Ma, N. Lin, A. Fan, B. Tang, *Appl. Surf. Sci.* 258 (2012) 10058–10063.
- [343] G. Flynn, Q.M. Ramasse, K.M. Ryan, *Nano Lett.* 16 (2016) 374–380.
- [344] K. Stokes, G. Flynn, H. Geaney, G. Bree, K.M. Ryan, *Nano Lett.* 18 (2018) 5569–5575.
- [345] W. Zhou, C. Cheng, J. Liu, Y.Y. Tay, J. Jiang, X. Jia, J. Zhang, H. Gong, H.H. Hng, T. Yu, H.J. Fan, *Adv. Funct. Mater.* 21 (2011) 2439–2445.
- [346] W.L. Ong, K.W. Yew, C.F. Tan, T.K. Tan Adrian, M. Hong, G.W. Ho, *RSC Adv.* 4 (2014) 27481–27487.
- [347] M. Lee, K. Yong, *Nanotechnology* 23 (2012) 194014.



- [348] D.C. Shye, C.C. Chou, B.H. Liou, K.Y. Hung, P.C. Juan, *Ferroelectrics* 383 (2009) 40–49.
- [349] M. Li, N. Muralidharan, K. Moyer, C.L. Pint, *Nanoscale* 10 (2018) 10443–10449.
- [350] C. Tan, Y. Chew, R. Duan, F. Weng, S. Sui, F.L. Ng, Z. Du, G. Bi, *Mater. Res. Lett.* 9 (2021) 291–299.
- [351] A. Reichardt, R.P. Dillon, J.P. Borgonia, A.A. Shapiro, B.W. McEnerney, T. Momose, P. Hosemann, *Mater. Des.* 104 (2016) 404–413.
- [352] C.H. Zhang, H. Zhang, C.L. Wu, S. Zhang, Z.L. Sun, S.Y. Dong, *Vacuum* 141 (2017) 181–187.
- [353] Y. Zoo, T.L. Alford, *J. Appl. Phys.* 101 (2007) 033505.
- [354] D. Faurie, P.O. Renault, E. Le Bourhis, P. Goudeau, *ACTA Mater.* 54 (2006) 4503–4513.
- [355] P. Zou, W. Yu, J.A. Bain, *IEEE Trans. Magn.* 38 (2002) 3501–3520.
- [356] N. Luo, H. Liang, X. Sun, X. Fan, H. liang Liang, X. Li, *Compos. Interfaces* 28 (2020) 1–16.
- [357] Y. Yang, J. Hu, X.Y. Liu, W. Xu, B. Li, G.P. Ling, X.Y. Pang, Y.Z. Tian, *Mater. Sci. Eng. A* 831 (2022) 142104 Contents.
- [358] S. Joo, D.F. Baldwin, *IEEE Trans. Electron. Packag. Manuf.* 33 (2010) 129–134.
- [359] C. Gaire, S. Rao, M. Riley, L. Chen, A. Goyal, S. Lee, I. Bhat, T.M. Lu, G.C. Wang,

Thin Solid Films 520 (2012) 1862–1865.

- [360] K. Asami, K. Hashimoto, Corros. Sci. 45 (2003) 2263–2283.
- [361] J. Mondal, A. Marques, L. Aarik, J. Kozlova, A. Simões, V. Sammelselg, Corros. Sci. 105 (2016) 161–169.
- [362] M. Resnik, M. Benčina, E. Levičnik, N. Rawat, A. Iglič, I. Junkar, Materials (Basel). 13 (2020) 1–22.
- [363] K.M. Perkins, M.R. Bache, Int. J. Fatigue 27 (2005) 1499–1508.
- [364] N. Kota, M.S. Charan, T. Laha, S. Roy, Ceram. Int. 48 (2022) 1451–1483.
- [365] R. Badyka, G. Monnet, S. Saillet, C. Domain, C. Pareige, J. Nucl. Mater. 514 (2019) 266–275.
- [366] A. Mateo, L. Llanes, M. Anglada, A. Redjaïmia, G. Metauer, J. Mater. Sci. 32 (1997) 4533–4540.
- [367] F. Danoix, P. Auger, D. Blavette, Microsc. Microanal. 10 (2004) 349–354.
- [368] L.Q. Guo, M.C. Lin, L.J. Qiao, A.A. Volinsky, Appl. Surf. Sci. 287 (2013) 499–501.
- [369] X.F. Wang, X.P. Yang, Z.D. Guo, Y.C. Zhou, H.W. Song, Adv. Mater. Res. 26–28 (2007) 1165–1170.
- [370] J.I. Yoon, J. Jung, H.H. Lee, J.Y. Kim, H.S. Kim, Met. Mater. Int. 25 (2019) 1161–1169.

- [371] Z. Wang, H. Li, Q. Shen, W. Liu, Z. Wang, *ACTA Mater.* 156 (2018) 158–171.
- [372] Z. Zhang, C. Shao, S. Wang, X. Luo, K. Zheng, H.M. Urbassek, *Crystals* 9 (2019) 584.
- [373] B. AlMangour, M.S. Baek, D. Grzesiak, K.A. Lee, *Mater. Sci. Eng. A* 712 (2018) 812–818.
- [374] B. Li, B. Qian, Y. Xu, Z. Liu, J. Zhang, F. Xuan, *Mater. Sci. Eng. A* 745 (2019) 495–508.
- [375] B. Almangour, D. Grzesiak, J.M. Yang, *J. Alloys Compd.* 680 (2016) 480–493.
- [376] O.O. Salman, C. Gammer, J. Eckert, M.Z. Salih, E.H. Abdulsalam, K.G. Prashanth, S. Scudino, *Mater. Today Commun.* 21 (2019) 100615.
- [377] B. AlMangour, D. Grzesiak, J.M. Yang, *Powder Technol.* 309 (2017) 37–48.
- [378] X. Zhao, Q.S. Wei, N. Gao, E.L. Zheng, Y.S. Shi, S.F. Yang, *J. Mater. Process. Technol.* 270 (2019) 8–19.
- [379] Z. Sun, Y. Xu, F. Chen, L. Shen, X. Tang, L. Sun, M. Fan, P. Huang, *Mater. Charact.* 180 (2021) 111420.
- [380] Y. Dong, J. Li, D. Xu, G. Song, D. Liu, H. Wang, M. Saleem Khan, K. Yang, F. Wang, *J. Mater. Sci. Technol.* 64 (2021) 176–186.
- [381] D. Sun, D. Xu, C. Yang, M.B. Shahzad, Z. Sun, J. Xia, J. Zhao, T. Gu, K. Yang, G. Wang, *Sci. Rep.* 6 (2016) 1–13.

- [382] Y. Sun, J. Zhao, L. Liu, T. Xi, C. Yang, Q. Li, K. Yang, *Mater. Technol.* 36 (2021) 118–130.
- [383] Z. Zhang, X.R. Zhang, T. Jin, C.G. Yang, Y.P. Sun, Q. Li, K. Yang, *Rare Met.* 41 (2021) 559–569.
- [384] A. Kalhor, M. Soleimani, H. Mirzadeh, V. Uthaisangsuk, *Arch. Civ. Mech. Eng.* 20 (2020) 1–14.
- [385] M. Soleimani, A. Kalhor, H. Mirzadeh, *Mater. Sci. Eng. A* 795 (2020) 140023.
- [386] S. Singh, T. Nanda, *IJSRD-International J. Sci. Res. Dev.* 2 (2014) 2321–0613.
- [387] J. Zhao, Z. Jiang, *Prog. Mater. Sci.* 94 (2018) 174–242.
- [388] T. Nanda, V. Singh, G. Singh, M. Singh, B.R. Kumar, *Arch. Civ. Mech. Eng.* 21 (2021) 1–24.
- [389] Y. characterization of G. in F. cast duplex stainless steel Chen, X. Dai, X. Chen, B. Yang, *Mater. Charact.* 149 (2019) 74–81.
- [390] L. Yin, D. Xu, C. Yang, T. Xi, X. Chen, K. Yang, *Corros. Sci.* 179 (2021) 109141.
- [391] N. Koga, T. Nameki, O. Umezawa, V. Tschan, K.P. Weiss, *Mater. Sci. Eng. A* 801 (2021) 140442.
- [392] N. Tsuchida, Y. Morimoto, T. Tonan, Y. Shibata, K. Fukaura, R. UEJI, *ISIJ Int.* 51 (2011) 124–129.
- [393] T. Iwamoto, T. Tsuta, Y. Tomita, *Int. J. Mech. Sci.* 40 (1998) 173–182.

- [394] J.A. Rodríguez-Martínez, R. Pesci, A. Rusinek, *Mater. Sci. Eng. A* 528 (2011) 5974–5982.
- [395] B.M. Gonzalez, C.S.B. Castro, V.T.L. Buono, J.M.C. Vilela, M.S. Andrade, J.M.D. Moraes, M.J. Mantel, *Mater. Sci. Eng. A* 343 (2003) 51–56.
- [396] J. Talonen, P. Nenonen, G. Pape, H. Hänninen, *Metall. Mater. Trans. A Phys. Metall. Mater. Sci.* 36 A (2005) 421–432.
- [397] A.A. Lebedev, V. V. Kosarchuk, *Int. J. Plast.* 16 (2000) 749–767.
- [398] J.A. Lichtenfeld, M.C. Mataya, C.J. Van Tyne, *Metall. Mater. Trans. A Phys. Metall. Mater. Sci.* 37 (2006) 147–161.
- [399] D.Y. Ryoo, N. Kang, C.Y. Kang, *Mater. Sci. Eng. A* 528 (2011) 2277–2281.
- [400] V. Muthupandi, P. Bala Srinivasan, V. Shankar, S.K. Seshadri, S. Sundaresan, *Mater. Lett.* 59 (2005) 2305–2309.
- [401] N. Tsuchida, S. Kawabata, K. Fukaura, R. Ueji, *J. Alloys Compd.* 577 (2013) S525–S527.
- [402] S.S.M. Tavares, J.M. Pardal, M.J.G. da Silva, H.F.G. Abreu, M.R. da Silva, *Mater. Charact.* 60 (2009) 907–911.
- [403] J. Talonen, H. Hänninen, *ACTA Mater.* 55 (2007) 6108–6118.
- [404] A. Ferraiuolo, S. Cicalè, A. Costa, *Metall. Ital.* 109 (2017) 37–48.
- [405] A. Hamada, J. Kömi, *Mater. Sci. Eng. A* 718 (2018) 301–304.

- [406] J. Mola, B.C. De Cooman, *Metall. Mater. Trans. A Phys. Metall. Mater. Sci.* 44 (2013) 946–967.
- [407] T. Tsuchiyama, J. Tobata, T. Tao, N. Nakada, S. Takaki, *Mater. Sci. Eng. A* 532 (2012) 585–592.
- [408] A.S. Hamada, L.P. Karjalainen, R.D.K. Misra, J. Talonen, *Mater. Sci. Eng. A* 559 (2013) 336–344.
- [409] L.D. Wegner, L.J. Gibson, *Int. J. Mech. Sci.* 43 (2001) 1771–1791.
- [410] L.D. Wegner, L.J. Gibson, *Int. J. Mech. Sci.* 42 (2000) 943–964.
- [411] L.D. Wegner, L.J. Gibson, *Int. J. Mech. Sci.* 43 (2001) 1061–1072.
- [412] X. Li, M. Ghasri-Khouzani, A.A. Bogno, J. Liu, H. Henein, Z. Chen, A.J. Qureshi, *Materials (Basel)*. 14 (2021) 3654.
- [413] B. Yao, Z. Zhou, Z. Chen, J. Wang, *Tribol. Trans.* 63 (2020) 543–556.
- [414] Z. Zhou, B. Yao, L. Duan, J. Qin, *Adv. Eng. Mater.* 20 (2018) 1–6.
- [415] B. Yao, Z. Zhou, L. Duan, J. Mater. Res. 33 (2018) 2477–2485.
- [416] A.R. Moustafa, R.B. Dinwiddie, A.E. Pawlowski, D.A. Splitter, A. Shyam, Z.C. Cordero, *Addit. Manuf.* 22 (2018) 223–229.
- [417] L.L. Poole, M. Gonzales, A.R. Moustafa, A.R.C. Gerlt, Z.C. Cordero, *AIP Conf. Proc.* 2272 (2020) 120020.

- [418] J. Cheng, M. Gussev, J. Allen, X. Hu, A.R. Moustafa, D.A. Splitter, A. Shyam, Mater. Des. 195 (2020) 109061.
- [419] Z. Zhou, B. Yao, L. Duan, J. Qin, J. Alloys Compd. 727 (2017) 146–152.
- [420] A.E. Pawlowski, Z.C. Cordero, M.R. French, T.R. Muth, J. Keith Carver, R.B. Dinwiddie, A.M. Elliott, A. Shyam, D.A. Splitter, Mater. Des. 127 (2017) 346–351.
- [421] W.J. Gao, W.W. Zhang, T. Zhang, C. Yang, X.S. Huang, Z.Y. Liu, Z. Wang, W.H. Li, W.R. Li, L. Li, L.H. Liu, Compos. Part B Eng. 224 (2021) 109226.
- [422] B. Yao, Z. Zhou, L. Duan, Z. Chen, Vacuum 155 (2018) 83–90.
- [423] L.L. Poole, M. Gonzales, M.R. French, W.A. Yarberry, A.R. Moustafa, Z.C. Cordero, Int. J. Impact Eng. 136 (2020) 103407.
- [424] B. Yao, Z. Zhou, L. Duan, Z. Chen, RSC Adv. 8 (2018) 16171–16177.
- [425] S. Wu, S. Wang, D. Wen, G. Wang, Y. Wang, Appl. Sci. 8 (2018) 2012.
- [426] Q. Li, P. Song, Q. Ji, Y. Huang, D. Li, R. Zhai, B. Zheng, J. Lu, Surf. Coatings Technol. 374 (2019) 189–200.
- [427] F. Cheng, S.M. Kim, J.N. Reddy, R.K. Abu Al-Rub, Int. J. Plast. 61 (2014) 94–111.
- [428] A. Agarwal, I. V. Singh, B.K. Mishra, Compos. Part B Eng. 51 (2013) 327–336.
- [429] S.K. Vajpai, M. Ota, Z. Zhang, K. Ameyama, Mater. Res. Lett. 4 (2016) 191–197.
- [430] K. Ameyama, H. Fujiwara, Mater. Sci. Forum 706–709 (2012) 9–16.

- [431] D. Orlov, H. Fujiwara, K. Ameyama, *Mater. Trans.* 54 (2013) 1549–1553.
- [432] M. Ota, S.K. Vajpai, R. Imao, K. Kurokawa, K. Ameyama, *Mater. Trans.* 56 (2015) 154–159.
- [433] D. Kong, C. Dong, S. Wei, X. Ni, L. Zhang, R. Li, L. Wang, C. Man, X. Li, *Addit. Manuf.* 38 (2021) 101804.
- [434] H. Zhang, M. Xu, Z. Liu, C. Li, Y. Zhang, *Mater. Charact.* 177 (2021) 111159.
- [435] L. Liu, Q. Ding, Y. Zhong, J. Zou, J. Wu, Y.L. Chiu, J. Li, Z. Zhang, Q. Yu, Z. Shen, *Mater. Today* 21 (2018) 354–361.
- [436] C. Elangeswaran, A. Cutolo, G.K. Muralidharan, C. de Formanoir, F. Berto, K. Vanmeensel, B. Van Hooreweder, *Int. J. Fatigue* 123 (2019) 31–39.
- [437] X. Lou, M.A. Othon, R.B. Rebak, *Corros. Sci.* 127 (2017) 120–130.
- [438] X. Wang, J.A. Muñoz-Lerma, M. Attarian Shandiz, O. Sanchez-Mata, M. Brochu, *Mater. Sci. Eng. A* 766 (2019) 138395.
- [439] Z. Shang, C. Fan, S. Xue, J. Ding, J. Li, T. Voisin, Y.M. Wang, H. Wang, X. Zhang, *Mater. Res. Lett.* 7 (2019) 290–297.
- [440] F. Yan, W. Xiong, E. Faierson, G.B. Olson, *Scr. Mater.* 155 (2018) 104–108.
- [441] P. Krakhmalev, G. Fredriksson, K. Svensson, I. Yadroitsev, I. Yadroitsava, M. Thuvander, R. Peng, *Metals (Basel)*. 8 (2018) 643.
- [442] Z. Li, T. Voisin, J.T. McKeown, J. Ye, T. Braun, C. Kamath, W.E. King, Y.M.



- Wang, *Int. J. Plast.* 120 (2019) 395–410.
- [443] A.M. Filimonov, O.A. Rogozin, D.G. Firsov, Y.O. Kuzminova, S.N. Sergeev, A.P. Zhilyaev, M.I. Lerner, N.E. Toropkov, A.P. Simonov, I.I. Binkov, I. V. Okulov, I.S. Akhatov, S.A. Evlashin, *Materials* (Basel). 14 (2020) 1–14.
- [444] M. Kawasaki, J.K. Han, X. Liu, Y. Onuki, Y.O. Kuzminova, S.A. Evlashin, A.M. Pesin, A.P. Zhilyaev, K.D. Liss, *Adv. Eng. Mater.* 2100968 (2021) 1–11.
- [445] D.J. Sprouster, W. Streit Cunningham, G.P. Halada, H. Yan, A. Pattammattel, X. Huang, D. Olds, M. Tilton, Y.S. Chu, E. Dooryhee, G.P. Manogharan, J.R. Trelewicz, *Addit. Manuf.* 47 (2021) 102263.
- [446] C.H. Yu, A. Leicht, R.L. Peng, J. Moverare, *Mater. Sci. Eng. A* 821 (2021) 141598.
- [447] D. Riabov, A. Leicht, J. Ahlström, E. Hryha, *Mater. Sci. Eng. A* 822 (2021) 141699.
- [448] L. Cui, F. Jiang, R.L. Peng, R.T. Mousavian, Z. Yang, J. Moverare, *Int. J. Plast.* 149 (2022) 103172.
- [449] S. Tekumalla, B. Selvarajou, S. Raman, S. Gao, M. Seita, *Mater. Sci. Eng. A* 833 (2022) 142493.
- [450] L. Cui, S. Jiang, J. Xu, R.L. Peng, R.T. Mousavian, J. Moverare, *Mater. Des.* 198 (2021) 109385.
- [451] A. Heidarzadeh, J. Zava, R. Shabadi, R.T. Mousavian, *Mater. Sci. Eng. A* 814 (2021) 141214 Contents.

- [452] H.E. Sabzi, E. Hernandez-Nava, X.H. Li, H. Fu, D. San-Martín, P.E.J. Rivera-Díaz-del-Castillo, *Mater. Des.* 212 (2021) 110246.
- [453] J. Samei, H. Asgari, C. Pelligra, M. Sanjari, S. Salavati, A. Shahriari, M. Amirmaleki, M. Jahanbakht, A. Hadadzadeh, B.S. Amirkhiz, M. Mohammadi, *Addit. Manuf.* 45 (2021) 102068.
- [454] Y. Zou, C. Tan, Z. Qiu, W. Ma, M. Kuang, D. Zeng, *Addit. Manuf.* 41 (2021) 101971.
- [455] T.S. Byun, B.E. Garrison, M.R. McAlister, X. Chen, M.N. Gussev, T.G. Lach, A. Le Coq, K. Linton, C.B. Joslin, J.K. Carver, F.A. List, R.R. Dehoff, K.A. Terrani, J. Nucl. Mater. 548 (2021) 152849.
- [456] X. Zhang, P. Kenesei, J.S. Park, J. Almer, M. Li, J. Nucl. Mater. 549 (2021) 152874.
- [457] A. Shahriari, M. Ghaffari, L. Khaksar, A. Nasiri, A. Hadadzadeh, B.S. Amirkhiz, M. Mohammadi, *Corros. Sci.* 184 (2021) 109362.
- [458] M. Shamsujjoha, S.R. Agnew, J.M. Fitz-Gerald, W.R. Moore, T.A. Newman, *Metall. Mater. Trans. A Phys. Metall. Mater. Sci.* 49 (2018) 3011–3027.
- [459] W. Chen, T. Voisin, Y. Zhang, J.B. Florien, C.M. Spadaccini, D.L. McDowell, T. Zhu, Y.M. Wang, *Nat. Commun.* 10 (2019) 1–12.
- [460] Z. Li, B. He, Q. Guo, *Scr. Mater.* 177 (2020) 17–21.
- [461] T. Voisin, J.B. Forien, A. Perron, S. Aubry, N. Bertin, A. Samanta, A. Baker, Y.M.

- Wang, *ACTA Mater.* 203 (2021) 116476.
- [462] Y.M. Wang, T. Voisin, J.T. McKeown, J. Ye, N.P. Calta, Z. Li, Z. Zeng, Y. Zhang, W. Chen, T.T. Roehling, R.T. Ott, M.K. Santala, P.J. Depond, M.J. Matthews, A. V. Hamza, T. Zhu, *Nat. Mater.* 17 (2018) 63–70.
- [463] H.G. Coe, S. Pasebani, *J. Manuf. Mater. Process.* 4 (2020) 8.
- [464] P. Krakhmalev, I. Yadroitsava, G. Fredriksson, I. Yadroitsev, *South African J. Ind. Eng.* May 28 (2017) 12–19.
- [465] N. Chen, G. Ma, W. Zhu, A. Godfrey, Z. Shen, G. Wu, X. Huang, *Mater. Sci. Eng. A* 759 (2019) 65–69.
- [466] M.L. Montero-Sistiaga, M. Godino-Martinez, K. Boschmans, J.P. Kruth, J. Van Humbeeck, K. Vanmeensel, *Addit. Manuf.* 23 (2018) 402–410.
- [467] O.O. Salman, C. Gammer, A.K. Chaubey, J. Eckert, S. Scudino, *Mater. Sci. Eng. A* 748 (2019) 205–212.
- [468] J. Suryawanshi, K.G. Prashanth, U. Ramamurty, *Mater. Sci. Eng. A* 696 (2017) 113–121.
- [469] Z. Sun, X. Tan, S.B. Tor, C.K. Chua, *NPG Asia Mater.* 10 (2018) 127–136.
- [470] R.I. Revilla, M. Van Calster, M. Raes, G. Arroud, F. Andreatta, L. Pyl, P. Guillaume, I. De Graeve, *Corros. Sci.* 176 (2020) 108914.
- [471] M. Godec, S. Zaefferer, B. Podgornik, M. Šinko, E. Tchernychova, *Mater. Charact.*

160 (2020) 110074.

- [472] M.J.K. Lodhi, K.M. Deen, M.C. Greenlee-Wacker, W. Haider, *Addit. Manuf.* 27 (2019) 8–19.
- [473] Y. Sun, R.J. Hebert, M. Aindow, *Mater. Des.* 140 (2018) 153–162.
- [474] D. Kong, X. Ni, C. Dong, L. Zhang, C. Man, J. Yao, K. Xiao, X. Li, *Electrochim. Acta* 276 (2018) 293–303.
- [475] D. Kong, C. Dong, X. Ni, L. Zhang, J. Yao, C. Man, X. Cheng, K. Xiao, X. Li, J. *Mater. Sci. Technol.* 35 (2019) 1499–1507.
- [476] D. Kong, C. Dong, X. Ni, Z. Liang, X. Li, J. *Mater. Sci. Technol.* 89 (2021) 133–140.
- [477] K. Saeidi, X. Gao, F. Lofaj, L. Kvetková, Z.J. Shen, *J. Alloys Compd.* 633 (2015) 463–469.
- [478] J.A. Cherry, H.M. Davies, S. Mehmood, N.P. Lavery, S.G.R. Brown, J. Sienz, *Int. J. Adv. Manuf. Technol.* 76 (2015) 869–879.
- [479] J.G. Kim, J.B. Seol, J.M. Park, H. Sung, S.H. Park, H.S. Kim, *Met. Mater. Int.* 27 (2021) 2614–2622.
- [480] D. Kumar, S. Jhavar, A. Arya, K.G. Prashanth, S. Suwas, *Int. J. Fract.* (2021) 1–18.
- [481] D. dependent strain hardening in additively manufactured stainless steel 316L  
Kumar, G. Shankar, K.G. Prashanth, S. Suwas, *Mater. Sci. Eng. A* 820 (2021)

141483.

- [482] D. Gonzalez-Nino, T. Strasser, G.S. Prinz, *Metals* (Basel). 11 (2021).
- [483] H. Zhang, M. Xu, P. Kumar, C. Li, W. Dai, Z. Liu, Z. Li, Y. Zhang, *Virtual Phys. Prototyp.* 16 (2021) 125–145.
- [484] Y. Wang, Y. ting Wang, R. di Li, P. da Niu, M. bo Wang, T. chui Yuan, K. Li, J. Cent. South Univ. 28 (2021) 1043–1057.
- [485] K.M. Bertsch, G. Meric de Bellefon, B. Kuehl, D.J. Thoma, *ACTA Mater.* 199 (2020) 19–33.
- [486] D. Kong, C. Dong, X. Ni, Z. Liang, C. Man, X. Li, *Mater. Res. Lett.* 8 (2020) 390–397.
- [487] D. Kong, X. Ni, C. Dong, X. Lei, L. Zhang, C. Man, J. Yao, X. Cheng, X. Li, *Mater. Des.* 152 (2018) 88–101.
- [488] D. Kong, C. Dong, X. Ni, L. Zhang, H. Luo, R. Li, L. Wang, C. Man, X. Li, *Appl. Surf. Sci.* 504 (2020) 144495.
- [489] C. Qiu, M. Al Kindi, A.S. Aladawi, I. Al Hatmi, *Sci. Rep.* 8 (2018) 1–16.
- [490] Y. Hong, C. Zhou, Y. Zheng, L. Zhang, J. Zheng, X. Chen, B. An, *Mater. Sci. Eng. A* 740–741 (2019) 420–426.
- [491] Q. Chao, V. Cruz, S. Thomas, N. Birbilis, P. Collins, A. Taylor, P.D. Hodgson, D. Fabijanic, *Scr. Mater.* 141 (2017) 94–98.

- [492] A. Heidarzadeh, M. Neikter, N. Enikeev, L. Cui, F. Forouzan, R.T. Mousavian, Mater. Sci. Eng. A 811 (2021) 141086.
- [493] L. Chen, W. Liu, L. Song, Mater. Sci. Eng. A 820 (2021) 141493.
- [494] J. Jeong, Y. Lee, J.M. Park, D.J. Lee, I. Jeon, H. Sohn, H.S. Kim, T.H. Nam, H. Sung, J.B. Seol, J.G. Kim, Addit. Manuf. 47 (2021) 102363.
- [495] Z. Yan, K. Zou, M. Cheng, Z. Zhou, L. Song, J. Mater. Res. Technol. 15 (2021) 582–594.
- [496] X.L. Liu, Q.Q. Xue, W. Wang, L.L. Zhou, P. Jiang, H.S. Ma, F.P. Yuan, Y.G. Wei, X.L. Wu, Materialia 7 (2019) 100376.
- [497] H. Chae, M.Y. Luo, E.W. Huang, E. Shin, C. Do, S.K. Hong, W. Woo, S.Y. Lee, Mater. Charact. 184 (2022) 111645.
- [498] D. Wolf, Curr. Opin. Solid State Mater. Sci. 5 (2001) 435–443.
- [499] D. Kuhlmann-Wilsdorf, Mater. Sci. Eng. A 113 (1989) 1–41.
- [500] E. Ma, T. Zhu, Mater. Today 20 (2017) 323–331.
- [501] B. Sharma, G. Dirras, K. Ameyama, Metals (Basel). 10 (2020) 1615–1631.
- [502] H. Fujiwara, R. Akada, A. Noro, Y. Yoshita, K. Ameyama, Mater. Trans. 49 (2008) 90–96.
- [503] L. Tang, Y. Zhao, R.K. Islamgaliev, C.Y.A. Tsao, R.Z. Valiev, E.J. Lavernia, Y.T. Zhu, Mater. Sci. Eng. A 670 (2016) 280–291.

- [504] B. Ravi Kumar, A. Gujral, *Metallogr. Microstruct. Anal.* 3 (2014) 397–407.
- [505] O. Renk, A. Hohenwarter, R. Pippan, *Adv. Eng. Mater.* 14 (2012) 948–954.
- [506] K. Selvam, J. Saini, G. Perumal, A. Ayyagari, R. Salloom, R. Mondal, S. Mukherjee, H.S. Grewal, H.S. Arora, *Tribol. Int.* 134 (2019) 77–86.
- [507] J. Gubicza, M. El-Tahawy, Y. Huang, H. Choi, H. Choe, J.L. Lábár, T.G. Langdon, *Mater. Sci. Eng. A* 657 (2016) 215–223.
- [508] M. El-Tahawy, Y. Huang, H. Choi, H. Choe, J.L. Lábár, T.G. Langdon, J. Gubicza, *Mater. Sci. Eng. A* 682 (2017) 323–331.
- [509] H.S. Arora, A. Ayyagari, J. Saini, K. Selvam, S. Riyadh, M. Pole, H.S. Grewal, S. Mukherjee, *Sci. Rep.* 9 (2019) 1972–1978.
- [510] M.H. Mosallanejad, B. Niroumand, A. Aversa, A. Saboori, *J. Alloys Compd.* 872 (2021) 159567.
- [511] R. Sampson, R. Lancaster, M. Sutcliffe, D. Carswell, C. Hauser, J. Barras, *Opt. Laser Technol.* 134 (2021) 106609.
- [512] B. Ravi Kumar, B. Mahato, S. Sharma, J.K. Sahu, *Metall. Mater. Trans. A Phys. Metall. Mater. Sci.* 40 (2009) 3226–3234.
- [513] S.H. Kim, H. Kim, N.J. Kim, *Nature* 518 (2015) 77–79.
- [514] M.G. Meozzi, J. Eiken, M.J. Santofimia, J. Sietsma, *Comput. Mater. Sci.* 112 (2016) 245–256.

- [515] J. Zhu, Y. Gao, D. Wang, T.Y. Zhang, Y. Wang, *ACTA Mater.* 130 (2017) 196–207.
- [516] N. Bontcheva, P. Petrov, G. Petzov, L. Parashkevova, *Comput. Mater. Sci.* 40 (2007) 90–100.
- [517] H.K. Yeddu, *Comput. Mater. Sci.* 154 (2018) 75–83.
- [518] A. Malik, J. Odqvist, L. Höglund, S. Hertzman, J. Ågren, *Metall. Mater. Trans. A Phys. Metall. Mater. Sci.* 48 (2017) 4914–4928.
- [519] M.S. Geshani, H. Mirzadeh, M.J. Sohrabi, *Steel Res. Int.* 2100676 (2022) 1–5.
- [520] H. Wang, X. Gao, S. Chen, Y. Li, Z. Wu, H. Ren, *J. Alloys Compd.* 846 (2020) 156386.
- [521] S. Jiang, H. Wang, Y. Wu, X. Liu, H. Chen, M. Yao, B. Gault, D. Ponge, D. Raabe, A. Hirata, M. Chen, Y. Wang, Z. Lu, *Nature* 544 (2017) 460–464.
- [522] H. Kong, C. Liu, *Technologies* 6 (2018) 36.
- [523] T. Zhang, D. Wang, Y. Wang, *ACTA Mater.* 196 (2020) 409–417.
- [524] J. Zhu, T. Zhang, Y. Yang, C.T. Liu, *ACTA Mater.* 166 (2019) 560–571.
- [525] Y. Wei, Y. Xu, Z. Dong, X. Zhan, *J. Mater. Process. Technol.* 209 (2009) 1466–1470.
- [526] L. Shi, S.A. Alexandratos, N.P. O’Dowd, *Proc. Inst. Mech. Eng. Part L J. Mater. Des. Appl.* 233 (2019) 13–27.



- [527] D.J. Srolovitz, G.S. Grest, M.P. Anderson, A.D. Rollett, *Acta Metall.* 36 (1988) 2115–2128.
- [528] D.J. Srolovitz, G.S. Grest, M.P. Anderson, *Acta Metall.* 34 (1986) 1833–1845.
- [529] A.D. Rollett, D.J. Srolovitz, M.P. Anderson, R.D. Doherty, *Acta Metall. Mater.* 40 (1992) 3475–3495.
- [530] D. Raabe, L. Hantcherli, *Comput. Mater. Sci.* 34 (2005) 299–313.
- [531] A.D. Rollett, D. Raabe, *Comput. Mater. Sci.* 21 (2001) 69–78.
- [532] X. Wang, J. Li, F. Cazes, A. Hocini, G. Dirras, *Int. J. Plast.* 133 (2020) 102793.
- [533] Z. Zeng, X. Li, D. Xu, L. Lu, H. Gao, T. Zhu, *Extrem. Mech. Lett.* 8 (2016) 213–219.
- [534] Y. Lin, J. Pan, H.F. Zhou, H.J. Gao, Y. Li, *ACTA Mater.* 153 (2018) 279–289.
- [535] L. Zhu, H. Ruan, A. Chen, X. Guo, J. Lu, *ACTA Mater.* 128 (2017) 375–390.
- [536] L. Zhu, C. Wen, C. Gao, X. Guo, J. Lu, *Scr. Mater.* 133 (2017) 49–53.
- [537] L. Zhu, C. Wen, C. Gao, X. Guo, Z. Chen, J. Lu, *Int. J. Plast.* 114 (2019) 272–278.
- [538] Y. Aoyagi, C. Watanabe, M. Kobayashi, Y. Todaka, H. Miura, *Iron Steel Inst Japan-J* 105 (2019) 140–149.
- [539] J. Peng, L. Li, F. Li, B. Liu, S. Zhrebtssov, Q. Fang, J. Li, N. Stepanov, Y. Liu, F. Liu, P.K. Liaw, *Int. J. Plast.* 145 (2021) 1–18.

- [540] J. Li, L. Li, C. Jiang, Q. Fang, F. Liu, Y. Liu, P.K. Liaw, *J. Mater. Sci. Technol.* 57 (2020) 85–91.
- [541] T.R. Bieler, P. Eisenlohr, F. Roters, D. Kumar, D.E. Mason, M.A. Crimp, D. Raabe, *Int. J. Plast.* 25 (2009) 1655–1683.
- [542] T.T. Nguyen, J. Yvonnet, Q.Z. Zhu, M. Bornert, C. Chateau, *Eng. Fract. Mech.* 139 (2015) 18–39.
- [543] T.T. Nguyen, D. Waldmann, T.Q. Bui, *J. Comput. Phys.* 386 (2019) 585–610.
- [544] R. Alessi, F. Freddi, *Compos. Struct.* 181 (2017) 9–25.
- [545] Y.J. Cao, W.Q. Shen, J.F. Shao, W. Wang, *Int. J. Plast.* 133 (2020) 102786.
- [546] U.F. Kocks, C.N. Tomé, H.-R. Wenk, *Texture and Anisotropy: Preferred Orientations in Polycrystals and Their Effect on Materials Properties*, Cambridge University Press, 1998.
- [547] S. Takajo, C.N. Tomé, S.C. Vogel, I.J. Beyerlein, *Int. J. Plast.* 109 (2018) 137–152.
- [548] L. Karlsson, J. Börjesson, *Sci. Technol. Weld. Join.* 19 (2014) 318–323.
- [549] L.K. Singhal, J.W. Martin, *Acta Metall.* 16 (1968) 1441–1451.
- [550] H. Jiao, M. Aindow, R.C. Pond, *Philos. Mag.* 83 (2003) 1867–1887.
- [551] Y. Higo, F. Lecroisey, T. Mori, *Acta Metall.* 22 (1974) 313–323.
- [552] I.J. Beyerlein, N.A. Mara, J. Wang, J.S. Carpenter, S.J. Zheng, W.Z. Han, R.F.

- Zhang, K. Kang, T. Nizolek, T.M. Pollock, JOM 64 (2012) 1192–1207.
- [553] S. Pathak, N. Velisavljevic, J. Kevin Baldwin, M. Jain, S. Zheng, N.A. Mara, I.J. Beyerlein, Sci. Rep. 7 (2017) 1–9.
- [554] T. Nizolek, I.J. Beyerlein, N.A. Mara, J.T. Avallone, T.M. Pollock, Appl. Phys. Lett. 108 (2016) 051903.
- [555] I.J. Beyerlein, J.R. Mayeur, R.J. McCabe, S.J. Zheng, J.S. Carpenter, N.A. Mara, ACTA Mater. 72 (2014) 137–147.
- [556] M. Ardeljan, M. Knezevic, M. Jain, S. Pathak, A. Kumar, N. Li, N.A. Mara, J.K. Baldwin, I.J. Beyerlein, J. Mater. Res. 33 (2018) 1311–1332.
- [557] A. Kumar, I.J. Beyerlein, J. Wang, Appl. Phys. Lett. 105 (2014) 071602.
- [558] J. Wang, M. Knezevic, M. Jain, S. Pathak, I.J. Beyerlein, J. Mech. Phys. Solids 152 (2021) 104421.
- [559] I.J. Beyerlein, J.R. Mayeur, S. Zheng, N.A. Mara, J. Wang, A. Misra, Proc. Natl. Acad. Sci. U. S. A. 111 (2014) 4386–4390.
- [560] K. Kang, J. Wang, I.J. Beyerlein, J. Appl. Phys. 111 (2012) 053531.
- [561] T. Chen, R. Yuan, I.J. Beyerlein, C. Zhou, Int. J. Plast. 124 (2020) 247–260.
- [562] T.J. Nizolek, M.R. Begley, R.J. McCabe, J.T. Avallone, N.A. Mara, I.J. Beyerlein, T.M. Pollock, ACTA Mater. 133 (2017) 303–315.
- [563] I.J. Beyerlein, N.A. Mara, D. Bhattacharyya, D.J. Alexander, C.T. Necker, Int. J.

Plast. 27 (2011) 121–146.

- [564] J.B. Liu, Y.W. Zeng, L. Meng, J. Alloys Compd. 464 (2008) 168–173.
- [565] J.W. Zhang, I.J. Beyerlein, W.Z. Han, Phys. Rev. Lett. 122 (2019) 255501.
- [566] H. Zhou, C. Huang, X. Sha, L. Xiao, X. Ma, H.W. Höppel, M. Göken, X. Wu, K. Ameyama, X. Han, Y. Zhu, Mater. Res. Lett. 7 (2019) 376–382.
- [567] Y.F. Wang, C.X. Huang, X.T. Fang, H.W. Höppel, M. Göken, Y.T. Zhu, Scr. Mater. 174 (2020) 19–23.
- [568] G. Cailletaud, Int. J. Plast. 8 (1992) 55–73.
- [569] N. Wang, Y. Chen, G. Wu, Q. Zhao, Z. Zhang, L. Zhu, J. Luo, Mater. Sci. Eng. A 836 (2022) 142728.
- [570] T.R. Smith, J.D. Sugar, C. San Marchi, J.M. Schoenung, ACTA Mater. 164 (2019) 728–740.
- [571] Y.S. Li, Y. Zhang, N.R. Tao, K. Lu, Scr. Mater. 59 (2008) 475–478.
- [572] I.S. Yasnikov, A. Vinogradov, Y. Estrin, Scr. Mater. 76 (2014) 37–40.
- [573] F. Yin, S. Hu, R. Xu, X. Han, D. Qian, W. Wei, L. Hua, K. Zhao, Int. J. Plast. 129 (2020) 102696.
- [574] P.M. Anderson, T. Foecke, P.M. Hazzledine, MRS Bull. 24 (1999) 27–33.
- [575] P.M. Anderson, C. Li, Nanostructured Mater. 5 (1995) 349–362.

- [576] R.W. Armstrong, Y.T. Chou, R.M. Fisher, N. Louat, *Philos. Mag.* 14 (1966) 943–951.
- [577] Q. Han, X. Yi, *J. Mech. Phys. Solids* 154 (2021) 104530.
- [578] S. Sin, Z. Hoe, Z. Wu, Y. Wei, *J. Mech. Phys. Solids* 88 (2016) 252–266.
- [579] C.E. Carlton, P.J. Ferreira, *ACTA Mater.* 55 (2007) 3749–3756.
- [580] S.N. Naik, *J. Mater. Sci.* 55 (2020) 2661–2681.
- [581] S.H. Sun, T. Ishimoto, K. Hagihara, Y. Tsutsumi, T. Hanawa, T. Nakano, *Scr. Mater.* 159 (2019) 89–93.
- [582] D. Orlov, J. Zhou, S. Hall, M. Ota-Kawabata, K. Ameyama, *IOP Conf. Ser. Mater. Sci. Eng.* 580 (2019) 012019.
- [583] M. Nakatani, Y. Fujiki, M. Ota, S.K. Vajpai, K. Ameyama, *Mater. Sci. Forum* 879 (2017) 2507–2511.
- [584] Y. Dong, Z. Zhang, Z. Yang, R. Zheng., X. Chen., *Materials (Basel)*. 15 (2021) 181.
- [585] A. Radi, P. Asghari-Rad, H.S. Kim, G.G. Yapici, *J. Alloys Compd.* 905 (2022) 164014.
- [586] G. Niu, Q. Tang, H.S. Zurob, H. Wu, L. Xu, N. Gong, *Mater. Sci. Eng. A* 759 (2019) 1–10.
- [587] M.X. Huang, B.B. He, *J. Mater. Sci. Technol.* 34 (2018) 417–420.

- [588] F.J. Humphreys, P.B. Prangnell, J.R. Bowen, A. Gholinia, C. Harris, *Philos. Trans. R. Soc. A Math. Phys. Eng. Sci.* 357 (1999) 1663–1681.
- [589] M. El-Tahawy, P.H.R. Pereira, Y. Huang, H. Park, H. Choe, T.G. Langdon, J. Gubicza, *Mater. Lett.* 214 (2018) 240–242.
- [590] A. Ohmori, S. Torizuka, K. Nagai, *ISIJ Int.* 44 (2004) 1063–1071.
- [591] J.N. Hall, J. Wayne Jones, A.K. Sachdev, *Mater. Sci. Eng. A* 183 (1994) 69–80.
- [592] D. Frómeta, A. Lara, L. Grifé, T. Dieudonné, P. Dietsch, J. Rehr, C. Suppan, D. Casellas, J. Calvo, *Metall. Mater. Trans. A Phys. Metall. Mater. Sci.* 52 (2021) 840–856.
- [593] P. Jacques, Q. Furnémont, A. Mertens, F. Delannay, *Philos. Mag. A Phys. Condens. Matter, Struct. Defects Mech. Prop.* 81 (2001) 1789–1812.
- [594] S. Wang, J. Li, Y. Cao, B. Gao, Q. Mao, Y. Li, *Vacuum* 152 (2018) 261–264.
- [595] A. M. F., *Philos. Mag.* 21 (1970) 399–424.
- [596] P. Sudharshan Phani, W.C. Oliver, *Mater. Des.* 164 (2019) 107563.
- [597] J.J. Roa, P. Sudharshan Phani, W.C. Oliver, L. Llanes, *Int. J. Refract. Met. Hard Mater.* 75 (2018) 211–217.
- [598] N.X. Randall, M. Vandamme, F.J. Ulm, *J. Mater. Res.* 24 (2009) 679–690.
- [599] H. Yu, M. Yan, C. Lu, A.K. Tieu, H. Li, Q. Zhu, A. Godbole, J. Li, L. Su, C. Kong, *Sci. Rep.* 6 (2016) 1–7.

- [600] W. Handoko, A. Anurag, F. Pahlevani, R. Hossain, K. Privat, V. Sahajwalla, *Sci. Rep.* 9 (2019) 1–11.
- [601] S. Kumar, S. Krisam, A. Jacob, F. Kiraly, A. Keplinger, R. Abart, E. Povoden-Karadeniz, *Mater. Des.* 194 (2020) 108951.
- [602] P.K. Rai, S. Shekhar, K. Yagi, K. Ameyama, K. Mondal, *Wear* 424–425 (2019) 23–32.
- [603] Y. Sun, R. Bailey, *Surf. Coatings Technol.* 253 (2014) 284–291.
- [604] H. Wang, I. Shuro, M. Umemoto, K. Ho-Hung, Y. Todaka, *Mater. Sci. Eng. A* 556 (2012) 906–910.
- [605] F.R. Zulfi, A.A. Korda, *J. Phys. Conf. Ser.* 739 (2016) 012039.
- [606] K. Stein-Fechner, J. Konys, O. Wedemeyer, *J. Nucl. Mater.* 249 (1997) 33–38.
- [607] D.S. Stone, K.B. Yoder, W.D. Sproul, *J. Vac. Sci. Technol. A Vacuum, Surfaces, Film.* 9 (1991) 2543–2547.
- [608] X. Pan, G. Qian, S. Wu, Y. Fu, Y. Hong, *Sci. Rep.* 10 (2020) 1–6.
- [609] Q. Pan, L. Lu, *Scr. Mater.* 187 (2020) 301–306.
- [610] H.S. Ho, W.L. Zhou, Y. Li, K.K. Liu, E. Zhang, *Int. J. Fatigue* 134 (2020) 105481.
- [611] Y.B. Lei, Z.B. Wang, J.L. Xu, K. Lu, *ACTA Mater.* 168 (2019) 133–142.
- [612] C. Wang, K. Luo, X. Bu, Y. Su, J. Cai, Q. Zhang, J. Lu, *Corros. Sci.* 177 (2020)

109027.

- [613] A. Sharma, M.C. Oh, B. Ahn, *Metals* (Basel). 10 (2020) 1–23.
- [614] S. Kikuchi, Y. Nukui, Y. Nakatsuka, Y. Nakai, M. Nakatani, M.O. Kawabata, K. Ameyama, *Int. J. Fatigue* 127 (2019) 222–228.
- [615] S. Kikuchi, Y. Nakatsuka, Y. Nakai, M. Natakani, M.O. Kawabata, K. Ameyama, *Frat. Ed Integrita Strutt.* 13 (2019) 545–553.
- [616] R. Casati, J. Lemke, M. Vedani, *J. Mater. Sci. Technol.* 32 (2016) 738–744.
- [617] Q. Li, F.K. Yan, N.R. Tao, D. Ponge, D. Raabe, K. Lu, *ACTA Mater.* 165 (2019) 87–98.
- [618] F. Cui, Q.S. Pan, N.R. Tao, L. Lu, *Int. J. Fatigue* 143 (2021) 105994.
- [619] A. Matsushita, Y. Mine, K. Takashima, *Scr. Mater.* 201 (2021) 113976.
- [620] W. Zhai, L. Bai, R. Zhou, X. Fan, G. Kang, Y. Liu, K. Zhou, *Adv. Sci.* 8 (2021) 1–29.
- [621] M. Khadem, O. V. Penkov, H.K. Yang, D.E. Kim, *Friction* 5 (2017) 248–262.
- [622] H. Bin Go, J.Y. Bang, K.N. Kim, K.M. Kim, J.S. Kwon, *Materials* (Basel). 14 (2021) 1–13.
- [623] J.D. Bressan, D.P. Daros, A. Sokolowski, R.A. Mesquita, C.A. Barbosa, *J. Mater. Process. Technol.* 205 (2008) 353–359.



- [624] X.H. Cui, S.Q. Wang, F. Wang, K.M. Chen, *Wear* 265 (2008) 468–476.
- [625] A. Jourani, S. Bouvier, *Tribol. Trans.* 58 (2015) 131–139.
- [626] P.K. Rai, S. Shekhar, M. Nakatani, M. Ota, S.K. Vajpai, K. Ameyama, K. Mondal, J. Mater. Eng. Perform. 26 (2017) 2608–2618.
- [627] M. Karimi, *Mater. Res. Express* 6 (2019) 125065.
- [628] P.L. Hurricks, *Wear* 26 (1973) 285–304.
- [629] M. Bahshwan, C.W. Myant, T. Reddyhoff, M.S. Pham, *Mater. Des.* 196 (2020) 109076.
- [630] J. Liu, X.T. Deng, L. Huang, Z.D. Wang, *Tribol. Int.* 152 (2020) 106520.
- [631] C. Allen, A. Ball, *Wear* 74 (1982) 287–305.
- [632] B. Wang, B. Yao, Z. Han, J. Mater. Sci. Technol. 28 (2012) 871–877.
- [633] M. Fellah, M. Labaiz, O. Assala, A. Lost, L. Dekhil, *Tribol. - Mater. Surfaces Interfaces* 7 (2013) 135–149.
- [634] J.S. Rau, S. Balachandran, R. Schneider, P. Gumbsch, B. Gault, C. Greiner, *ACTA Mater.* 221 (2021) 117353.
- [635] J.F. Archard, *J. Appl. Phys.* 24 (1953) 981–988.
- [636] T. Telliskivi, *Wear* 256 (2004) 817–831.
- [637] A. Berradja, *Corros. Inhib.* (2019) 1–24.

- [638] Z. Nasiri, S. Ghaemifar, M. Naghizadeh, H. Mirzadeh, *Met. Mater. Int.* 27 (2021) 2078–2094.
- [639] J. Yan, T. Asami, T. Kuriyagawa, *Precis. Eng.* 32 (2008) 186–195.
- [640] W.F. Gaertner, E.E. Hoppe, M.A. Omari, R.S. Sorbello, C.R. Aita, *J. Vac. Sci. Technol. A Vacuum, Surfaces, Film.* 22 (2004) 272–280.
- [641] M.A. Almomani, C.R. Aita, *J. Vac. Sci. Technol. A Vacuum, Surfaces, Film.* 27 (2009) 449–455.
- [642] R.B. Inturi, Z. Szklarska-Smialowska, *Corrosion* 48 (1992) 398–403.
- [643] D.E. Williams, M.R. Kilburn, J. Cliff, G.I.N. Waterhouse, *Corros. Sci.* 52 (2010) 3702–3716.
- [644] C. Pan, L. Liu, Y. Li, F. Wang, *Corros. Sci.* 73 (2013) 32–43.
- [645] C. Punckt, M. Bölscher, H.H. Rotermund, A.S. Mikhailov, L. Organ, N. Budiansky, J.R. Scully, J.L. Hudson, *Science* (80-. ). 305 (2004) 1133–1136.
- [646] ASM Handbook Committee, *ASM Handbook. Corrosion: Fundamentals, Testing, and Protection*, ASM International, 2003.
- [647] M. Abdulstaar, M. Mhaede, L. Wagner, M. Wollmann, *Mater. Des.* 57 (2014) 325–329.
- [648] P. jun Wang, L. wei Ma, X. qun Cheng, X. gang Li, *Int. J. Miner. Metall. Mater.* 28 (2021) 1112–1126.

- [649] P. Reccagni, L.H. Guilherme, Q. Lu, M.F. Gittos, D.L. Engelberg, *Corros. Sci.* 161 (2019) 108198.
- [650] Z. Zhang, H. Jing, L. Xu, Y. Han, L. Zhao, J. Zhang, *Appl. Surf. Sci.* 394 (2017) 297–314.
- [651] S. Atamert, J.E. King, *Acta Metall. Mater.* 39 (1991) 273–285.
- [652] R.C. Newman, *Shreir's Corros.* (2010) 864–901.
- [653] X. Cheng, Y. Wang, C. Dong, X. Li, *Corros. Sci.* 134 (2018) 122–130.
- [654] X. Cheng, Y. Wang, X. Li, C. Dong, *J. Mater. Sci. Technol.* 34 (2018) 2140–2148.
- [655] R.A. Cottis, R.C. Newman, *Stress Corrosion Cracking Resistance of Duplex Stainless Steels*, United Kingdom, 1995.
- [656] G. Palumbo, S.J. Thorpe, K.T. Aust, *Scr. Metall. Mater.* 24 (1990) 1347–1350.
- [657] L. Liu, Y. Li, F. Wang, *J. Mater. Sci. Technol.* 26 (2010) 1–14.
- [658] R. Kirchheim, X.Y. Huang, P. Cui, R. Birringer, H. Gleiter, *Nanostructured Mater.* 1 (1992) 167–172.
- [659] Z.B. Wang, N.R. Tao, W.P. Tong, J. Lu, K. Lu, *ACTA Mater.* 51 (2003) 4319–4329.
- [660] C. Pan, L. Liu, Y. Li, B. Zhang, F. Wang, *J. Electrochem. Soc.* 159 (2012) C453–C460.
- [661] G. Tranchida, M. Clesi, F. Di Franco, F. Di Quarto, M. Santamaria, *Electrochim.*

Acta 273 (2018) 412–423.

- [662] C. Zhang, Z.W. Zhang, L. Liu, *Electrochim. Acta* 210 (2016) 401–406.
- [663] L. Liu, Y. Li, F. Wang, *Electrochim. Acta* 55 (2010) 2430–2436.
- [664] F. Yan, N. Tao, C. Pan, L. Liu, *Adv. Eng. Mater.* 18 (2016) 650–656.
- [665] T. Fujita, Z. Horita, T.G. Langdon, *Mater. Sci. Eng. A* 371 (2004) 241–250.
- [666] A.Q. Lu, Y. Zhang, Y. Li, G. Liu, Q.H. Zang, C.M. Liu, *Acta Metall. Sin. (English Lett.* 19 (2006) 183–189.
- [667] L. Romero-Resendiz, M. Hernández, J.M. Cabrera, S. Elizalde, I.A. Figueroa, A. Covelo, G. Gonzalez, *J. Appl. Res. Technol.* (2022) Article in press.
- [668] L. Romero-Resendiz, J.M. Cabrera, S. Elizalde, I.A. Figueroa, G. Gonzalez, *J. Mater. Res. Technol.* 18 (2022) 1281–1294.
- [669] L. Romero-Resendiz, V. Amigo-Borras, A. Vicente-Escuder, S. Elizalde, J.M. Cabrera, D. Pineda-Ruiz, I.A. Figueroa, G. Gonzalez, *J. Mater. Res. Technol.* 15 (2021) 4564–4572.
- [670] D. Enning, J. Garrelfs, *Appl. Environ. Microbiol.* 80 (2014) 1226–1236.
- [671] T.J.M. J.W. Costerton, K.J. Cheng, G.G. Geesey, T.I. Ladd, J.C. Nickel, M. Dasgupta, *Ann. Rev. Microbiol.* 41 (1987) 435–464.
- [672] R. Javaherdashti, *Microbiologically Influenced Corrosion: An Engineering Insight*, 1st, Springer, 2008.

- [673] C.A. Loto, *Int. J. Adv. Manuf. Technol.* 92 (2017) 4241–4252.
- [674] S.E. Coetser, T.E. Cloete, *Crit. Rev. Microbiol.* 31 (2005) 213–232.
- [675] M.A. Javed, P.R. Stoddart, E.A. Palombo, S.L. McArthur, S.A. Wade, *Corros. Sci.* 86 (2014) 149–158.
- [676] F.M. AlAbbas, C. Williamson, S.M. Bhola, J.R. Spear, D.L. Olson, B. Mishra, A.E. Kakpovbia, *Int. Biodeterior. Biodegrad.* 78 (2013) 34–42.
- [677] X. Shi, C. Yang, W. Yan, D. Xu, M. Yan, Y. Shan, K. Yang, *J. Chinese Soc. Corros. Prot.* 39 (2019) 9–17.
- [678] K. Yang, X. Shi, W. Yan, Y. Zeng, Y. Shan, Y. Ren, *Jinshu Xuebao/Acta Metall. Sin.* 56 (2020) 385–399.
- [679] I.B. Beech, C.C. Gaylarde, *J. Appl. Bacteriol.* 67 (1989) 201–207.
- [680] T.L. Mai, D.E. Conner, *Int. J. Food Microbiol.* 120 (2007) 282–286.
- [681] R.J. Crawford, H.K. Webb, V.K. Truong, J. Hasan, E.P. Ivanova, *Adv. Colloid Interface Sci.* 179–182 (2012) 142–149.
- [682] M.A. Javed, P.R. Stoddart, S.L. McArthur, S.A. Wade, *Biofouling* 29 (2013) 939–952.
- [683] B. Tribollet, *Nucl. Corros. Sci. Eng.* (2012) 230–261.
- [684] E. Huttunen-Saarivirta, M. Honkanen, T. Lepistö, V.T. Kuokkala, L. Koivisto, C.G. Berg, *Appl. Surf. Sci.* 258 (2012) 6512–6526.

- [685] W. Liu, Eng. Fail. Anal. 42 (2014) 109–120.
- [686] H. Li, E. Zhou, D. Zhang, D. Xu, J. Xia, C. Yang, H. Feng, Z. Jiang, X. Li, T. Gu, K. Yang, Sci. Rep. 6 (2016) 1–12.
- [687] E. Zhou, H. Li, C. Yang, J. Wang, D. Xu, D. Zhang, T. Gu, Int. Biodeterior. Biodegrad. 127 (2018) 1–9.
- [688] Y. Dong, Y. Lekbach, Z. Li, D. Xu, S. El Abed, S. Ibnsouda Koraichi, F. Wang, J. Mater. Sci. Technol. 37 (2020) 200–206.
- [689] S. Yu, Y. Lou, D. Zhang, E. Zhou, Z. Li, C. Du, H. Qian, D. Xu, T. Gu, Bioelectrochemistry 133 (2020) 107477.
- [690] Y. Lekbach, Z. Li, D. Xu, S. El Abed, Y. Dong, D. Liu, T. Gu, S.I. Koraichi, K. Yang, F. Wang, Bioelectrochemistry 128 (2019) 193–203.
- [691] D. Xu, J. Xia, E. Zhou, D. Zhang, H. Li, C. Yang, Q. Li, H. Lin, X. Li, K. Yang, Bioelectrochemistry 113 (2017) 1–8.
- [692] H. Liu, M. Sharma, J. Wang, Y.F. Cheng, H. Liu, Int. Biodeterior. Biodegrad. 129 (2018) 209–216.
- [693] G. Fan, G., Liu, J., Zhang, G., Li, Y., Luo, G., Lian, X., & Li, Int. J. Comput. Mater. Sci. Surf. Eng. 9 (2020) 38–52.
- [694] B. Varbai, T. Pickle, K. Májlínger, Period. Polytech. Mech. Eng. 62 (2018) 247–253.
- [695] V.A. Hosseini, M.A. Valiente Bermejo, J. Gårdstam, K. Hurtig, L. Karlsson, Weld.

World 60 (2016) 233–245.

- [696] S. Gao, S. Geng, P. Jiang, G. Mi, C. Han, L. Ren, Mater. Sci. Eng. A 815 (2021) 141303.
- [697] K. RamReddy, N.K. E, R. Jeyaraam, J.R. Janaki, S.S. V., Mater. Charact. 142 (2018) 115–123.
- [698] Y. Zhou, A. Kablan, D.L. Engelberg, Mater. Charact. 169 (2020) 110605.
- [699] V. A Hosseini, L. Karlsson, Materialia 6 (2019) 100325.
- [700] D. Du, R. Fu, Y. Li, L. Jing, Y. Ren, K. Yang, Mater. Sci. Eng. A 616 (2014) 246–251.
- [701] T.H. Chen, J.R. Yang, Mater. Sci. Eng. A 338 (2002) 166–181.
- [702] B. Varbai, T. Pickle, K. Májlíng, Int. J. Press. Vessel. Pip. 176 (2019) 103952.
- [703] M. Amraei, S. Afkhami, V. Javaheri, J. Larkiola, T. Skriko, T. Björk, X.L. Zhao, Thin-Walled Struct. 157 (2020) 107072.
- [704] Y. Yang, B. Yan, J. Li, J. Wang, Corros. Sci. 53 (2011) 3756–3763.
- [705] J. Wang, M.X. Lu, L. Zhang, W. Chang, L.N. Xu, L.H. Hu, Int. J. Miner. Metall. Mater. 19 (2012) 518–524.
- [706] Y.H. Guo, L. Lin, D. Zhang, L. Liu, M.K. Lei, Metals (Basel). 8 (2018) 773.
- [707] B.J. Kutelu, E.G. Adubi, S.O. Seidu, J. Miner. Mater. Charact. Eng. 06 (2018) 531–

540.

- [708] K. Sun, M. Zeng, Y. Shi, Y. Hu, X. Shen, J. Mater. Process. Technol. 256 (2018) 190–201.
- [709] Y. Wan, W. Jiang, W. Wei, X. Xie, M. Song, G. Xu, X. Xie, X. Zhai, Mater. Sci. Eng. A 822 (2021) 141640.
- [710] C. Ma, Q. Peng, J. Mei, E.H. Han, W. Ke, J. Mater. Sci. Technol. 34 (2018) 1823–1834.
- [711] Q. Nguyen, A. Azadkhoh, M. Akbari, A. Panjehpour, A. Karimipour, J. Manuf. Process. 56 (2020) 206–215.
- [712] Y. Li, D. Parfitt, P.E.J. Flewitt, X. Hou, J. Quinta de Fonseca, B. Chen, Mater. Sci. Eng. A 796 (2020) 139992.
- [713] I. Magnabosco, P. Ferro, F. Bonollo, L. Arnberg, Mater. Sci. Eng. A 424 (2006) 163–173.
- [714] B.O. Okonkwo, H. Ming, J. Wang, F. Meng, X. Xu, E.H. Han, Int. J. Press. Vessel. Pip. 190 (2021) 104297.
- [715] G. Dak, C. Pandey, Int. J. Press. Vessel. Pip. 194 (2021) 104536.
- [716] M. Shojaati, S.F. Kashani Bozorg, M. Vatanara, M. Yazdizadeh, M. Abbasi, Int. J. Press. Vessel. Pip. 188 (2020) 104205.
- [717] A. Mortezaie, M. Shamanian, Int. J. Press. Vessel. Pip. 116 (2014) 37–46.



- [718] Z. Zhang, Z. Wang, W. Wang, Z. Yan, P. Dong, H. Du, M. Ding, *Mater. Des.* 68 (2015) 114–120.
- [719] W. Wu, S. Hu, J. Shen, *Mater. Des.* 65 (2015) 855–861.
- [720] M. Shakil, M. Ahmad, N.H. Tariq, B.A. Hasan, J.I. Akhter, E. Ahmed, M. Mehmood, M.A. Choudhry, M. Iqbal, *Vacuum* 110 (2014) 121–126.
- [721] K.R. Sreekumari, K. Nandakumar, Y. Kikuchi, *Biofouling* 17 (2001) 303–316.
- [722] X. Shi, K. Yang, M. Yan, W. Yan, Y. Shan, *Front. Mater.* 7 (2020) 1–11.
- [723] R.P. George, P. Muraleedharan, K.R. Sreekumari, H.S. Khatak, *Biofouling* 19 (2003) 1–8.
- [724] F. Li, M. An, G. Liu, D. Duan, *Mater. Chem. Phys.* 113 (2009) 971–976.
- [725] S.J. Yuan, S.O. Pehkonen, *Corros. Sci.* 51 (2009) 1372–1385.
- [726] S. Yuan, B. Liang, Y. Zhao, S.O. Pehkonen, *Corros. Sci.* 74 (2013) 353–366.
- [727] J.R. Ibars, D.A. Moreno, C. Ranninger, *Int. Biodeterior. Biodegrad.* 29 (1992) 343–355.
- [728] L. Nan, J. Cheng, K. Yang, *J. Mater. Sci. Technol.* 28 (2012) 1067–1070.
- [729] T. Wu, J. Xu, M. Yan, C. Sun, C. Yu, W. Ke, *Corros. Sci.* 83 (2014) 38–47.
- [730] V.B. Rodin, S.K. Jigletsova, V.S. Kobelev, N.A. Akimova, N. V. Aleksandrova, G.E. Rasulova, V.P. Kholodenko, *Appl. Biochem. Microbiol.* 36 (2000) 589–593.

- [731] M. Benčina, M. Resnik, P. Starič, I. Junkar, *Molecules* 26 (2021) 1418.
- [732] H. Hermawan, D. Ramdan, J.R. P. Djuansjah, *Biomed. Eng. - From Theory to Appl.* 1 (2011) 411–430.
- [733] S.R. Paital, N.B. Dahotre, *Mater. Sci. Eng. R Reports* 66 (2009) 1–70.
- [734] H. Gleiter, in: *Adv. Struct. Funct. Mater.*, Springer, Germany, 1991, pp. 1–37.
- [735] K. Wang, D. Wang, F. Han, *Acta Mech. Sin. Xuebao* 32 (2016) 181–187.
- [736] S. Dasgupta, S. Tarafder, A. Bandyopadhyay, S. Bose, *Mater. Sci. Eng. C* 33 (2013) 2846–2854.
- [737] C. Zhou, C. Deng, X. Chen, X. Zhao, Y. Chen, Y. Fan, X. Zhang, *J. Mech. Behav. Biomed. Mater.* 48 (2015) 1–11.
- [738] B. An, Z. Li, X. Diao, H. Xin, Q. Zhang, X. Jia, Y. Wu, K. Li, Y. Guo, *Mater. Sci. Eng. C* 67 (2016) 34–41.
- [739] Y. Ito, N. Hoshi, T. Hayakawa, C. Ohkubo, H. Miura, K. Kimoto, *Mater. Sci. Eng. B Solid-State Mater. Adv. Technol.* 245 (2019) 30–36.
- [740] S. Bagherifard, R. Ghelichi, A. Khademhosseini, M. Guagliano, *ACS Appl. Mater. Interfaces* 6 (2014) 7963–7985.
- [741] V.K. Truong, S. Rundell, R. Lapovok, Y. Estrin, J.Y. Wang, C.C. Berndt, D.G. Barnes, C.J. Fluke, R.J. Crawford, E.P. Ivanova, *Appl. Microbiol. Biotechnol.* 83 (2009) 925–937.

- [742] A. Nouri, C. Wen, *Introduction to Surface Coating and Modification for Metallic Biomaterials*, Elsevier Ltd, 2015.
- [743] P.G. Laing, A.B. Ferguson, E.S. Hodge, *J. Biomed. Mater. Res.* 1 (1967) 135–149.
- [744] H. Maleki-Ghaleh, J. Khalil-Allafi, M. Sadeghpour-Motlagh, M.S. Shakeri, S. Masoudfar, A. Farrokhi, Y. Beygi Khosrowshahi, A. Nadernezhad, M.H. Siadati, M. Javidi, M. Shakiba, E. Aghaie, *J. Mater. Sci. Mater. Med.* 25 (2014) 2605–2617.
- [745] S. Bagherifard, D.J. Hickey, A.C. de Luca, V.N. Malheiro, A.E. Markaki, M. Guagliano, T.J. Webster, *Biomaterials* 73 (2015) 185–197.
- [746] K.L. Ou, H.H. Chou, C.M. Liu, P.W. Peng, *Surf. Coatings Technol.* 206 (2011) 1142–1145.
- [747] H.J. Lee, J.Y. Song, B.S. Kim, *J. Chem. Technol. Biotechnol.* 88 (2013) 1971–1977.
- [748] M. Raffi, S. Mehrwan, T.M. Bhatti, J.I. Akhter, A. Hameed, W. Yawar, M.M. Ul Hasan, *Ann. Microbiol.* 60 (2010) 75–80.
- [749] U. Bogdanović, V. Lazić, V. Vodnik, M. Budimir, Z. Marković, S. Dimitrijević, *Mater. Lett.* 128 (2014) 75–78.
- [750] S. Fernando, T. Gunasekara, J. Holton, *Sri Lankan J. Infect. Dis.* 8 (2018) 2.
- [751] B. Khodashenas, *Indian Chem. Eng.* 58 (2016) 224–239.
- [752] M.C. Sportelli, M. Izzi, E.A. Kukushkina, S.I. Hossain, R.A. Picca, N. Ditaranto, N. Cioff, *Nanomaterials* 10 (2020) 1–12.

- [753] Environmental Protection Agency (EPA), List N Append. Suppl. Residual Antimicrob. Prod. Coronavirus (2021).
- [754] G. Borkow, J. Gabbay, *Curr. Chem. Biol.* 3 (2009) 272–278.
- [755] S.L. Warnes, S.M. Green, H.T. Michels, C.W. Keevil, *Appl. Environ. Microbiol.* 76 (2010) 5390–5401.
- [756] C.E. Santo, E.W. Lam, C.G. Elowsky, D. Quaranta, D.W. Domaille, C.J. Chang, G. Grass, *Appl. Environ. Microbiol.* 77 (2011) 794–802.
- [757] G. Borkow, J. Gabbay, *Curr. Chem. Biol.* 3 (2009) 272–278.
- [758] V. Doremalen, *N. Engl. J. Med.* 382 (2020) 1564–1567.
- [759] L.T. Liu, A.W.H. Chin, P. Yu, L.L.M. Poon, M.X. Huang, *Chem. Eng. J.* 433 (2022) 133783.
- [760] L. Fedrizzi, A. Molinari, F. Deflorian, A. Tiziani, P.L. Bonora, *Br. Corros. J.* 26 (1991) 46–50.
- [761] C. Lei, X. Li, X. Deng, Z. Wang, G. Wang, *Mater. Sci. Eng. A* 709 (2018) 72–81.
- [762] F. Yin, R. Xu, S. Hu, K. Zhao, S. Yang, S. Kuang, Q. Li, Q. Han, *ACS Biomater. Sci. Eng.* 4 (2018) 1609–1621.
- [763] A. Tevlek, H.M. Aydın, E. Maleki, R. Varol, O. Unal, *Surf. Coatings Technol.* 366 (2019) 204–213.
- [764] J. Sheng, J. Wei, Z. Li, K. Man, W. Chen, G. Ma, Y. Zheng, F. Zhan, P. La, Y. Zhao,

- A. Husain, J. Mater. Res. Technol. 17 (2022) 404–411.
- [765] M.J. Sohrabi, M. Naghizadeh, H. Mirzadeh, Arch. Civ. Mech. Eng. 20 (2020) 1–24.
- [766] A. Etienne, B. Radiguet, C. Genevois, J.M. Le Breton, R. Valiev, P. Pareige, Mater. Sci. Eng. A 527 (2010) 5805–5810.
- [767] F. Najafkhani, S. Kheiri, B. Pourbahari, H. Mirzadeh, Arch. Civ. Mech. Eng. 21 (2021) 1–20.
- [768] M. Shirdel, H. Mirzadeh, M.H. Parsa, Mater. Charact. 97 (2014) 11–17.
- [769] M. Shirdel, H. Mirzadeh, M. Habibi Parsa, Metall. Mater. Trans. A Phys. Metall. Mater. Sci. 45 (2014) 5185–5193.
- [770] W. Jiang, Y. Cao, Y. Jiang, Y. Liu, Q. Mao, H. Zhou, X. Liao, Y. Zhao, J. Mater. Res. Technol. 12 (2021) 376–384.
- [771] H. Miura, M. Kobayashi, T. Tsuji, T. Osuki, T. Hara, N. Yoshinaga, Mater. Trans. 63 (2022) 402–405.
- [772] R. Motallebi, Z. Savaedi, H. Mirzadeh, Curr. Opin. Solid State Mater. Sci. 26 (2022) 100992.
- [773] Z. Savaedi, R. Motallebi, H. Mirzadeh, J. Alloys Compd. 903 (2022) 163964.
- [774] N. Hirota, F. Yin, T. Inoue, T. Azuma, ISIJ Int. 48 (2008) 475–482.
- [775] O.N. Senkov, D.B. Miracle, S.A. Firstov, Metallic Materials with High Structural Efficiency, Kluwer Academic Publishers, 2004.

- [776] A.T. Krawczynska, S. Gierlotka, P. Suchecki, D. Setman, B. Adamczyk-Cieslak, M. Lewandowska, M. Zehetbauer, J. Mater. Sci. 53 (2018) 11823–11836.
- [777] T. Xi, M. Babar Shahzad, D. Xu, J. Zhao, C. Yang, M. Qi, K. Yang, Mater. Sci. Eng. A 675 (2016) 243–252.
- [778] J.W. Bai, P.P. Liu, Y.M. Zhu, X.M. Li, C.Y. Chi, H.Y. Yu, X.S. Xie, Q. Zhan, Mater. Sci. Eng. A 584 (2013) 57–62.
- [779] A. Umantsev, G.B. Olson, Scr. Metall. Mater. 29 (1993) 1135–1140.
- [780] H. Miura, M. Kobayashi, C. Watanabe, N. Sugiura, N. Yoshinaga, Mater. Trans. 61 (2020) 416–419.
- [781] M. Naghizadeh, H. Mirzadeh, Metall. Mater. Trans. A Phys. Metall. Mater. Sci. 47 (2016) 5698–5703.
- [782] J. Mizera, J.W. Wyrzykowski, K.J. Kurzydłowski, Mater. Sci. Eng. 104 (1988) 157–162.
- [783] A. Kisko, T. Juho, D.A. Porter, L.P. Karjalainen, ISIJ Int. 55 (2015) 2217–2224.
- [784] M. Tikhonova, A. Belyakov, R. Kaibyshev, Mater. Sci. Forum 783–786 (2014) 1021–1026.
- [785] L.S. Aota, P. Bajaj, K.D. Zilnyk, D. Ponge, H.R.Z. Sandim, Materialia 20 (2021) 101243.
- [786] B. Murgas, B. Flipon, N. Bozzolo, M. Bernacki, Materials (Basel). 15 (2022) 2434.

- [787] Y. Liu, M. Militzer, M. Perez, *Materials* (Basel). 12 (2019) 4048.
- [788] P.R. Rios, D. Zöllner, *Mater. Sci. Technol.* (United Kingdom) 34 (2018) 629–638.
- [789] T. Oršulová, P. Palček, J. Kúdelčík, *Prod. Eng. Arch.* 14 (2017) 15–18.
- [790] C. de S. Pereira Mendonça, A.F. Oliveira, L.A. Oliveira, M.R. da Silva, M. de L.N. Motta Melo, G. Silva, *Mater. Res.* 21 (2018) 1–6.
- [791] T. Kobayashi, 92 (2003) 92–96.
- [792] L.A.A. Warnes, H.W. King, *Cryogenics* (Guildf). 16 (1976) 659–667.
- [793] M.J.R. Sandim, V. Mauro, S.S.M. Tavares, K.D. Zilnyk, H.R.Z. Sandim, J. Magn. Mater. 539 (2021) 168336.
- [794] S.S.M. Tavares, P.D.S. Pedrosa, J.R. Teodósio, M.R. Da Silva, J.M. Neto, S. Pairis, *J. Alloys Compd.* 351 (2003) 283–288.
- [795] I.R. Souza Filho, M.J.R. Sandim, R. Cohen, L.C.C.M. Nagamine, J. Hoffmann, R.E. Bolmaro, H.R.Z. Sandim, J. Magn. Mater. 419 (2016) 156–165.
- [796] S. Kobayashi, N. Kikuchi, S. Takahashi, Y. Kamada, H. Kikuchi, *J. Appl. Phys.* 108 (2010) 043904.
- [797] N. Mubarak, H.A. Notonegoro, *FLYWHEEL J. Tek. Mesin Untirta* (2021) 26–30.
- [798] T. Oršulová, P. Palček, M. Roszak, M. Uhrčík, M. Smetana, J. Kúdelčík, *Procedia Struct. Integr.* 13 (2018) 1689–1694.

- [799] S.S.M. Tavares, J.M. Pardal, J.A. de Souza, J.M. Neto, M.R. da Silva, J. Alloys Compd. 416 (2006) 179–182.
- [800] S.S.M. Tavares, J.M. Pardal, J.L. Guerreiro, A.M. Gomes, M.R. da Silva, J. Magn. Mater. 322 (2010) L29–L33.
- [801] L. Zhang, S. Takahashi, Y. Kamada, H. Kikuchi, K. Mumtaz, K. Ara, M. Sato, AIP Conf. Proc. 760 (2005) 1576–1583.
- [802] H. Alinejad, M. Abbasi, J. Magn. Mater. 537 (2021) 168244.
- [803] A. Mitra, P.K. Srivastava, P.K. De, D.K. Bhattacharya, D.C. Jiles, Metall. Mater. Trans. A Phys. Metall. Mater. Sci. 35 A (2004) 599–605.
- [804] Q. Mao, Y. Zhang, J. Liu, Y. Zhao, Nano Lett. 21 (2021) 3191–3197.
- [805] L. Li, B. Xie, Q. Fang, J. Li, Metall. Mater. Trans. A Phys. Metall. Mater. Sci. 52 (2021) 439–448.



1. **Dr Liliana Romero-Resendiz** is a postdoctoral researcher at the Department of Materials Science and Engineering at the City University of Hong Kong, China. She obtained her PhD in Materials Science and Engineering under a project co-guided by the National Autonomous University of Mexico, Mexico, and the Polytechnic University of Valencia, Spain. She performed as a lecturer at the Engineering college of the National Autonomous University of Mexico. Her research interest includes studying the processing-microstructure-properties relationship of heterostructured and nanostructured alloys with advanced structural performance, as well as developing scalable and low-cost biomaterials for antimicrobial and biomedical implant applications. More details:

<https://scholar.google.com.mx/citations?user=c8S8LdYAAAAJ&hl=es>. Contact:

[lromeror@cityu.edu.hk](mailto:lromeror@cityu.edu.hk)

2. **Dr Moustafa El-Tahawy** is a lecturer at the Physics Department, Faculty of Science of the Tanta University, Egypt. He obtained his PhD in Materials Science and Solid-State Physics from the Eötvös Loránd University, Hungary. His research lines include the study of the physical and mechanical properties of ultrafine-grained (UFG) and nanocrystalline (NC) materials, including light alloys, steel, and heterogeneous materials, for different structural applications produced by severe plastic deformation (SPD) techniques. More details:

<https://scholar.google.com/citations?hl=en&user=XGGG2->

[kAAAAJ&view\\_op=list\\_works&sortby=pubdate](https://scholar.google.com/citations?hl=en&user=XGGG2-kAAAAJ&view_op=list_works&sortby=pubdate). Contact: [moustafa.el-](mailto:moustafa.el-tahawy@science.tanta.edu.eg)

[tahawy@science.tanta.edu.eg](mailto:tahawy@science.tanta.edu.eg)

3. **Dr Tianlong Zhang** is currently a postdoctoral researcher at the Department of Materials Science and Engineering at the City University of Hong Kong, China. He

obtained his PhD degree from the City University of Hong Kong and Xi'an Jiaotong University under the supervision of Prof. C.T. Liu and Prof. Yunzhi Wang. He mainly focuses on designing advanced alloys with heterogeneous microstructures and supreme properties by integrating the additive manufacturing (3D printing) technology, phase-field simulation method, and CALPHAD approaches and has published five papers in Science, Acta Mater., Scr. Mater., etc., as the first author. More details: <https://scholar.google.com/citations?user=80Zw31AAAAAJ&hl=zh-CN>. Contact: [tzhang289@cityu.edu.hk](mailto:tzhang289@cityu.edu.hk)

4. **Dr Mariana C. Rossi** is a postdoctoral researcher at the Munir Rachid Corrosion Laboratory of the Department of Materials Engineering, Federal University of São Carlos, Brazil. She obtained her PhD from the São Paulo State University. She seeks for understanding the surface physics and chemistry of alloys in biological environments. She is a specialist in the in-vitro cell behaviour assessment of titanium alloys produced by casting, additive manufacturing, or powder metallurgy for biomedical implants. Currently, she is starting a new research line on bioactive surface treatments for titanium biomedical devices. More details: <https://bv.fapesp.br/en/pesquisador/687596/mariana-correa-rossi/>. Contact: [mariana.rossi@unesp.br](mailto:mariana.rossi@unesp.br)

5. **Professor Diana M. Marulanda-Cardona** is a lecturer at the Faculty of Engineering, Universidad Militar Nueva Granada, Colombia. She obtained her PhD degree from the National University of Colombia, Colombia. Her research lines include the design of thermomechanical routes to improve the mechanical behaviour of widely used metallic materials through severe plastic deformation techniques and surface treatments by physical and chemical deposition methods. More details:

<https://scholar.google.com/citations?user=02wcDgkAAAAJ&hl=es>, Contact:

[diana.marulanda@unimilitar.edu.co](mailto:diana.marulanda@unimilitar.edu.co)

6. **Professor Tao Yang** is currently an Assistant Professor at the Department of Materials Science and Engineering at the City University of Hong Kong, China. His research focuses on the innovative design and fabrication of advanced metallic materials for structural and functional applications, including the intermetallic compounds, high-entropy alloys, heterogenous materials, high-temperature superalloys, nano-steels, etc. His current work is primarily focused on the control of nanoprecipitation, grain-boundary characters, and atomic structures by using multiple state-of-the-art techniques, such as the 3D atom probe tomography (3D-APT), high-resolution transmission electron microscope (HETEM), and additive manufacturing. More details: [https://scholars.cityu.edu.hk/en/persons/tao-yang\(37757c09-68fb-417f-b3f6-40a6292b24e2\).html](https://scholars.cityu.edu.hk/en/persons/tao-yang(37757c09-68fb-417f-b3f6-40a6292b24e2).html). Contact: [taoyang6@cityu.edu.hk](mailto:taoyang6@cityu.edu.hk)

7. **Professor Vicente Amigó-Borrás** is a chair professor at the Polytechnic University of Valencia, Spain. He was Director of the Institute of Materials Technology of the Polytechnic University of Valencia from 2012 to 2020. He obtained his PhD degree from the Polytechnic University of Valencia in 1986. His research lines include the design and development of innovative metallic biomaterials with low-elastic modulus to decrease the failure rate of the current biomedical implants. He also has plenty of experience in the mechanical assessment of metallic materials with superior mechanical properties obtained by severe plastic deformation, surface treatments, additive manufacturing, powder metallurgy, or casting combined with

thermal treatments. More details: <https://www.upv.es/ficha-personal/VAMIGO>.

Contact: [yamigo@mcm.upv.es](mailto:yamigo@mcm.upv.es)

- 8. Professor Yi Huang** has been a Senior Lecturer in Engineering at the Bournemouth University, UK, since 2018. She received her PhD in Metallurgy and Materials from the University of Birmingham. After that, she worked as a research fellow and senior research fellow at the University of Southern California, University of Cambridge, University of Strathclyde, and the University of Southampton. Prof. Huang's research covers a wide range of materials (Ni-based superalloys, Al alloys, Mg alloys, Ti alloys, Fe alloys and metal matrix composites). She is interested in the relationship between the microstructure and mechanical properties of advanced engineering materials for aerospace, automotive, marine and biomedical applications. Prof. Huang is a Fellow of the Institute of Materials, Minerals and Mining (IMMM) and a member of EPSRC Peer Review College. According to Google Scholar, she has published more than 150 peer-reviewed journal papers with more than 3,300 citations and an h-index of 34. More details:

<https://staffprofiles.bournemouth.ac.uk/display/yhuang2>. Contact:

[yhuang2@bournemouth.ac.uk](mailto:yhuang2@bournemouth.ac.uk)

- 9. Professor Hamed Mirzadeh** is an associate professor at the University of Tehran, Iran. He is the Prominent Young Scientist of the Academy of Sciences of Iran and an Editorial Member of prestigious journals such as Metals and Materials International, Journal of Ultrafine Grained and Nanostructured Materials, and Journal of Magnesium and Alloys. He is also head of the Advanced Steels and Thermomechanically Processed Engineering Materials Laboratory. Formerly, he was a researcher at Universitat Politècnica de Catalunya and Isfahan University of

Technology. His research interest includes thermomechanical processing, advanced high-strength steels (AHSS), magnesium-based alloys and composites, high-entropy alloys (HEAs), superalloys, mechanical properties, heat treatment, phase transformations, metalforming, hot deformation, constitutive modeling, physical metallurgy, mechanical alloying, severe plastic deformation (SPD), and superplasticity. According to Google Scholar, his work has gained more than 6,400 citations and an h-index of 47. More details: <https://meteng.ut.ac.ir/en/~hmirzadeh>.  
Contact: [hmirzadeh@ut.ac.ir](mailto:hmirzadeh@ut.ac.ir)

**10. Professor Irene J. Beyerlein** is a Mehrabian Interdisciplinary professor at the College of Engineering and a professor at the Mechanical Engineering and Materials Department of the University of California at Santa Barbara, USA. She obtained her PhD in Theoretical and Applied Mechanics from Cornell University. Her scientific contributions have gained multiple honours as Fellow of the Materials Research Society, Light Metals Magnesium Best Paper - Fundamental Research Award, Brinacombe Medal from The Minerals, Metals, and Materials Society (TMS), TMS/AIME Champion H. Mathewson Award, NSF Advanced STEM Professor Fellowship from the University of New Hampshire, Visiting Professor Fellowship, at the University of Lorraine, Metz, LANL Distinguished Postdoc Mentor Award, International Journal of Plasticity Young Researcher Award, and LANL Fellow's Prize for Research. Her research interest includes radically improving the mechanical performance of advanced materials via the multiscale understanding of processing-microstructure-property relationships. Her current research brings together multiscale modeling, experimentation, and theory to guide the design of materials manufacturing processes or microstructures for target

properties. According to Google Scholar, her work has gained more than 23,500 citations and an h-index of 85. More details:

<https://labs.me.ucsb.edu/beyerlein/irene/>. Contact: [beyerlein@engineering.ucsb.edu](mailto:beyerlein@engineering.ucsb.edu)

**11. Professor Jacob C. Huang** is the Executive Director of the Hong Kong Institute for Advanced Study of the City University of Hong Kong (CityU) and chair professor of Materials Science at the CityU, China. He received his PhD degree from the University of California, Los Angeles, in 1986. He was a postdoctoral research fellow in Los Alamos National Laboratory, USA, from 1987 to 1989 and advanced to associate, full, and chair professor in the NSYSU in 1989, 1994, and 2006, respectively. He has acted as department chair, dean, chair of the institutional research (IR) office, vice-president at the National Sun Yat-Sen University (NSYSU), program manager at the National Science Council (NSC), and vice-chair of MRS-T society in Taiwan. He has been awarded many times by NSC and the Ministry of Education of Taiwan, TECO Award, Ho-Jin-Tua Award, Lu-Chih-Ming Award, elected as MRS-T and ASM Fellow, and awarded as National Chair Professor in Taiwan. His research areas include thin film metallic glasses, multilayer and interface study, low density high entropy alloys, 3D printing additive manufacture, biocompatible implant-used gradient porous Ti foams, and nanocrystalline materials. According to Google Scholar, his papers have gained more than 16,300 citations and an h-index of 60. More details:

<https://www.ias.cityu.edu.hk/en/profile/jacob-huang>. Contact: [chihuang@cityu.edu.hk](mailto:chihuang@cityu.edu.hk)

**12. Professor Terence G. Langdon** is a professor of Materials Science (since 2005) and Director of the Centre for Bulk Nanostructured Materials at the University of





Southampton, UK, William E. Leonhard Professor of Engineering at the University of Southern California, USA (since 2003), and professor at the Department of Materials Science, Mechanical Engineering and Earth Sciences of the University of Southern California, USA (since 1976). He obtained his PhD degree in Physical Metallurgy from the Imperial College of the University of London, U.K. (1965). He has been included in the highly cited researchers list by Thomson Reuters/Institute for Scientific Information (ISI) due to high citations received during 11 years (2002 to 2012) and ranked by ISI as #2 and #3 worldwide most cited scientist in the field of materials science due to his papers published in the periods 1996-2006 and 1981-2001, respectively. The scientific research of Prof. Langdon is highly influential in the investigations of the mechanical behaviour of severe plastic deformed metallic materials. Prof. Langdon has published more than 1,100 international papers with a total number of citations greater than 89,000 and an h-index of 141 on Google Scholar. More details:

<https://www.southampton.ac.uk/engineering/about/staff/langdon.page>. Contact: [langdon@soton.ac.uk](mailto:langdon@soton.ac.uk)

- 13. Professor Yuntian T. Zhu** is a visiting fellow at the Hong Kong Institute for Advanced Study and chair professor of the Materials Science and Engineering Department of the City University of Hong Kong, China (since 2020). He is the founding Editor-in-Chief of the Materials Research Letters journal (since 2012). He was a Distinguished Professor at North Carolina State University, USA (2012 to 2020). He was appointed as an Adjunct Professor and Director at Nano Heterogeneous Materials Center of the Nanjing University of Science and Technology, China (2017-2020). Professor Zhu received his PhD degree in

Materials Science and Engineering from the University of Texas at Austin (1994). He received the TMS SMD Distinguished Scientist/Engineer Award, ASM International Albert Sauveur Award, TMS Leadership Award, and IUMRS Sômiya Award, among others. He was listed among Highly Cited Researchers in 2014 and 2016 by Thomson Reuters (ISI). His research focuses on the deformation mechanisms at the dislocation level and mechanical behaviours of heterostructured materials and nano/ultrafine-grained materials. He has a primary interest in fundamental aspects of materials science and designing materials with superior strength and ductility. According to Google Scholar, his publications have been collectively cited over 48,700 times with an h-index of 115. More details: <https://www.ias.cityu.edu.hk/en/profile/id=49>. Contact: [y.zhu@cityu.edu.hk](mailto:y.zhu@cityu.edu.hk)



 A portrait of Dr. Liliana Romero-Resendiz, a woman with dark hair pulled back in a bun, wearing glasses and a dark, sleeveless top. She is smiling at the camera.	<b>1. Dr Liliana Romero-Resendiz</b>
 A portrait of Professor Moustafa El-Tahawy, a man with short dark hair, wearing a dark suit jacket, a light pink shirt, and a pink tie. He is looking directly at the camera.	<b>2. Professor Moustafa El-Tahawy</b>
 A portrait of Dr. Tianlong Zhang, a man with short dark hair, wearing a dark collared shirt. He is looking directly at the camera.	<b>3. Dr Tianlong Zhang</b>
 A portrait of Dr. Mariana C. Rossi, a woman with long dark hair, wearing a dark jacket and a light-colored scarf. She is smiling at the camera.	<b>4. Dr Mariana C. Rossi</b>



**5. Professor Diana M. Marulanda-Cardona**



**6. Professor Tao Yang**



**7. Professor Vicente Amigó-Borrás**



**8. Professor Yi Huang**



**9. Professor Hamed Mirzadeh**



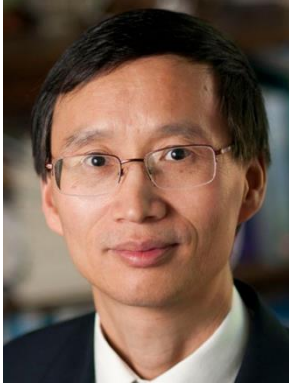
**10. Professor Irene J. Beyerlein**



**11. Professor Jacob C. Huang**



**12. Professor Terence G. Langdon**



**13. Professor Yuntian T. Zhu**



- Heterostructures (HS) reduce strength-ductility trade-off on stainless steel (SS)
- The processing-microstructure-properties relationship on HS SS was discussed
- Critical discussion of experimental and modelling findings on HS SS
- Multidisciplinary perspectives to guide future works on HS SS are discussed
- This review is a reference for understanding and designing multi-functional HS SS

**Declaration of interests**

☒The authors declare that they have no known competing financial interests or personal relationships that could have appeared to influence the work reported in this paper.

☐The authors declare the following financial interests/personal relationships which may be considered as potential competing interests: